Thesis Report

On

Experimental Investigation on Micro Electrochemical Drilling of Hybrid Al/(Al_2O_3p-SiCp-Cp)-MMC

Submitted in fulfillment of the requirement for the award of the degree of

DOCTOR OF PHILOSOPHY
In
(Mechanical Engineering)

Submitted By

Charanjit Singh
Reg. No. 951008002

THAPAR INSTITUTE
OF ENGINEERING & TECHNOLOGY
(Deemed to be University)

DEPARTMENT OF MECHANICAL ENGINEERING

THAPAR INSTITUTE OF ENGINEERING & TECHNOLOGY

PATIALA– 147004, PUNJAB, INDIA

May 2018

LIST OF RESEARCH PUBLICATIONS

Research Publications in Journals

1. Charanjit Singh Kalra, Vinod Kumar and Alakesh Manna, Analysis of electrochemical behavior on micro-drilling of cast hybrid Al/ (Al2O3p+SiCp+Cp)-MMC using micro-ECM process. Journals of Materials: Design and Applications, IMechE (L), Sage Publications, U.K., October 2015, DOI: 10.1177/1464420715615907, **(SCI-Indexed; Thomson Reuters).**

2. Charanjit Singh Kalra, Vinod Kumar and Alakesh Manna, The wear behavior of Al/(Al_2O_3+SiC+C) hybrid composites fabricated stir casting assisted squeeze, Particulate Science and Technology, Taylor & Francis Publications, USA, Accepted in August 2017, **(SCI-Indexed; Thomson Reuters).**

3. Charanjit Singh Kalra, Vinod Kumar and Alakesh Manna, Multi-response optimization of electrochemical micro machining of hybrid MMC using desirability function approach. International Journal of Electrochemical Science, Communicated in March 2017, **(SCI-Indexed; Thomson Reuters).**

4. Charanjit Singh Kalra, Vinod Kumar and Alakesh Manna, Response surface methodology based optimization of electrochemical micromachining process. Advances in Mechanical Engineering, Sage Publications, U.K., resubmitted after 1st revision in August 2017, **(SCI-Indexed; Thomson Reuters).**

5. Charanjit Singh Kalra, Vinod Kumar and Alakesh Manna, An Investigation on the micro electrochemical machining of Aluminium based hybrid composites using Box Behnkan Design, International Journal of Mechanical Engineering and Management Technology, Inderscience Publications, Communicated in August 2017.

6. Charanjit Singh Kalra, Vinod Kumar and Alakesh Manna, Microstructure Analysis and Material Transformation of Hybrid Al/Al_2O_3/Sic/C Metal Matrix Composites after Electrochemical Micromachining Process. Journal of Mechanical Engineering, Communicated in July 2017, **(SCI-Indexed; Thomson Reuters).**

Research Publications in Conferences

1. Charanjit Singh Kalra, Vinod Kumar and Alakesh Manna, Experimental investigation on wear test and electrochemical micro machining of $Al/Al_2O_3/SiC/C$ hybrid MMCs. 25^{th} Annual International Conference on COMPOSITES/NANO ENGINEERING (ICCE-25), being held from 16 to 22 July 2017 at Rome, Italy, Paper accepted.

2. C.S. Kalra, Alakesh Manna and V.K. Singla, An experimental investigation during micro drilling of hybrid Al/(Al2O3p+SiCp+Cp)-MMC on developed ECMM setup. 5th International & 26th National Conference on All India Manufacturing Technology, Design and Research Conference, 12-14 December 2014, 643-1 to 643-6, Indian Institute of Technology Guwahati, Assam.

3. C.S. Kalra, Alakesh Manna and V.K. Singla, An Experimental Investigation during Micro Drilling of Hybrid Al/(Al_2O_3p+SiCp+Cp)-MMC on Fabricated ECMM Setup. International Conference on Precision Meso, Micro and Nano Engineering (COPEN-2013), NIT, Calicut, pp. 149-155, Kerala, India.

4. C. S. Kalra, Alakesh Manna, and V. K. Singla, Micro drilling of hybrid Al/(Al_2O_3+SiC+C)-MMC on design and fabricated ECMM setup. International Conference on Advancements and Futuristic Trends in Mechanical and Materials Engineering (October 3-6, 2013), Punjab Technical University, Jalandhar, pp. 234-236, Punjab-144601, India.

ACKNOWLEDGEMENT

I would like to express a deep sense of gratitude and thank greatly to my supervisors **Dr. Vinod Kumar,** Associate Professor, Department of Mechanical Engineering, Thapar Institute of Engineering & Technology, Patiala and **Dr. Alakesh Manna,** Professor, Department of Mechanical Engineering, PEC (Deemed to be University), Chandigarh for their sincere and invaluable guidance, support, suggestion and attitude which inspired me to submit thesis in present form. Their dynamism and diligent enthusiasm have been an innate intelligent application has crowned my task with task.

I am grateful to **Dr. Prakash Gopalan,** Director, Thapar University and Dr. O. P. Pandey, Dean Research and Sponsored Projects, Thapar Institute of Engineering & Technology,, for encouraging me time to time and providing necessary guidance to complete my work. I wish to express my warm and sincere thanks to DRC Chairman **Dr. S.K. Mohapatra,** Senior Professor and Head, Department of Mechanical Engineering, Thapar Institute of Engineering & Technology, and members of DRC Dr. V.K. Jain and Dr. Anant Kumar Singh who helped me in exploring new idea and concepts which had remarkable influence on my thesis. I am also very thankful to entire and staff member of Mechanical Engineering department of Thapar Institute of Engineering & Technology, for their cooperation.

I would be also like to express my sincere thanks to Mr. Harshit Dewan, Mr. Anup Malik and Mr. Gurpreet Singh for their valuable guidance and support during fabrication of my setup. It's because of their support through technical discussion I was able to develop my experimental setup.

I really appreciate the help provided by Mr. Ram Niranjan, Mr. Vinod Kumar and Mr. Kuwar Bisht in conduction experiments. The service of other staff member of Mechanical Engineering Department, PEC Engineering College is also acknowledged.

I am also thankful to all my family members specially my father Harbans Singh and mother Paramjeet Kaur for their constant support during difficult times and always motivated me to complete this dissertation. I am also thankful to my wife Er. Saravjeet Kaur and my son Gurjas Singh for bearing with me during conducting experiments and writing of this thesis and providing all kinds of support when needed.

Finally, I am indebted to all whosoever have contributed in this thesis work and friendly.

Charanjit Singh

CERTIFICATE

Certified that the thesis entitled "**Experimental Investigation on Micro Electrochemical Drilling of Hybrid Al/(Al_2O_{3p}-SiC_p-C_p)–MMC**" which is being submitted by "Mr. Charanjit Singh" to the Department of Mechanical Engineering of Thapar Institute of Engineering & Technology,, Patiala, in the fulfillment of the requirements for the award of degree of **DOCTOR OF PHILOSOPHY** is record of bonafide research work carried out by him under our guidance and supervision. The matter presented in this thesis has not been submitted for the award of any other degree of this or any other University / Institute.

09/05/2018

Dr. Vinod Kumar
Associate Professor
Mechanical Engineering Department
Thapar Institute of Engineering & Technology
Patiala

09/5/2018

Dr. Alakesh Manna
Professor
Mechanical Engineering Department
PEC Engineering College
Chandigarh

ABSTRACT

Composite material is a heterogeneous solid consisting of two or more than two different materials that are mechanically or metallurgical bonded together. The industrial applications of Al-MMC's are gradually increasing due to of their surprising physical and mechanical properties as compared to monolithic materials. Again, physical and mechanical properties of these composites can be enhanced by adding two or more than two different reinforced materials i.e. hybriding in composite. As hybrid Al/(Al_2O_{3p}+SiC_p+C_p)-MMC has three distinct reinforced abrasive particles which accessible better properties and strength to weight ratio as compared to any commercially available Al-MMC's. The addition of Al_2O_3 and SiC reinforced particles with Al-matrix improves the wear resistance of the composite. Presence of carbon particles in hybrid composite reduces the coefficient of friction, enhanced resistance of wear. A composite has high damping capacity if it is made of both SiC and Gr reinforcement particles. The workpiece specimens were prepared from fabricated Al/SiC-MMC, Al/Al_2O_3p-MMC, Al/Cp-MMC, Al/(Al_2O_3p+SiCp)-MMC, Al/(Al_2O_3p+Cp)-MMC, Al/(SiCp+Cp)-MMC, and Al/(Al_2O_3p+SiCp+Cp)-MMC samples. These workpiece specimens were used for wear test and mechanical properties analysis. The liquid stir cast technique was utilized for fabrication of metal matrix composites (MMCs) samples with varying the weight fraction of reinforced particles alumina (Al_2O_3), silicon carbide (SiC) and carbon (C). The fabricated MMCs and hybrid MMCs samples were tested to analyze the mechanical properties and wear test. The impact load was improved by 7.42%, 11.31% and 10.58% for hybrid Al/(10 wt% Al_2O_3 + 10 wt% SiC + 5 wt% C)-MMC over Al/(10 wt% Al_2O_3 + 10 wt% SiC)-MMC, Al/(10 wt% Al_2O_3 + 5 wt% C)-MMC and Al/(10 wt% SiC + 5 wt% C)-MMC respectively. The hardness was improved by 30.39% and 31.41% for hybrid Al/(10 wt% Al_2O_3p + 10 wt% SiCp + 5 wt% Cp)-MMC over Al/(10 wt% Al_2O_3p + 5 wt% Cp)-MMC and Al/(10 wt% SiCp + 5 wt% Cp)-MMC respectively. From SEM micrograph of wear surface, it was noticed that some hard particles were pulled out, as a result formation of grooves. It is observed that the surface of composite Al/(10 wt% SiCp + 3 wt% Cp + 5 wt% Al_2O_3p)- MMC and Al/(15 wt% SiCp + 5 wt% Cp + 7.5 wt% Al_2O_3p)- MMC were rough with deep grooves as compared to composite specimen Al/(20 wt% SiCp + 7.5 wt% Cp + 10 wt% Al_2O_3p)-MMC. The surface of Al/(20 wt% SiCp + 7.5 wt% Cp + 10 wt% Al_2O_3p)-MMC was fine grooves. The surface of composite Al/(20 wt% SiCp + 7.5 wt% Cp + 10 wt% Al_2O_3p)- MMC was smooth, it may be due to the presence of carbon. It smears out during

sliding and acts as a layer, protecting the specimen from direct contact with the disc as a result increase the wear resistance.

However, the presence of hard and abrasive reinforcement in MMC reduces the machinability of the composites. The finishing of difficult to machine material in micro domain requires application of special technique. To fulfil the aim a special technique in machining i.e. an electrochemical micro machining (ECMM) set-up has been fabricated and utilized for micro drilling of Al/(Al_2O_3p+SiCp+Cp)-MMC. The feasibility test was carried out on fabricated set-up to identify the suitability of the fabricated set-up for finishing of liquid stir cast hybrid Al/(Al_2O_3p+SiCp+Cp)-MMC workpiece in micro domain. The developed ECMM set-up has different parameters such as DC supply voltage, supply current, pulse on time, pulse off time, electrolyte concentration and electrolyte flow rate. At high supply voltage, increase the impact of discharge energy in the machining area, this leads to increase the dissolution rate of metal thereby deteriorates the machined surface. The machined surface was poor and it may be due to the presence of small particles of sodium and chloride on the periphery of machined hole. Taguchi's methods based design of experiments, L_{27} (3^{13}) orthogonal array and response surface methodology (RSM) Box–Behnken design were employed and made out the experimental planned accordingly. The percentage of contribution of each parameter was evaluated for various output quality characteristics. It was found that the parameters such as supply voltage, pulse on time and electrolyte concentration are the most significant parameters for response characteristics i.e. MRR, EWR, TC and SR.

The surface roughness height, Ra (μ) increases with increase in electrolyte concentration, supply voltage and pulse on time. It may be due to the non-uniform metallic dissolution of material. The large number of ions associated in the inter electrode gap at supply of higher concentration of electrolyte and higher voltage. The material removal rate and electrode wear rate both increase with increase in supply voltage, electrolyte concentration and pulse-on time. These may be due to increase of current density, which in turn increases the ionization of electrolyte. The flow rate of electrolyte is an important parameter that directly affects the quality of micro-holes. The debris generated during micro electrochemical machining usually does not flush away when machining operation was carried out at low flow rate of electrolyte. Based on the RSM methodology, the optimal combination for multi response optimization of ECMM parameters for effective machining of hybrid Al/MMC is supply current (IP) 0.5 A,

supply voltage (V) 2.03 V, pulse on time (Ton) 3.38 μs, pulse off time (Toff) 6.26 μs, electrolyte concentration (EC) 14.38 g/l, and electrolyte flow rate (Fr) 0.60 l/sec.

Micro machined surface was analyzed through SEM and EDS photographs. The deposition of debris, voids and micro-cracks were identified on some of the machined surfaces. Some deeper and wider micro cracks were also identified on the machined surface and it may be due to supply of high peak current. The formation of ferropargasite chlorous compound was identified, it was due to chemical dissolution of ferrous material and reaction with sodium chloride. The micro tool worn out rate increases with increase in pulse-on time. From EDS analysis, it is noticed that the reinforced particles presence in hybrid MMC deposited on micro tool. This is due to the melting and re-solidification of hybrid Al/MMC during machining by micro sparking at high supply voltage and pulse on time.

LIST OF FIGURES

LIST OF TABLES

LIST OF ABBREVIATIONS

PMC	Polymer Matrix Composite
MMC	Metal Matrix Composites
CMC	Ceramic Matrix Composite
AMC	Aluminum Matrix Composites
Al_2O_3p	Aluminum Oxide Particulates
SiCp	Silicon Carbide Particulates
Cp	Carbon Particulates
ECM	Electrochemical Machining
ECMM	Electrochemical Micro Machining
MRR	Material Removal Rate
EWR	Electrode Wear Rate
SR	Surface Roughness
Ra	Average Roughness Height
TC	Taper Cut
OC	Over Cut
MSAZ	Micro Spark Affected Zone
Ip	Supply Current
V	Supply Voltage
Ton	Pulse On Time
Toff	Pulse Off Time
EC	Electrolyte Concentration
g/*l*	Gram per liter
FR	Flow Rate
l/min	Liter per Minute
RSM	Response Surface Methodology
BBD	Box–Behnken Design
DC	Direct Current
Si	Silicon
Fe	Iron
Cu	Copper
Mo	Molybdenum
Mg	Manganese

Cr	Chromium
Zn	Zink
Ti	Titanium
Fe_2O_3	Iron Oxide
TiO_2	Titanium Oxide
Pb	Lead
Na_2O	Sodium Oxide
Cl	Chlorine
SO_4	Sulfate
wt%	Weight Fraction
CAD	Computer Aided Design
UTS	Ultimate Tensile Strength
SEM	Scanning Electron Microscope
EDS	Energy Dispersive Spectrometer
XRD	X-ray Diffraction Analysis
AC	Alternative Current
IEG	Inter Electrode Gap
µm	Micro Meter
NaCl	Sodium Chloride
D_{avg}	Average Diameter
R_i	Inlet Radius
R_{avg}	Average Radius
D_e	Exit Diameter
D_i	Inlet Diameter
S/N ratio	Signal to Noise Ratio
ANOVA	Analysis of Variance
DF	Degree of Freedom
Seq SS	Sequential of Sum of Squares
Adj SS	Adjacent of Sum of Squares
Adj MS	Adjacent of Mean of Squares

TABLE OF CONTENTS

Chapter 1

INTRODUCTION AND LITERATURE REVIEW

1.1 COMPOSITE MATERIALS

A composite material is a combination of two or more materials chemically distinct and having different properties mechanically or metallurgical bonded together. The properties and structural performance of the composites are superior to those of its individual constituents. Composite materials are multi phase materials of heterogeneous structure obtained through the artificial combination of different materials in order to attain properties that the individual component by itself cannot attain.

Composite materials should be distinguished from alloys, which can comprise two more components but are formed naturally through processes such as casting. Composite materials can be tailored for various properties by appropriately choosing their components, their proportions, their distributions, their morphologies, their crystallographic textures, as well as the structure and composition of the interface between components. Due to this strong tailorability, composite materials can be designed to satisfy the needs of technologies relating to the aerospace, automobile, electronics, construction, energy, biomedical and other industries. As a result, composite materials constitute most commercial engineering materials [6].

1.2 MATRIX PHASE

The matrix is the monolithic material into which the reinforcement is embedded, and is completely continuous e.g. metallic, ceramic, and polymer. This means that there is a path through the matrix to any point in the material, unlike two materials sandwiched together. In structural applications, the matrix is usually a lighter metal such as aluminium, magnesium, or titanium, and provides a compliant support for the reinforcement example of metallic matrix.

1. The primary phase, having a continuous character,
2. Usually more ductile and less hard phase,
3. Holds the reinforcing phase and shares a load with it.

- Polymeric matrix: thermoplastic resins (polypropylene, polyphenylene, sulfone, polyamide, polyetheretherketone, etc.) and thermoset resins (polyesters, phenolics, melamines, silicones, polyurethanes, epoxies).
- Ceramic matrix: silicon carbide, carbon. They can be used at high temperatures
- Metallic matrix: aluminum alloys, titanium alloys, oriented eutectics.

1.3 REINFORCING PHASE

The reinforcement material has embedded into the matrix. The reinforcement does not always serve a purely structural task (reinforcing the compound), but is also used to change physical properties such as wear resistance, strength, friction coefficient, or thermal conductivity. The reinforcement can be either continuous, or discontinuous in the form of powder or fiber, or short fibers.

1. Second phase (or phases) is imbedded in the matrix in a discontinuous form,
2. Usually stronger than the matrix, therefore it is sometimes called reinforcing phase.

The composites typically have a fiber or particle phase that is stiffer and stronger than the continuous matrix phase. Many types of reinforcements also often have good thermal and electrical conductivity, a coefficient of thermal expansion (CTE) that is less than the matrix, and/ or good wear resistance. The bonding between reinforcement and matrix has created during the manufacturing phase of the composite material. This has fundamental influence on mechanical properties of the composite material.

1.4 CLASSIFICATION OF COMPOSITES

(a) On the basis of Matrix:

1. Metal Matrix Composites (MMC)

Metal Matrix Composites are composed of a metallic matrix (aluminum, magnesium, iron, cobalt, copper) and a dispersed ceramic (oxides, carbides) or metallic (lead, tungsten, molybdenum) phase.

2. Ceramic Matrix Composites (CMC)

Ceramic Matrix Composites are composed of a ceramic matrix and imbedded fibers of other ceramic material (dispersed phase).

3. Polymer Matrix Composites (PMC)

Polymer Matrix Composites are composed of a matrix from thermoset (Un-saturated polyester (UP), Epoxy) or thermoplastic (PVC, Nylon, Polystyrene) and embedded glass, carbon, steel or Kevlar fibers (dispersed phase).

(b) On the basis of Material Structure

1. Particulate Composites

Particulate Composites consist of a matrix reinforced by a dispersed phase in form of particles.

(i) Composites consist of random orientation of reinforced particles.

(ii) Composites consist of preferred orientation of particles. Dispersed phase of these materials consists of two-dimensional flat platelets (flakes), laid parallel to each other.

2. Fibrous Composites

(i). Short-fiber reinforced composites. Short-fiber reinforced composites consist of a matrix reinforced by a dispersed phase in form of discontinuous fibers (length < 100*diameter).

(ii). Long-fiber reinforced composites. Long-fiber reinforced composites consist of a matrix reinforced by a dispersed phase in form of continuous fibers.

(iii). Composites consist of random orientation of fibers.

(iv). Composites consist of preferred orientation of fibers.

(v). Unidirectional orientation of fibers.

(vi). Bidirectional orientation of fibers (woven).

3. Laminate Composites

When a fiber reinforced composite consists of several layers with different fiber orientations, it is called multilayer (angle-ply) composite.

1.5 METAL MATRIX COMPOSITE

In Metal Matrix Composite (MMC) the matrix materials are usually Aluminium, Aluminium-Lithium, Magnesium, Copper, Titanium, Carbon etc. Reinforced materials can be graphite, Aluminium oxide, Silicon carbide, Boron, Molybdenum, Zirconium Oxide, and Tungsten etc in the form of Fiber, Particle and Laminate. Aluminium alloys are widely used in the automotive industry because of their high strength to weight ratio as well as high thermal conductivity. It is used particularly in automobile engines as cylinder liners as well as other rotating and reciprocating parts, such as the piston, drive shafts, brake rotors and in other applications in automotive and aerospace industries [123]. The major advantages of AMC's compared to unreinforced materials are as follows:

1. More strength
2. Improved stiffness
3. Reduced density(weight)
4. Improved high temperature properties
5. Controlled thermal expansion coefficient
6. Thermal/heat management
7. Enhanced and tailored electrical performance
8. Improved abrasion and wear resistance
9. Control of mass (especially in reciprocating applications)

1.6 ENGINEERING APPLICATIONS OF MMC

Advance engineering materials are gradually becoming very important material for their scope and use in advance manufacturing industries due to their high fatigue strength, thermal

shock resistance, high strength to weight ratio etc. Because of such superior properties, engineering composite have wide industrial applications, which have stated as follows in form of table 1.1.

Table 1.1 Industrial Applications of MMC

S. No	MMC Types	Industrial Applications	Special Features
1	Graphite reinforced in aluminium	Bearings	Lighter in weight, self-lubricating
2	Graphite , Silicon carbide and aluminium oxide reinforced in aluminium	Automobile pistons, Cylinder liners, Piston rings, Connecting rods	Reduce wear, anti seizing, cold start, lighter
3	Graphite reinforced in copper	Sliding electrical contacts	Good electrical conductivity
4	Silicon carbide reinforced in aluminium	Turbocharger impellers	High temperature use
5	Glass or Carbon bubbles reinforced in aluminium	Automobile parts	Ultra light Material
6	Cast Carbon fiber reinforced magnesium fiber composites	Tubular composites for space structures	Zero thermal expansion, high temperature strength, good Specific strength and stiffness.

1.7 HYBRID COMPOSITES

In hybrid composites, the plies can include fibers of two or may be more types, i.e., carbon and glass, glass and aramid, Al_2O_3 and SiC, Al_2O_3 and C and more. The properties of hybrid composites are more excellent than those of the single reinforcement reinforced composites, because of the interaction of various reinforcements, especially, the hybrid effectiveness produced by these reinforcements, such as low thermal expansion coefficient, better wear resistance, high strength, high hardness and low cost. A promising application of these materials is associated with the so-called thermo-stable structures, which do not change their dimensions under heating or cooling. For some composites, i.e., with glass or boron fibers,

the longitudinal coefficient of thermal expansion is positive, whereas for other materials, i.e., with carbon or aramid fibers, it is negative. The appropriate combination of fibers with positive and negative coefficients can result in material with zero thermal expansion. The range of applications of composite materials is very large. The hybrid materials are used in different fields as Electrical, Electronics, Buildings and Public Works, Road Transports, Rail Transports, Marine Transports, Cable Transports, Air Transports, Space Transports, and Sports and Recreation [36].

1.8 Al/ (Al_2O_{3p} + SiC_p + C_p) – METAL MATRIX HYBRID COMPOSITE

Aluminium alloys are widely used in the automotive industry because of their high strength to weight ratio as well as high thermal conductivity. It is used particularly in automobile engines as cylinder liners as well as other rotating and reciprocating parts, such as the piston, drive shafts, brake rotors and in other applications in automotive and aerospace industries.

Alumina (Al_2O_3) is one of the most popular ceramic materials used as reinforcement due to its exceptional properties in hardness, strength, wear resistance, resistance to chemical degradation, low thermal expansion, good creep behaviour, low density and low cost. They are widely used as high speed rotating or reciprocating mass items such as pistons, connecting rods, drive shafts, cylinder liner, bushing, bearing, brake rotors, applications in aerospace and automotive industries due to their excellent combination of high specific strength and good wear resistance.

Ceramic particles such as SiC has commonly added as a second reinforcement material in MMC hybrid composite to an increase in wear resistance, elastic modulus; and decrease in the thermal expansion coefficient for contact sliding application, i.e. brake disk rotors. Wear resistance of Al/ Al_2O_3 – SiC hybrid composites are higher than for Al/ Al_2O_3 and Al/ SiC [49].

Carbon particle has considered as very important reinforcement for aluminium and its alloys in fabricating metal matrix hybrid composite material. Carbon fibers reinforced metal matrix composite are widely used due to it's improve the fracture toughness, high specific strength, specific modulus, high thermal and electric conductivity, low expansion coefficient, a good self lubricant properties, increase dimensional stability and elevate temperature property of the composite. It is varied applications in the areas such as electronic remission sources, electronics wave screening materials, and fuel cells [2, 18, 58, & 97].

The purpose of applying Al_2O_3 and SiC particles in the metal matrix hybrid composite to ensure high wear resistance whilst carbon particle are used as to lower the friction coefficient and prevent wear of the material cooperating with the composite.

Table 1.2 Mechanical Properties of Structural Materials and Fibers [49].

Material	Ultimate tensile stress, σ (MPa)	Modulus, E (GPa)	Specific gravity	Maximum specific strength, k_σ× 103 (m)	Maximum specific modulus, k_E× 103 (m)
Metal alloys Aluminum	140–700	69–72	2.7–2.85	26.5	2670
Metal wires Aluminum (150 μm)	290	69	2.7	10.7	2550
Carbon (5–11 μm) High-strength	7000	300	1.75	400	17,100
Carbon (5–11 μm) High-modulus	2700	850	1.78	150	47,700
Alumina – Al_2O_3 (20–500 μm)	2400–4100	470–530	3.96	100	13,300
Silicon Carbide – SiC (10–15 μm)	2700	185	2.4–2.7	110	7700

1.9 STIR CASTING

Stir Casting is a liquid state method for fabrication of composite materials, in which a dispersed phase (ceramic particles, short fibers) mixed with a molten matrix metal by means of mechanical stirring. Stir casting method involves incorporation of ceramic particulate into liquid aluminium melt and allowing the mixture to solidify. Here, the crucial thing is to create good wetting between the particulate reinforcement and the liquid aluminium alloy melt. The simplest and most commercially used technique for fabrication of composite, which is known as vortex technique or stir-casting technique. The vortex technique involves the introduction of pre-treated ceramic particles into the vortex of molten alloy created by the rotating impeller. Figure 1 shows the schematic diagram of stir casting technique.

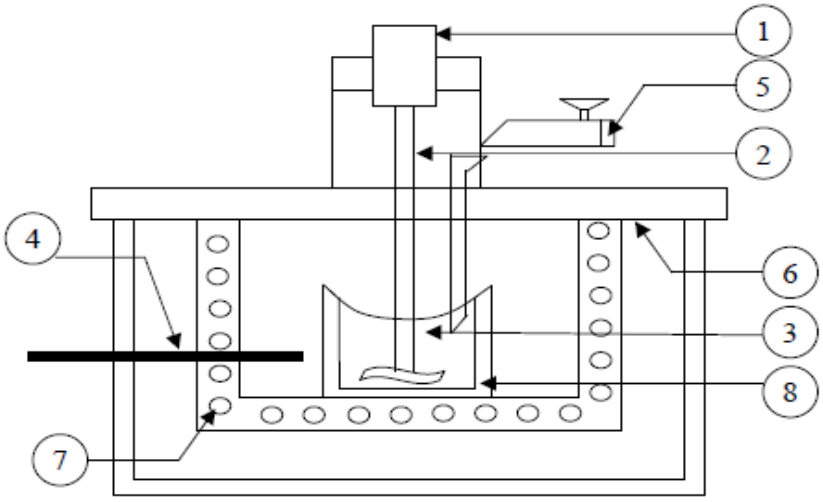

Schematic view of setup for Fabrication of composite

1. Motor	5. Particle injection chamber
2. Shaft	6. Insulation hard board
3. Molten aluminium	7. Furnace
4. Thermocouple	8. Graphite crucible

Fig. 1.1 Schematic Diagram of Stir Casting

Stir Casting is characterized by the following features: Content of dispersed phase is limited (usually not more than 30 vol. %). Distribution of dispersed phase throughout the matrix is not perfectly homogeneous:

1. There are local clouds (clusters) of the dispersed particles (fibers);

2. There may be gravity segregation of the dispersed phase due to a difference in the densities of the dispersed and matrix phase.

1.10 SQUEEZE CASTING

Squeeze casting is a popular technique especially for the fabrication of aluminium-based composites. It is a unidirectional pressure infiltration (pressure is typically between 70 and 150 MPa). The process consists of melting the metal, and forging of solidified metal. The pressure is applied as soon as the metal begins to solidify and is maintained until its complete solidification. The high pressure is applied with immediate contact with the metal surface of the die, causing a rapid transfer of heat that leads to a casting characterized by fine-grained crystalline, no internal porosity and mechanical properties that are similar to those of articles made by plastic deformation. The integrity of the obtained casting, virtually free of porosity, allows the possibility to work on them a heat treatment, which is impossible with the pressure die-castings. Figure 1.2 shows the basic working of squeeze casting method.

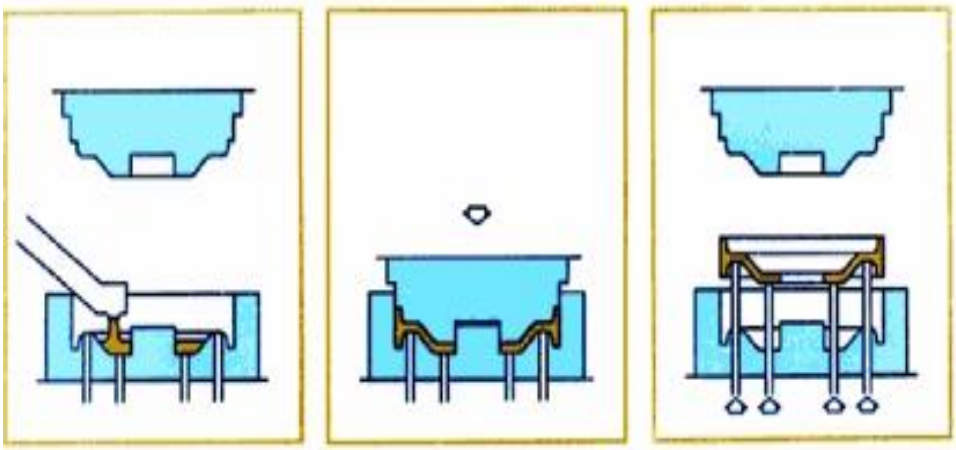

Fig. 1.2 Squeeze Casting [136]

The process is easily automated, allowing the realization of high quality components and minimize machining, that results particularly advantageous in the case of components made of composite materials. The basic parameters of such a process are the infiltration speed (which is mainly caused by applied pressure), the capillary, the space between particles of reinforcement, the viscosity of the liquid metal, the permeability of pre-forms, the die temperature, the performs and the cast. The final components are void free and have a small grain size microstructure. It is a fast process with a good surface finish and has used for selective reinforcement. It is most common to use performs (exceptionally premix or pellets are used). The infiltration rate depends upon the applied pressure, the capillarity, the spacing between the dispersed particles (whiskers), the viscosity of the liquid metal, the pre-form permeability, the temperature of the die, pre-form and melts.

1.11 WEAR TEST

Wear is common phenomenon of all metal having relative motion such as reciprocating and rotating motion of piston cylinder bores, connecting rods, drive shaft, brake rotors bearing etc. It is now well recognized that the metal matrix composite (MMCs) possess not only superior wear property but also high specific strength and stiffness in comparison with their corresponding monolithic alloys. Therefore, wear is an important aspect to be duly considered while designing with these elements to ensure better and reliable performance in any tribological applications. MMCs have received wide attention in the field of tribological to explore their wear characteristics from different point of view.

Wear test is used to find the tribological properties such as friction wear ratio, coefficient of friction, wear rate etc. The wear test has performed on pin on disc machine. The pin on disc wear test is one of the most spread test for sliding wear behaviour and friction of material pairs. A pin on disc tribometer consists of a stationary "pin" under an applied load in contact with a rotating disc. The pin can have any shape to simulate a specific contact, but spherical

tips have often used to simplify the contact geometry. Coefficient of friction has determined by the ratio of the frictional force to the loading force on the pin. The pin on disc test has proved useful in providing a simple wear and friction test for low friction coatings such as diamond-like carbon coatings on valve train components in internal combustion engines.

1.12 BASIC PRINCIPLE OF PIN ON DISC MACHINE

A pin on disc machine consists of a stationary "pin" under an applied load in contact with a rotating disc. The pin can have any shape to simulate a specific contact, but spherical tips have often used to simplify the contact geometry. Coefficient of friction has determined by the ratio of the frictional force to the loading force on the pin. Figure 1.3 shows the schematic diagram of pin on disc machine.

1.13 PIN ON DISC MACHINE SET UP

The pin on disc machine consists of three units.

a) The Mechanical unit

Comprising the hardware, test-setup housed in a sealed chamber for gaseous environment around the sample.

b) Instrumentation and Control Panel

Housing of electronics components such as amplifiers and displays.

c) Computer and DAQ software

Computer with data acoustic software for measuring frictional forces and display its results on screen. Figure 1.4 shows the used pin on disc machine setup for wear test.

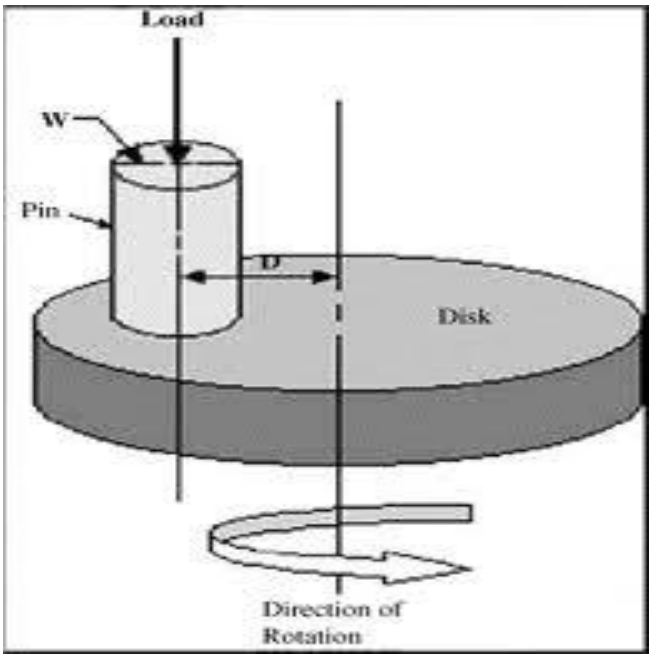

Fig 1.3 Schematic View of the Pin Specimen and Disc [133]

Fig. 1.4 Pin on Disc Machine Setup [Tribology Lab MMU]

1.14 SPECIFICATIONS OF PIN ON DISC MACHINE

- Pin size 4, 8, 10 & 12 mm diameter
- Disc Size 165 x 8 mm
- Disc Rotation Speed 0 – 2950 RPM
- Wear Track dia. Mean 50 – 100 mm
- Load 5 – 200 N (any steps possible)
- Sliding Speed Range 0 to 10 m/s
- Frictional Force 0 – 200 N
- Wear Measurement 0 – 2000 micrometer (1 µm LC)
- Temperature ambient to 300 deg C
- Power 230V, 50 Hz S phase

1.15 ELECTROCHEMICAL MACHINING

Electrochemical Machining (ECM) is a process of material removal from the electrically conductive material by metallic dissolution of the work piece (i.e. anode) and make a replica of the tool (i.e. cathode) separated by a thin film of an electrolyte. In this process material is removed based on the principles of Faraday's law of electrolysis (1833). The material is removed during this process by supply continues pulse DC with varying a supply current across the anode and cathode i.e. inter electrode gap between work piece and tool. For effective machining, an electrolyte is continuously flowing and maintain a constant flow rate in between the inter electrode gap. The electrolyte removes the dissolution products, such as

metal hydroxides, heat, and gas bubbles, which are generated in the inter electrode gap. Different reactions usually occur at the cathode and anode during electro chemical action while machining of an electrically conductive materials. Figure 1.5 shows a Schematic diagram within the anode and cathode during ECM.

ECM can be used for machining of different components related to aeronautics, nuclear technology, space vehicles, automobile, turbine etc, as it has several advantages like machining of hard and complicated materials, production of miniature and complex shapes parts etc with free from burrs and residual stress on machined surface. However, it can be used only for electrically conductive materials machining. Further, the accuracy of the machined components depends on the following factors such as tool design, degree of the process control imposed, incapable of economically producing the dimensional tolerances desired on work-piece. Production of removal of material from the undesired part which required special attention during machining usually some coating or masks are used on work piece and tool.

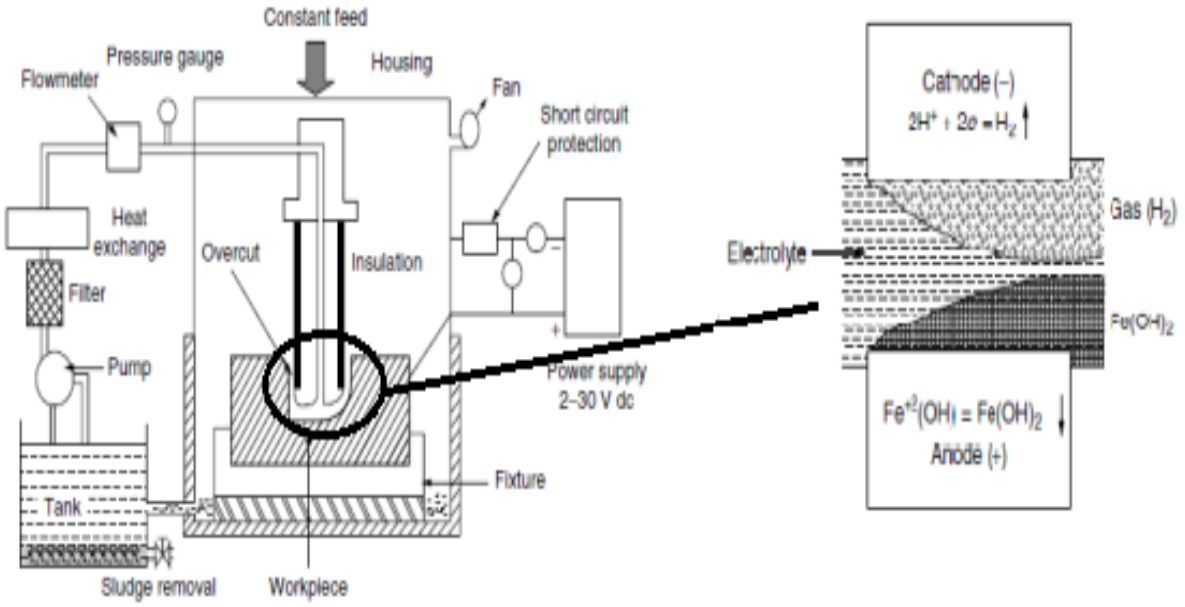

Fig. 1.5 Schematic Diagram of ECM, [42]

1.16 MICRO MACHINING

The term micro-machining refers to material removal in terms of chips or debris having of small dimensions/size in the ranging from 1-999 μm. Advanced micro-machining may consist various ultra-precision activities to be performed on very small and thin workpiece; small and micro-sized holes, slots and complex surfaces are needed in large numbers [59]. Micro Machining have numerous industrial applications particularly in aerospace, medical treatment, astronautics, military, electronics, computer and micro mechanics industries. Figure 1.6 shows a brief representation of micro machining.

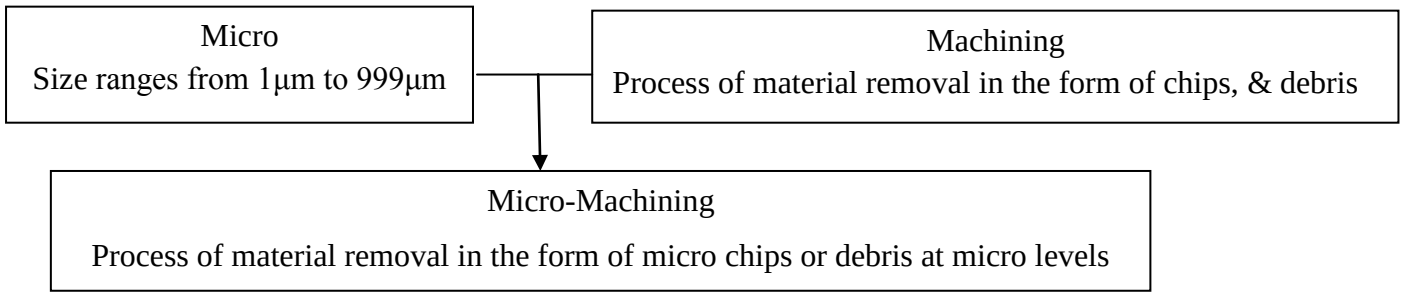

Fig. 1.6 Micro Machining Definition

1.17 NEED OF MICRO MACHINING

Micro machining techniques have their roots in 1960's when the need for miniaturized electronics components arose. Recent changes in demand from industry have forced the introduction of more and more micro parts in various types of industrial products. For example, complex 3-D components (turbine blades), miniature features better for food processing and textile industries having a few tens of micrometers as hole diameter and thousands in numbers. Nano level surface finish on complex geometries which are impossible to achieve by any traditional method (thousand of turbulated cooling holes in turbine blade) making and finishing of micro fluidic channels in the electrically conducting and non-conducting materials (glass, quartz, ceramics) etc. Inspection of the internal organs of the human body and surgery without pain are universally desired. Miniaturization of medical tools is an effective approach to arrive at this target Micro-machining technology plays an increasingly decisive role in the miniaturization of components ranging from biomedical applications to chemical micro-reactors and sensors. However, micro machining is extremely needed for machining of highly miniature components with miniature features.

Micro machining is gaining popularity due to the recent advancement in miniaturization of products and Micro Electro Mechanical System (MEMS). Micro-machining technology plays decisive role in the miniaturization of components ranging from biomedical applications to chemical micro reactors, sensors, semiconductor, ultra precision machinery, thousands of tabulated cooling holes in a turbine blade as explained by Park et al. (2002). Mobile telephone and multimedia equipments i.e. camera, music players, laptop, pendrive, hard disc, CD and DVD players etc, have rapidly decreased in size but their functionality have increased to save energy, space and resources as stated by Rangelow (2001). This process can be utilized to fabricated micro moulds. Appropriate micro moulds for mass production of high precision parts are now in demand as claimed by Kurita et al. (2006).

Engineering on the micro scale has become increasingly attractive and important due to the further requirements for smaller, finer, accurate and more precision parts and components.

However, the fabrication of small parts of dimensions in micrometer is still a challenge for modern manufacturing systems, especially composite and ceramics micro machining.

1.18 MICRO MACHINING METHODS

The problem usually encountered are high tool wear, lack of rigidity of the process and heat generation at the tool and work piece interface, during micro shaped produced by using conventional machining techniques as stated by Jain (2002). However if use mechanical type non-conventional machining processes (AJM, USM, WJM etc) for production of miniaturization parts or micro domain part, the problem usually encountered during machining are such as some of abrasive particle is embedded with the work piece, formation of some burr and micro crack. In the same way if use some thermal type non-conventional machining processes (LBM, EDM, IBM etc) in the micro machining domain, the problem encountered during machining are such as generation of thermal distortion, HAZ, thermal cracks even overcut and tapering effect. Chemical machining is thermal free process and impact free process, but chemical machining cannot be controlled properly in the micro machining domain because mask coating in lefting micro area for machining is very difficult otherwise dissolution occur overall contact area of chemical.

Electrochemical machining is combination of electrical and chemical energy but there is no formation of heat affected zone (HAZ) because of deionization of electrolyte which in terms helping in carrying of electrons and positive ions, so thereby minimizing the HAZ area and formation of impact free machined surface. Hence, ECM can be considered as one of the suitable process for micro manufacturing domain. Bhattacharyya, explained in a chapter of a book edited by Jain (2010) that the electrochemical micro machining (EMM) is suitable process for micro machining domain. When electrochemical process is used in microscopic domain or micro range manufacturing, then it is known as Electrochemical Micro Machining (EMM) as stated by Bhattacharyya et al. (2002). Authors claimed that this is a very promising micro machining technology as there are numbers of advantages such as high machining rate, good surface finish, better precision, control, reliable, flexible, stress free, burr free, no heat affected layer, no tool wear, and environmentally acceptable process. The EMM process permits micro machining of micro groove, micro drilling, cavity, punches, micro dimple array, 3D complex shape, etc on chemical resistant materials irrespective of their hardness and toughness like titanium, copper alloys, super alloys, stainless steel, hard and brittle material with high aspect ratio which are widely used in space, automobile, biomedical, electronics, computers printed circuit boards, surgical implants, optics; and MEMS applications as stated by various researchers Datta et al. (1996), Osenbrugger and

Regt. C. (1985), Datta (1998), Rajurkar et al. (1999), Landolt et al. (2003), Kozak et al. (2004), Sen and Shan (2005), Zhao et al. (2006), Fang et al. (2006), Shin et al. (2008), Qian et al. (2010); and Yang et al. (2011).

1.19 ELECTROCHEMICAL MICRO MACHINING (ECMM) SYSTEM

Electrochemical Micro Machining (ECMM) is a non-contact metal removal process for electrically conductive materials, which is done without applying any cutting forces on the work-piece materials. A low pulse DC voltage is applied between the micro tool (cathode) and the work-piece (anode), which are separated by a continuous flowing electrolyte. The ECM machining process can be applied to manufacturing micro domain products with precision shapes. When this machine is applied to fabricate the parts under micro machining range that may well known as electrochemical micro-machining process. The electrochemical micro-machining process system mainly consists of a mechanical machining unit, micro tooling unit, electrical power supply unit, tool controlling unit and electrolyte flow system as explained by Bhattacharyya et al. (2001). A schematic diagram of electrochemical micro-machining process setup developed by Bhattacharyya et al. (2004) is shown in Figure 1.7.

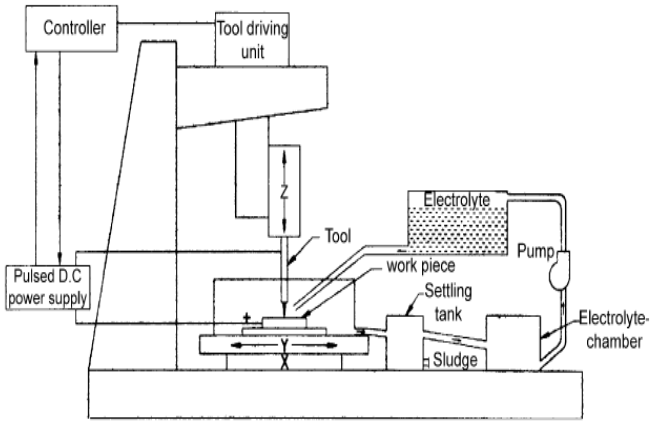

Fig. 1.7 Schematic Diagram of Electrochemical Micro-Machining Setup, [28]

The electrochemical micro-machining process has different advantages over other nonconventional machining like Abrasive Jet Machining, Abrasive Water Jet Machining, Water Jet Machining, Abrasive flow machining, EDM, ION Beam Machining, and LBM.

- Include high MRR
- Better precision and control
- Good surface finish
- No tool wear, as the tool is not in direct contact with workpiece
- Simultaneously drilling of large number of holes by using multi electrodes
- Stress free, and burr free surface are produced
- The regulation of process rates by potential or current control

- It also permits the machining of chemically resistant materials like titanium, copper alloys and stainless steel, which are widely used in biomedical, electronic and micro-electro-mechanical systems (MEMS) applications

The general comparison between ECM and ECMM is shown in Table 1.3.

Table 1.3 General Comparison between ECM and ECMM [28]

S. No	Major machining Characteristics	Electrochemical Machining(ECM)	Electrochemical Micro Machining (ECMM)
1.	Voltage	10–30 V	<10 V
2.	Current	150–10000 A	<1 A
3.	Current density	20–200 A/cm^2	75–100 A/cm^2
4.	Power supply—DC	Continuous/pulsed	Pulsed
5.	Frequency	Hz–kHz range	kHz–MHz range
6.	Electrolyte flow	10–60 m/s	<3 m/s
7.	Electrolyte type	Salt solution	Natural salt or dilute acid/alkaline solution
8.	Electrolyte temperature	24–65 ^{0}C	37–50 ^{0}C
9.	Electrolyte concentration	>20 g/l	<20 g/l
10.	Size of the tool	Large to medium	Micro
11.	Inter-electrode gap	100–600 μm	5–50 μm
12.	Operation	Maskless	Mask/maskless
13.	Machining rate	0.2–10 mm/min	5 μm/min
14.	Side gap	>20 μm	<10 μm
15.	Accuracy	±0.1 mm	±0.02–0.1 mm
16.	Surface finish	Good, 0.1–1.5 μm	Excellent, 0.05–0.4 μm
17.	Problems due to waste disposal/toxicity	Low	Low to moderate

1.20 EFFECTS OF ELECTROCHEMICAL MICRO-MACHINING PROCESS VARIABLE

In electrochemical micro-machining process, accuracy of micro surface and rate of dissolution depends on various process parameters such as applied voltage, pulse duration (pulse on time and pulse off time), supply current, electrolyte type, concentration, flow rate and inter electrode gap (IEG) etc. These parameter influence major machining criteria e.g. material removal rate (MRR), surface finish and profile accuracy etc. In order to achieve the

effective and high precision machining in microns, the proper knowledge about the ECMM process variables is essential to enhance the efficiency and productivity, better quality with minimum cost. Figure 1.8 shows a fishbone diagram, which represents the cause and effect of various major process variables of ECMM on machining performance criteria.

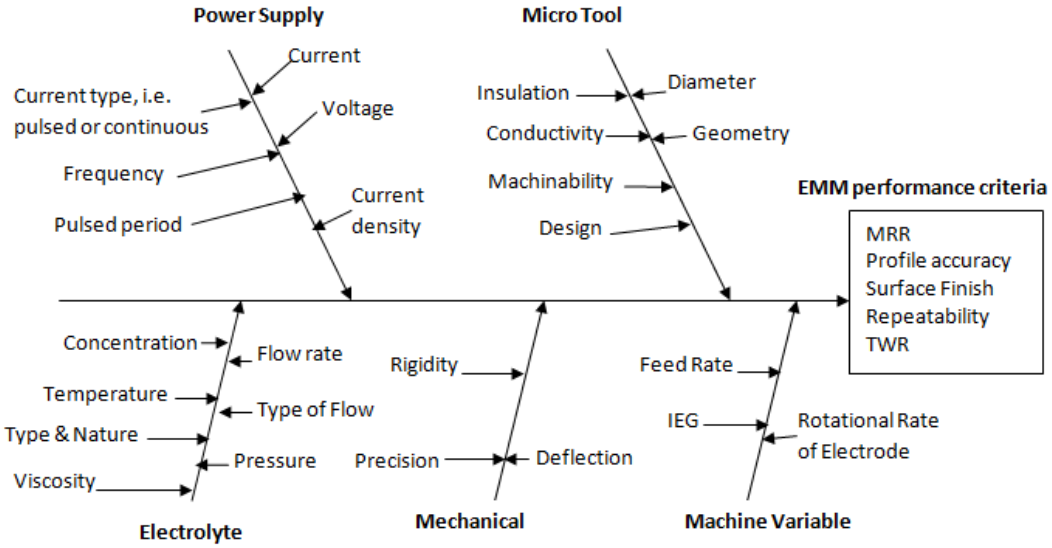

Fig. 1.8 Fishbone Diagram of ECMM Process

The relations are usually used to determine the material removal rate (MRR), over cut (OC), and taper cut (TC) as explain below.

$$\text{Material Removal Rate (MRR)} = \frac{Mbm - Mam}{\rho m \times tm} \quad (1.1)$$

$$\text{Over Cut (OC)} = \frac{Di - Dt}{2} \quad (1.2)$$

$$\text{Taper Cut (TC)} = \frac{Di - De}{2} \quad (1.3)$$

Where M_{bm} – Mass before machining, M_{am} – Mass after machining, ρ_m – Density of material t_m – machining time, D_i – internal or entrance diameter of machined hole, D_t – external diameter of tool, and D_e – exit diameter of machined hole

1.21 EFFECTS OF DIFFERENT PARAMETERS ON EMM PERFORMANCE CHARACTERISTICS

1.21.1 Power Supply

Supply voltage is one of the dominant process parameter of EMM process for controlling the shape and surface finish during generation of micro holes. A step-down transformer and silicon controlled rectifier unit can be utilized to convert AC main supply into DC with

variance of DC supply ranges from 0-20 V DC can be effectively use during EMM process. If the power supply nature is continuous mode then increasing contamination, which is cause, deposited on the micro tool, so the work-piece material no longer dissolves uniformly. This problem can overcome by supplying a pulsed voltage rather than supplying a continuous voltage as claimed by Kozak et al. (1994) and Bhattacharyya et al. (2004). As per the Ohomie law's machining current is increase with increase in supply voltage. As Faraday's law stated that the material removal rate is proportional to the machining current. So that material removal rate increases with increase in supply voltage as dissolution efficiency is increase, as stated by Bhattacharyya and Munda (2003), Bhattacharyya et al. (2005), Kurita et al. (2006), Wang et al. (2008); and Liu et al. (2010). Size of micro holes increases with increase in supply voltage as MRR increases as stated by Li et al. (2010). The machining accuracy reduces with increase in supply voltage of EMM process. A higher voltage produces ir-regular shaped of micro holes. This ir-regularity shape of machined hole may be caused by micro-sparking occurring due to the presence of sludge that is not cleaned completely by the flow of electrolyte in the inter electrode gap (IEG). At higher machining voltage, a non-uniform current dissolution in the gap and resulting thus generation of overcut, yields larger lateral removal and the total discharge time is shorter at the bottom of the hole than at the entrance, thus generation of taper claimed by Fan and Hourang (2011), Wang et al. (2008), Liu et al. (2010), Bhattacharyya and Munda (2003). The influences of the supply voltage on MRR and overcut claimed by Bhattacharyya and Munda (2003) represented in Figure 1.9.

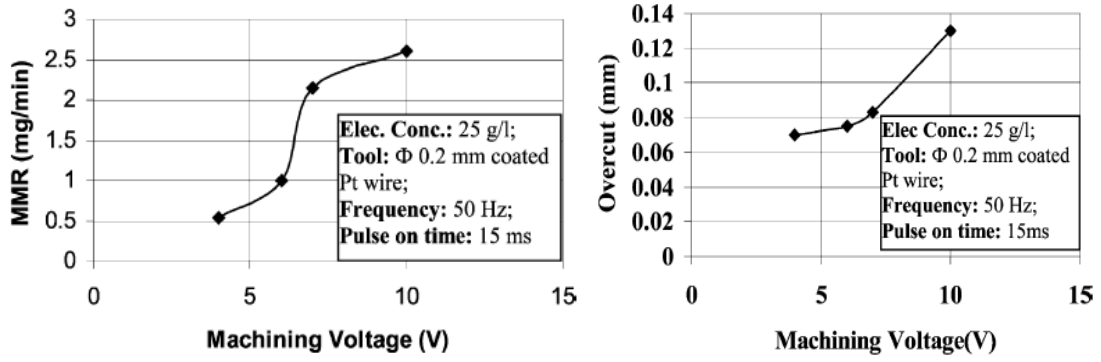

Fig. 1.9 Influences of Supply Voltage on MRR and Overcut, [22]

Duty cycle is proportion of pulse on time to the regular interval or period of time cycle. The relations are usually used to determine the duty cycle as explain below.

$$\text{Duty Cycle} = \frac{\text{PulseOnTime}}{\text{PulseOnTime} + \text{PulseOffTime}} \quad (1.4)$$

With the increase in the duty cycle, both the faradic current and the period of faradic current are increases, therefore, the amount of faradic effects increase rapidly. Hence Material

removal rate is increase and machining time decrease with an increasing in duty cycle. With increase in pulse on time, which leads to increase the dissolution efficiency, and resulting thus increment of MRR, because more time has been allowed to machine the work piece for fixed duration as stated by Bhattacharyya and Munda (2003), Park et al. (2006), Lee et al. (2007), Kurita et al. (2006) and Mithu et al. (2011). The machining accuracy becomes poor as the pulse on time increase. For larger pulse on time, the average current is also larger. For the larger current, the localization effect reduces and thus increases the overcut phenomena. If pulse off time becomes shorter this is not sufficient for the complete removal of all the machined products from micromachining gap. The presence of machined products in the micro inter electrode gap may cause sparking i.e. uncontrolled phenomenon, which leads to more overcut as explained by Kurita et al. (2006), Wang et al. (2008), Liu et al. (2010), and Bhattacharyya and Munda (2003). The influence of Pulse on time on side gap observed by Wang et al. (2008) is shown in Figure 1.10.

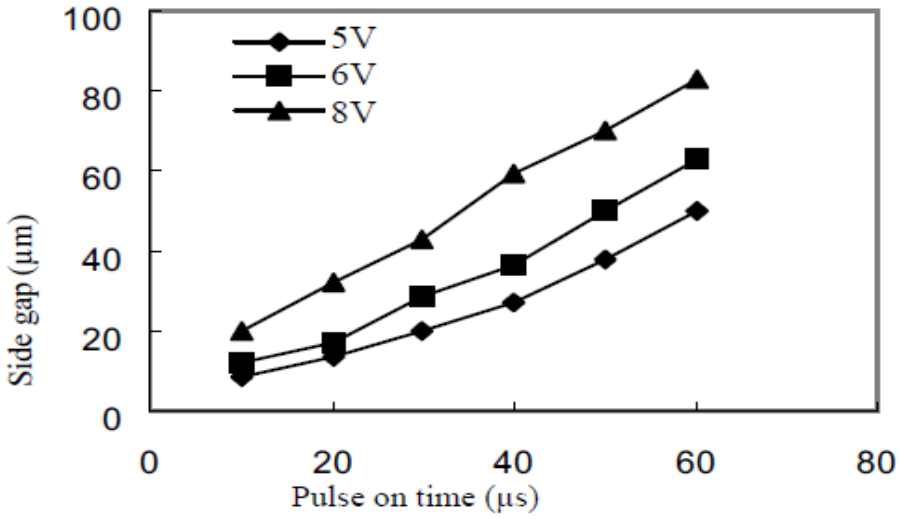

Fig 1.10 Influence of Pulse On Time on Side Gap, [132]

1.21.2 Type of Electrolyte, Flow; and Concentration

The electrolyte must be a good electrically conductor and should produce a slight passivation of the work piece surface. The electrolyte completes the electric circuit between the tool (cathode) and work piece (anode), it must move very fast to remove dissolution product, heat, gas bubbles and allows the desired machining reactions to occur. Electrolyte is generally classified into two categories; passivity electrolyte and non-passivity electrolyte. Passivity electrolyte are containing oxidizing anions e.g. sodium nitrate and sodium chlorate, etc. Passivity electrolytes used as electrolyte gives better machining precision. This is due to their ability to form oxide films on the work piece and stray current decreases as described by Bhattacharyya et al. (2002) and Wang et al. (2008). Non-passivity electrolytes are containing

relatively aggressive anions such as sodium chloride. However, acidic electrolytes have advantages due to formation of soluble reaction products, which can completely swept clean from the small narrow inter electrode gap (IEG) during machining without micro tool being affected as explained by Bhattacharyya et al. (2005). Further it can addition of some additive chemicals like $NaHSO_4$ to the electrolyte to reduce the concentration of dissolved reaction products and eliminates the phenomenon of micro sparks that in turn improve the accurate shape generation as claimed by Li et al. (2010). $NaNO_3$ used as electrolyte gives better results as claimed by Rosenkranz et al. (2005). The improvement of machining accuracy in normal ECM can be achieved by modified electrolyte flow distribution. The material removal rate increases with flow rate because there is more mobility of the ions from the metal to the solution increasing the speed of the chemical reactions stated by Benedict (1987). Concentration of electrolyte is another variable of electrolyte in the EMM process for controlling the conductivity, the micro-electrodes dimensions and shape. At higher concentration of electrolyte, the larger number of ions associated in the machining process increase the machining current and thus results in higher MRR as claimed by Bhattacharyya and Munda (2003), Kurita (2006), and Bhattacharyya et al. (2007).

Response characteristics e.g. overcut increases with increase in electrolyte concentration. Higher electrolyte concentration results in higher electrolyte conductivity and current density, resulting increase the radial and lateral stray etching and generation of overcut and taper cut of machined holes as claimed by Bhattacharyya and Munda (2003), Bhattacharyya et al. (2004), Fan and Hourng (2011); and Kurita et al. (2006). The effect of $NaNO_3$ concentration on overcut claimed by Fan and Hourng (2011) is shown in Figure 1.11.

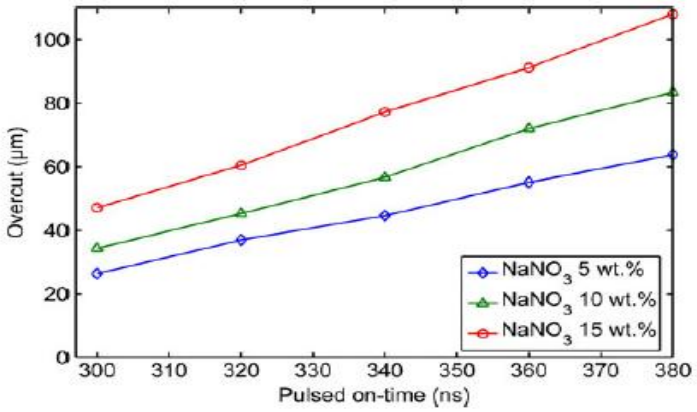

Fig. 1.11 Effect of Electrolyte Concentration on Overcut; [44]

1.21.3 Electrode Shape, Size; and Material

The accuracy of the generated micro hole directly depends upon the accuracy of the micro tool shape and surface finish. Tool design deals with determination of tool shape which is perfect negative mirror image of work piece to be produced. The tool desired for ECM is high electrical conductive, thermal conductive, high corrosion resistance, high stiffness and must be highly machinable. Platinum alloys, tungsten alloys, titanium, molybdenum, stainless steel, copper alloys and super alloys etc can be utilized as micro tool materials for effective machining of different metals as suggested by Bhattacharyya et al. (2002); and Choi et al. (2007). Micro tools can be fabricated using electrochemical etching, wire EDM, EDM, WEDG, ECM, μEDM, μWEDM, and hybrid μEDM turning etc; as explained by Masuzava et al. (1994), Lim and Kim (2001), Ohmari et al. (2003), Park et al. (2006), Jo et al. (2009), Li et al. (2010), Asad et al. (2011) and Zhang et al. (2011). A micro tool (electrode) machined on μECM by Li et al. (2010) is shown in Figure 1.12.

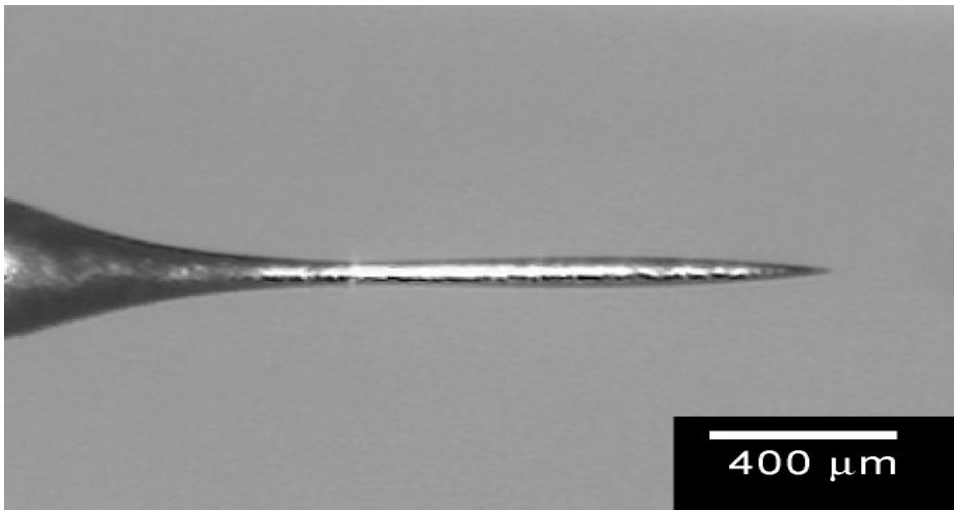

Fig. 1.12 Micro Electrode Machined by Micro ECM; [79]

At the front end of the cylindrical tool electrode, material on the outside area of the electrode removed, electrolyte can then infiltrate into the hole and gradually from a gas film, where material rate also commences. The above material removal mechanism accounts for delay the machining of material along with machining depth for the cylindrical tool electrode. The machining gap increase with increase in depth, cause the taper shape of structure, which as shown in figure 1.13 (a). For machining of structure without taper, a disk type electrode as recommended by Kim et al. (2005) as shown in figure 1.13 (b).

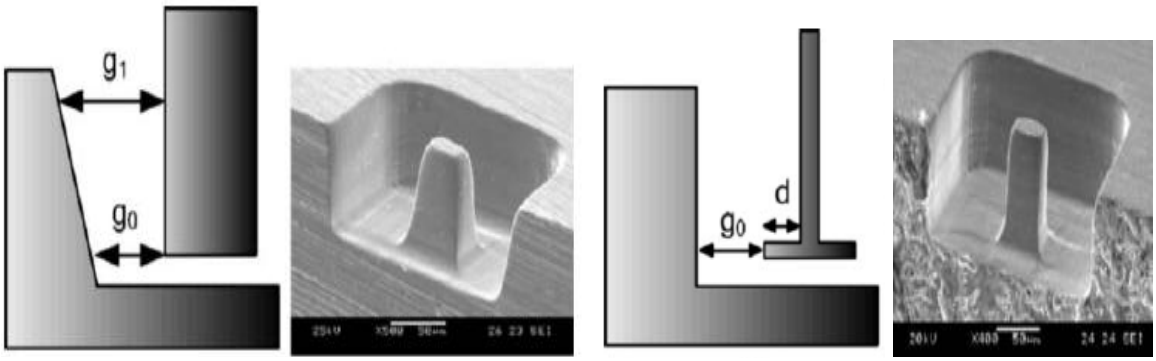

Fig. 1.13 (a) **Fig. 1.13 (b)**

Fig 1.13 (a) Micro Column by Cylindrical Electrode (B) Micro Column by Disk Electrode; [65]

The curve surface on the tool reduces the contact area between the electrode and work piece thus facilitating the flow of electrolyte to the electrode end. This enables rapid formation of a gas film enveloping the electrode, resulting in efficient micro hole drilling and increase of material removal rate as claimed by Yang et al. (2011). The cylindrical electrode with spherical end as shown in Figure 1.14 (b) can be used to fabricated micro hole on structures with minor taper due to its smaller current density along the sidewall of the work piece rather than cylindrical electrode as claimed by Liu et al. (2011) shown in Figure 1.14 (a).

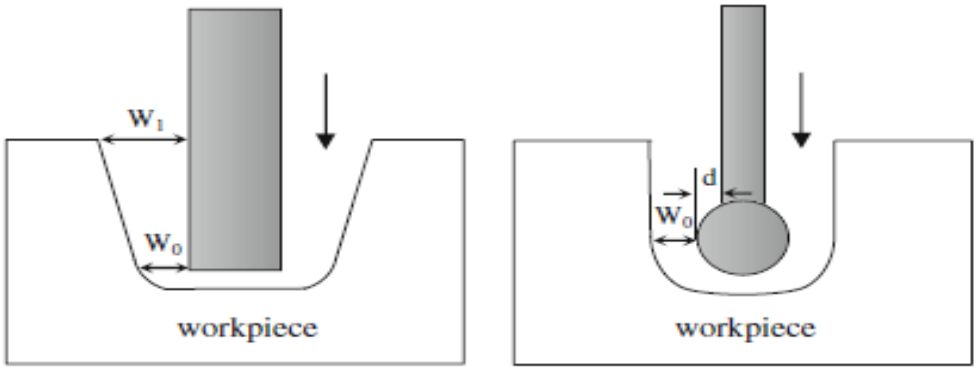

Fig 1.14 (a) **Fig 1.14 (b)**

Fig 1.14 Schematic Diagram of Taper Reduction with Spherical End; [83]

When machining operation was performed with large electrode and short pulse duration, thus resulting in the rising up of sufficient potential for dissolution of material from anode requires more time. As a result, the machining rate decreases with large tool electrode at short pulse on-time. Hence larger tool electrodes require longer pulse on-time for the effective machining as stated by Fan and Hourng (2011). The material removal rate increase with the increase of micro tool diameter. This is due to fact that the surface of electrode area increase, the electrical double layer capacitance increases and electrolyte resistance decreases. The decreased electrolyte resistance increases the current density resulting in rapid increase material dissolution rate as claimed by Mithu et al. (2011). The increase of electrode

diameter, the groove width increases rapidly as observed by Liu et al. (2010) as shown in Figure 1.15. They suggested that the diameter of electrode as small as possible for effective micro machining operation.

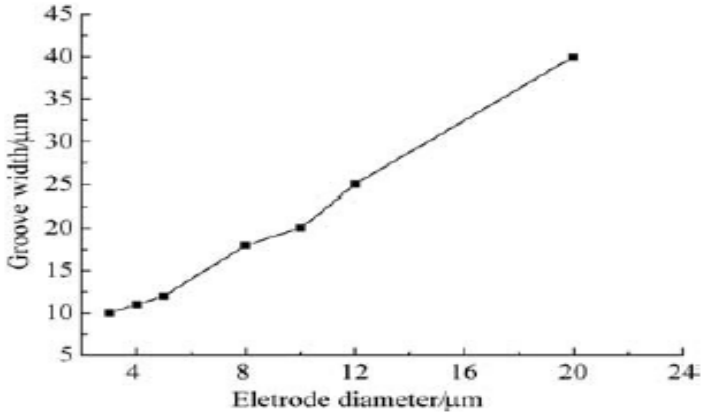

Fig 1.15 Variation of Groove Width with Electrode Diameter; [84]

It is evident that the faradic effect decreases and increase in electrolyte resistance with increase in the tool length. So that material removal rate decreases with increase in tool length as stated by Mithu et al. (2011).The machining rate with insulated electrode is much higher than that of un-insulated tool electrode because the rising time of the double layer potential is minimized. The machining depth can be achieved more because there is no side effect on the micro hole by electrode (tool) due to insulation. Therefore, the machining rate and the machining gap are uniform, for higher machining depth; taper shape of machined hole can be effectively prevented by insulated electrode as claimed by Park et al. (2006) is shown figure 1.16.

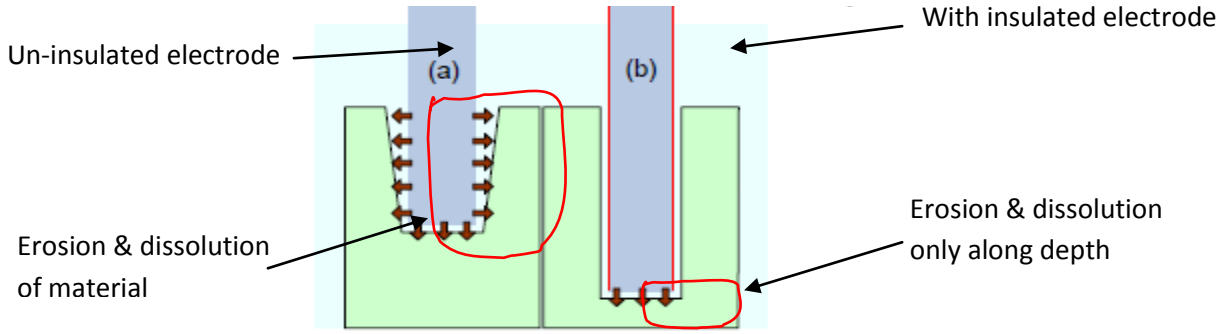

Fig 1.16 Side Effect by (a) Un-Insulated Tool, (b) Insulated Tool; [105]

1.21.4 Inter Electrode Gap (IEG)

The gap in between two electrode i.e. micro tool (cathode) and work piece (anode) is called inter electrode gap (IEG). Machining inaccuracy is directly proportional to the IEG of EMM. When the IEG becomes small, the electrical resistance between the cathode and anode decrease. This relationship enhances the electrochemical reaction and as results, the depth of groove increases. When the gap becomes too narrow, the anode surface profile becomes coarser. This may be due to non-uniform flow of electrolyte flow within the gap. On the other hand, when the electrode gap becomes too large, the electrochemical reaction and localized dissolution cannot occur at the anode surface because the electrical resistance between the cathode and anode is too high, explained by Park et al. (2002).

In EMM process, inter electrode gap increases with increase in machining time. The increase in IEG causes the taper shape of structure. It may cause for short-circuiting during EMM operations due to smaller IEG as claimed by De-Silva et al. (2000). This short-circuiting may be avoided by using micro tool vibration as claimed by Munda et al. (2007).If the machining gap is not maintained at the specified minimal value, the shape of the tool will not be accurately duplicated in the work piece. In this case roughness can be affected as discussed by Da Silva et al. (2006).

1.21.5 Feed Rate

The feed system of electrochemical micro machining are use to feed the micro tool (cathode) towards work piece (anode) during pulse-off time to maintaining IEG. According to electrolytic theory the gap in the inter electrode becomes narrow with the increase of feeding speed as explained by Wang et al. (2008). If increase the feed rate, the average current density around the tool increase, which leads to the increase of dissolution efficiency resulting decrease the side gap and overcut as stated by Da Silva et al. (2006) and Liu et al. (2010) is shown in Figure 1.17.

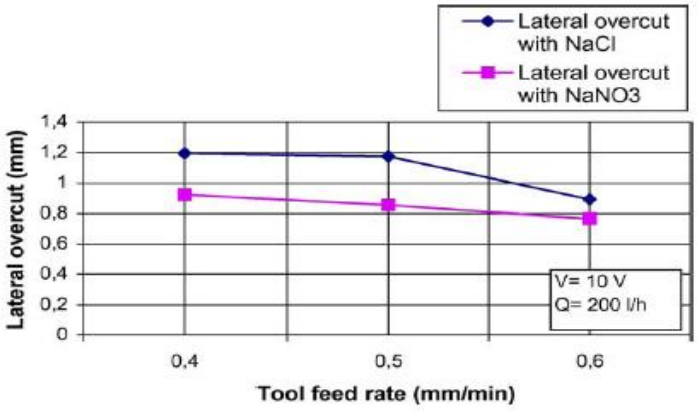

Fig. 1.17 Variation of Tool Feed Rate with Later Overcut, [35]

But high feeding rate is very much dangerous both for micro tool and work piece, results the distortion of the micro tool tip, bending the micro tools and micro tool will come into contact with work piece so that damage of micro tool because of short circuit as stated by Fan and Hourng (2011) and Mithu et al. (2011). Hence micro tool feed rate should be chosen in such a way so that it is always equal to the linear material removal rate to avoid short circuit during generation of micro holes as described by Bhattacharyya and Munda (2003).Table 1.4 shows the summary of electrochemical micro machining reviewed. The most of researchers were used low voltage ranges from 1.5 to 10V, low pulse duration ranges from 15ns-25μs, and frequency ranges from 10 KHz-2MHz during EMM operation for producing micro structures. The different researchers were used different electrolyte such as H_2SO_4, $NaNO_3$, NaOH, and HCl but Huaiqain (2008) was used the Pure water as electrolyte and produced the square cavity. Li et al. (2010) was added the $NaHSO_4$ to the electrolyte to reduce the concentration of dissolved reaction products and improve shape of generated of micro products. Most of the researchers were used the tungsten electrodes having diameter ranges from 5μm to 300μm. Jo et al. (2009) was used the insulated electrode to minimize the taper effects. The rotational of electrode at 3000 rpm (Li et al. 2010) and 800 – 5000 rpm (Fan and Hourg 2009) performed better performance during micro machining. The ranges of electrode gap varies from 5μm to 32μm and the wide variation of feed motion of electrode ranges from 2μm/min to 72μm/min were be used in generation of micro holes diameter ranges from 5μm to 500μm.

1.21.6 Rotation Rate of Electrode

From the literature reviewed, it is noted that various researchers on electrochemical micro machining without rotation of electrode carried out the major work. Rotation of electrode i.e. tool (cathode) is helpful to remove the sludge and dissipate the heat from machining zone by improving the electrolyte flow. As the electrode does not rotate, sludge emerging during micro ECM, and it will block the side machining gap because of short supply of electrolyte. When fresh electrolyte is difficult to enter the micro machining zone, so it is easy to form an ion accumulation, a serious concentration polarization and which influence the machining accuracy. Although the effect of the rotational rate on the overcut is small as claimed by Fan and Hourang (2011) and Li et al. (2010).

TABLE 1.4 Summary of Micro Machining Operations Monitoring and Variable Solutions

Ref.	Emphasis	Power supply variables			Electrolyte		Electrode	Machining variables		
		Voltage (V)	Pulse Duration	Frequency	Type	Concentration	Shape and Material	Rotation rate of Electrode	Feed	Electrode Gap
[79]	Profiled micro holes, micro array square columns, micro spiral beam with high aspect ratio on stainless steel were fabricated by NC micro EC Milling.	4.5, 5.5, 6.5, 7.5, 8, & 10	25µs	20 kHz	$NaHSO_4$ is addition of $NaClO_3$	25g/l, & 30 g/l	Tungsten with Φ12, & Φ30µm	3000 r/min	70µm /min	10µm
[45]	Fabricated the tungsten cylindrical shape micro electrode with diameter 100µm by ECM	1.4, 1.6, 1.8, & 2.0	30 -150ns	------	NaOH	9%, 12%, 15%, & 18%	Nickel plate 3cm x 1cm	800 - 5000rpm	------	10mm

[63]	By controlling pulse conditions and machining time, micro features are machined on the side wall of a micro hole.	6	30 - 160 ns	------	------	------	Φ35, insulated electrode	------	0.1µ m/s	5µm, 10µm, 15µm, 20µm
[105]	Fabricated of deep micro hole 500 µm depth on stainless steel, with Φ 58µm tool insulatedof 3 µm thick enamel	2.5, 3, & 6	15 - 50ns	------	H_2SO_4	0.1M	Tungsten with Φ40, 80, 120, 160, 200, 300	------	------	------
[116]	Micro holes, Square and circular micro cavities were fabricated by Micro ECM Milling.	6, 6.5, 7, & 8	300ns, 350ns	≤1M Hz	Citric Acid	0.2M and 0.3 M	Tungsten	------	≤0.15 µm/s	24µm, 32µm

[26]	Recommended the 150–200 Hz range of tool vibration frequency to improve the MRR and accuracy for machining of thin copper by EMM.	Range 1-8.5	------	25-300Hz or 2.5-25KHz	$NaNO_3$	10 - 30g/l	Stainless steel with Φ50-596μm, Platinum with Φ275μm	------	0.144 mm/min	------
[56]	Trilateral, Square cavity & trilateral hole were fabricated on stainless steel plate by Pure water micro ECM.	18-28	------	------	Pure water	------	Stainless Steel with 0.484mm side length trilateral tool	------	3μm/min, 6μm/min, & 8μm/min	20μm, 40μm
[65]	Hole array & micro grooves were fabricated on Stainless steel by disk type electrode.	5-6	40-60 ns	------	H_2SO_4	0.1 M	Tungsten Carbide with Φ10-50μm	------	0.05μm/s 0.1μm/s	10-25μm

[142]	Fabricated the cross micro grooves on nickel sheet by micro electrochemical machining.	3.5	40ns	------	HCl	0.1 M	Tungsten with Φ8μm	------	20μm /m	5μm
[144]	Generate micro dimple and hole array in chrome and steel work piece by providing insulation layer between cathode and anode having thickness 100 μm.	18	------	------	$NaNO_3$	16% wt	Copper tool with 30μm thickness	------	------	100 μm

[4]	micro hole with Φ 8µm was drilled on 304 stainless steel foil with 20µm thickness by using ultra short pulses with tens of nanosecond duration	4-8	20, 40, 60, & 80 ns	------	H_2SO_4	------	Tungsten Carbide with Φ4, 6, 20, 30, 50µm	------	2µm/m	------
[90, 91]	Investigate the effects of electrochemical micromachining parameters to fabricate the micro holes on nickel plate.	10.6	0.6µs	0.5-2MHz	HCl	0.2 M	Tungsten with Φ0.38 mm	------	0.05-0.8µm/s	------
[76]	Tool electrodes Φ 5 µm with 1 mm in length was developed and micro holes with Φ40µm were manufactured on stainless steel using these tool electrodes by using EMM.	1.5-3	100ns-5µs	10KHz-1MHz	HCl	0.5 M	Tungsten Carbide with Φ5µm	------	------	------

[107]	Generated micro dimple array on the hard chrome coated surface on ductile cast iron by mask electrochemical micromachining.	8-15	------	------	$NaNO_3$	16% wt	Copper tool with 30μm thickness	------	------	------

1.22 LITERATURE ON HYBRID COMPOSITE

The developments in the field of materials Science, materials with super properties have been produced, tungsten, tantalum, beryllium, hast alloy, Ti alloy, wasp alloy, nimonics, carbide, diamond, ceramics, stainless steel many other high strength temperature resistant (HSTR) alloy and composite materials. These materials find wild application in aerospace, nuclear engineering, automobile and other industries. Composite materials have been subject of permanent interest of various specialists during the last decades. The innovations in the composite area have allowed significant weight reduction in structural design. Competing materials like advanced aluminium alloys and fibre reinforced composites have potential to increase the cost effectiveness of the structure. Composite materials are more difficult to machine than metals mainly because they are anisotropic, non-homogeneous and their reinforcing fibres are very abrasive. During machining, defects have been identified on the workpiece, and absorbed tools wear rapidly as observed by **Abrate; and Walton (1992).** Till now the use of MMC and Al hypereutectic alloys in the automotive, railway and aerospace industries has been limited by the following aspects: (i) the high machining costs due to the shorter tool life; (ii) the PCD tooling are not available for complex-shape cutting tools (e.g. taps, or very small drills and reamers); (iii) during machining of MMC having SiC reinforced particles, a SiC powder formation occurs with the coolant pollution and, moreover, with a degradation of workpiece surface components by abrasion of hard particles, and with a drastic decrease the performance of the PCD tool due to formation of built-up edge formation etc described by **Durantea et al. (1997).** These materials still have their advantages and disadvantages, like the poor fatigue strength of the aluminium alloys and the poor impact and residual strength properties of carbon fibre reinforced composites. At the end of the seventies, the idea was the using of more than one reinforced particles to form a hybrid composite structural material to overcome most of the disadvantages of the monolithic material for structural application as recommended by **Vogelesang and Vlot (2000).** Particle Reinforced Metal Matrix Composites (PRMMC's) have proved to be extremely difficult to machine using conventional machining processes due to heavy tool wear caused by the presence of the hard reinforcement as observed by **Muller and Monaghan (2000).** The applications of MMCs are limited by their poor machinability, which is a result of their highly abrasive nature. This causes excessive tool wear in cutting of SiC-reinforced aluminium matrix composites with tungsten carbide tools and even with coated carbides tool as explained by **Manna and Bhattacharya (2003).** Composites offer many advantages when compared to metallic alloys, especially where high strength to weigh ratio; and stiffness to weigh ratio. Additionally, they provide excellent fatigue properties, high wear resistance; and corrosion

resistance in applications as discussed by **Botelho et al (2006)**. The aluminium alloy–silicon carbide particle composite could be considered as an excellent material where high strength and wear resistance are of prime importance as explained by **Rao et al. (2009).** Few of the review already carried out and reported in the area of fabrication of composite materials, characteristics; and machining of composite materials are described here in after.

Yixiong et al. (2015) investigated the effects of metallic Ti particles on the aging behaviour of squeeze – cast (SiCp+Ti)/ 7075Al hybrid composites and the mechanical properties of the aging treated composites. After aging treated under the optimum aging conditions, the tensile strength of both composites was improved because of the precipitation hardening of the matrix alloy. **Shamanian et al. (2015)** used the accumulative roll bonding process to manufacture a high-strength aluminium matrix composite dispersed with anodized alumina and zirconium carbide particles. The composites produced exhibited a higher tensile strength, elongation than the starting aluminum strips. The composites exhibited higher hardness due to work hardening and grain refinement. **Montalba et al. (2015)** prepared a novel type of piezoelectric aluminium-based hybrid composite containing silicon carbide (SiC) and piezoelectric lead lanthanum zirconatetitanate (PLZT) using powder metallurgy technique. Results confirmed that PLZT and SiC are promising reinforcements for aluminium metal matrix to obtain high damping capacities at an elevated temperature without sacrificing the mechanical strength and stiffness of matrix and composite. **Iacob et al. (2015)** fabricated the $Al/Al_2O_3/Gr$ hybrid metal matrix composite by powder metallurgy technique. The micro-hardness improve when increasing the milling time and the reinforcement content due to presence of hard Al_2O_3 particles. **Jeyasimman et al. (2014)** investigated the dry sliding wear behaviour of AA 6061 nano composites reinforced with various nano level reinforcements, such as titanium carbide (TiC), gamma phase alumina($c\text{-}Al_2O_3$) and hybrid ($TiC + Al_2O_3$) nano particles. The wear rate was found to increase with the load and sliding velocity for all prepared nano composites. **Reihanian et al. (2014)** fabricated an $Al/Al_2O_3/SiC$ hybrid metal matrix composite by accumulative roll bonding (ARB). The tensile strength of the hybrid composite and the monolithic Al reaches to about 195 MPa and 150 MPa, respectively, about 5.3 and 4 times larger than that of annealed Al. The hardness of the composite and the monolithic Al was measured as 83 and 58 VHN, respectively. **Baradeswaran et al. (2014)** fabricated the al composite reinforced with 10 wt.% of boron carbide (B_4C) and 5 wt.% of graphite through liquid casting technique. The wear resistance of the composites was increased with the addition of 10 wt.% B_4C and 5 wt.% graphite particles. The optimum combination of applied load (10 N), sliding speed (0.8 m/s) and sliding distance (2000 m) for

the minimum wear rate. **Tahamtan et al. (2014)** study the integrated composite fabrication process by semi-solid stir casting and ball milling processes. Two different microstructures were characterized including well distributed Al_2O_{3np} and Al_3T_i particles and a network-structure containing Al_3T_{ip} + Al_2O_{3np}. This unique architecture of network structure brought about increment in tensile properties compared to well distributed reinforcement particles, ascribed to the strewing of Al_3T_{ip} + Al_2O_{3np} around matrix grain boundaries, act as a three-dimensions skeletal structure with high local volume fraction of Al_3T_{ip} + Al_2O_{3np}. **Kiran et al. (2014)** investigated the dry sliding wear behavior of zinc based alloy and composite reinforced with SiCp (9 wt%) and Gr (3 wt%) fabricated by stir casting method. Heat treatment (HT) and aging of the specimen were carried out, followed by water quenching. They observed that the applied load significantly influenced the wear volume loss (WVL), followed by sliding speed implying that increase in either applied load or sliding speed increases the WVL. **Suresh et al. (2014)** presented work includes the effect of addition of graphite for improving the properties of Al6061–TiB2 composite using the high-energy stir casting method. The composite of composition Al6061– 20% TiB2 with 2% graphite shows the greatest improvement in mechanical behavior. **Wang; and Song (2011)** manufactured Al_2O_3 fiber (Al_2O_{3f}) and SiC particle (SiC_p) hybrid metal matrix composites (MMCs) by a squeeze casting method. The morphologies of the worn surfaces were examined using a scanning electron microscope (SEM) to observe the wear characteristics and investigate the wear mechanism. An optical microscope (OM) was used to examine the precipitations of the MMCs after wear tests under different temperatures. Authors concluded that the wear resistance of normal (N) MMCs was superior to that of planer random (PR) MMCs as the PR-fibers were easily pulled out whole from the worn surface. The wear resistance of dry sliding wear decreased as the SiC_p content and increased at 100 ^{0}C and 150^{0}C, independently of the fiber orientation. **Alidokht et al. (2011)** fabricated the A356/SiCp/MOS_2 surface hybrid composite by the Friction Stir Processing (FSP). The hybrid composite displays higher hardness compared with the base material. The incorporation of SiCp reinforcement to A356 alloy increases the wear resistance of the composites. Authors concluded that the addition MOS_2 reinforcement in A356/SiCp composites as a hybrid reinforcement further increases the wear resistance of the composite. **Sharifi and Karimzadeh (2011)** investigated the dry sliding wear behavior of aluminum matrix nano composites containing various amounts of Al_2O_3–AlB_{12} (5, 10 and 15 wt.%) particles. Friction values and wear mechanisms were discussed based on scanning electron microscopy pictures and energy-dispersive spectroscopy analysis of wear tracks and wear debris morphology. The average hardness of the nano composite increased with the percentage of added Al_2O_3–AlB_{12} particles. Authors

concluded that the higher content of Al_2O_3–AlB_{12} in the nano composite promotes stronger material transfer from the counter face and oxidation reaction and, consequently, causes formation of protective MML with higher amount of oxide compounds content on the worn surface of nano composite, leading to the lower wear rate. **Babu et al. (2011**) studied the wear behaviour of aluminum based hybrid composites reinforced with graphite nano fiber (GNF) and alumina short fiber (Al_2O_{3sf}) in different volume fraction of fibers (10%, 15% and 20%) under dry sliding conditions. They concluded that the coefficient of friction decreases with increasing applied load and sliding speed whereas it increases with increasing sliding distance. **Suresha and Sridhara (2011)** investigated the sliding friction response of stir cast hybrid aluminium composites reinforced with equal weight fraction of SiC and Gr particulates of 2.5%, 5%, 7.5% and 10% reinforcement. They concluded that the hardness of the composites decreases with increase in % reinforcement. **Mazaheri et al. (2011)** fabricated A356/Al_2O_3 surface nano composite by friction stir processing (FSP) method. X-ray diffractometery, optical and scanning electron microscopy, micro hardness and nano indentation tests were used to characterize the samples. They concluded that the nano indentation technique showed better micro hardness and elastic modulus values for A356/Al_2O_3 surface composites in comparison with as-received A356 and FSPed sample (no Al_2O_3). **Ozdemir et al. (2011)** produced aluminium based SiC and Al_2O_3 particle reinforced composites by semi-solid direct squeeze forming of composite powder at temperatures of 635–645 ^{0}C. Ball milling improves the interface formation between reinforcement and matrix and influences the re-melting behaviour. They described that by increasing ball milling time and decreasing semi-solid forming temperature with isothermal holding time resulted in relatively homogenous microstructures and in a reduced amount of interaction between SiC and metal matrix. They concluded that the best results can be obtained for 5 vol.% SiCp composites after 3 h ball milling, semi-solid formed at 635 ^{0}C and held for 10 min. **Teng et al. (2011)** investigated the thermal conductivity of epoxy composites containing two hybrid fillers which are Multi-Walled Carbon Nano Tubes (MWCNTs) and aluminium nitride (AlN). To form covalent bonds between the fillers and the epoxy resin, poly glycidyl methacrylate (PGMA) were used by the authors and grafted onto the surface of nano-sized MWCNTs via free radical polymerization and Micro-sized AlN was modified by zirconate coupling agent. They concluded that functionalized fillers improve thermal conductivity of epoxy composites, due to the good dispersion and interfacial adhesion. Authors also concluded that the thermal conductivity of epoxy composites containing 25 vol% modified AlN and 1 vol% functionalized MWCNTs is 1.21W/mK, comparable to that of epoxy composites containing 50 vol% untreated AlN (1.25 W/mK), which can reduce the half

quantity of AlN filler used. **Shahzad et al. (2011)** investigated the influence of anodizing process on fatigue life of aluminium alloy 7050-T7451 by performing axial fatigue tests at stress ratio 'R' of 0.1. They concluded that pickling and anodizing processes reduce the fatigue strength of the base material and this could be attributed to surface pits which can facilitate an early fatigue crack initiation and accelerate subsequent crack growth. **Babu and Kang (2010)** performed Nanoindentation on Al based hybrid composites containing graphite nanofiber/ alumina short fiber. Measurement of hardness and elastic modulus were carried out using the Continuous Stiffness Method (CSM) with an indentation depth of about 2000 nm. They concluded that the hardness and elastic modulus found to be increased when the indentation was near the GNFs/Al_2O_{3sf} region within the matrix. **Feng et al. (2010)** fabricated situ Al12W particles reinforced aluminium matrix composite by reaction sintering. They concluded that the ultimate tensile strength is higher than that of matrix. **Suresha and Sridhara (2010)** find Aluminium matrix composites with multiple reinforcements (hybrid AMCs) increased applications because of improved mechanical and tribological properties. They showed that the influence of addition of graphite (Gr) particulates as a second reinforcement on the tribological behaviour of aluminium matrix composites reinforced with silicon carbide (SiC) particulates. The values of wear of these composites are 0.0323 g, 0.0252 g and 0.0223 g, respectively, at % reinforcement of 3%, 7.5% and 10% clearly indicating that hybrid composites exhibit better wear characteristics compared to composites reinforced with SiC alone. **Suresha and Sridhara (2010)** reported the use of graphite (Gr) reinforcement in aluminium matrix composites to be beneficial in reducing wear due to its solid lubricant property, but it results in reduction of mechanical strength. An addition of silicon carbide (SiC), on the other hand, improves both strength and wears resistance of composites, but high amount of SiC makes machining difficult and composites become brittle. Hybrid composites exhibit better wear characteristics compared to Gr reinforced composites. They concluded that the decrease of wear with increase of speed and increase of wear with increase of either load or sliding distance or both. **Mahmouda et al. (2010)** fabricated aluminum-base hybrid composites reinforced with mixtures of SiC and Al_2O_3 particles 1.25µm in average size on an A 1050-H24 aluminum plate. They concluded that the average hardness decreased with increasing the relative content of Al_2O_3 particles. **Wang et al. (2010)** investigated the room temperature sliding wear behaviours of Al_2O_{3f} and SiC_p reinforced aluminium matrix hybrid composites under both the dry and lubricant conditions. They concluded that the F20P0 un-hybrid composites with normal (N)-orientation of fibers had better wear behaviours than those with Planer Random (PR)-orientation of fibers. **Rao et al. (2009)** was examined of dry sliding wear tests of aluminium alloy (Al–Zn–Mg) and

aluminium (Al–Zn–Mg) – 10, 15 and 25 wt.% SiCp composite under varying applied pressure (0.2 to 2.0 MPa) at a fixed sliding speed of 3.35 m/s. They concluded that the wear rate of the alloy was noted to be significantly higher than that of the composite and is suppressed further due to addition of silicon carbide particles. **Guo et al. (2009)** prepared epoxy based composites, filled with hybrid nano-SiO_2 particles and short pitch based carbon fiber. The composite with 4 wt.% nano-SiO_2 and 6 wt.% carbon fiber offered the greatest improvement of the tribological performance. They concluded that the by nano-SiO_2 that act as lubricant which increased surface hardness, wear resisting and friction reducing behaviours and increased lubricating effect of the sheet-like wear debris reinforced. **Urenaet al. (2009)** studied the dry sliding wear of an AA 6061 alloy reinforced with both modified SiC particles and metal coated carbon fibres. SiC particles were used to increase the hardness of the composite while short carbon fibres are supposed to act as a solid lubricant. They concluded that the wear resistance of the composites increased when carbon fibres were added as secondary reinforcement and when coated reinforcements were used. **Mutasher (2009)** investigated the maximum torsion capacity of the hybrid aluminum/composite shaft for different winding angle, number of layers and stacking sequences. They concluded that the increasing the number of layers can increase the static torque capacities of the hybrid shaft for both carbon and glass fiber composite materials. **Liu et al. (2009)** studied the friction and wear properties of Short Carbon Fibers (SCFs) reinforced aluminium matrix composite. They concluded that SCFs/Al composite had better tribological properties than Al alloy. SCF reduced direct contact between the matrix and counterpart and improved the wear resistance of SCFs/Al composite greatly. **Kumar et al. (2009)** made to machine the A356/SiCp composite work material using Electro Chemical Machining process. Silicon carbide with an average particle size of 40 microns is tried in three different proportions, namely 5%, 10% and 15% by weight. They concluded that the feed rate (40%) influences highly the response characteristic, followed by concentration of electrolyte (26%) and by the applied voltage (14%). **Feng et al. (2008)** fabricated Aluminum matrix hybrid composite reinforced with tungsten oxide particles (WO_{3p}) and aluminium borate whiskers (ABOw) by squeeze casting. They concluded that the ultimate tensile strength, yield strength and elastic modulus of the hybrid composite were higher than those of matrix, but the elongation of the hybrid composite is relatively low. **Arik (2008)** produced Al–α-Si3N4 metal matrix composite (MMCs) materials by using powder metallurgy technique. They concluded that the ideal sintering temperature and amount of α -Si3N4 were 660 ^{0}C and 10 wt%, respectively for better mechanical properties. **Bartolome et al. (2008)** fabricated the multi-scale and multi-phase hybrid composite materials Al_2O_3–nZrO_2–Nb. They concluded that bridging of the Nb

inclusions was main factor that can increase the initial level of the driving force for critical micro crack extension, and shield an advancing crack and exert crack closure stresses on the crack wake. **Kwak and Kim (2008)** presented the fabrication by the pressure-less infiltration process under the nitrogen gas atmosphere, and the grinding of the aluminum-based MMCs reinforced with SiC particles. They concluded that the contents of the SiC and the Mg for making a good achievement were 30 and 9 wt%, respectively. **Basavarajappa et al. (2008)** discussed the influence of cutting parameters on drilling characteristics of hybrid metal matrix composites (MMCs)—Al2219/15SiCp and Al2219/15SiCp–3Gr. They concluded that the surface finish increases with increase in cutting speed but decreases with increase in feed rate for both the composites. **Oh and Han (2007)** studied the effects of short-fiber/particle hybrid reinforcement on fracture toughness and fatigue crack growth in metal matrix composites. They concluded that the fracture toughness (KIC) increases with increasing of particle contents. Short-fiber/particle hybrid composites can provide better control of damage tolerance properties over conventional discontinuously reinforced composites. **Zhao et al. (2007)** fabricated a new type of hybrid SiC foam–SiC particles–Al composites by squeeze casting technique. The Coefficients of Thermal Expansion (CTEs) of the hybrid composites in the range of 20–100 0C were found to be between 6.6 and 7.7 ppm/^{0}C. They concluded that theCTEs of the hybrid composites increase from 6.6 to 7.7 ppm/^{0}C when the volume fraction of SiC goes down from 59.9% to 53%. **Khalid et al. (2007)** carried out a bending fatigue analysis for hybrid aluminium/composite drive shafts. They concluded that the increasing the number of composite layers would increase the fatigue strength for a hybrid aluminium/composite drive shaft. **Basavarajappa et al. (2007)** investigated the influence of sliding speed on dry sliding wear behaviour and the extent of subsurface deformation in aluminium metal matrix composites, namely Al 2219/15 SiCp and Al 2219/15 SiCp-3 graphite all fabricated by the liquid metallurgy route. They concluded that with increasing sliding speeds in the mild wear region the degree of subsurface deformation was also increasing. **Basavarajappa et al. (2007)** prepared aluminium metal matrix composites reinforced with SiC and graphite (Gr) particles by liquid metallurgy route. Dry sliding wear behaviour of the composite was tested and compared with Al/SiCp composite. They concluded that the graphite particles are effective agents in increasing dry sliding wear resistance of Al/SiCp composite. **Kim et al. (2006)** applied a smart curing method for the co-cured aluminium/composite hybrid shaft which can reduce the thermal residual stresses generated during co-curing bonding operation between the composite layer and the aluminium tube. The decrease of the fabrication thermal residual stress as well as the full cure of composite specimen was realized by the smart cure cycle with the abrupt cooling.

Belingardi et al. (2006) performed a material characterization on a carbon– glass hybrid composite, characterized by the presence of biaxial intraply glass–carbon laminate as well as biaxial glass laminate and biaxial carbon laminate. They concluded that the tensile failure occurs due to shear failure of the matrix at a 45^0 direction with respect to the specimen axis. **Zhang et al. (2006)** made hybrid performs containing SiC whiskers and nano scale SiC particles by wet blending. Al-based hybrid composites, with 20 vol.% SiC whiskers and 0, 2, 5, 7 vol.% SiC nano particles, by squeeze casting route. They concluded that the strength of the composites can be increase with increasing content of the nano particles. The addition of SiC whiskers and SiC nano particles into 2024 Al alloy increases its elastic modulus and strength. **Gupta et al. (2006)** synthesized a novel aluminum-based hybrid composite containing titanium particulates (discontinuous/particulates reinforcement) and iron mesh (continuous/interconnected reinforcement) using a solidification processing route involving disintegrated melt deposition coupled with hot extrusion. They concluded that the presence of hybrid reinforcement led to a reduction in coefficient of thermal expansion (∼7.6%) and an increase in hardness, elastic modulus (∼10%), 0.2% yield strength (20%) and ultimate tensile strength (∼27%). **Ahlatci et al. (2006)** investigated the dry sliding metal–metal and metal–abrasive wear behaviours of the aluminium matrix hybrid composites produced by pressure infiltration technique. They concluded that the while matrix hardness and compression strength increased, amount of porosity and impact toughness decreased, increase wear resistance with increasing Mg content of the matrix. **Grosz et al. (2005)** fabricated a composite alloy Al–FeAl–TiAl–Al_2O_3 by casting method (gravity casting, mechanical mixing) after which its structure was determined. Presence of aluminium, Al_3Ti and $Al_{13}Fe_4$ phases and dispersed Al_2O_3 was confirmed in the composite by XRD method. **Babbage and Mallick (2005)** describe an experimental investigation on the static axial crush performance of aluminum–composite hybrid tubes, containing filament-wound E-glass fiber reinforced epoxy over-wrap around aluminum tubes. They showed that static axial crush performance of both round as well as square hybrid tubes can be improved using an E-glass fiber/epoxy overwrap. The axial crush parameters that improve very significantly by the use of a composite overwrap are the maximum load, mean crush load and crush energy absorption. **Zhu and Kishawy (2005)** developed a plane-strain thermo-elasto-plastic finite element model and used to simulate orthogonal machining of alumina/aluminium 6061 metal matrix composite using a tungsten carbide tool. They concluded that the due to the failure of alumina particle's interface, the hard particles are debonded or partly debonded and scratch the tool rake face, leading to a high tool wear due to the high shear stress on the alumina particle. **Fu et al. (2004)** investigated the wear properties of Saffil/Al, Saffil/Al_2O_3/Al and Saffil/SiC/Al

hybrid metal matrix composites (MMCs) fabricated by squeeze casting method. Under dry sliding condition, Saffil/SiC/Al showed the best wear resistance under high temperature and high load, while the wear resistances of Saffil/Al and Saffil/ Al_2O_3/Al were very similar. **Ibrahim et al. (2004)** produced three SiC/Al metal matrix composites (MMCs) with SiC particles of 30, 45 and 110 μm in mean sizes using a melt stirring-squeeze casting route. Machining tests were carried out on the MMCs using cubic boron nitride (CBN) cutting tools at various cutting speeds under a constant feed rate and depth of cut. The results showed that tool wear was mainly dominated by flank wear and strongly influenced by reinforcement particulate size.

1.23 LITERATURE ON MICRO ECM

Electrochemical machining uses the electrochemical dissolution (ECD) phase to remove the machining allowance using ion transfer in an electrolytic cell using the Principles of Faraday's (1833). Gusseff introduced the first patent on ECM in 1929, and the first significant development occurred in the 1950s, when the process was used for machining high-strength and heat-resistant alloys. ECM is a major technology in the aircraft, computer, aerospace, electronics components; and micro- mechanics industries for shaping, finishing, deburring, cavity sinking; and milling operations of large parts as explained by **Rajurkar et al. (1999).** The Micro ECM (EMM) method can be effectively used for high precision machining operations such as removal of burrs, making patterns in foils, and 3D micro machining. Results of recent research indicate that the applications of electrochemical metal removal in micro machining offer many opportunities that have been unexplored till now. Further research into EMM will open up many challenging possibilities for effective utilization of ECM in micro machining domain as discussed by **Bhattacharyya et al. (2004), Sen and Shan (2005).** Few of the review already carried out and reported in the area of Micro ECM are described here in after.

Solaiyappan and Karuppan (2015) an investigation was made to study the electrochemical machining characteristics of 20MnCr5 alloy steel. Two electrolytes, namely, aqueous sodium chloride (NaCl)and potassium dichromate (K2Cr2O7) mixed aqueous NaCl, were used to investigate the machining performance. It was noted in the study that the presence of K2Cr2O7 in aqueous NaCl electrolyte increases the material removal rate significantly. **Rathod et al. (2015)** presents the experimental study into fabrication of microgrooves on stainless steel by electrochemical micromachining. Machining accuracy improves, that is, overcut decreases, with decrease in applied voltage, duty ratio, and electrolyte concentration and with increase in pulse frequency and scanning speed of micro tool. **Chen et al. (2015)**

study is the first to focus on removing islands by using a Through-Mask Electrochemical Micro-Machining (TMEMM). The results indicate that the dimensions of micro-dimples are mainly determined by the applied voltage: the micro-dimple diameter increases with increasing voltage, and machining localization increases sharply. With prolonged machining time at constant voltage, only a slight increase in dimple diameter is observed. **Xu et al. (2015)** used cathode travelling and anode vibration to enhance mass transport and to improve the machining surface roughness, because electrolytic products accumulate easily in the machining gap, which causes a rough surface. Moreover, changes in the surface roughness under cathode travelling, anode vibration and pulse conditions were experimentally investigated, and surfaces with Ra= 0.058 μm and Rmax= 0.670 μm were obtained. **Spieser and Ivanov (2015)** presents the design of a next generation μECM machine for the automotive, aerospace, medical and metrology sectors. For the experiments, NaNO3 mixed with a small amount of HCl was used as electrolyte. The design of the electrochemical cell and the innovative pulse PSU implies that the developed μECM machine is both able to perform on-line tool fabrication as well as workpiece machining without any intervention on the hardware (no need to change any cable connection). **Liu et al. (2015)** study focuses on Electrochemical slurry jet micro-machining (ESJM)of tungsten carbide (WC) using a pH-neutral NaCl electrolyte rather than an alkaline solution which ismore commonly used in the electrochemical processing of WC. They found that to involve erosion of the developed oxide layer and subsequent exposure of un-corroded WC, leading to a much higher machining current density, corrosion rate, and machining localization than using ESJM alone. **Rathod et al. (2014)** presented a new approach for sidewall insulation of micro tool by dip coating using liquid solution made of polymer and resin dissolved in isopropyl alcohol and use of acetone for opening the front end of the micro tool. The machining accuracy of the micro features machined were compared in terms of overcut and taper angle generated on micro features. In this way, 33.78% reduction in radial overcut of micro hole and 58.64% reduction in width overcut of microgroove were observed. Taper angle was reduced from 40.57^0 to 18.00^0 and 58.39^0 to 25.20^0 for micro hole and microgroove, respectively. **Ningsong et al. (2014)** studied a dry-film photo resist is used as a mask during through-mask electrochemical micromachining to successfully prepare micro-dimple arrays with dimples 94 μm in diameter and 22.7 μm deep on cylindrical inner surfaces, with a machining time of 9 s and an applied voltage of 8 V. It is also shown that for a fixed dimple depth, a smaller dimple diameter can be obtained using a combination of lower current density and longer machining time in sodium nitrate electrolyte. **Nguyen et al. (2013)** study presents the modelling of radial gap distance in simultaneous micro-EDM and micro-ECM drilling by predicting the thickness of

material layer further dissolved by electrochemical reaction. It is observed that the applied pulse parameters directly affect the final dimension of obtained micro-holes. **Choi et al. (2013)** studied the micro electrochemical machining (ECM) of tungsten carbide with cobalt binder (WC–Co) using ultrashort pulses. In ECM, the machining characteristics were investigated according to machining conditions such as electrolyte, workpiece potential, and applied voltage pulse. Using a mixture of sulphuric acid and nitric acid, microstructures with a sharp edge and good surface quality were machined on tungsten carbide alloy. **Chiou et al. (2012)** proposed a novel electrochemical micro-machining method to fabricate a tungsten micro rod with a high aspect ratio. In this method, the periphery of the iron needle is surrounded by an insulator so that only its end face with the diameter of 50 μm is exposed on the electrolyte as the cathode of the tool electrode. A tungsten rod with a diameter of 200μm is taken as the workpiece and the anode. These two electrodes are immersed to a depth of 3 mm in the electrolyte of 2 wt% sodium hydroxide. An extremely thin straight rod in diameter of 2 μm with an aspect ratio of 120 is fabricated. **Mithu et al. (2012)** study and characterization of the micro electrochemical machining process an experimental setup has been developed. Numerous micro tools have been produced by reverse μECM technique and used to investigate the effect of tool diameter, length and applied frequency on the shape and size of the fabricated micro holes. It has been observed that MRR and machining time increase and decrease respectively with an increase of tool diameter. On the other hand they decrease and increase respectively with an increase of tool length. **Wang et al. (2011)** presented the preparatory investigations of slicing solar silicon ingot into wafers by an abrasive electrochemical method based on a multi-wire saw system. Authors concluded that the anodic passivation on silicon can be controlled by applying an anodic potential during the mechanical slicing process, which improves the surface integrity and material removal rate. **Hyunseop et al. (2011)** proposed a sequential process of Electrolytic In-Process Dressing (ELID) grinding and Chemical Mechanical Polishing (CMP) for hard–brittle materials used in Light-Emitting Diodes (LED), with applications to silicon carbide (SiC), sapphire and gallium nitride (GaN). The advantage of the ELID grinding–CMP process is to dramatically reduce process time and achieve high surface quality by adopting ELID grinding instead of general mechanical polishing, which has a low material removal rate and takes considerable process time. **Kunieda et al. (2011)** described the development of a novel machining method capable of micro-milling and electrochemical turning using a flat electrolyte jet. The workpiece is machined locally in the area hit by the jet which moves when an electrical current is applied to it. They concluded that the use of the flat jet increases the machining speed without sacrificing the micromachining capability. **Yang et al. (2011)** proposed using a

tool electrode with a spherical end whose diameter (150 μm) is larger than that of its cylindrical body (100 μm). They concluded that the curve surface of the spherical tool electrode reduces the contact area between the electrode and the workpiece, thus facilitating the flow of electrolyte to the electrode end, and enables rapid formation of gas film, resulting in efficient micro-hole drilling. **Zhu et al. (2011)** presented a hybrid process of grinding and electrochemical removal for machining of precision small holes with hard-to-machine materials. In the process, a metal rod with coated abrasives as cathode tool rotates at high speed and removes material electrochemically and mechanically for a pre-machined pilot hole. The effects of process parameters on the hole surface quality and dimensional accuracy were demonstrated experimentally. Material removals on grinding and electrochemical machining are well balanced by rationally determining machining voltage, tool rotation speed and feed rate. Precision holes of diameters down to 0.6 mm with sharp edges and without burrs have been produced. **Yang et al. (2011)** presented a new electrochemical micromachining method, which uses everyday mineral water as an electrolyte. The advantages of the new method include totally green machining, high precision, high efficiency, and low-cost. In this study, a WC micro pin with the diameter in the range of 20–30 μm was obtained from a WC pin of 300 μm diameter in about 10 min. They concluded that the machining properties using mineral water as the electrolyte is much faster than the conventional electrolytes, such as $NaNO_3$. **Deconinck et al. (2011)** simulated the ECM process with a moving cathode tool, with the aim to study the influence of the temperature on the uniformity or copying quality of the removal rate. They concluded that the low flow rates result in high temperatures downstream, leading to an asymmetric removal rate. **Hao et al. (2011)** developed a new method for fabricating large-scale three-dimensional (3D) microstructures for cylindrical objects with Proximity Rolling-Exposure Lithography (PREL) and electrochemical micromachining (EMM). A cylindrical rod covered with photo resist was subarea-exposed with a collimated ultraviolet source through a mask by rotating the rod through a definite angle to expose each area. They concluded that the ideal exposure time for a cylindrical layer is three to four times longer than that for a planar layer with the same thickness. **Zhu et al. (2009)** proposed a method of electrochemical micro machining of micro hole or dimple array, in which a patterned insulation plate coated with metal film as cathode was closely attached to workpiece plate. When voltage was applied across the workpiece and cathode film over which the electrolyte flows at high speed, hole or dimple array would produced. The proposed technology offers unique advantages such as short lead time and low cost. **Chan et al. (2009)** investigated the application of micro electrochemical machining (ECM) for the micromachining of internal features. A micro disk-shaped electrode with an

insulating layer on its surface was introduced to machine micro grooves inside the hole. In ECM, the machining gap can be controlled by increasing or decreasing pulse on-time, pulse voltage, or machining time. They concluded that the by using this method, it was possible to control the diameter of the hole during drilling and to make the hole's entrance size smaller than the inside. **Ryu (2009)** described micro electrochemical machining of stainless steel in an environmentally friendly electrolyte of citric acid. Micro ECM was conducted with pulse amplitude range of 5.0–10.0 V and pulse duration time of 100–500 ns. They concluded that the at 6.5 V, as feeding depth increases, mechanical contacts also increase between tool electrode and work material. **Pa (2009)** investigated a super finishing process that uses ultrasonic and magnetic assistance in electrochemical micromachining (EMM) with high efficiency to assist in the discharging of dregs out of the electrodes' gap on free-form surfaces. Ultrasonic and magnetic assistance in electrochemical micromachining (EMM) was used as a super finish process for workpiece surfaces to assist in discharging dregs out of the electrode gap. They concluded that the higher current density with ultrasonic assistance and magnetic assistance was avoid the difficulties related to dreg discharge, and thus reduce the finishing time. **Fan and Hourng (2009)** used 510 μm tungsten rod as the anode, and nickel plates were used as the cathode to fabricate the micro-pin used in Scanning Tunnelling Microscope (STM) by electrochemical polishing. Different from the needle shape in STM, a cylindrical shape of micro electrode was desired for the application in electrochemical drilling. The influence of working parameters on the electrode shape was investigated. They concluded that the microelectrode does not rotate during the electro- chemical machining, its surface will be too rough to be used and its shape is not in a cylindrical form. As the rotational rate is around 1000 RPM, a cylindrical microelectrode can be fabricated. If the rotational rate is around 1500 RPM, a reversely conical electrode is made. As the rotational rate exceeds 2000 RPM, the electrode will become a conical form. The electrode surfaces have screw scrapes and the density of the screw decreases as rotational rate increases. **Lee et al. (2008)** developed an electrochemical micro-machining (EMM) process. In order to have better process control a finite element analysis was employed to ensure machine tool platform rigidity; an electric field analysis was applied for the electrode design. An electrolytic flow analysis was carried out for the fixture design and the selection of the operational parameter. The results of the finite element analysis verified the robustness of the prototype machine. The electric field analysis demonstrated the importance of the insulation layer on the electrode for reducing the diffusive electric current and improving the accuracy of the geometric profile of the finished product. **Holstein et al (2008)** performed electrochemical investigations showed that tungsten was dissolved similar to steels by applying a newly

adopted electrolyte which overcomes passivation. These results opened the paths to examine different ECM variants (M-ECM, C-ECM) for electrochemical structuring processes of tungsten. In M-ECM, an electrical insulating mask deposited onto the tungsten anode surface protects the areas not to be removed, whereas all the uncovered areas, which are in contact with the bulk electrolyte, will be uniformly dissolved. Because of the direct electrolyte contact, physical parameters like electrode distance, shape of work pieces and orientations have only a minor influence. **Xiaohai Li et al. (2008)** developed a new micro ECM setup to fabricate micro parts and explore the feasibility of micro ECM. A micro hole about 30 μm in diameter was drilled by rotating micro electrode. The hole was drilled by no-rotating electrode, whose edge is irregular under the machining conditions. They concluded that the rotation of electrode is helpful to remove the insoluble electrolytic product and the heat in machining gap and it can improve the shape accuracy of holes. **Natsu et al. (2008)** proposed a method to generate three-dimensional surfaces with micro-electrolyte jet machining. Authors concluded that the three-dimensional surfaces can be generated by superimposing elemental curved grooves, and good agreement between the cross-sectional shapes of the superimposed and machined surfaces with those of the target surface proves the effectiveness of the proposed method. **Zhu et al. (2007)** developed a micro wire electrochemical cutting process. Because of no electrode wear in this process a very thin metal wire was used as the wire electrode. The machining gap was dependent on the feed rate of the wire electrode, pulse voltage and pulse on-time. The high feed rate leads to the decrement of machining gap, i.e. the improvement of machining accuracy. They concluded that the machining accuracy becomes poor as the pulse voltage and pulse on-time increase. Therefore, the feed rate as high as possible under a steady machining process was suggested for the improvement of the machining accuracy. **Hewidy et al. (2007)** presented an analytical approach to establish mathematical model in an endeavour to assess the mechanism of metal removal for this novel and hybrid technique. Authors concluded that the increase of feed rate is an advantage in the ECM process because it decreases the side gap value, which consequently improves both the product accuracy and the process productivity. The increase of the tool velocity increases the pumping action in the machining zone, which leads to an improvement in the machining conditions. **Bhattacharyya et al. (2007)** developed a suitable micro-tool vibration system. In normal EMM operation, machined products were not flushed away from the narrow machining gap, as electrolyte was normally kept stagnant. Compared to normal EMM operation without tool vibration, it was evident that MRR and accuracy were better during EMM operation with micro-tool vibration. It generates small pressure waves in the machining zone that destroy the passive layer from the copper test-piece surface, which

improves the flow direction of current flux results in higher and controlled MRR that leads to better accuracy. This also permits the use of high current densities in order to improve the quality of the machined micro-products. **Munda et al. (2007)** made to establish comprehensive mathematical model for correlating the interactive and higher-order influences of various machining parameters of micro ECM. From the developed mathematical model, the optimal machining parametric combination, i.e., pulse on/off ratio of 2.1618, machining voltage of 2.8347V, electrolyte concentration of 10 g/l, voltage frequency of 35Hz and tool vibration frequency as 100 Hz was found out to achieve the lowest value of micro-spark and stray-current affected zone, i.e., 0.0001 mm. **Asad et al (2007)** introduced the achievements in the area of tool-based micro machining. Micro-machining is the most basic technology for the production of such miniaturized parts and components. Since miniaturization of industrial products had been the trend of technological development, micro-machining is expected to play increasingly important roles in today's manufacturing technology. Micro-turning, micro-grinding, micro-EDM and micro-ECM have many advantages in productivity, efficiency, flexibility and cost effectiveness. **Kurita and Hattori (2006)** investigated EDM (Electro Discharge Machining) and ECM (Electrochemical Machining) ECM-lapping complex machining. The EDM surface of 1 mm Ra is improved to 0.2 mm Ra by applying ECM. Second, in order to get a smoother surface, a new EDM and ECM-lapping complex machining technology was developed. The surface roughness of a machined hole was improved to 0.07 mm Ra by applying 2 min of ECM lapping. **Zhu and Yun (2006)** presented the characteristics of MEMS (Micro-Electro-Mechanical System). They concluded that the micro-USM method has lower productivity and poor procession, direct current micro-USM and ECM has highest productivity, pulse electrical current micro USM and ECM has best procession. Micro holes and axis of round procession can be machine by combined micro USM and ECM. **Park et al. (2006)** studied the effects of tool electrode size on micro ECM. As the tool electrode becomes larger, the actual rising time of the double layer potential increases because cell impedance decreases. Therefore, there was a minimum pulse on-time to obtain an effective potential for the successful machining according to the tool electrode size. **Xiong and Yang (2005)** employed a new ECM technique, jet-electrochemical micromachining (Jet-EMM), to produce micro-hole patterns on titanium specimens. Surface holes, which are hundreds of micrometers in diameter and have an aspect ratio of over 1.3, were machined by combining jet flow impingement and electrochemical reaction. Compared with Through Mask Electrochemical Micro Machining (TMEMM), Jet-EMM exhibits an advantage in producing surface features with a high aspect ratio and in producing the features on curved surfaces. **Rosenkranz et al. (2005)** performed

machining, during electrochemical micro machining (ECMM) metals were electrochemically dissolved at very high current densities up to 100 A/cm^2 in aqueous electrolytes like $NaNO_3$andNaCl. Different anode processes take place during the electrochemical machining (ECM) process of iron in $NaNO_3$. The different reaction products were analysed quantitatively and time resolved for pulses 10 ms $\leq t_{pulse} \leq$ 5000 ms under ECM conditions by a combination of our flow-through-microcell with an UV–vis - spectrometer and a pulse generator. **Zhijian et al. (2004)** performed ECM simulation tests and the technological experiments using a permanent magnet on the machine tool. Due to the extra energy provided by the magnetic field, the critical voltage decreases with the increase the probability for the particles to be excited to higher energy level from the ground state. They concluded that the dispersion corrosions in ECM are reduced by the properly designed magnetic field. **Kozaket al. (2004)** presented the results of theoretical and experimental investigations of the relationship between the characteristic shape dimensions imported upon the anode-workpiece surface by the micro-features of the cathode-tool electrode under given machining conditions. For improving micro-machining capabilities of ECM processes, the application of ultra-short pulse current and ultra-small gap size was recommended. **Ahn et al. (2004)** applied Electro-chemical machining (ECM) in micro machining because the electric field was not localized. The ultra short pulses with tens of nanosecond duration were used to localize dissolution area. High quality micro hole with 8μm diameter was drilled on 304 stainless steel foil with 20μm thickness. The primary factors considered for the selection of electrolyte concentration were the minimum machining gap, sufficient ionic concentration and good machined surface quality.

1.24 GAPS IN LITERATURE REVIEW

From literature review, it is understood that composite materials have good mechanical and physical properties, so that they are used in different industry applications. The applications of MMCs are limited by their poor machinability, which is a result of their highly abrasive nature. This causes excessive tool wear in cutting of ceramic reinforced aluminium matrix composites with conventional machining. Non-conventional machining methods like EDM, USM, LBM, ECM and ECSM produced better result while machining of composites. Results of recent research indicate that the applications of electrochemical metal removal in micro machining offer many opportunities that have been unexplored till now. However, from literature review the following drawback are enlisted below:

1. Metal Matrix Composites (MMC's) have proved to be extremely difficult to machine using conventional machining processes due to heavy tool wear caused by the presence of hard reinforcement.
2. Formation of built-up-layer and built-up-edge during machining of Al/SiC-MMC, Al/Al_2O_3-MMC etc
3. Poor surface finish is obtaining by machining of hybrid components.
4. A little research available for machining of hybrid composite like Al/ (SiC+Al_2O_3+C)-MMC with varying wt% of reinforced particulates in metal matrix composites.
5. A less works reported on machining of hybrid composites by micro electrochemical machining process.

1.25 PROBLEM FORMULATION

Different traditional casting methods are employed for producing composite parts but it has been difficult to achieve required tolerances and closer dimensional accuracy feature in practice through such processes. The production of through and blind holes, grooves, slots and odd shaped complex contours with high dimensional accuracy in micro level on the hybrid composite parts have also been difficult to obtain with traditional casting process. Hence, it is required to finish the parts with subsequent machining processes. In traditional machining technique, relatively harder cutting tool material has been required to machine comparatively softer work piece material in which the work piece is transferred into a finish product or parts of specific size, shape and by achieving required configuration with the interaction of harder cutting tool material. But, advance hybrid composite has reinforced SiC, Al_2O_3, Carbon, Glass fibres, which are harder than tungsten carbide (WC) a common cutting tool material. As hybrid composites have very high value of hardness and stiffness, the selection of proper cutting tool material and machining process for proper machining of such composites have really been very difficult.

From the literature review, it is clear that by the non-conventional machining process, machining of composite is difficult and cost inflation. The problems encountered during processing of composites, well known non-conventional machining methods are irregular material removal rate, requires large current, unstable machining due to fluctuation of spark gap, wear on electrode, very poor surface finish, etc. These problems have resisted the wide spread application of composite in industry.Although some research on traditional and non-traditional machining of composites have been carried out by the previous researchers but still no such research available for machining of hybrid composite like Al/Al_2O_{3p}-SiC_p-C_p

with varying wt% metal matrix composites. Hence a lot of applied research on hybrid composite is quite important for modern manufacturing engineers. As literature a knowledge that metal matrix composite machining is really very difficult and cost inflation; hence hybrid metal matrix composites obviously resist its wide spared application in industry due to poor machinability. As the hybrid composite materials having better mechanical and physical properties as compare to ordinary material and composite material, therefore it is important to search a new machining method for effective machining such hybrid composite. Keeping in view, the Electrochemical Micro Machining (ECMM) process is selected to machine $Al/(Al_2O_{3p}+SiC_p+C_p)$ – MMC hybrid composite.

For this purpose, an Electrochemical Micro Machining (ECMM) set-up has been designed, fabricated and utilized to conduct the experiment on hybrid composite.

1.26 PROBLEM ENCOUNTERED DURING MACHINING OF COMPOSITE MATERIALS

The machining of composite materials is one of the major problem, which resist its wide spread application in industry. From the past literature review, few of the problems encountered during machining of composite materials are:-

- Rapid Tool Failure,
- Irregular and Fluctuating Metal Removal Rate,
- Requirement of Large Current Values,
- Very Poor Surface Finish,
- Difficult to Cut a Complicated Profile,
- Frequent Electrode Wear During Machining by ECM

1.27 OBJECTIVES OF PRESENT RESEARCH WORK

The objectives of present research are listed below:

1. To carry out the study for understanding the particular hybrid aluminium metal matrix composite materials by indentifying some of the key factors, machining characteristics of hybrid composite will be investigated thoroughly at micro level.
2. To analyze the fundamental characteristics and principles underlying the material removal mechanism in micro electrochemical drilling of hybrid composite.
3. To analyze the fundamental characteristics of machinability and principle underlying the electrode wear rate, i.e. to analyze the basic causes of electrode wear rate during micro electrochemical drilling of hybrid composite.

4. To conduct an experiment investigation for optimization of cutting condition for better surface structure during micro electrochemical drilling of hybrid composite using Taguchi design concept.
5. Analysis of test results for investigating the influence of various parameters on wear rate of electrode, material removal rate, taper effect, surface structure.
6. To study the wear condition of electrode and surface structure of drilled hole through scanning electron microscope (SEM) micrographs.

1.28 PHASING OF RESEARCH WORK

Experiments will be conducted on the basis of the initial chosen parameters and at random parameters setting for both the machining processes to validate the developed models. The phasing of research work is representing by following flow chart:-

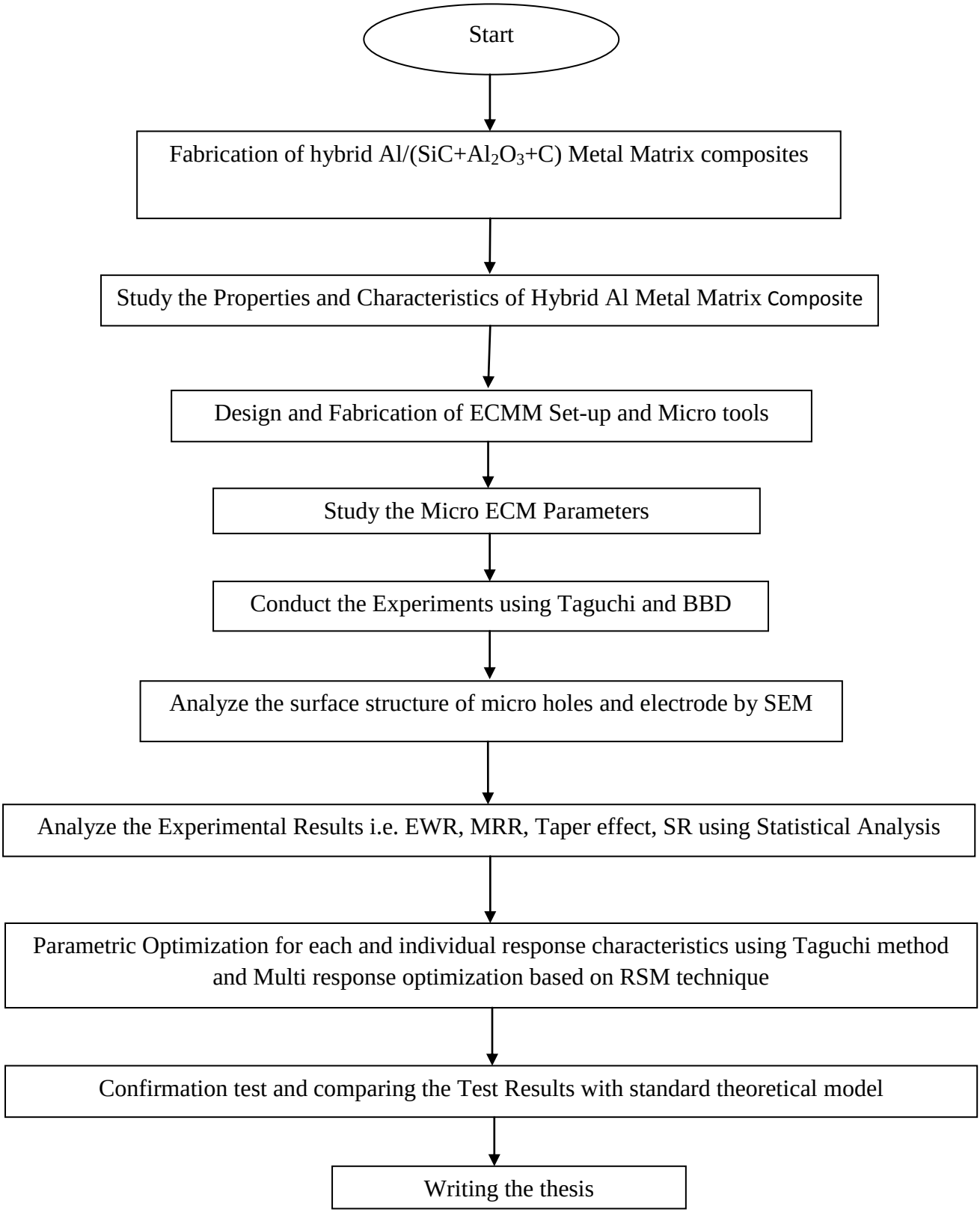

Fig. 1.18 Phases of Research Work

Chapter 2

FABRICATION OF METAL MATRIX COMPOSITES, MECHANICAL PROPERTY AND WEAR TEST

Introduction

The workpiece specimens were prepared from fabricated Al/SiCp-MMC, Al/Al_2O_3p-MMC, Al/Cp-MMC, Al/(Al_2O_3p+SiCp)-MMC, Al/(Al_2O_3p+Cp)-MMC, Al/(SiCp+Cp)-MMC, and Al/(Al_2O_3p+SiCp+Cp)-MMC samples. These workpiece specimens were used for wear test and mechanical properties analysis. The liquid stir cast technique was utilized for fabrication of metal matrix composites (MMCs) samples with varying the weight fraction of reinforced particles alumina (Al_2O_3), silicon carbide (SiC) and carbon (C). The cast round shape Al/MMCs and hybrid Al/MMCs samples were machined and prepared in cylindrical shape having diameter 8mm and length 35mm for wear test. The turning operations were carried out to prepare the workpiece specimens. Commercially available A6061-aluminum was used as a matrix material. The different sets of tests were carried out to identify the best hybrid Al/MMC through wear and mechanical property tests. Based on the wear test results and mechanical properties analysis the best quality of hybrid Al/MMC was selected for further experiments. The selected fabricated hybrid Al/MMC was utilized as workpiece specimens for further processing through micro drilling on fabricated Micro ECM set-up. A Micro ECM set-up was designed, fabricated and utilized for experimental investigation as explained in the Chapter 3. The feasibility tests were carried out on the fabricated set-up to identify the suitability of the set-up for micro drilling of Al/(Al_2O_3p+SiCp+Cp)-MMC. The A-6061 aluminum was procured from M/s Mohan Metals and used as matrix for fabrication of Al/MMCs. The average particles size (APS) of Al_2O_3 was 400 mesh (i.e. 38µm), SiC was 400 mesh (38µm), and C was 1000 mesh (15.2 µm), these three abrasive reinforced particles were procured from M/s Machine Store Co. Ludhiana, M/s Gyatri Abrasives Ltd. Udhaypur, and M/s Allied Ind. Ltd. Jalandhar respectively. These three particulates were used as abrasive reinforced particles for fabrication of hybrid Al/MMCs. A designed dimension of workpiece specimen was selected in such a way so that the workpiece can be easily machined without damage of the workpiece surface on the fabricated set-up. The scheme for fabrication of Al/MMCs and hybrid Al/MMCs, and their wear and mechanical

properties analysis are explained in the successive articles. The preparation of workpiece specimens for further experiments through conventional machining operations are also described in the following sub-sections.

2.1 RAW MATERIAL FOR Al/MMC AND HYBRID Al/MMCs

The Al/SiCp-MMC, Al/Al_2O_3p-MMC, Al/Cp-MMC, Al/(Al_2O_3p+SiCp)-MMC, Al/(Al_2O_3p+Cp)-MMC, Al/(SiCp+Cp)-MMC, and Al/(Al_2O_3p+SiCp+Cp)-MMC were fabricated utilizing liquid stir cast technique. The fabrication of MMCs were planned in such a way so that the different weight fractions of reinforcement Al_2O_3, SiC and C particulates can be used to fabricate the Al/MMCs and hybrid Al/MMCs as explained in Table 2.1. The following raw materials were unitized to fabricate the different weight fraction reinforced hybrid Al-MMCs such as (i) A-6061 Aluminum used as matrix, and (ii) Al_2O_3, SiC and C used as reinforced particles. The metal mould made of IS 2002-1962, high temperature service pipe, medium grade of 40 mm nominal diameter x 3.15 m wall thickness was used as mould cavity to fabricate the MMCs samples by liquid stir casting.

Table 2.1 MMCs with Different Weight Percentage of Reinforced Particles C, Al_2O_3 and SiC

Sl. No.	Different types of MMCs	C (wt%)	Al_2O_3 (wt%)	SiC (wt%)
1.	Al/Cp-MMC	15	--	--
2.	Al/Al_2O3_p-MMC	--	10	--
3.	Al/SiCp-MMC	--	--	10
4.	Hybrid Al/(Cp + Al_2O_3p)-MMC	5	10	--
5.	Hybrid Al/ (SiCp + Cp)-MMC	5	--	10
6.	Hybrid Al/(SiCp + Al_2O_3p)-MMC	--	10	10
7.	Hybrid Al/(SiCp + Al_2O_3p + Cp)-MMC	5	10	10

2.1.1 Aluminum Ingot

The aluminum ingot A-6061 of 99.99% pure procured from M/s Mohan Metals. It was used as a metal matrix for fabrication of Al-MMCs samples. The ingot was cut into small pieces of

different shape and sizes for proper melting in the resistance furnace on a graphite crucible. Figure 2.1 shows the small pieces of different shape and size of pure aluminum used as matrix material for fabrication of MMCs and hybrid MMCs samples.

Fig. 2.1 Pure Aluminum Pieces for Matrix Metal

Table 2.2 represents the chemical composition of A-6061 aluminum ingot used as matrix material.

Table 2.2 Composition of A-6061 Aluminum Ingot Material

Grade	**UNS NO.**	**Si (%)**	**Fe (%)**	**Cu (%)**	**Ma (%)**	**Mg (%)**	**Cr (%)**	**Zn (%)**	**Ti (%)**	**Un-Specified elements (%)**	**Aluminium**
6061	A96061	0.40-0.8	0.7	0.15-0.40	0.15	0.8-1.2	0.04-0.35	0.25	0.15	0.15	Remaining

2.1.2 Al_2O_3 Abrasive Particulates

Alumina (Al_2O_3) particulate of average particle size 400 mesh (38µm) was used as abrasive reinforced particles. The MMCs were fabricated with varying the weight fraction of Al_2O_3 such as 5wt.%, 7.5wt.% and 10wt.%. Figure 2.2 show the Al_2O_3 particulate was procured from the M/s Machine Store Co. Ludhiana and used as reinforced particles. Table 2.3 represents the grades and constituents of Al_2O_3 abrasive particles. Table 2.4 represents the physical and mechanical properties of Al_2O_3 abrasive particles used for fabrication of hybrid MMCs.

Fig. 2.2 Al_2O_3 Reinforced Particulates

Table 2.3 Grade and Constituents of Al_2O_3 Abrasive Particles

Grade	Mesh size and Micro (µm)	Pb	Na_2O	Cl	SO_4	Al_2O_3
Puriss	400 (38µm)	≤0.005%	≤0.2%	0.1%	0.1%	Remaining

Table 2.4 Physical and Mechanical Properties of Al_2O_3

Name	Density (gm/cm^3)	Elastic module (Tensile) (GPa)	Tensile strength (MPa)	Vickers hardness (kgf/mm^2)	Knoop hardness (kgf/mm^2)	Compressive Strength (MPa)	Thermal conductivity (W/mK)	Co efficient of Thermal expansion
Al_2O_3	3.985	350-390	250-400	1600-1800	2000	2100	32.6	6.8 x 10^{-6}/K

2.1.3 SiC Abrasive Particulates

Silicon carbide (SiC) particulate of average particle size 400 mesh (38µm) was used as hard reinforced particles. The aluminum metal matrix composite with varying weight fraction of SiC i.e. 10wt.%, 15wt.% and 20wt.% cast samples were fabricated and utilized as raw materials for experimental investigation. Figure 2.3 show the SiC particulate was procured from the M/s Gyatri Abrasives Ltd. Udhaypur and used as reinforced particles. Table 2.5 represents the grades and constituents of SiC abrasive particles. Table 2.6 represent the physical and mechanical properties of SiC abrasive particles used for fabrication of hybrid MMCs.

Table 2.5 Grade and Constituents of SiC Abrasive Particles

Grade	Mesh size and Micro (µm)	Fe_2O_3%	SiO_2%	TiO_2%	SiC
P600	400 (38µm)	0.003	0.02	0.003	Remaining

Fig. 2.3 SiC Reinforced Particulates

Table 2.6 Physical and Mechanical Properties of SiC

Name	Density (gm/cm^3)	Elastic module (Tensile) (GPa)	Tensile strength (MPa)	Vickers hardness (kgf/mm^2)	Knoop hardness (kgf/mm^2)	Thermal conductivity (W/mK)	Co efficient of Thermal expansion ($10^{-6}/^0C$)
SiC	3.1	410	129	2800	2540	120	4

2.1.4 C Reinforced Particulates

Carbon (C) particulate of average particle size 1000 mesh (15.2µm) was used as hard reinforced particles. The aluminum metal matrix composite with varying weight fraction of C i.e. 3wt.%, 5wt.%, 7.5wt.% and 15wt.% cast samples were fabricated and utilized as raw materials for experimental investigation. Figure 2.4 show the C particulate was procured from the M/s Allied Ind. Ltd. Jalandhar and used as reinforced particles.

Fig. 2.4 C Reinforced Particulates

2.2 FABRICATION OF MMCS BY LIQUID STIR CAST TECHNIQUE

The available fabricated liquid stir cast set-up (fabricated by the previous researcher at PEC, Chandigarh) was utilized to fabricate the MMCs and hybrid MMCs. The round shape of 40 mm diameter samples was fabricated. The cast round shape samples were used for the preparation of test specimens to carryout different tests for mechanical properties analysis and wear test

analysis. These cast samples were also used for preparation of workpiece specimens and the prepared workpiece specimens were utilized for feasibility and details experiments.

For sound casting of MMCs and hybrid MMCs specimen effective stirring is very much essential to achieve uniform mixing of all constituents so as to achieve desired properties. Figure 2.5 shows a schematic diagram of the available fabricated stir cast set-up.

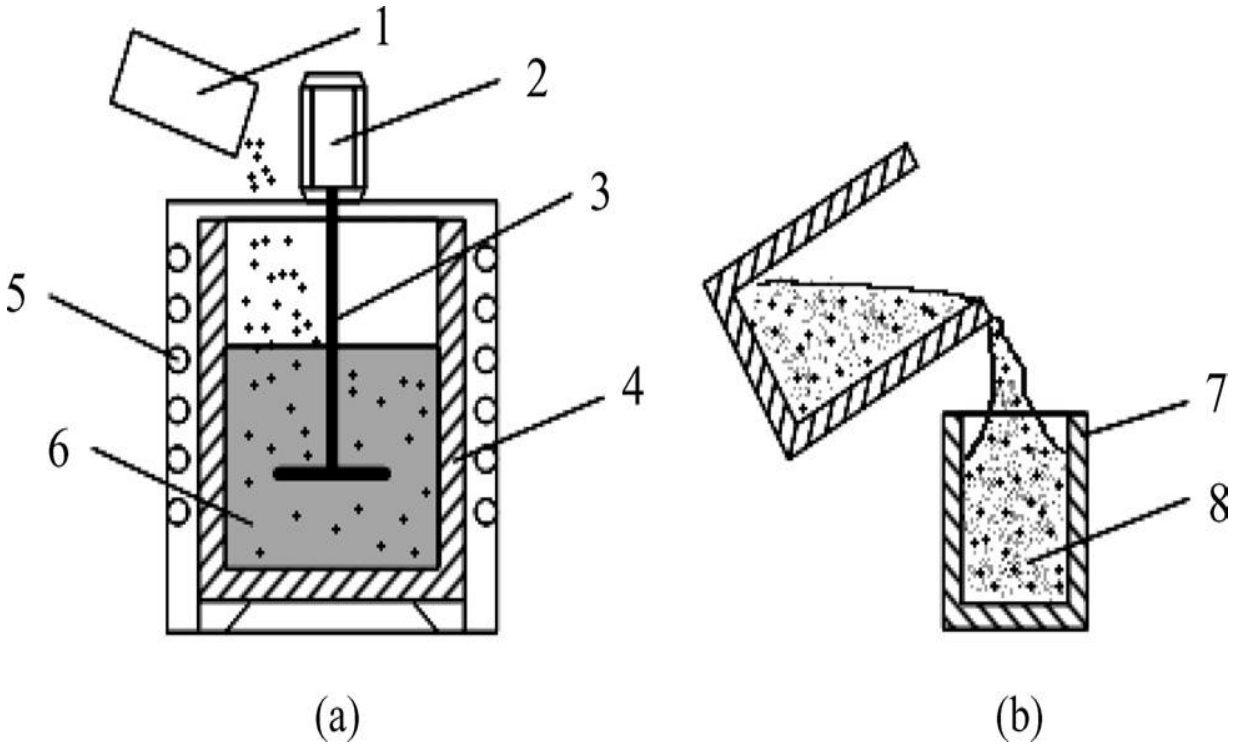

Fig. 2.5: Schematic Diagram of Liquid Stir Casting Set-Up

1. Particulate; 2. Stirrer; 3. Graphite impeller; 4. Crucible, 5. Induction Furnace; 6. Molten metal; 7. Mould; 8. Composite

Three electric furnaces were simultaneously used during casting of MMCs and hybrid MMCs. Three furnaces of capacity 1250^0C, 1150^0C, and 550^0C are simultaneously used for melting Al-matrix, pre-heating of reinforced particles (Al_2O_3, SiC, and C) and backing of clay coated metal mold cavity respectively. Figure 2.6 shows one of the furnaces used for stir casting of MMCs. Stir casting method involves incorporation of ceramic particulate into liquid aluminum melt and allowing the mixture to solidify. Here, the crucial thing is to create good wetting between the particulate reinforcement and the liquid aluminum alloy melt. Aluminum was preheated up to a temperature of 450^0C in induction furnace before melting. Particles of Silicon Carbide (SiC), Carbon (C) and Aluminum oxide (Al_2O_3) were also preheated up to a temperature of 1100^0C in

second induction furnace for 2 hours. Crucible used for pouring of composite slurry in the mould was also heated up to 760 ^{0}C to make their surfaces oxidized.

Fig. 2.6 Resistance Furnace of Capacity 1250^{0}C Used for Pre-Heating of Reinforced Particles (Al_2O_3, SiC, and C)

2.2.1 Preparation of Metal Mould

The permanent metal molds were fabricated from IS 2002-1962/ high-temperature service pipe, medium grade of 40 mm nominal diameter x 3.15 mm thickness. One mold was also fabricated from IS 226/10 mm thick plate. The mould size was 70 mm x 30 mm x 350 mm long. The rectangular and circular shape cast samples of Al-MMCs were fabricated with varying the percentage of weight fraction of reinforced particles (Table 2.7). These fabricated cast Al-MMCs samples were utilized for testing of mechanical properties. Figure 2.7 shows the round shape metal mold cavity used for fabrication of MMCs and hybrid MMCs in CAD model. Figure 2.8 shows the rectangular shape metal mold cavity used for fabrication of MMCs and hybrid MMCs in CAD model. Figure 2.9 shows the clay coated actual mold used for fabrication of MMCs and hybrid MMCs.

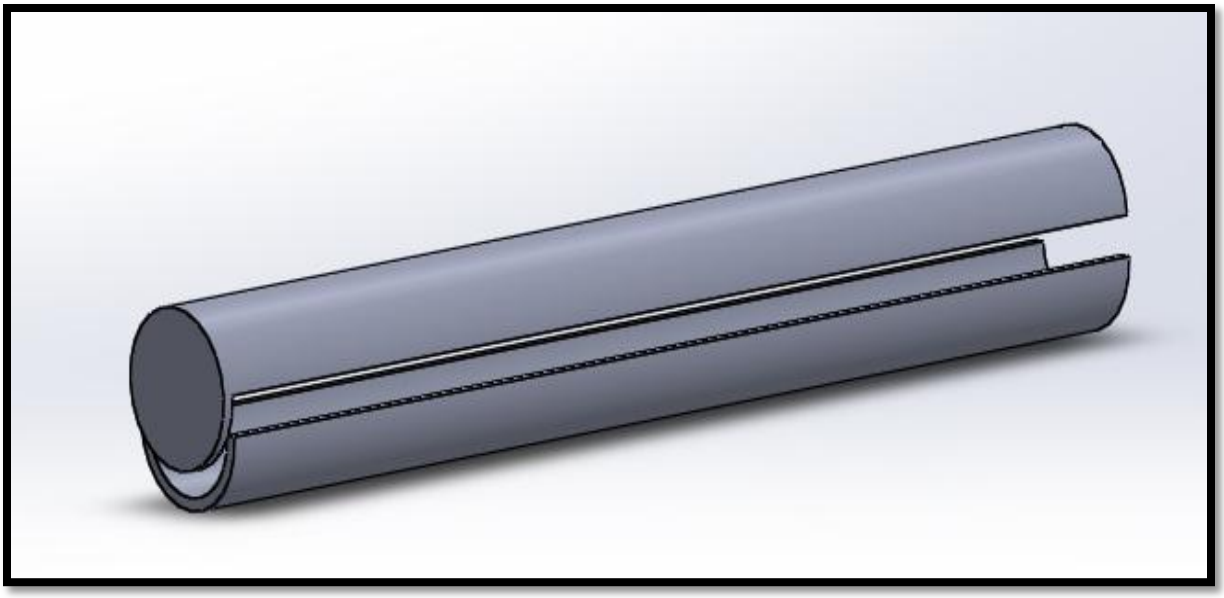

Fig. 2.7: CAD Model of Round Shape Metal Mold Cavity Used for Fabrication of Al-MMCs Samples

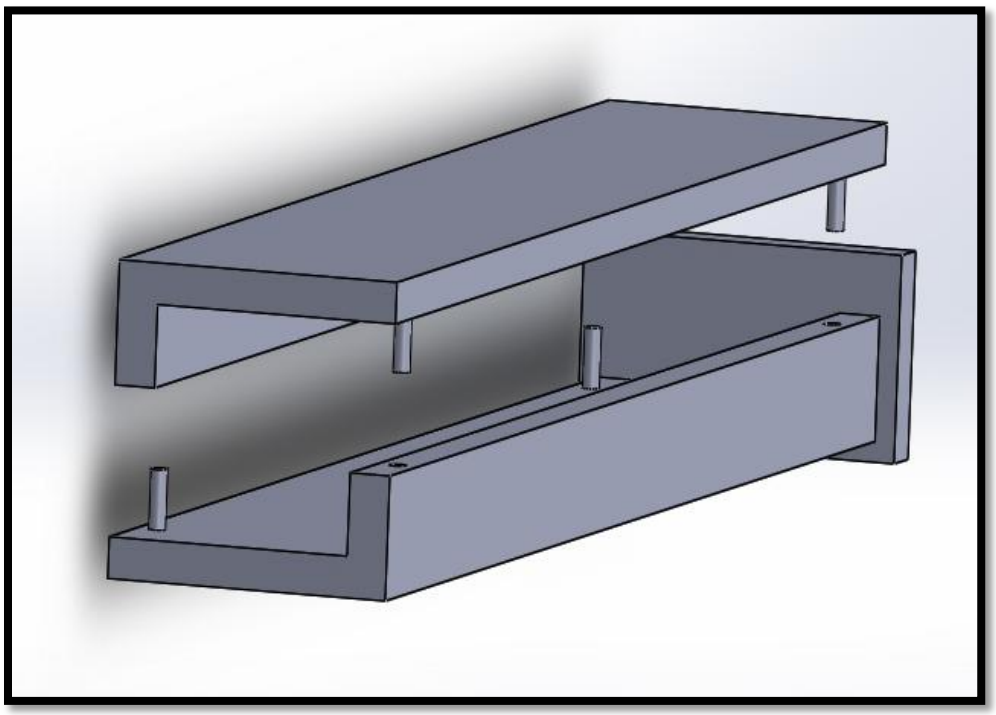

Fig. 2.8: CAD Model of Rectangular Shape Metal Mold Cavity Used for Fabrication of Al-MMCs Samples

Fig. 2.9 Clay Coated Actual Mold Used with Cast MMCs

2.2.2 Liquid Stir Casting of MMCs and Hybrid MMCs

The following steps were carried out during fabrication of MMCs and hybrid MMCs by stir casting as follows:

- Aluminum was preheated to 450^0C for 2 hrs before melting in a furnace of capacity 1150^0C. The temperature of the aluminum was raised above its liquids state temperature (660^0C) to melt the aluminum pieces. Then molten metal cooled to just below the liquid temperature to keep slurry in a semi-solid state. Sludge removal from molten matrix metal was done during each casting operation to maintain its purity.
- The reinforced particulates (Al_2O_3, SiC, and C) were simultaneously pre-heated to 1150^0C for 2 hrs in another furnace of capacity 1250^0C.
- The clay coated metal mold was pre-heated simultaneously at 400^0C for 2 hrs in the third furnace of capacity 550^0C.
- The preheated Silicon Carbide (SiC), Carbon (C) and Aluminum oxide (Al_2O_3) particles from second furnace was taken and added to molten metal Al-matrix at 680 ± 10^0C.
- The mixture of the pre-heated reinforced particles and molten matrix was stirred up thoroughly to form a proper heterogeneous mixture. Automatic stirring has carried out with the help of electric machine for about 10 minutes at stirring rate of 300 rpm.
- Melt mixture is then poured into the pre-heated metal mold cavity (shown in Figure 2.9) which is in rectangular, and cylindrical shapes and allowed it for solidification.

- Stir cast specimens were removed and cleaned for mechanical properties testing, wear testing and prepared the workpiece specimens for micro drilling experiments. Figure 2.10 show the stir cast specimens.

Fig. 2.10 Cast MMCs Specimens

2.3 IMPACT TEST RESULTS

The Charpy impact test known as the Charpy v-notch test is a standardized high strain rate test, which helps to determine the amount of energy absorbed by a material during fracture. This absorbed energy gives the material toughness. Table 2.7 represents the test results acquired during impact test on MMCs and hybrid MMCs.

Table 2.7 Impact Test Results Acquired During Testing

Serial No	Pure Al and Composites	Trial				Average Force N
		1	2	3	Total Force N	
1	Al Alloy	6.2	6.1	5.9	18.2	6.06
2	Al/15 wt% Cp-MMC	6.4	6.3	6.5	19.2	6.4
3	Al/10 wt% Al_2O_3p-MMC	8.5	8.3	8.6	25.4	8.46
4	Al/10 wt% SiCp-MMC	8.6	8.9	8.8	26.3	8.76
5	Hybrid Al/(5 wt% Cp + 10% wt Al_2O_3p)-MMC	8.9	9.3	9.1	27.3	9.1
6	Hybrid Al/(10 wt% SiCp + 5 wt% Cp)- MMC	8.9	9.5	9.1	27.5	9.16
7	Hybrid Al/(10 wt% SiCp + 10 wt% Al_2O_3p)- MMC	9.2	9.4	9.7	28.3	9.43
8	Hybrid Al/(10 wt% SiCp + 10% wt Al_2O_3p+ 5 wt% Cp)- MMC	9.8	10.2	10.4	30.4	10.13

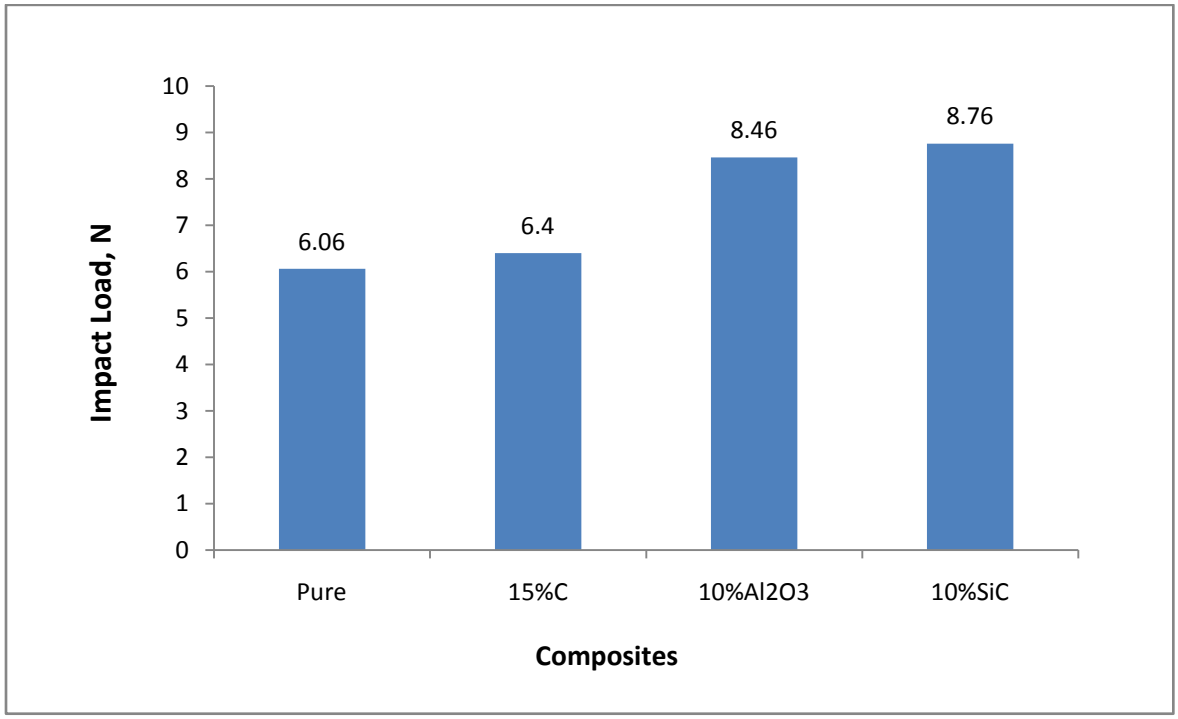

Fig. 2.11 Impact Strength of Pure Al and Al MMCs

Figure 2.11 shows the variation in impact strength of Al materials with addition of SiC, Al_2O_3 and C constituent. Impact strength increases with addition of reinforced particles like C, Al_2O_3 and SiC. This is due to proper dispersion of SiC, Al_2O_3 and C into the matrix. This may also happen due to strong interfacial bonding in between the matrix Al, and reinforced particles SiC, Al_2O_3 and C interfaces. The following points are highlighted as below:

- The impact load increases from 6.06 N to 6.40 N when Al matrix is reinforced with 15 wt% C. As pure Al matrix has impact load is only 6.06 N. It implies that impact load has increased by 5.61% with addition of 15 wt% C.
- The impact load increases from 6.06 N to 8.46 N when Al matrix is reinforced with 10 wt% Al_2O_3. It implies that impact load has increased by 39.60% with addition of 10 wt% Al_2O_3.
- The impact load increases from 6.06 N to 8.76 N when Al matrix is reinforced with 10 wt% SiC. It implies that impact load has increased by 44.55% with addition of 10 wt% SiC.

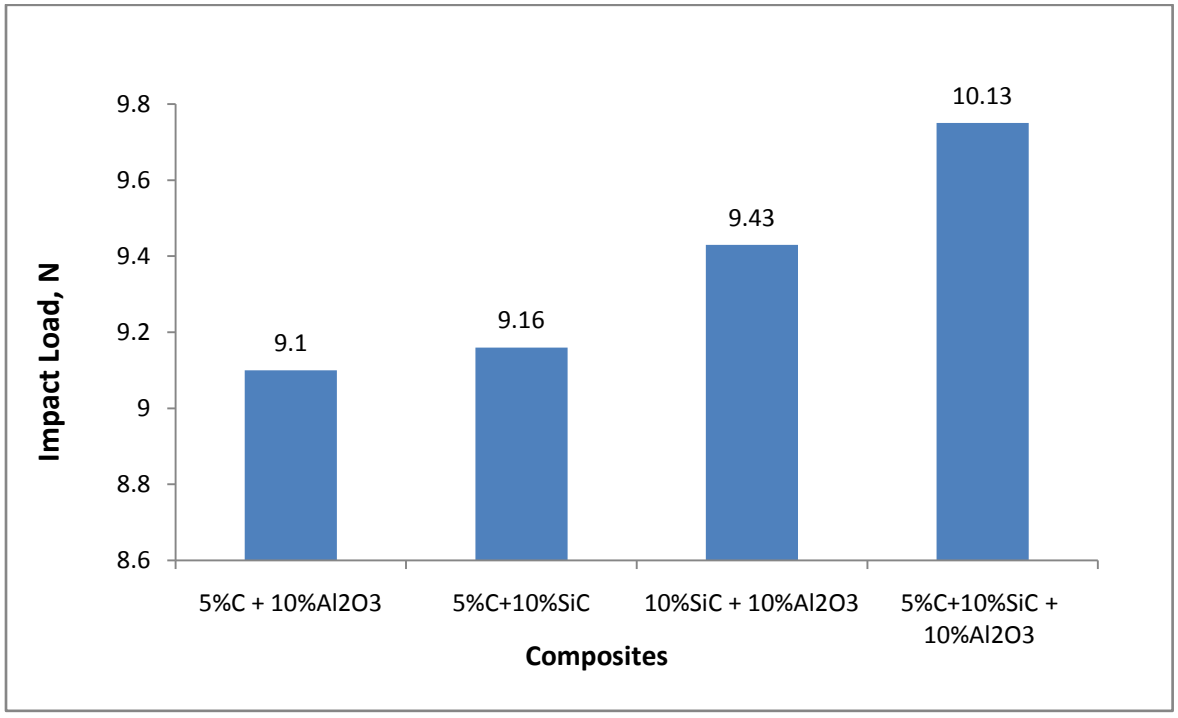

Fig. 2.12 Variation of Impact Strength of Hybrid Al-MMCs with wt% of Reinforcement

Figure 2.12 shows the variation of impact strength with reinforcements and their weight fraction.

- The impact load increases from 6.06 N (for Al) to 9.1 N when Al matrix is reinforced with 10 wt% Al_2O_3 and 5 wt% C i.e. for Al/(10 wt% Al_2O_3p + 5 wt% Cp)-MMC. As pure Al matrix has impact load is only 6.06 N (Figure 2.11). It implies that impact load has increased by 50.16% with addition of 10wt% Al_2O_3 and 5 wt% C with Al matrix.
- The impact load increases from 6.06 N (for Al) to 9.16 N when Al matrix is reinforced with 10 wt% SiC and 5 wt% C i.e. for Al/(10 wt% SiCp + 5 wt% Cp)-MMC. It implies that impact load has increased by 51.15% with addition of 10 wt% SiC and 5 wt% C with Al matrix.
- The impact load increases from 6.06 N (for Al, Figure 2.11) to 9.43 N when Al matrix is reinforced with 10 wt% Al_2O_3 and 10 wt% SiC i.e. for Al/(10 wt% Al_2O_3p + 10 wt% SiCp)-MMC. It implies that impact load has increased by 55.61% with addition of 10 wt% Al_2O_3 and 10 wt% SiC with Al matrix.
- The impact load increases from 6.06 N (for Al, Figure 2.11) to 9.75 N when Al matrix is reinforced with 10 wt% Al_2O_3, 10 wt% SiC and 5 wt% C i.e. for Al/(5 wt% Cp + 10 wt% Al_2O_3p + 10 wt% SiCp)-MMC. It implies that impact load has increased by 60.89% with addition of 10 wt% Al_2O_3, 10 wt% SiC and 5 wt% C with Al matrix.
- The addition of 10 wt% alumina and 5 wt% carbon particles as reinforcement with Al-matrix i.e. for Al/(10 wt% Al_2O_3p + 5 wt% Cp)-MMC the impact load increased by 7.56% over Al/ 10 wt% Al_2O_3-MMC. As impact load is 8.46 N for Al/ 10 wt% Al_2O_3p-MMC (Figure 2.11) and impact load is 9.1 N for Al/(10 wt% Al_2O_3p + 5 wt% Cp) MMC (Figure 2.12).
- The impact load for Al/10 wt% Al_2O_3-MMC is 8.46 N and for Al/(10 wt% Al_2O_3p + 10 wt% SiCp) MMC is 9.43 N. It implies that impact load was increased by 11.46% when 10 wt% Al_2O_3 and 10 wt% SiC is added with Al matrix over addition of 10 wt% Al_2O_3 only.
- The impact load for Al/ 10 wt% SiC-MMC is 8.76 N (Figure 2.11) where as impact load is 9.43 N for Al/(10 wt% Al_2O_3p + 10 wt% SiCp)-MMC. It implies that impact load was increased by 7.64% with addition of 10 wt% Al_2O_3 and 10 wt% SiC with Al matrix over addition of 10 wt% SiC only.
- The addition of 5 wt% carbon and 10 wt% silicon carbide particles as reinforcement with Al metal matrix i.e. Al/(10 wt% SiCp + 5 wt% Cp)-MMC the impact load increased by

4.56% over Al/10 wt% SiC-MMC. As impact load is 8.76 N for Al/10 wt% SiCp-MMC (Figure 2.11) and impact load is 9.16 N for Al/(10 wt% SiC + 5 wt% C)-MMC (Figure 2.12).

- The addition of 10 wt% Al_2O_3, 10 wt% SiC, and 5 wt% C (carbon particles) as reinforcements with Al metal matrix i.e. for hybrid Al/(10 wt% Al_2O_3p + 10 wt% SiCp + 5 wt% Cp)-MMC the impact load increased by 7.42% over Al/(10 wt% Al_2O_3p + 10 wt% SiCp)-MMC. As impact loads were 9.43 N and 10.13 N for hybrid Al/(10 wt% Al_2O_3p + 10 wt% SiCp)-MMC and Al/(10 wt% Al_2O_3p + 10 wt% SiCp + 5 wt% Cp)-MMC respectively (Figure 2.12).
- The addition of 10 wt% Al_2O_3, 10 wt% SiC, and 5 wt% C as reinforcements with Al metal matrix i.e. for hybrid Al/(10 wt% Al_2O_3p + 10 wt% SiCp + 5 wt% Cp)-MMC the impact load increased by 11.31% over Al/(10 wt% Al_2O_3p + 5 wt% Cp)-MMC. As impact loads were 9.1 N and 10.13 N for Al/(10 wt% Al_2O_3p + 5 wt% Cp)-hybrid MMC and Al/(10 wt% Al_2O_3p + 10 wt% SiCp + 5 wt% Cp)-MMC respectively (Figure 2.12).
- The addition of 10 wt% Al_2O_3, 10 wt% SiC, and 5 wt% C as reinforcements with Al metal matrix i.e. for hybrid Al/(10 wt% Al_2O_3p + 10 wt% SiCp + 5 wt% Cp)-hybrid MMC the impact load increased by 10.58% over Al/(10 wt% SiCp + 5 wt% Cp)-MMC. As impact loads were 9.6 N and 10.13 N for Al/(10 wt% SiCp + 5 wt% Cp)-MMC and Al/(10 wt% Al_2O_3p + 10 wt% SiCp + 5 wt% Cp)-hybrid MMC respectively (Figure 2.12).

2.4 HARDNESS TEST RESULTS

A Rockwell hardness-testing machine (Model MRB 250) was used for measuring hardness of Al-MMCs specimens. Before hardness testing, the test specimens were cleaned and finished by successive utilized 100, 220, 400, 600 and 1000 grit size emery papers. Load used on Rockwell's hardness tester was 200g at dwell time 20sec for each specimen. Table 2.8 represents the test results acquired during hardness test of different Al-MMCs specimens.

Table 2.8 Hardness Test Results

Sample No	Pure Al and Composites	Trail				Mean Hardness (HRB)
		1	2	3	4	
1	Al Alloy	52.3	52.6	53.5	53.4	52.95
2	Al/15 wt% Cp-MMC	62.3	62.8	63.1	63.4	62.9
3	Al/10 wt% Al_2O_3p-MMC	98.3	99.2	99.8	98.1	98.8
4	Al/10 wt% SiCp-MMC	95.3	95.2	94.8	95.1	95.1
5	Hybrid Al/(5 wt% Cp + 10% wt Al_2O_3p)-MMC	100.2	99.8	99.9	98.9	99.7
6	Hybrid Al/(10 wt% SiCp + 5 wt% Cp)- MMC	97.5	97.4	97.4	97.8	97.52
7	Hybrid Al/(10 wt% SiCp + 10 wt% Al_2O_3p)- MMC	120	122	125	124	122.75
8	Hybrid Al/(10 wt% SiCp + 10% wt Al_2O_3p+ 5 wt% Cp)-MMC	129	130	131	130	130

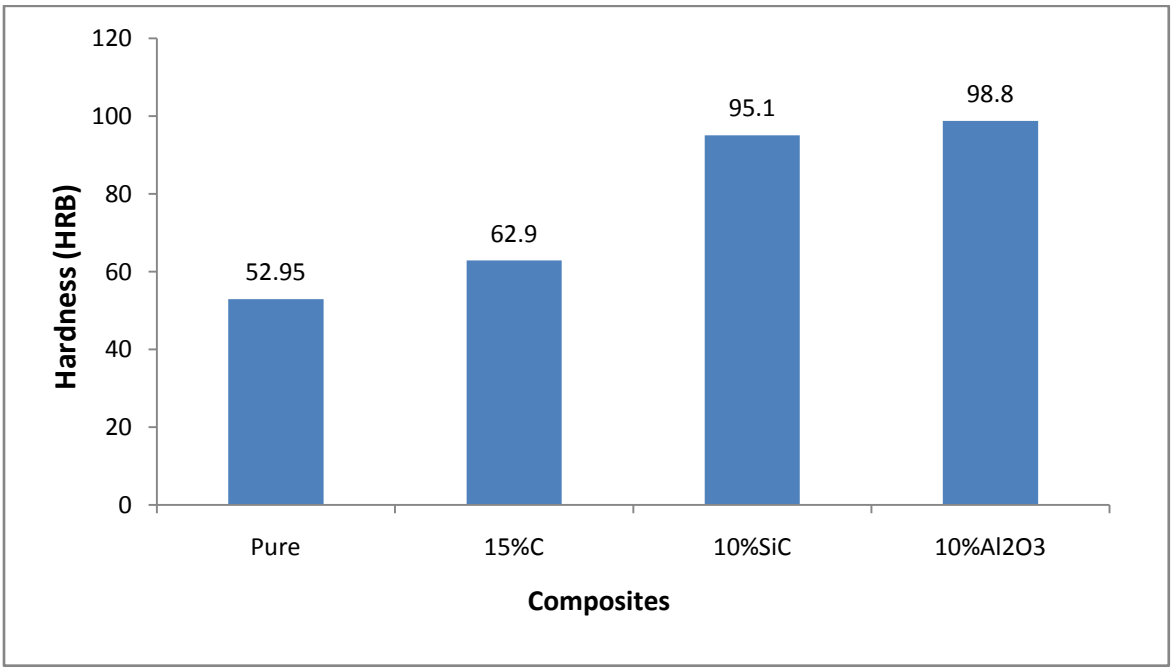

Fig. 2.13 Hardness of Pure Al and Al-MMCs

Figure 2.13 shows the variation in hardness of Al materials with addition of SiC, Al_2O_3 and C constituent. Hardness increases with addition of reinforcement particles like SiC, Al_2O_3 and C with Al-matrix. This is due to proper dispersion and hardness of SiC, Al_2O_3 and C reinforced particles into the matrix. This may be due to strong interfacial bonding in between the Al-matrix and reinforced particles SiC, Al_2O_3 and C. The following points regarding the variation of hardness with reinforcement in Al-matrix are highlighted as below:

- The hardness increases from 52.95 HRB to 62.9 HRB when Al matrix is reinforced with 15 wt% carbon particle. As pure Al matrix has hardness is only 52.95 HRB. It implies that hardness was increased by 18.79% with addition of 15 wt% C in Al-matrix.
- The hardness increases from 52.95 HRB to 98.8 HRB when Al matrix is reinforced with 10 wt% Al_2O_3. It implies the increase of hardness by 86.59% in addition of 10 wt% Al_2O_3 with Al-matrix.
- The hardness increases from 52.95 HRB to 95.1 HRB when Al matrix is reinforced with 10 wt% SiC. It implies the increase of hardness by 79.60% in addition of 10 wt% SiC with Al-matrix.

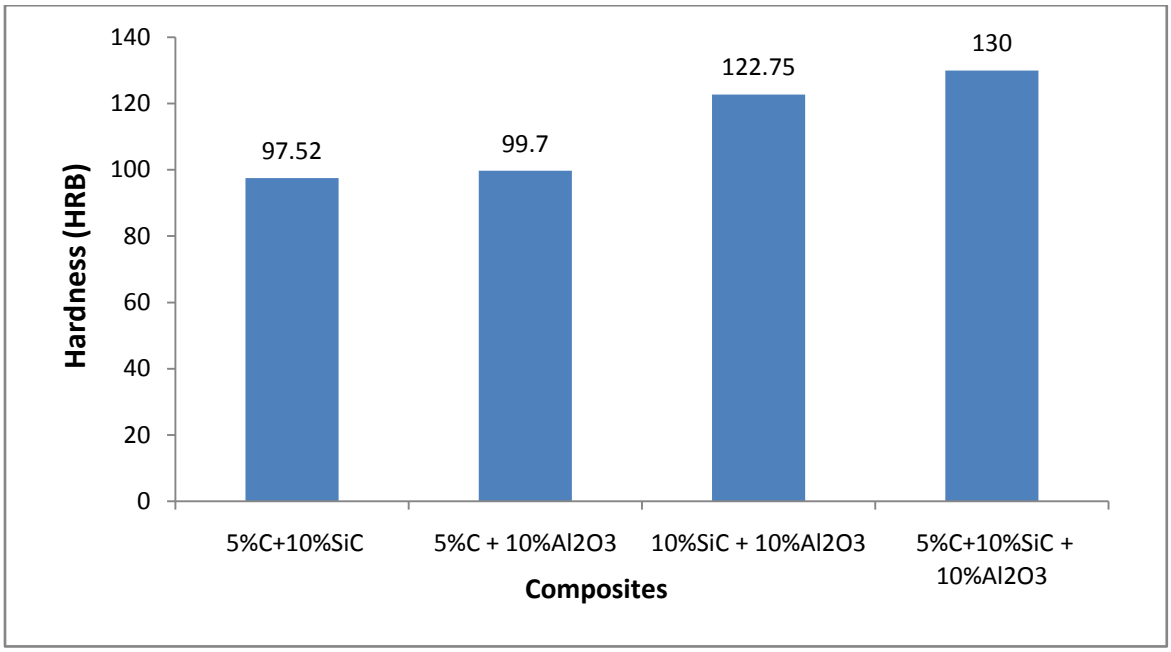

Fig. 2.14 Variation of Hardness of Hybrid Al-MMCs with wt% of Reinforcements

Figure 2.14 shows the variation in hardness of Al-MMCs with addition of SiC, Al_2O_3, and C reinforcement. The following points regarding the variation of hardness with reinforcement in Al-matrix are highlighted as below:

- The hardness increases from 52.95 HRB (for Al, Figure 2.13) to 97.52 HRB when Al matrix is reinforced with 10wt% SiC and 5 wt% C particles i.e. for Al/(10 wt% SiCp + 5 wt% Cp)-MMC. It implies that the hardness was increased by 84.17% in addition of 10wt% SiC and 5 wt% C with Al matrix.
- The hardness increases from 52.95 HRB (for Al) to 99.7 HRB when Al matrix is reinforced with 10wt% Al_2O_3 and 5 wt% C particles i.e. for Al/(10 wt% Al_2O_3p + 5 wt% Cp)-MMC. It implies that the hardness was increased by 88.29% with addition of 10wt% Al_2O_3 and 5 wt% C in Al matrix.
- The hardness increases from 52.95 HRB (for Al) to 122.75 HRB when Al matrix is reinforced with 10wt% SiC and 10 wt% Al_2O_3 particles i.e. for Al/(10 wt% SiCp + 10 wt% Al_2O_3p)-MMC. It implies that the hardness was increased by 131.82% with addition of 10wt% SiC and 10 wt% Al_2O_3 in Al matrix.
- The hardness increases from 52.95 HRB (for Al) to 130 HRB when Al matrix is reinforced with 10wt% SiC, 10wt% Al_2O_3 and 5 wt% C particles i.e. for Al/(10 wt% SiCp + 10wt% Al_2O_3p + 5 wt% Cp)-MMC. It implies that the hardness was increased by 145.51% with addition of 10wt% SiC, 10wt% Al_2O_3 and 5 wt% C in Al matrix.
- The addition of 10 wt% silicon carbide and 5 wt% carbon particles as reinforcement with Al-matrix i.e. for Al/(10 wt% SiCp + 5 wt% Cp) MMC the hardness was increased by 55.03 % over Al/ 15 wt% C-MMC. As hardness was 62.9 HRB for Al/15 wt% C-MMC (Figure 2.13) and hardness was 97.52 HRB for hybrid Al/(10 wt% SiCp + 5 wt% Cp)-MMC (Figure 2.14).
- The addition of 10 wt% alumina and 5 wt% carbon particles as reinforcement with Al-matrix i.e. for Al/(10 wt% Al_2O_3p + 5 wt% Cp) MMC the hardness was increased by 0.91% over Al/ 10 wt% Al_2O_3-MMC. As hardness was 98.8 HRB for Al/ 10 wt% Al_2O_3-MMC (Figure 2.13) and hardness was 99.7 HRB for Al/(10 wt% Al_2O_3p + 5 wt% Cp) MMC (Figure 2.14).
- The addition of 10 wt% alumina and 10 wt% silicon carbide as reinforcement with Al-matrix i.e. for Al/(10 wt% Al_2O_3p + 10 wt% SiCp) MMC the hardness was increased by

24.24% over Al/ 10 wt% Al_2O_3-MMC. As hardness was 98.8 HRB for Al/ 10 wt% Al_2O_3-MMC (Figure 2.13) and hardness was 122.75 HRB for Al/(10 wt% Al_2O_3p + 10 wt% SiCp) MMC (Figure 2.14).

- The addition of 10 wt% alumina and 10 wt% silicon carbide as reinforcement with Al-matrix i.e. for Al/(10 wt% Al_2O_3p + 10 wt% SiCp) MMC the hardness was increased by 29.07% over Al/ 10 wt% SiC-MMC. As hardness was 95.1 HRB for Al/ 10 wt% SiCp-MMC (Figure 2.13) and hardness was 122.75 HRB for Al/(10 wt% Al_2O_3p + 10 wt% SiCp) MMC (Figure 2.14).
- The addition of 10 wt% silicon carbide and 5 wt% carbon particles as reinforcement with Al-matrix i.e. for Al/(10 wt% SiCp + 5 wt% Cp)-MMC the hardness was increased by 2.55% over Al/ 10 wt% SiC-MMC. As hardness was 95.1 HRB for Al/ 10 wt% SiCp-MMC (Figure 2.13) and hardness was 97.53 HRB for Al/(10 wt% SiCp + 5 wt% Cp) MMC (Figure 2.14).
- The addition of 10 wt% alumina, 10 wt% silicon carbide and 5 wt% carbon particles as reinforcement with Al-matrix i.e. for Al/(10 wt% Al_2O_3p + 10 wt% SiCp + 5 wt% Cp) MMC the hardness was increased by 5.90% over Al/(10 wt% Al_2O_3p + 10 wt% SiCp)-MMC. As hardness was 122.75 HRB for Al/(10 wt% Al_2O_3p + 10 wt% SiCp)-MMC and 130 HRB for Al/(10 wt% Al_2O_3p + 10 wt% SiCp + 5 wt% Cp) MMC (Figure 2.14).
- The addition of 10 wt% alumina, 10 wt% silicon carbide and 5 wt% carbon particles as reinforcement with Al-matrix i.e. for Al/(10 wt% Al_2O_3p + 10 wt% SiCp + 5 wt% Cp) MMC the hardness was increased by 30.39% over Al/(10 wt% Al_2O_3p + 5 wt% Cp)-MMC. As hardness was 99.7 HRB for Al/(10 wt% Al_2O_3p + 10 wt% Cp)-MMC and 130 HRB for Al/(10 wt% Al_2O_3p + 10 wt% SiCp + 5 wt% Cp)- MMC (Figure 2.14).
- The addition of 10 wt% alumina, 10 wt% silicon carbide and 5 wt% carbon particles as reinforcement with Al-matrix i.e. for Al/(10 wt% Al_2O_3p + 10 wt% SiCp + 5 wt% Cp) MMC the hardness was increased by 33.29% over Al/(10 wt% SiCp + 5 wt% Cp)-MMC. As hardness was 97.52 HRB for Al/(10 wt% SiCp + 5 wt% Cp)-MMC and 130 HRB for Al/(10 wt% Al_2O_3p + 10 wt% SiCp + 5 wt% Cp) MMC (Figure 2.14).

2.5 TENSILE STRENGTH TEST RESULTS

Tensile tests were carried out to identify the most important mechanical property i.e. tensile strength of the fabricated cast Al-MMCs samples. The cast Al-MMCs were machined to prepare the tensile test specimens with 12.5 mm diameter and 85 mm gauge length each (Figure 2.15). The ultimate tensile strength (UTS) is the maximum stress that a material can withstand while being stretched or pulled before necking, which is when the specimen's cross-section starts to significantly contract. Table 2.9 represents the test results acquired during tensile test on Al-MMCs specimens.

Fig. 2.15 Tensile Strength Test Specimen

Table 2.9 Tensile Strength Results

Sample Name	Yield Strength N/mm^2	UTS N/mm^2	Elongation (%)
Al Alloy	60	175	9
Al/15 wt% Cp-MMC	80	200	8.5
Al/10 wt% Al_2O_3p-MMC	160	270	2.9
Al/10 wt% SiCp-MMC	190	310	2.2
Hybrid Al/(5 wt% Cp + 10 wt% Al_2O_3p)-MMC	175	290	2.7
Hybrid Al/(10 wt% SiCp + 5 wt% Cp)-MMC	210	330	2.0
Hybrid Al/(10 wt %SiCp + 10 wt% Al_2O_3p)-MMC	240	390	1.4
Hybrid Al/(10 wt% SiCp + 10 wt% Al_2O_3p + 5 wt% Cp)-MMC	255	410	1.1

2.5.1 Stress - Strain Curves

The stress–strain curve is a graphical representation of the relationship between stress, derived from measuring the load applied on the sample, and strain, derived from measuring the deformation of the sample, i.e. elongation, compression, or distortion. The slope of stress-strain curve at any point is called the tangent modulus; the slope of the elastic (linear) portion of the curve is a property used to characterize materials and is known as the Young's modulus. The area under the elastic portion of the curve is known as the modulus of resilience.

I. Stress vs. Strain Curves for Aluminium Alloy

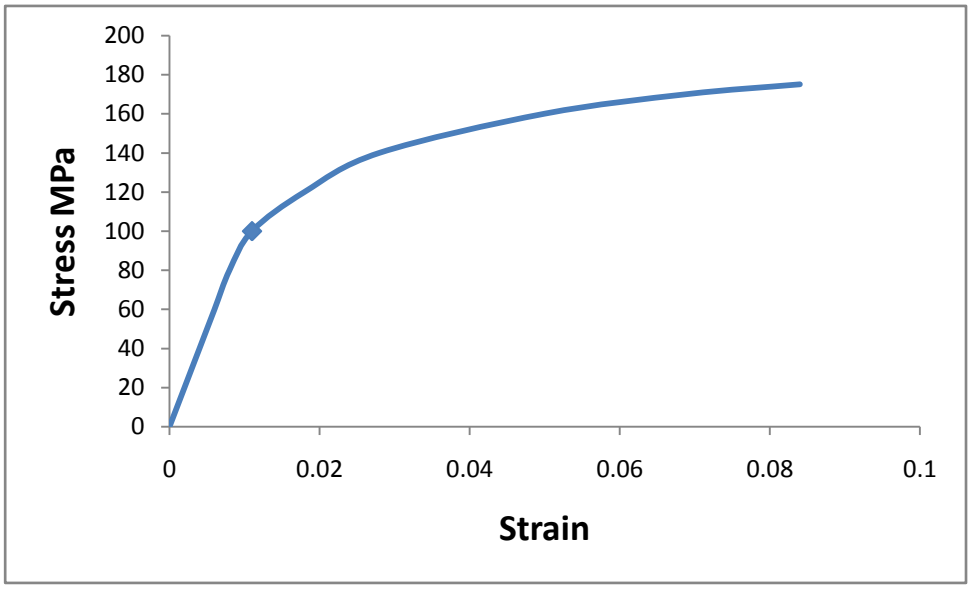

Fig. 2.16 Stress vs. Strain Curves for Aluminium Alloy

II. Stress vs. Strain Curves for Al/15 wt% Cp-MMC

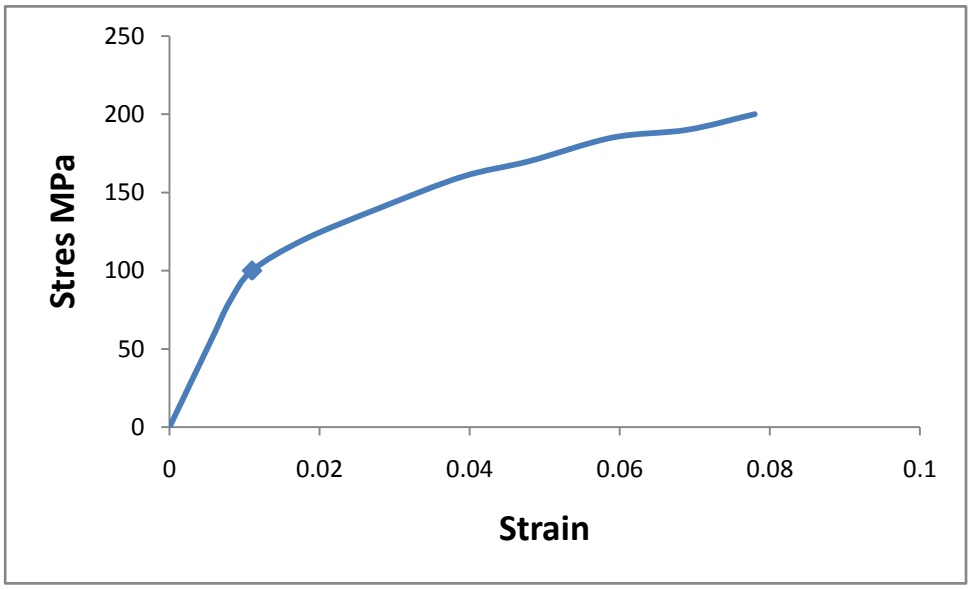

Fig. 2.17: Stress vs. Strain Curves for Al/15 wt% Cp-MMC

III. Stress vs. Strain Curves for Al/10 wt% Al_2O_3p-MMC

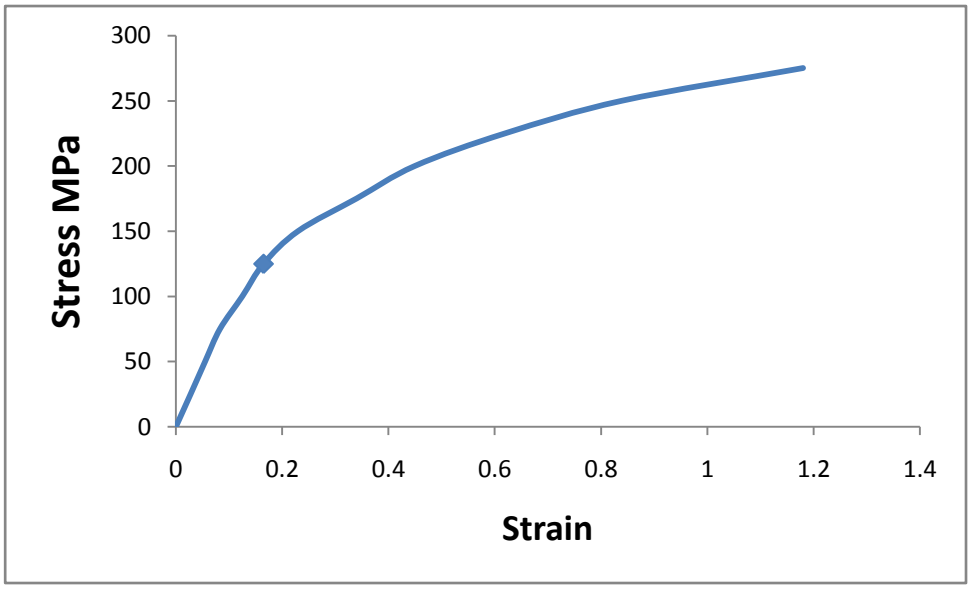

Fig. 2.18: Stress vs. Strain Curves for Al/10 wt% Al_2O_3p-MMC

IV. Stress vs. Strain Curves for Al/10 wt% SiCp-MMC

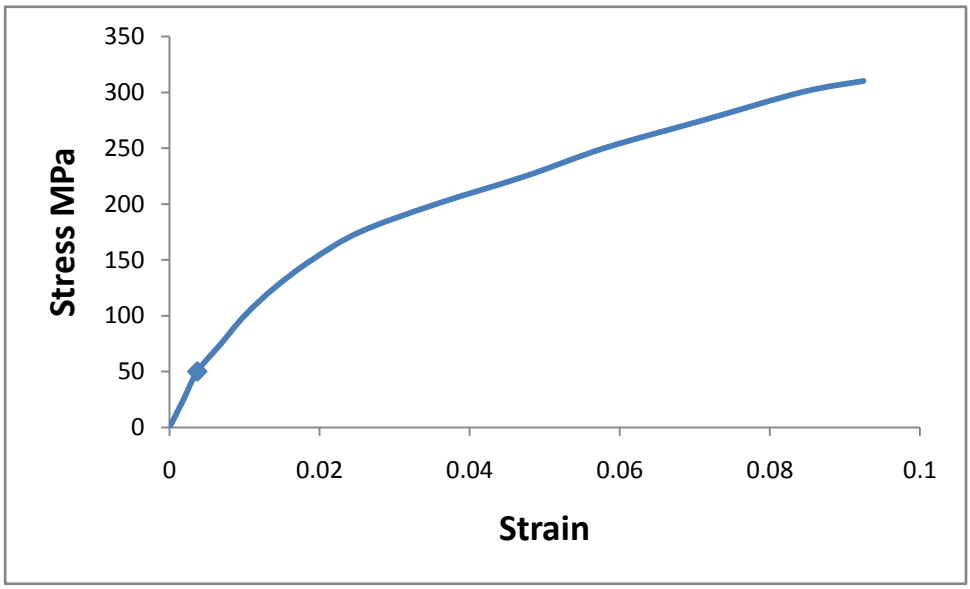

Fig. 2.19: Stress vs. Strain Curves for Al/10 wt% SiCp-MMC

V. Stress vs. Strain Curves for Hybrid Al/(5 wt% Cp + 10 wt% Al_2O_3p)-MMC

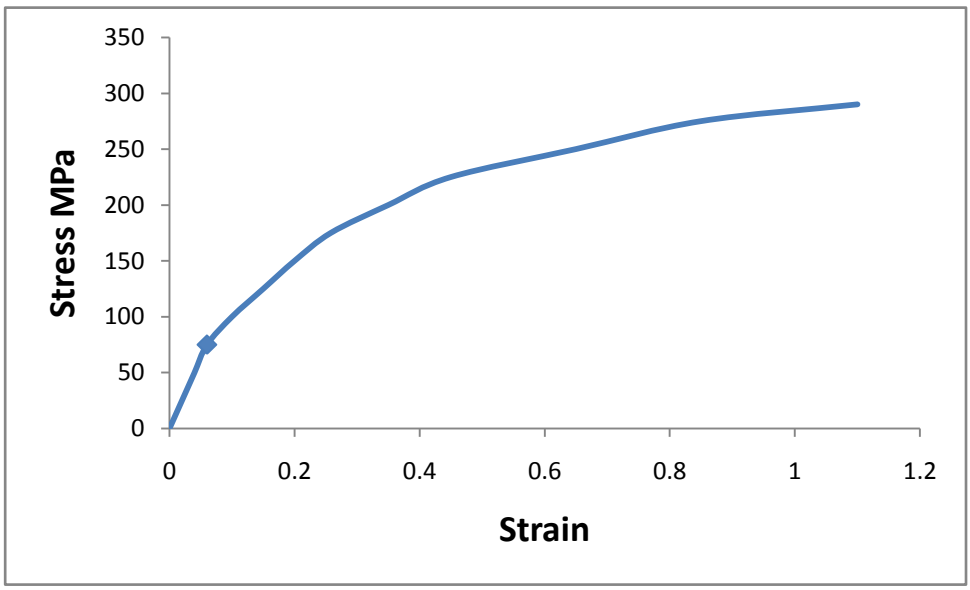

Fig. 2.20: Stress vs. Strain Curves for Hybrid Al/(5 wt% Cp + 10 wt% Al_2O_3p)-MMC

VI. Stress vs. Strain Curves for Hybrid Al/(10 wt% SiCp + 5 wt% Cp)-MMC

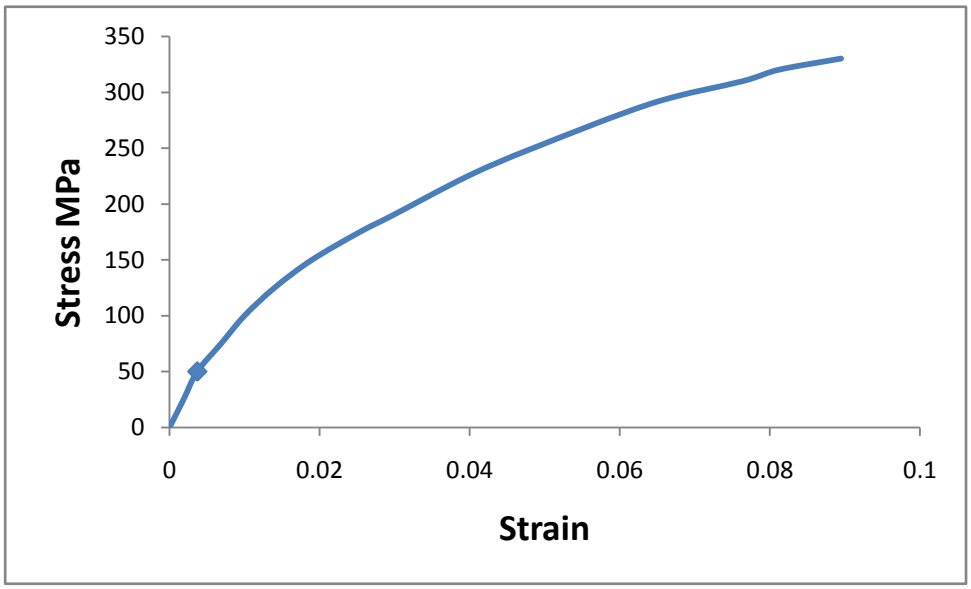

Fig. 2.21 Stress vs. Strain Curves for Hybrid Al/(10 wt% SiCp + 5 wt% Cp)-MMC

VII. Stress vs. Strain Curves for Hybrid Al/(10 wt% SiCp + 10 wt% Al_2O_3p) -MMC

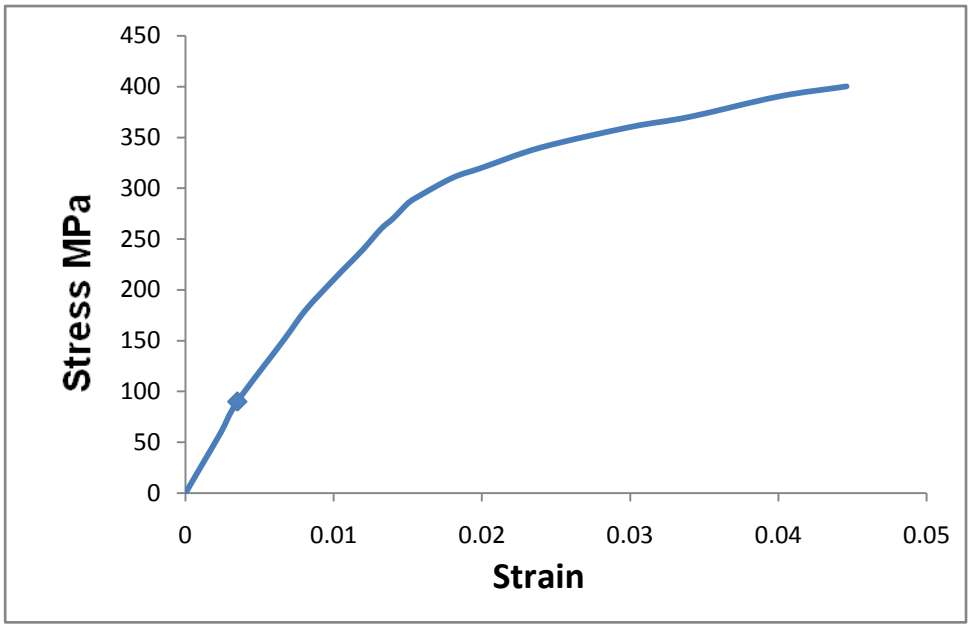

Fig. 2.22: Stress vs. Strain Curves for Hybrid Al/(10 wt% SiCp + 10 wt% Al_2O_3p)-MMC

VIII. Stress vs. Strain Curves for hybrid Al/(10 wt% SiCp + 10 wt% Al_2O_3p + 5 wt% Cp)-MMC

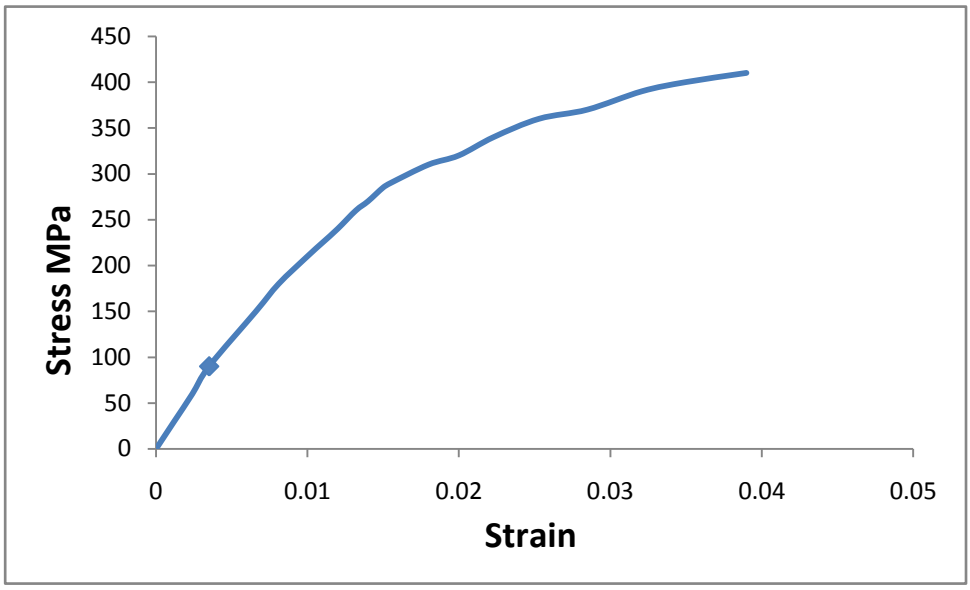

Fig. 2.23: Stress vs. Strain Curves for Hybrid Al/(10 wt% SiCp + 10 wt% Al_2O_3p + 5 wt% Cp)-MMC

It exhibits a very linear stress–strain relationship up to a well defined yield point. The linear portion of the curve is the elastic region and the slope is the modulus of elasticity or Young's Modulus. As deformation continues, the stress increases on account of strain hardening until it reaches the ultimate strength. Until this point, the cross-sectional area decreases uniformly because of Poisson contractions. The actual rupture point is in the same vertical line as the visual rupture point. The work hardening rate increases with addition of reinforcement.

2.6 YIELD STRENGTH COMPARISON

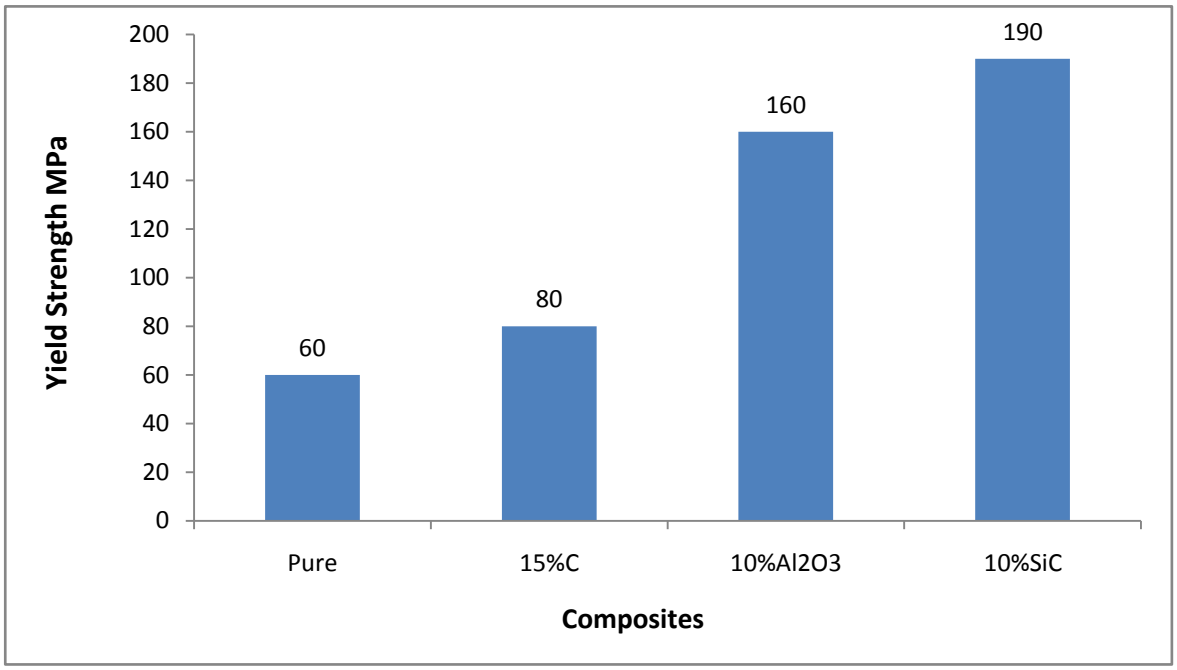

Fig. 2.24 Yield Strength of Pure Al and Al-MMCs

Figure 2.24 shows the variation of Yield strength with addition of SiC, Al_2O_3 and C constituent. The yield strength increases with addition of reinforcement particles like SiC, Al_2O_3 and C with Al-matrix. This is due to proper dispersion and hardness of SiC, Al_2O_3 and C reinforced particles. This may be due to strong interfacial bonding in between the Al-matrix and reinforced particles SiC, Al_2O_3 and C. However, the following points regarding the variation of yield strength with addition of reinforced particles in Al-matrix are highlighted as below:

- The yield strength increases from 60 N/mm^2 to 80 N/mm^2 when Al matrix is reinforced with 15 wt% carbon particles. As yield strength of Al-matrix is only 60 N/mm^2. It implies that the yield strength was increased by 33.33% with addition of Al/ 15 wt% C in Al-matrix.
- The yield strength increases from 60 N/mm^2 to 160 N/mm^2 when Al matrix is reinforced with 10 wt% Al_2O_3 particles. It implies that the yield strength was increased by 166.66% with addition of 10 wt% Al_2O_3 in Al-matrix.

- The yield strength increases from 60 N/mm^2 to 190 N/mm^2 when Al matrix is reinforced with 10 wt% SiC particles. It implies that the yield strength was increased by 216.66% with addition of 10 wt% SiC.

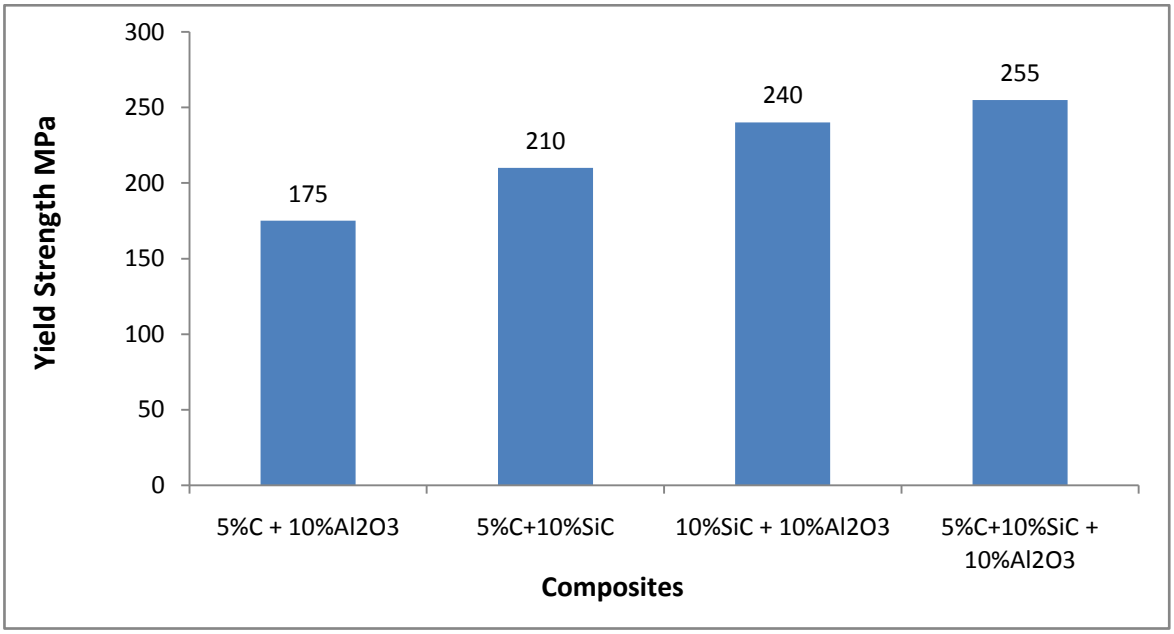

Fig. 2.25 Yield Strength of Hybrid Al-MMCs

Figure 2.25 shows the variation of yield strength with addition of SiC, Al_2O_3 and C particles in Al-matrix. Yield Strength increases with addition of reinforcement particles. It is may be due to the hardness of SiC, C and Al_2O_3 particles. This is due to increase in resistance to deformation by adding SiC, C and Al_2O_3 as reinforcement with Al-matrix and strong interfacial bonding in between the Al-matrix and SiC, Al_2O_3 and C particles interfaces. This may also results in due to elimination of micro pores caused by applied pressure.

The following points regarding to the variation of yield strength with addition of reinforcement particles in Al-matrix are highlighted as below:

- The addition of 10 wt% alumina and 5 wt% carbon particles as reinforcement with Al-matrix i.e. for Al/(10 wt% Al_2O_3p + 5 wt% Cp) MMC the yield strength was increased by 118.75% over Al/ 15 wt% C-MMC. As yield strength of Al/10 wt% Cp-MMC is 80 N/mm^2 (Figure 2.24) and yield strength of Al/(10 wt% Al_2O_3p + 5 wt% Cp)-MMC is 175 N/mm^2 (Figure 2.25).

- The addition of 10 wt% silicon carbide and 5 wt% carbon particles as reinforcement with Al-matrix i.e. for Al/(10 wt% Al_2O_3p + 5 wt% Cp) MMC the yield strength was increased by 162.5% over Al/ 15 wt% Cp-MMC. As yield strength was 80 N/mm^2 for Al/10 wt% Cp-MMC (Figure 2.24) and 210 N/mm^2 for Al/(10 wt% Al_2O_3p+ 5 wt% Cp) MMC (Figure 2.25).
- The addition of 10 wt% alumina and 5 wt% carbon particles as reinforcement with Al-matrix i.e. for Al/(10 wt% Al_2O_3p + 5 wt% Cp) MMC the yield strength was increased by 9.73% over Al/ 10 wt% Al_2O_3p-MMC. As yield strength was 160 N/mm^2 for Al/10 wt% Al_2O_3p-MMC (Figure 2.24) and 175 N/mm^2 for Al/(10 wt% Al_2O_3p + 5 wt% Cp) MMC (Figure 2.25).
- The addition of 10 wt% alumina and 10 wt% silicon carbide particles as reinforcement with Al-matrix i.e. for Al/(10 wt% Al_2O_3p + 10 wt% SiCp) MMC the yield strength was increased by 50% over Al/ 10 wt% Al_2O_3p-MMC. As yield strength was 160 N/mm^2 for Al/10 wt% Al_2O_3p-MMC (Figure 2.24) and 240 N/mm^2 for Al/(10 wt% Al_2O_3p + 5 wt% Cp) MMC (Figure 2.25).
- The addition of 10 wt% alumina and 10 wt% silicon carbide particles as reinforcement with Al-matrix i.e. for Al/(10 wt% Al_2O_3p + 10 wt% SiCp) MMC the yield strength was increased by 26.31% over Al/ 10 wt% SiCp-MMC. As yield strength was 190 N/mm^2 for Al/10 wt% Al_2O_3p-MMC (Figure 2.24) and 240 N/mm^2 for Al/(10 wt% Al_2O_3p + 5 wt% Cp) MMC (Figure 2.25).
- The addition of 5 wt% alumina and 10 wt% silicon carbide particles as reinforcement with Al-matrix i.e. for Al/(10 wt% SiCp + 5 wt% Cp) MMC the yield strength was increased by 10.52% over Al/10 wt% SiCp-MMC. As yield strength was 190 N/mm^2 for Al/10 wt% SiCp-MMC (Figure 2.24) and 210 N/mm^2 for Al/(10 wt% SiCp + 5 wt% Cp) MMC (Figure 2.25).
- The addition of 10 wt% alumina, 10 wt% silicon carbide and 5 wt% carbon particles as reinforcement with Al-matrix i.e. for Al/(10 wt% Al_2O_3p + 10 wt% SiCp + 5 wt% Cp) MMC the yield strength was increased by 6.25% over Al/(10 wt% Al_2O_3p + 10 wt% SiCp)-MMC. As yield strength was 240 N/mm^2 for Al/(10 wt% Al_2O_3p + 10 wt% SiCp)-MMC and 255 N/mm^2 for Al/(10 wt% Al_2O_3p + 10 wt% SiCp + 5 wt% Cp)-MMC (Figure 2.25).

- The addition of 10 wt% alumina, 10 wt% silicon carbide and 5 wt% carbon particles as reinforcement with Al-matrix i.e. for Al/(10 wt% Al_2O_3p + 10 wt% SiCp + 5 wt% Cp) MMC the yield strength was increased by 45.71% over Al/(10 wt% Al_2O_3p + 5 wt% Cp)-MMC. As yield strength was 175 N/mm^2 for Al/(10 wt% Al_2O_3p + 5 wt% Cp)-MMC and 255 N/mm^2 for Al/(10 wt% Al_2O_3p + 10 wt% SiCp + 5 wt% Cp) MMC (Figure 2.25).
- The addition of 10 wt% alumina, 10 wt% silicon carbide and 5 wt% carbon particles as reinforcement with Al-matrix i.e. for Al/(10 wt% Al_2O_3p + 10 wt% SiCp + 5 wt% Cp) MMC the yield strength was increased by 21.42% over Al/(10 wt% SiCp + 5 wt% Cp)-MMC. As yield strength was 210 N/mm^2 for hybrid Al/(10 wt% SiCp + 5 wt% Cp)-MMC and 255 N/mm^2 for hybrid Al/(10 wt% Al_2O_3p + 10 wt% SiCp + 5 wt% Cp)-MMC (Figure 2.25).

2.7 ULTIMATE TENSILE STRENGTH RESULT

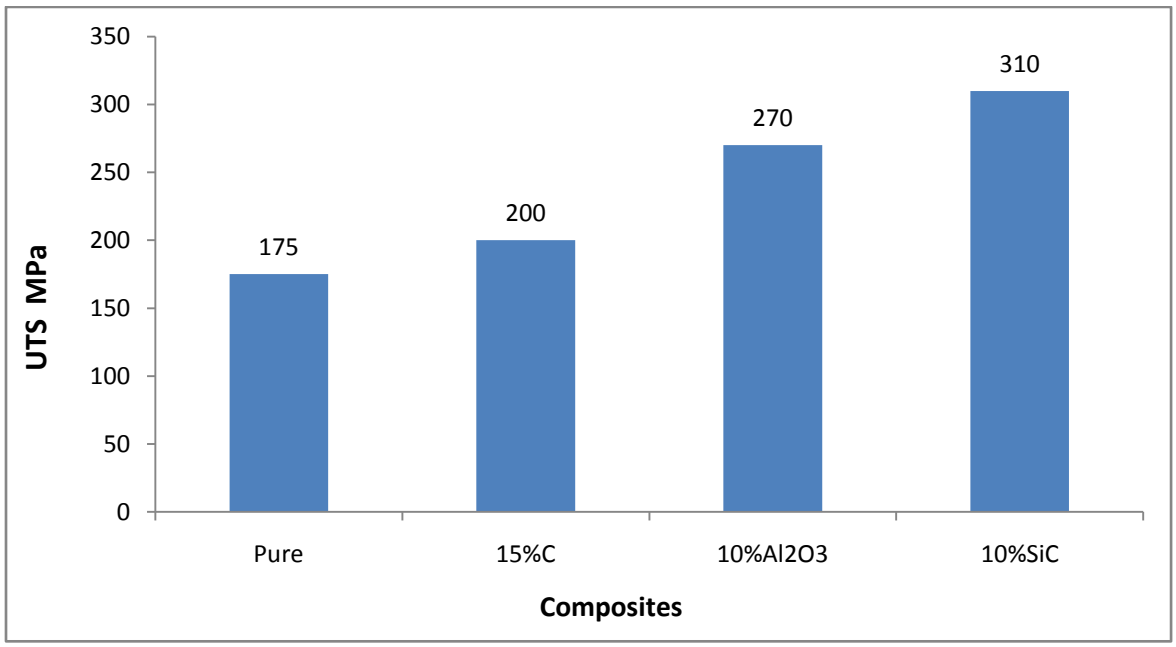

Fig. 2.26 Ultimate Tensile Strength of Pure Al and Al-MMCs

Figure 2.26 shows the variation of ultimate tensile strength (UTS) with addition of SiC, Al_2O_3 and C reinforcement in Al-matrix. The UTS increases with addition of reinforcement particles like SiC, Al_2O_3 and C particles. This is due to proper dispersion and hardness of SiC, Al_2O_3 and C particles present in the Al-matrix. This is also happen due to strong interfacial bonding in between the matrix Al, and reinforced particles SiC, Al_2O_3 and C interfaces. The following points regarding this issue are highlighted as below:

- The ultimate tensile strength increases from 175 N/mm^2 to 200 N/mm^2 when Al matrix was reinforced with 15 wt% carbon particle. As the yield strength of pure Al matrix was only 175 N/mm^2. It implies that the ultimate tensile strength was increased by 14.28% with addition of 15 wt% C.
- The ultimate tensile strength increases from 175 N/mm^2 to 270 N/mm^2 when Al matrix was reinforced with 10 wt% Al_2O_3. It implies that the ultimate tensile strength was increased by 54.28% with addition of 10 wt% Al_2O_3.
- The ultimate tensile strength increases from 175 N/mm^2 to 310 N/mm^2 when Al matrix was reinforced with 10 wt% SiC. It implies that the ultimate tensile strength was increased by 77.14% with addition of 10 wt% SiC.

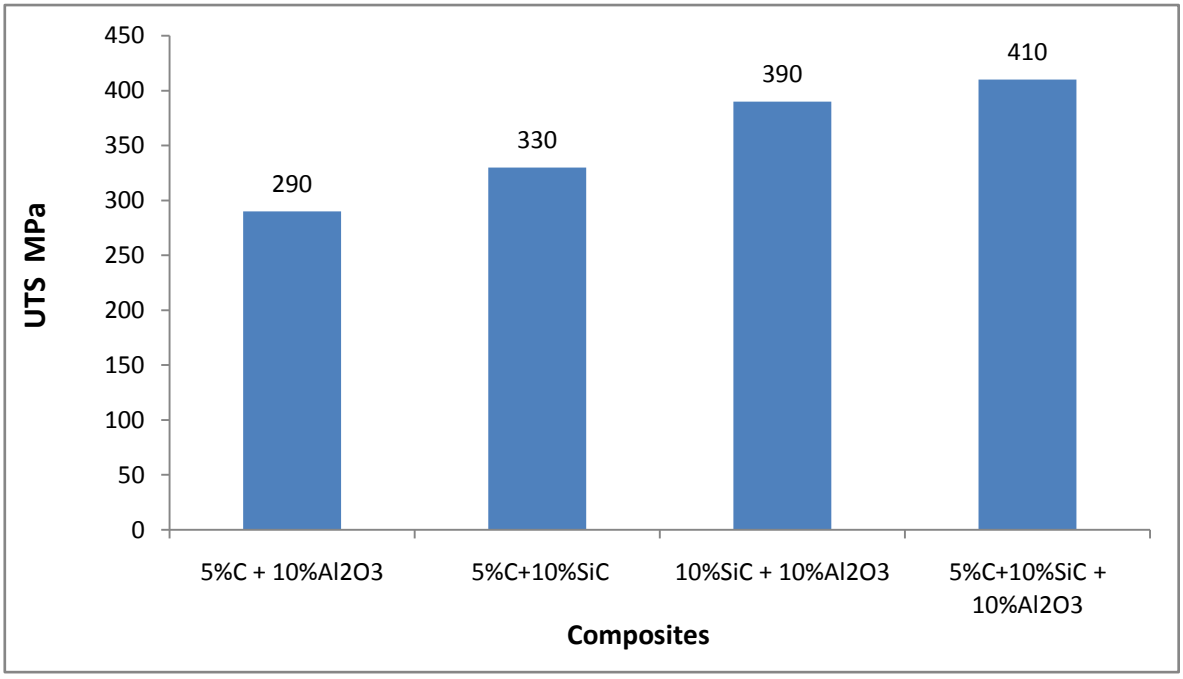

Fig. 2.27 Ultimate Tensile Strength of Hybrid Al-MMCs

Figure 2.27 shows the variation of ultimate tensile strength with addition of SiC, Al_2O_3 and C reinforcement particles. Ultimate tensile strength increases with addition of reinforcement particles. It is may be due to dispersion and hardness of SiC, C and Al_2O_3 which create hindrance to dislocation motion. This is also increase in resistance to deformation by adding SiC, C and Al_2O_3 as reinforcement in Al-matrix and strong interfacial bonding in between the Al-matrix and SiC, Al_2O_3 and C interfaces. It is may be due to elimination of micro pores thereby increases tensile strength. The following points regarding this issue are highlighted as below:

- The addition of 10 wt% alumina and 5 wt% carbon particles as reinforcement with Al-matrix i.e. for Al/(10 wt% Al_2O_3p + 5 wt% Cp) MMC the tensile strength was increased by 45% over Al/ 15 wt% Cp-MMC. As tensile strength of Al/10 wt% Cp-MMC was 200 N/mm^2 (Figure 2.26) and tensile strength of Al/(10 wt% Al_2O_3p + 5 wt% Cp)-MMC was 290 N/mm^2 (Figure 2.27).
- The addition of 10 wt% silicon carbide and 5 wt% carbon particles as reinforcement with Al-matrix i.e. for Al/(10 wt% Al_2O_3p + 5 wt% Cp) MMC the tensile strength was increased by 65% over Al/ 15 wt% Cp-MMC. As tensile strength was 200 N/mm^2 for Al/10 wt% Cp-MMC (Figure 2.26) and 330 N/mm^2 for Al/(10 wt% Al_2O_3p+ 5 wt% Cp) MMC (Figure 2.27).
- The addition of 10 wt% alumina and 5 wt% carbon particles as reinforcement with Al-matrix i.e. for Al/(10 wt% Al_2O_3p + 5 wt% Cp) MMC the tensile strength was increased by 7.4% over Al/ 10 wt% Al_2O_3p-MMC. As tensile strength was 270 N/mm^2 for Al/10 wt% Al_2O_3p-MMC (Figure 2.26) and 290 N/mm^2 for Al/(10 wt% Al_2O_3p + 5 wt% Cp) MMC (Figure 2.27).
- The addition of 10 wt% alumina and 10 wt% silicon carbide particles as reinforcement with Al-matrix i.e. for Al/(10 wt% Al_2O_3p + 10 wt% SiCp)-MMC the tensile strength was increased by 44.44% over Al/ 10 wt% Al_2O_3p-MMC. As tensile strength was 270 N/mm^2 for Al/10 wt% Al_2O_3p-MMC (Figure 2.26) and 390 N/mm^2 for Al/(10 wt% Al_2O_3p+ 5 wt% Cp) MMC (Figure 2.27).
- The addition of 10 wt% alumina and 10 wt% silicon carbide particles as reinforcement with Al-matrix i.e. for Al/(10 wt% Al_2O_3p + 10 wt% SiCp) MMC the tensile strength was increased by 25.80% over Al/ 10 wt% SiCp-MMC. As tensile strength was 310 N/mm^2 for Al/10 wt% Al_2O_3p-MMC (Figure 2.26) and 390 N/mm^2 for Al/(10 wt% Al_2O_3p+ 5 wt% Cp) MMC (Figure 2.27).
- The addition of 5 wt% alumina and 10 wt% silicon carbide particles as reinforcement with Al-matrix i.e. for Al/(10 wt% SiCp+ 5 wt% Cp) MMC the tensile strength was increased by 6.45% over Al/10 wt% SiCp-MMC. As tensile strength was 310 N/mm^2 for Al/10 wt% SiCp-MMC (Figure 2.26) and 330 N/mm^2 for Al/(10 wt% SiCp + 5 wt% Cp) MMC (Figure 2.27).

- The addition of 10 wt% alumina, 10 wt% silicon carbide and 5 wt% carbon particles as reinforcement with Al-matrix i.e. for Al/(10 wt% Al_2O_3p + 10 wt% SiCp + 5 wt% Cp) MMC, the tensile strength was increased by 5.12% over Al/(10 wt% Al_2O_3p + 10 wt% SiCp)-MMC. As tensile strength was 390 N/mm^2 for Al/(10 wt% Al_2O_3 + 10 wt% SiC)-MMC and 410 N/mm^2 for Al/(10 wt% Al_2O_3p + 10 wt% SiCp + 5 wt% Cp) MMC (Figure 2.27).
- The addition of 10 wt% alumina, 10 wt% silicon carbide and 5 wt% carbon particles as reinforcement with Al-matrix i.e. for Al/(10 wt% Al_2O_3p + 10 wt% SiCp + 5 wt% Cp) MMC, the tensile strength was increased by 41.37% over Al/(10 wt% Al_2O_3p + 5 wt% Cp)-MMC. As tensile strength was 290 N/mm^2 for Al/(10 wt% Al_2O_3p + 5 wt% Cp)-MMC and 410 N/mm^2 for Al/(10 wt% Al_2O_3p + 10 wt% SiCp + 5 wt% Cp) MMC (Figure 2.27).
- The addition of 10 wt% alumina, 10 wt% silicon carbide and 5 wt% carbon particles as reinforcement with Al-matrix i.e. for Al/(10 wt% Al_2O_3p + 10 wt% SiCp + 5 wt% Cp) MMC, the tensile strength was increased by 24.24% over Al/(10 wt% SiCp + 5 wt% Cp)-hybrid MMC. As tensile strength was 330 N/mm^2 for Al/(10 wt% SiCp + 5 wt% Cp)-MMC and 410 N/mm^2 for Al/(10 wt% Al_2O_3p + 10 wt% SiCp + 5 wt% Cp)-MMC (Figure 2.27).

2.8 EXPERIMENTATION FOR WEAR TEST

Wear test were performed using a pin on disc machine at room temperature. The specimens in the dimension of length 35 mm and 8 mm diameter were washed in acetone before test. The intial weight of the specimen was measured in electronic weighting machine with an accuracy of 0.01mg. The friction coefficient was continuously measured during the test. The test were carried out at a normal loads of 4.91, 9.82 and 14.72 N. The sliding speed was 300, 600 and 1200 rpm and track diameter was 60 mm. Finally, the weight loss due to wearing of the pin was determined by difference of final and the initial weight of the test specimens. Wear test time was also recoded and determined the wear rate. Figure 2.28 shows the test sample of 8 mm diameter and 35 mm long each used for wear test.

Fig. 2.28 Pin Shape of Size 8 mm dia. x 35 mm Long/Each

A pin on disc wear test apparatus consists of a stationary "pin" under an applied load in contact with a rotating disc. The pin on disc tester consists of a rotating disc of the material to be tested against a stationary pin.

Sliding wear test are carried out using Pin-On-Disc machine is shown in Figure 2.29. The disc is allowed to rotate with the help of motor, having different speeds. The pins which are held against the rotating disc are of 8 mm diameter and 35 mm length. The pressure on the specimens is applied by means of a precision dead weight pressure tester operated manually. In the experimentation, the specimens to be tested are taken in the form of a pin and are allowed to slide against a heat treated steel disc. The dry sliding wear tests were carried out with varying the disc rotational speed and applied the different load on pin as well as varying the sliding distance according to the experimental plan is explained in Table 2.10. The wear rate is calculated from weight loss measured. For analyzing the wear rate, 27 specimens were used and test was carried out on each specimen for 1 min. The measured results were analyzed using software MINITAB 15.

Table 2.10 Experimental Values of Wear

S. No.	Material Notations	Material Composition	Sliding Speed (rpm)	Load (N)	Coefficient of friction	Wear Rate (mg/min)
1	A	Al/(10 wt% SiCp + 3 wt% Cp + 5 wt% Al_2O_3p)- MMC	300	4.91	0.223	0.4
2	A	Al/(10 wt% SiCp + 3 wt% Cp + 5 wt% Al_2O_3p)-MMC	600	9.82	0.314	0.7
3	A	Al/(10 wt% SiCp + 3 wt% Cp + 5 wt% Al_2O_3p)- MMC	1200	14.72	0.326	3.4
4	B	Al/(15 wt% SiCp + 5 wt% Cp + 7.5 wt% Al_2O_3p)-MMC	600	4.91	0.397	0.9
5	B	Al/(15 wt% SiCp + 5 wt% Cp + 7.5 wt% Al_2O_3p)-MMC	1200	9.82	0.400	1.4
6	B	Al/(15 wt% SiCp + 5 wt% Cp + 7.5 wt% Al_2O_3p)-MMC	300	14.72	0.324	1.5
7	C	Al/(20 wt% SiCp + 7.5 wt% Cp + 10 wt% Al_2O_3p)-MMC	1200	4.91	0.321	0.5
8	C	Al/(20 wt% SiCp + 7.5 wt% Cp + 10 wt% Al_2O_3p)-MMC	300	9.82	0.260	0.3
9	C	Al/(20 wt% SiCp + 7.5 wt% Cp + 10 wt% Al_2O_3p)-MMC	600	14.72	0.281	0.6

Fig 2.29 Pin on Disc Machine used for Wear Test of MMC and Hybrid MMC Specimens

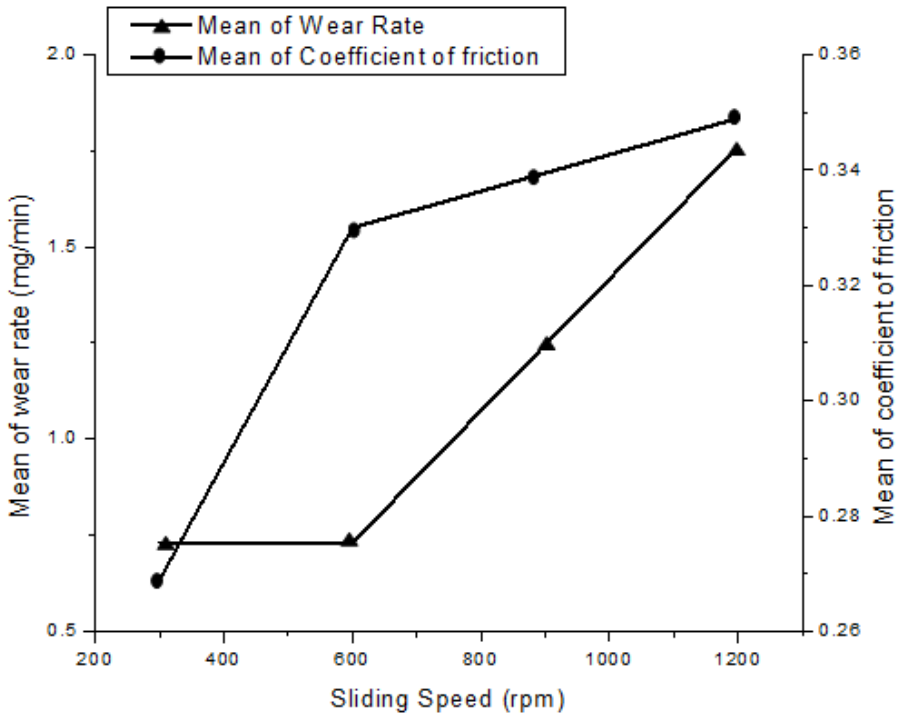

Fig 2.30 Effect of Sliding Speed on Mean Wear Rate and Coefficient of Friction

As the sliding speed increases from 300 to 600 rpm the wear rate remain almost constant. But wear rate increases gradually with increases in sliding speed from 600 to 1200 rpm. The wear

loss decreases with increase in sliding speed, it is due to the formation of a mechanically mixed layer. The formation of mixed layer reduces the wear by covering more area of contact, which makes a good agreement with J.S.S. Babu et al. (2011). The presence of SiC and Al_2O_3 in the composite increases the hardness of composites. The presence of carbon in hybrid composite which act as an effective insulating layer between the two mating surfaces which leads to improve wear resistance. The coefficient of friction increases with increase in sliding speed from 300 to 1200 rpm.

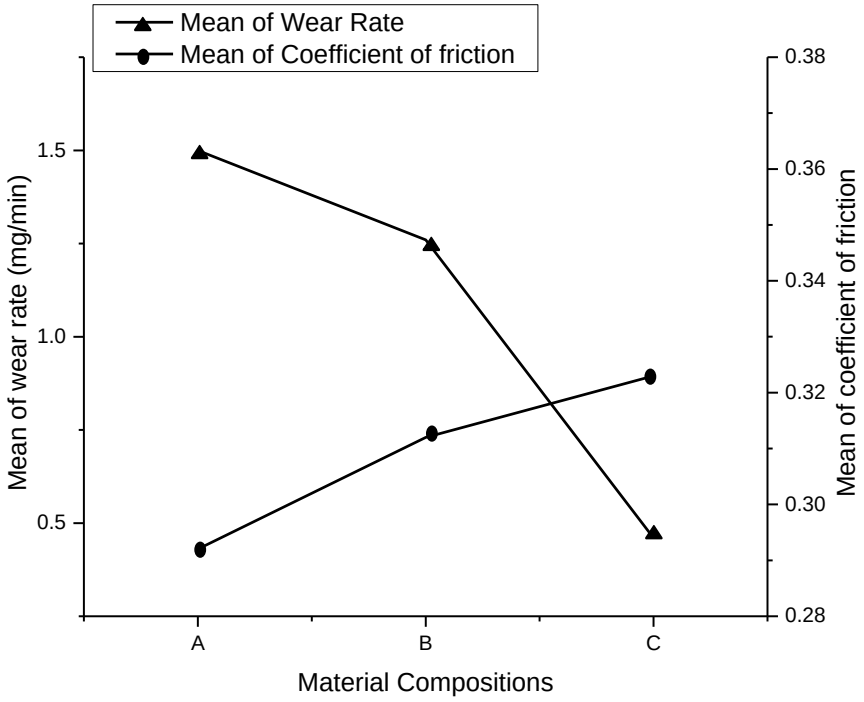

Fig 2.31 Effect of Material Compositions on Wear Rate and Coefficient of Friction

Figure 2.31 shows the variation of wear rate and coefficient of friction with material compositions. From Figure 2.31, it is clear that the mean value of wear is lower at composition of material notation C (Table 2.10). As % of carbon increases with composites, decreases wear rate. Carbon/Graphite plays an important role in reducing the wear rate because of its self lubricant property as discussed by Narasimha et al. (2014). From Figure 2.31, it is also clear that the mean value of coefficient of friction is low for composition of material notation A (Table 2.10) but mean value of coefficient of friction is high at composition of material notation C.

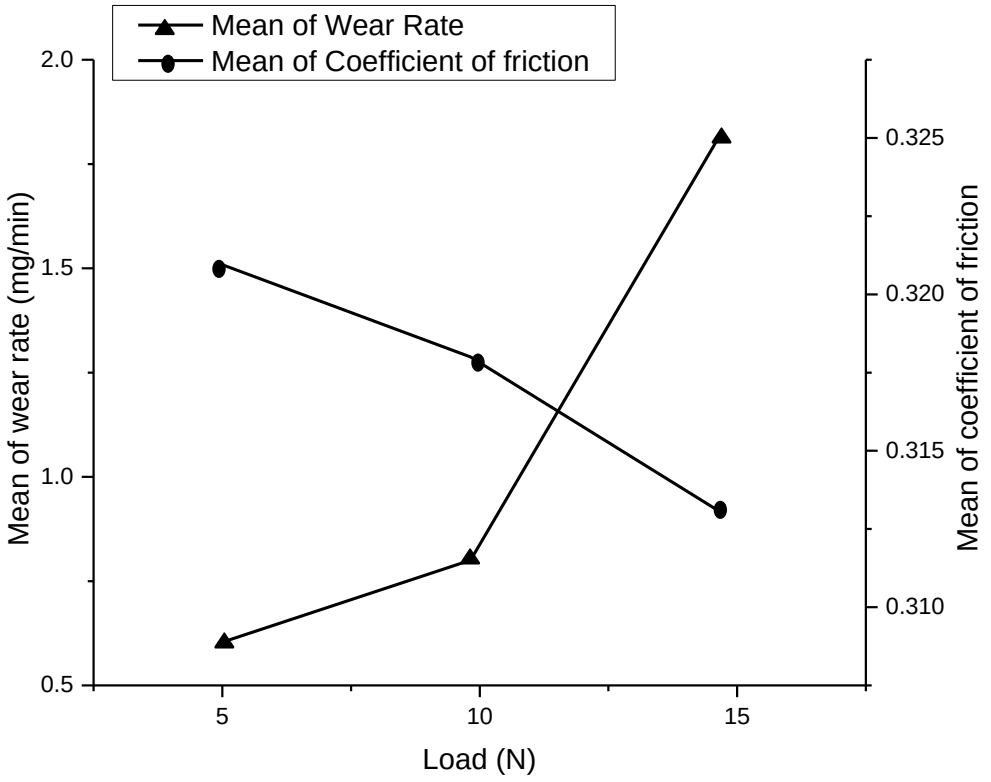

Fig 2.32 Effect of Load on Wear Rate and Coefficient of Friction

Figure 2.32 shows the variation of wear rate and coefficient of friction with load. From Figure 2.32, it is clear that the wear rate is very low at 4.91 N. The wear rate increases continuously with increasing the test load from 4.91 to 14.72 N, which bears a good agreement with Baradeswaran et al. (2013). The coefficient of friction decreases with increase the test load from 4.91 to 9.82 N but it decreases with further increase of load from 9.82 to 14.72 N. This can be attributed to the enhancement in the hardness of hybrid composites by adding the SiC and Al_2O_3. The self lubricating property increases with adding of carbon in hybrid composites. The high load and rotating speed imposed severe deformation of surface as well as increases the frictional force as a results increase the wear rate , which is matched with claimed by Liu et al. (2009).

2.9 ANALYSIS OF WORN SURFACES

The wear behaviour of worn surfaces was done using scanning electron microscope (SEM). Figure 2.33 (a) and Figure 2.33 (b) show the worn out surfaces of material notation A (Table 2.10) composites at a sliding speed of 300 rpm, track diameter 60 mm and at different applied

loads. The friction force was recorded against time. The surface profilometer charts of the worn out wear tracks is shown in Figure 2.34. Abrasion is the main wear mechanism as various scratches and grooves were identified parallel to the sliding direction. From graph Figure 2.34, it was found that some wear grooves appears on the worn surface of composite material notation A (Table 2.10). It is because of the wear mechanism at room temperature. Because of abrasive wear some hard particles were pulled out, as a result formed serious grooves.

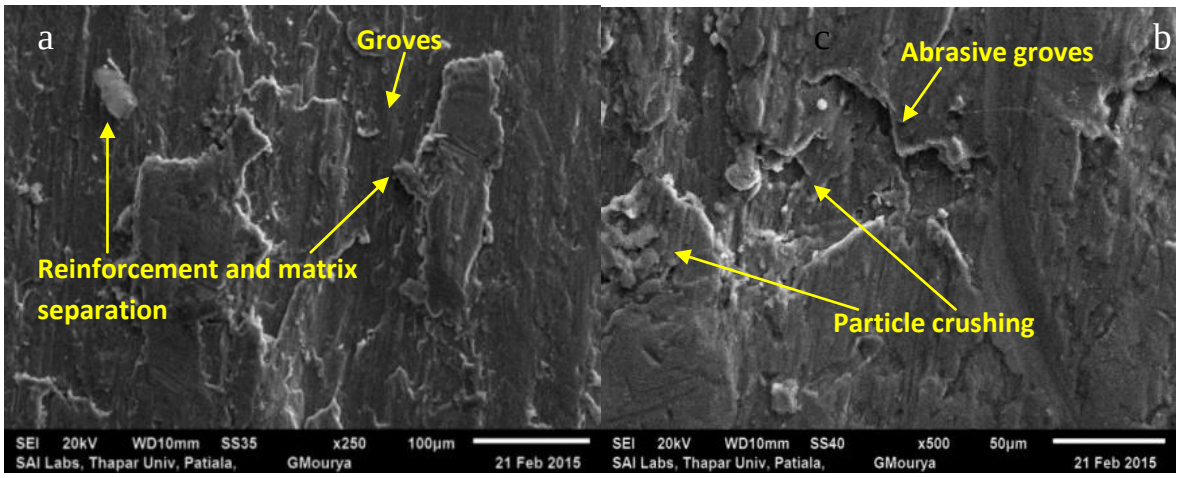

(a) **(b)**

Fig 2.33 (a) & (b) SEM Photographs of Worn Surface of Composite Material Notation A

The worn out surfaces of composite material notation A (Table 2.10) was identified during wear tests with test loads 4.91 N [Figure 2.33 (a)] and 14.72 N [Figure 2.33 (b)]. Due to the increase in applied load, the morphology shows that the composite A has experienced severe wear under the absence of reinforcements. The development of cracks is possible due to the indentation effect exerted when the rotating disk contacts the samples. Continues groves, some cracks and pits are observed on wear track. The single arrow shows the sliding direction of worn surface. The increase in applied load resulted in severe plastic deformation of worn surface in the sliding direction. Both the adhesive and abrasive wear mechanisms were found to be responsible for the wear of the composites. It is evident that the surface of composite A, is rough with deep grooves compared with the composite specimen C (Figure 2.37) with fine grooves. This analysis proves that the wear resistance of the metal matrix composites can be improved with addition of SiC, Al_2O_3, and C reinforced particles. It also concluded that hybrid composites have good potential of the tribological behaviour as compared to simple i.e. single reinforcement composites.

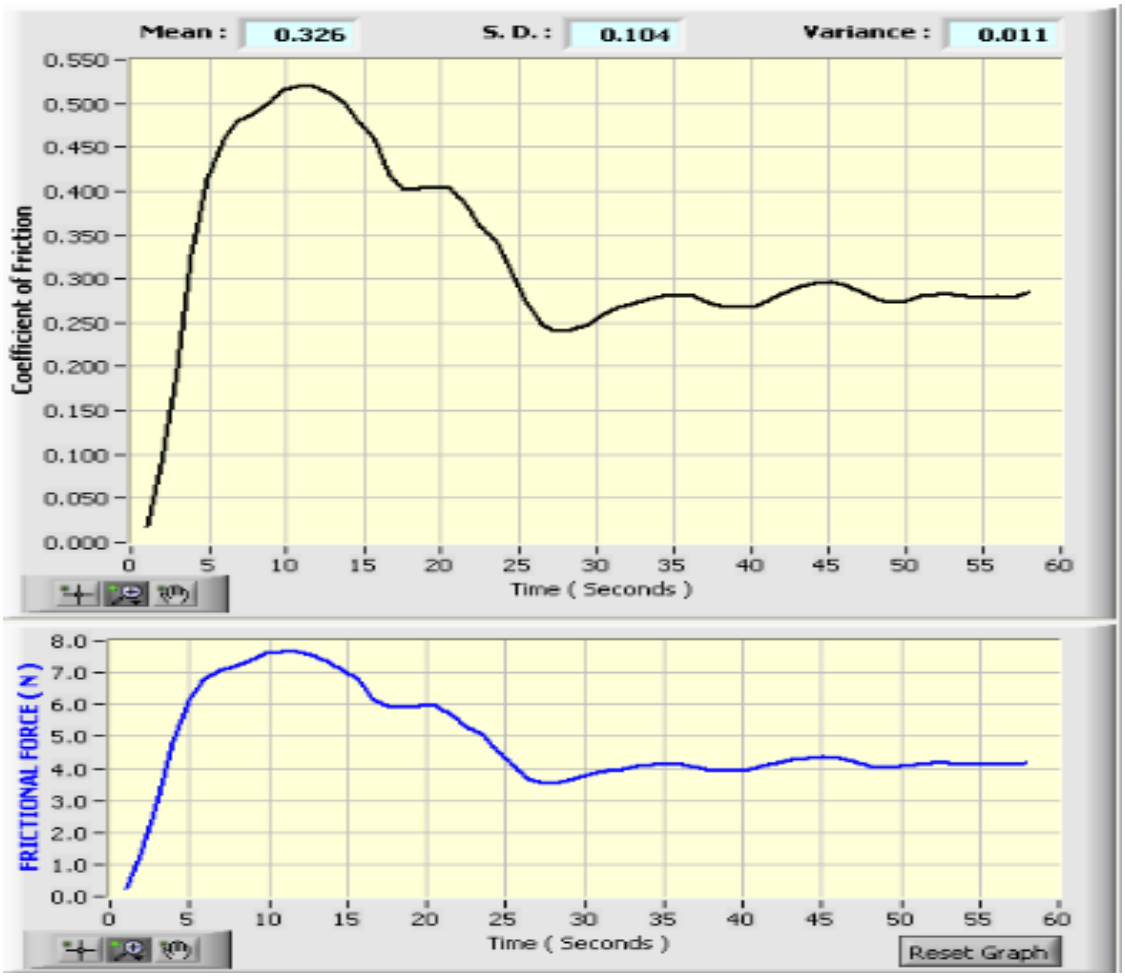

Fig. 2.34 Variation of Coefficient of Friction and Frictional Force with Time for Composite A

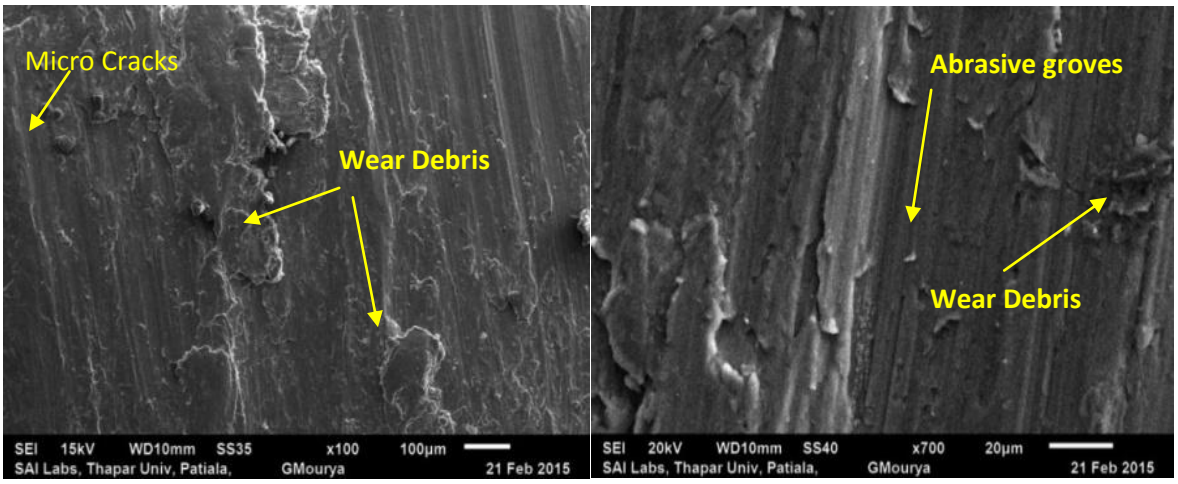

(a) (b)

Fig 2.35 (a) & (b) SEM Photographs of Worn Surfaces of Composite B

Figure 2.35 (a) and Figure 2.35 (b) show the worn out surfaces of composite B (Table 2.10) tests at applied load 4.91 N and 14.72 N respectively. The recorded frictional force and coefficient of friction of the cross-section area of the wear tracks for composite B is shown in Figure 2.36. The morphology of the composite B has experienced harsh wear with increase of applied load, it is observed along with the wear tracks over the sliding surface. The wear surface is possible due to the indentation effect exerted when the rotating disk contacts the samples. Continues groves, some cracks and pits were identified on wear track.

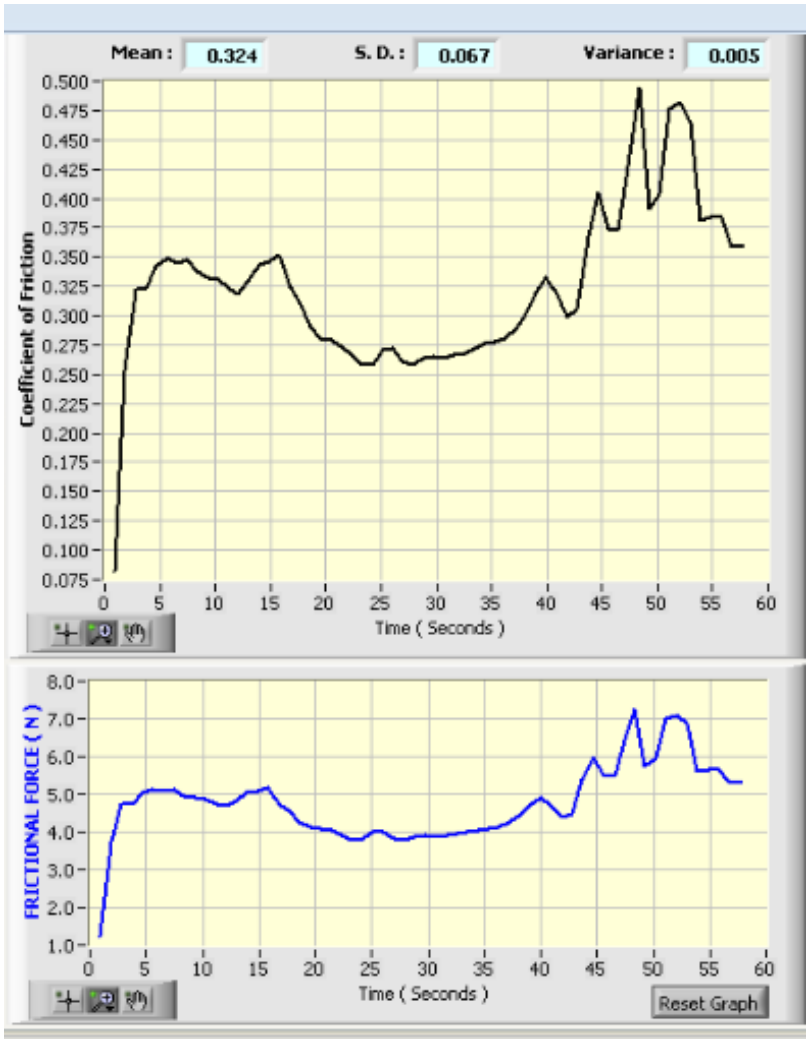

Fig. 2.36 Variation of Coefficient of Friction and Frictional Force on Time for Composite B

It was found from Figure 2.37 that the worn surface of composite C (Table 2.10) having grooves parallel to the sliding direction. The recorded frictional force and coefficient of friction of the cross-section area of the wear tracks for composite C are shown in Figure 2.38. This composite

provides smooth surface in black region (double arrow), it is due to the presence of carbon that smears out during sliding and acts as a layer, protecting the specimen from direct contact with the disc, enhancing wear resistance. The addition of SiC, Al_2O_3, and C reinforcements with Al matrix increases the hardness of hybrid composite as a result reduction of groove size on the composite specimens.

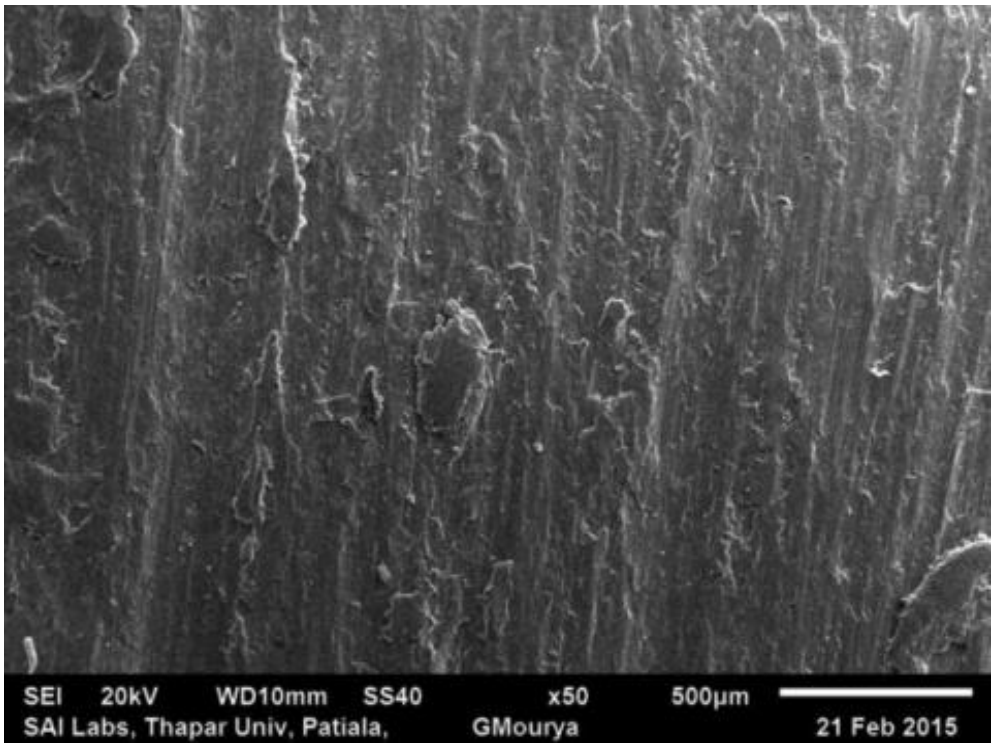

Fig. 2.37 SEM Photograph of Worn Surface of Composite C

From the above analysis, it is clear that the rate of wear is decreased with addition of carbon content, which has great importance in applications of composites related to wear resistance. This phenomenon also bears a good agreement with the explanation given by Lacob et al. (2015). The EDS profile of the worn surface of hybrid composite is shown in Figure 2.39.

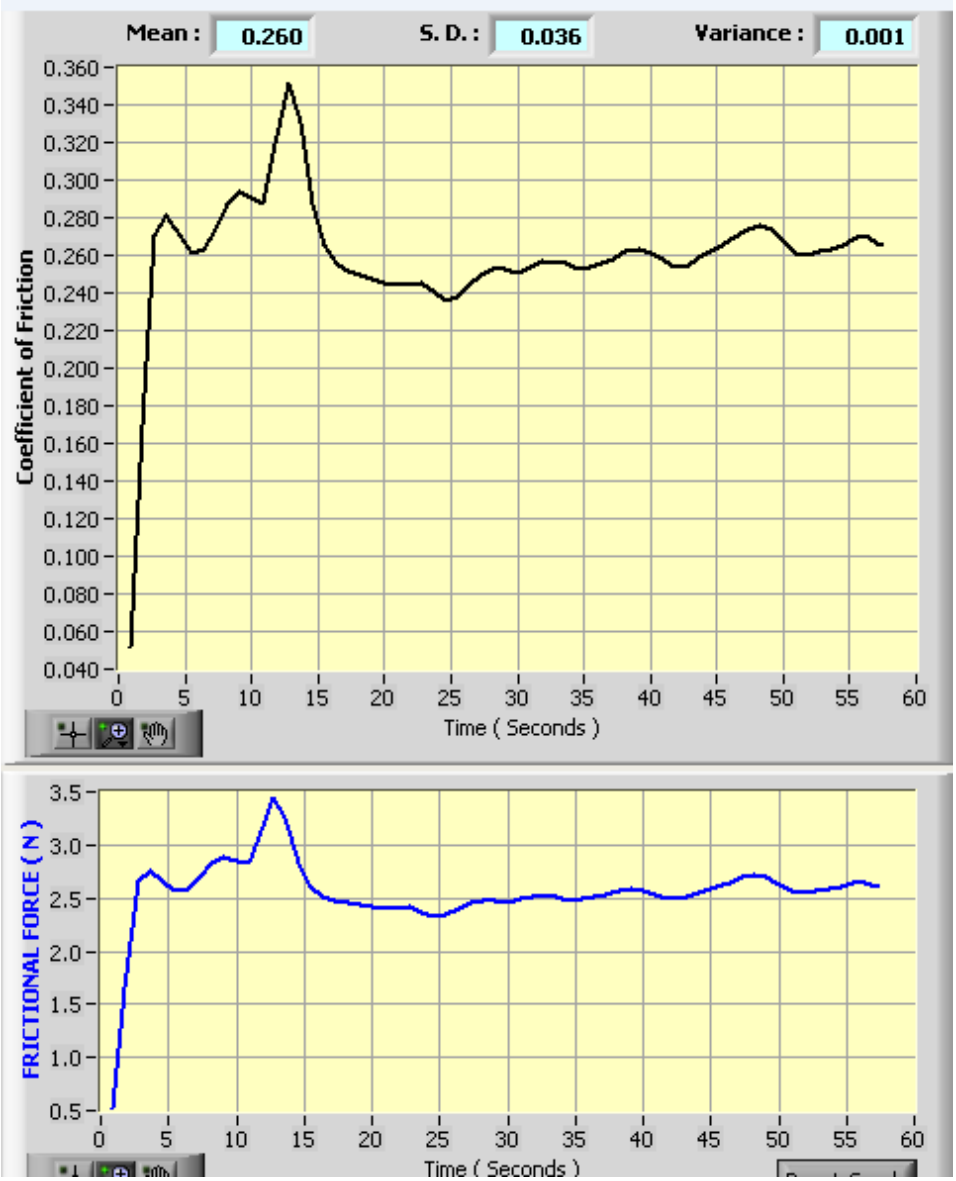

Fig. 2.38 Variation of Coefficient of Friction and Frictional Force on Time for Composite C

From Figure 2.39, the predominant peaks of aluminum composites and reinforced particles with C, Si and O are identified. The oxide present in the worn surface act as protective layer. The present of carbon and Si in the hybrid composite will lead to further enhance the wear resistance of the hybrid composite, it is due to self lubricant property of carbon and hardness of Si.

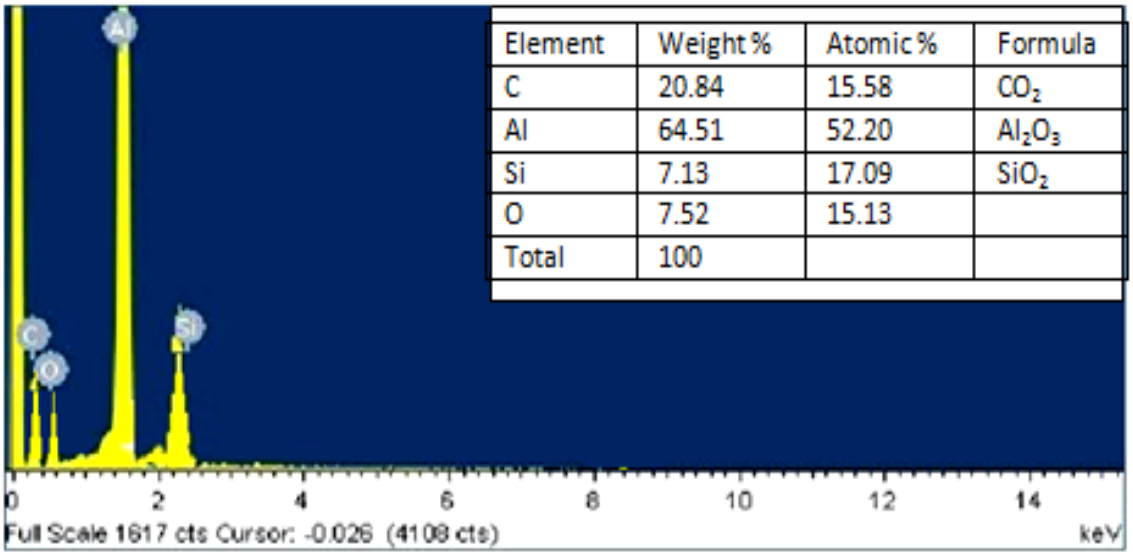

Element	Weight %	Atomic %	Formula
C	20.84	15.58	CO_2
Al	64.51	52.20	Al_2O_3
Si	7.13	17.09	SiO_2
O	7.52	15.13	
Total	100		

Fig. 2.39 Presentation of EDS for SiC- 20%, C-7.5%, Al_2O_3-10%

Summary

The Al/SiCp-MMC, Al/Al_2O_3p-MMC, Al/Cp-MMC, hybrid Al/(Al_2O_3p+SiCp)-MMC, Al/(Al_2O_3p+Cp)-MMC, Al/(SiCp+Cp)-MMC, and Al/(Al_2O_3p+SiCp+Cp)-MMC samples were fabricated by liquid stirring technique. The fabricated MMCs and hybrid MMCs samples were tested to analyze the mechanical properties and wear test. The SEM photographs of wear surface of MMCs and hybrid MMCs were analyzed in this chapter. The workpiece specimens were prepared from fabricated MMCs and hybrid MMCs samples by facing, turning and slicing operation on a center lathe. Prepared workpiece specimens were utilized for feasibility and detailed experiments on developed ECMM set-up. The design and fabrication of the electrochemical micro machining (ECMM) set-up was explained in the next chapter 3. The feasibility test, detailed experiments, acquired results etc. were highlighted and discussed in the next subsequent chapters.

Chapter 3

DESIGN AND FABRICATION OF ECMM SET-UP, FEASIBILITY EXPERIMENTATIONS AND PLANNING OF DETAIL EXPERIMENTATIONS

Introduction

The finishing of difficult to machine material in micro domain requires application of special technique. To fulfil the aim a special technique in machining i.e. an electrochemical micro machining (ECMM) set-up has been fabricated and utilized for micro drilling of Al/(Al_2O_3p+SiCp+Cp)-MMC. Again, machining accuracy is one of the important criteria which affect the quality of the machined surface. Keeping in view, the fabrication of the ECMM set-up has been done in well-planned way and meticulously to ascertain quality of machined surface. The feasibility test carried out on fabricated machine to identify the suitability of the machine for finishing of micro machined surface of liquid stir cast hybrid Al/(Al_2O_3p+SiCp+Cp)-MMC workpiece. The developed ECMM set-up has different parameters such as DC supply voltage, supply current, pulse on time, pulse off time, electrolyte concentration and electrolyte flow rate. The details about the fabrication and development of ECMM set-up are explained in the subsequent articles.

This chapter also presents the feasibility test results acquired during micro drilling of hybrid Al-MMC on fabricated ECMM set-up. The experimental investigations were carried out in two stages (i) feasibility experimentation and (ii) detailed experimentation. The feasibility experiments were carried out to study the suitability of the fabricated set-up for machining of hybrid composites. This chapter presents the feasibility study and analysis of the feasibility test results. It is important to select the different input process parameters and their levels of the developed ECMM set-up for detail experimental investigation. The selection of process parameters and their levels were decided based on the results acquired during feasibility tests. The planning for detail experiments is also explained in this chapter. The detail experiments were also carried out based on Taguchi design of experiment L_{27} (3^{13}) orthogonal array and Response Surface Methodology (RSM). The detail experimental results were analysed in the next chapter 4.

3.1 DESIGN AND FABRICATION OF ECMM SETUP

An ECMM set-up has been design, fabricated and used for micro-drilling of hybrid Al/(Al_2O_3p+SiCp+Cp)-MMC. Figure 3.1 and Figure 3.2 show the schematic diagram and

fabricated ECMM setup respectively. The fabricated ECMM set-up has the following main units such as:

(i) Machine unit
(ii) Electrical power supply and control unit
(iii) Electrolyte flow and control unit
(iv) Servo control and electrode feed unit

The function of the mechanical unit is to hold all other units and basic structure of ECMM set-up. The electric power supply and control unit is to provide DC supply power to the terminals connected to the anode (i.e. workpiece) and cathode (i.e. micro tool). The purpose of electrolyte flow and control unit is to control and circulate the electrolyte during micro drilling. The main function of servo control and electrode feed unit is to control the inter electrode gap by providing feed to micro tool. Following important features were considered while designed and fabricated the ECMM set-up for effective and economic micro drilling of hybrid Al-MMC as follows:

a) Workpiece should be completely immersed in the electrolyte solution.

b) Provision to supply DC power with varying supply voltage from 1V – 40 V.

c) Provision to supply DC power with varying supply current from 0.1 Amp – 15 Amp.

d) Provision to supply DC power with varying pulse on time from 0.1 µs– 20 µs.

e) Provision to supply DC power with varying pulse off time from 0.1 µs– 20 µs.

f) Electrolyte flow control unit must flow control regulator and filter that can be effectively control the flow rate and filtration of electrolyte during micro drilling.

g) Provision to circulate electrolyte flow rate in between machining chamber from 0.2 to 1.5 *l*/min.

h) Use of power shut off to minimize the short circuit (sparking) effect during micro drilling of hybrid Al-MMC.

i) Provides robust structure of job holding device to hold the workpiece during micro drilling.

j) Provision of visibility of workpiece surface during electrochemical micro drilling of hybrid Al-MMC.

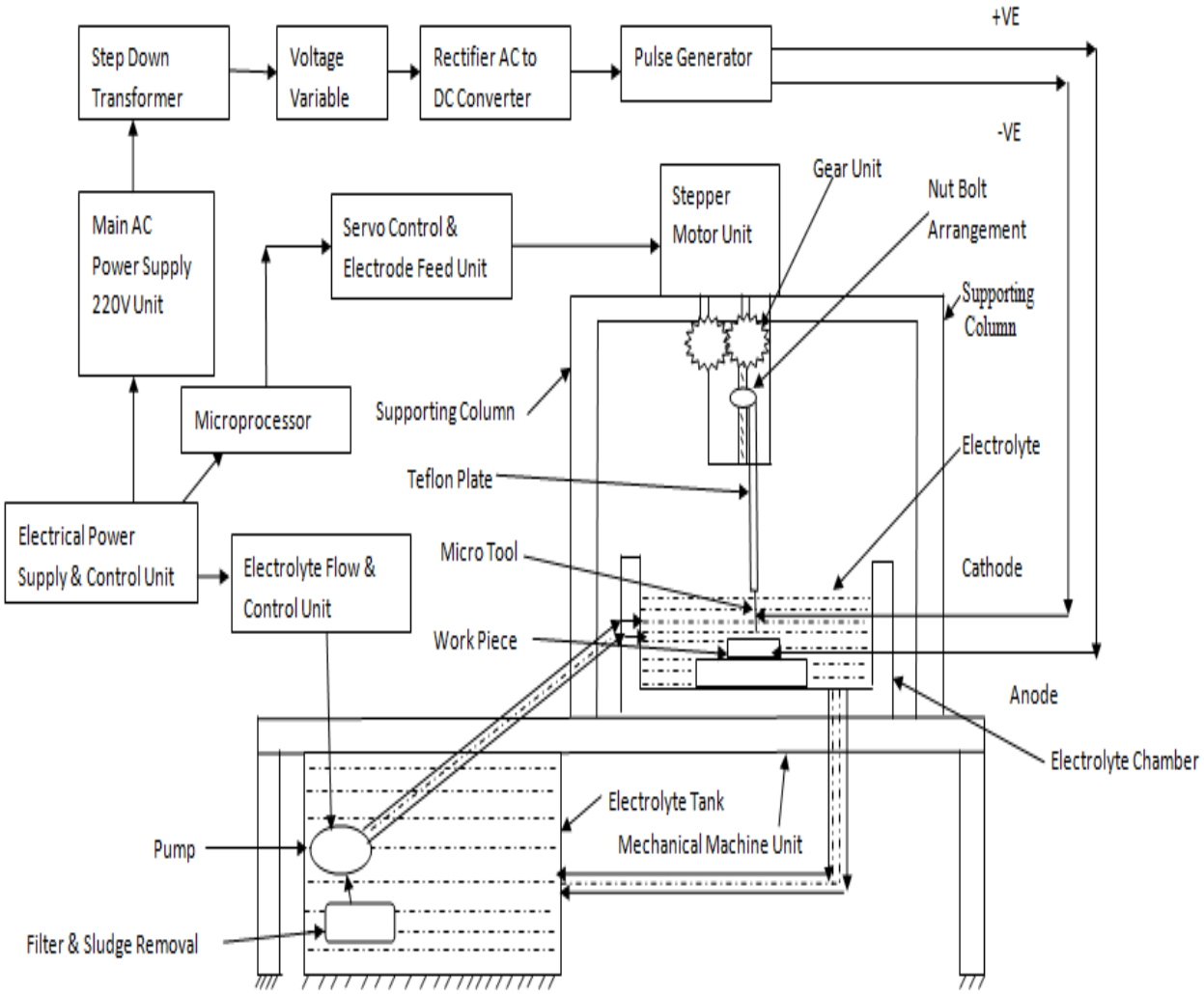

Fig. 3.1 Schematic Diagram of ECMM Setup

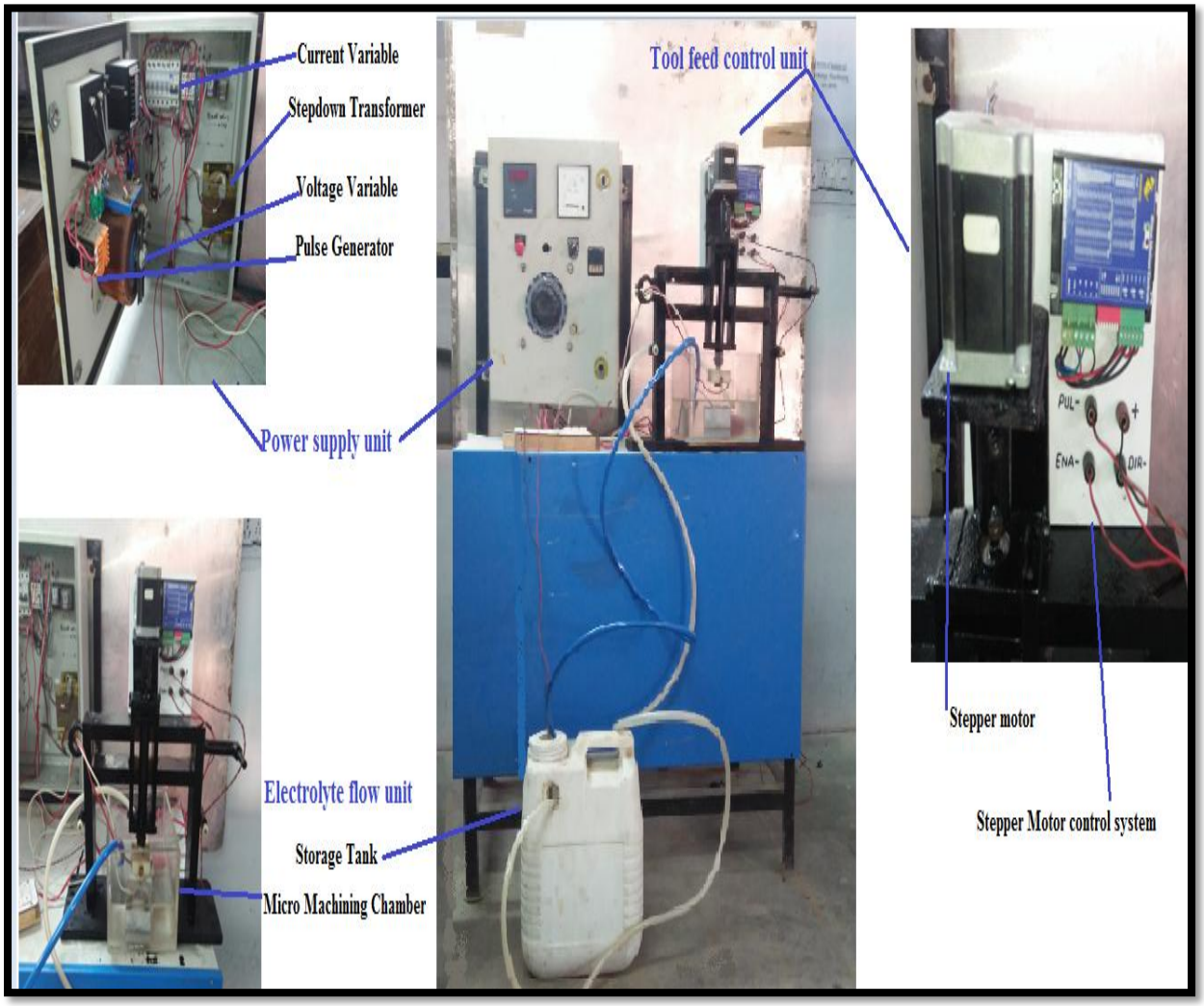

Fig. 3.2 Fabricated ECMM Setup

3.2 MECHANICAL MACHINE UNIT

IS-226/Class-II steel is use, to make the structure of the machine body. The parts made of this steel are chromium plated for aesthetic looks and corrosion resistance. The parts that are come into contact with electrical system, required electrical insulation, so that these parts are need to be made by plastic fibre material. The acrylic material is used and made the parts that come into contact with electrolyte as these parts required noncorrosive materials.

The mechanical machine unit consists of main body frame, machining chamber, work holding arrangement; and tool feeding device. The main body frame has been made of mild steel as rectangular block, which is supported by four legs. A variable electrical power supply and control unit is mounted on rectangular block. A machining chamber is rest on the base plate, which holds sufficient quantity of electrolyte, accommodates micro tool, workpiece,

workpiece clamping arrangement. The size of the angle plate fabricated is 250 × 100 × 8 mm. It is suitable to accommodate the stepper motor and other associated discrete parts. The other two angle plates support the lead screw with the help of bearings. The lead screw is keyed with the stepper motor shaft and passes through the internally threaded hole of the electrode feeding section made of mild steel. The diameter and the length of the main screw rod are 14 mm and 200 mm respectively. In order to achieve very fine feed of the electrode used a screw rod of 30 threads per inch x 100 mm long. It enables the linear up and downward motion of micro tool to a required level in accordance with the depth of the machining chamber and depth of the micro holes to be machined on hybrid Al-MMC workpiece. A micro tool holding unit made of an insulated Teflon plate was coupled at the lower end of the screw rod. Insulated Teflon plate has different adjustable micro holes used to hold different sizes of micro tools. Used a stepper motor, it gives the feed motion to the micro tool through rotary movement of the lead screw.

3.3 ELECTRICAL POWER SUPPLY AND CONTROL UNIT

The main function of the electrical power supply and control unit is to supply the DC power supply to the workpiece (anode) and micro tool (cathode). Electrical power supply and control unit consists of step-down transformer, rectifier, voltage variable, and pulse generator. A step-down transformer and silicon controlled rectifier unit are utilized to convert AC main power supply into DC power output with variation of supply range from 0 - 40 V. If the nature of power supply is continuous mode which increases contamination and deposited the same on the micro tool vicinity, hence work-piece material no longer dissolves uniformly. This problem can be overcome by supplying a pulsed voltage rather than supplying a continuous voltage as claimed by Kozak et al. (1994) and Bhattacharyya et al. (2004). Keeping in view, a pulse-generating unit is provided to supply pulsed power during machining. The pulse generator is used to supply DC power with varying pulse on time from 0.1 µs– 20 µs and varying pulse off time from 0.1 µs– 20 µs. The supply voltage and current is noted with a voltmeter and ammeter fitted with the output circuit. The power shunt is provided to shut down the power supply whenever micro tool become contact with workpiece and generates micro sparks. Figure 3.3 shows a schematic circuit diagram of the electrical power supply unit.

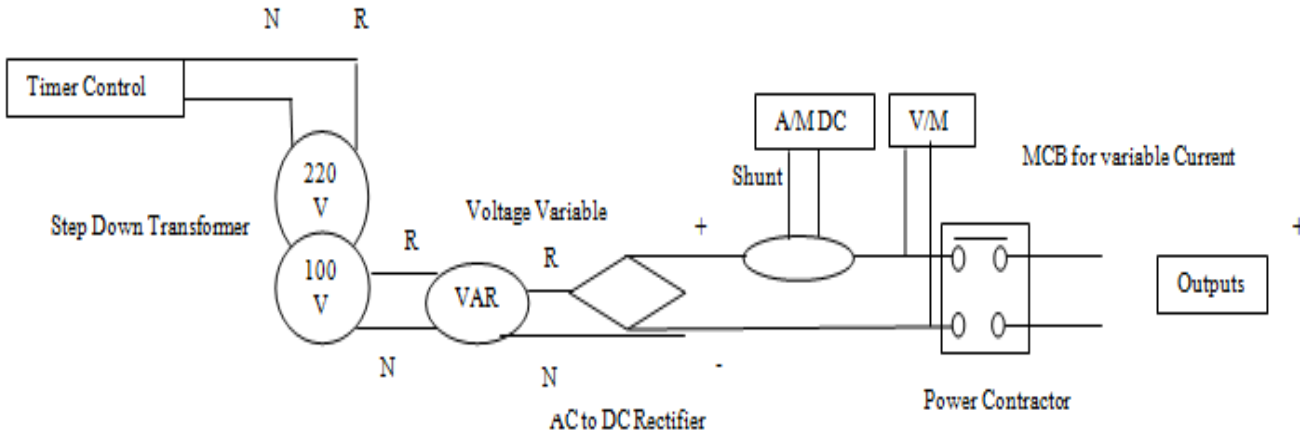

Fig 3.3 Power Supply Circuit Diagram

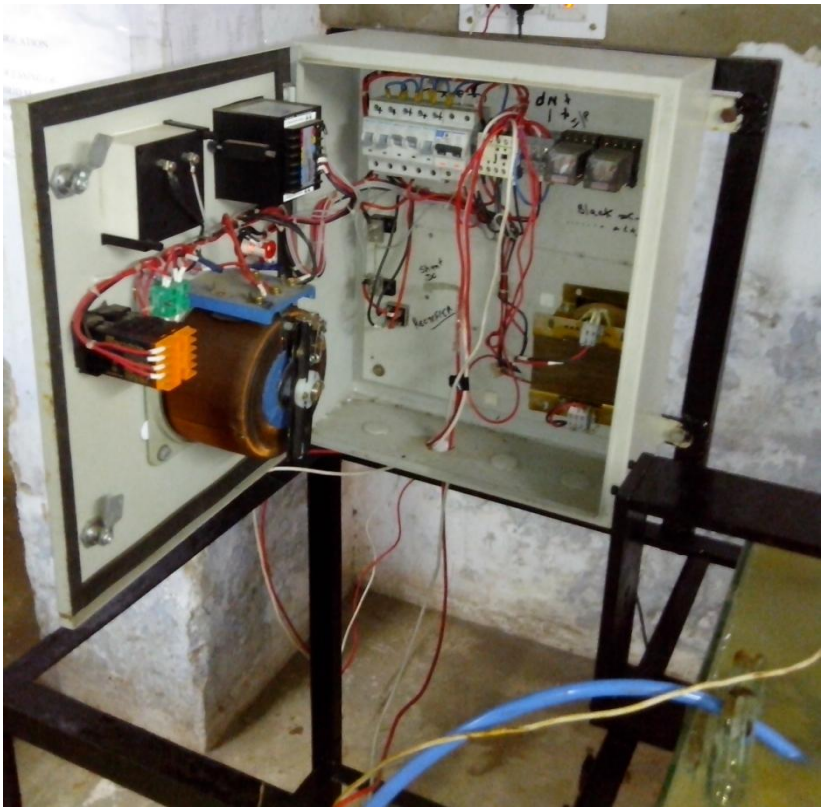

Fig. 3.4 Electrical Power Supply Unit

3.4 ELECTROLYTE FLOW AND CONTROL UNIT

The function of electrolyte flow and control unit is to maintained the level of electrolyte in the machining chamber and circulate electrolyte to remove generated dissolution products from machining zone. Electrolyte flow unit consists of pump, hose-pipes, nozzle, filter, and storage tank used for continuous flow of electrolyte and passes over the machining zone. The flow of electrolyte can be control with the help of feed control valve. The flow rate of electrolyte varies from 0.2 – 1.0 *l*/s.

3.4.1 Machining Chamber

A 15 litre capacity hydraulic machining chamber was fabricated and used for micro drilling experiments. It holds sufficient quantity of electrolyte and accommodates micro tool, workpiece and workpiece clamping arrangement which are essential for electrochemical micro machining. The machining chamber was designed and fabricated in such way so that it can facilitate turbulent free circulation of fresh electrolyte during micro drilling. The inlet and outlet electrolyte flow pipe are fitted with the machining chamber to maintain smooth incoming and outgoing electrolyte flow from storage tank to machining chamber and vise-versa. The machining chamber made of transparency glass so that can enable to see the machining operation and level of electrolyte inside the tank.

3.4.2 Storage Tank

A 15 litre capacity hydraulic storage tank was fabricated and used to store and supply the electrolyte in the machining chamber during experiments. This storage tank is designed in such a way to hold and accommodate the different pipes used for circulation of electrolyte. A cover made of plastics material with filling cap is fitted on the top of the storage tank to prevent the absorption of dust and dirt particles by the electrolyte.

3.4.3 Filter

A micronic filter of capacity 1.5 l/min was fitted in the electrolyte flow control unit to separate the sludge and microchips formed during electrochemical micro machining of hybrid MMC. The effective filtration is very much important during ECMM of hybrid composites, otherwise frequently required to change the electrolyte to maintain the continuity of dissolution of metal. The ineffective filtration may affect the economy of the process and deteriorate the finishing. To restore the effectiveness of electrochemical action excellent filtration of electrolyte is also important for ECMM. The wire mesh with felt covered filters was used for the purpose.

3.4.4 Hydraulic Pump

A hydraulic pump of capacity 2 *l*/min at 2 N/cm^2 is incorporated in the circuit to enable continuous flow of electrolyte during machining of hybrid MMC. A hydraulic pump is driven by 230V AC electric motor.

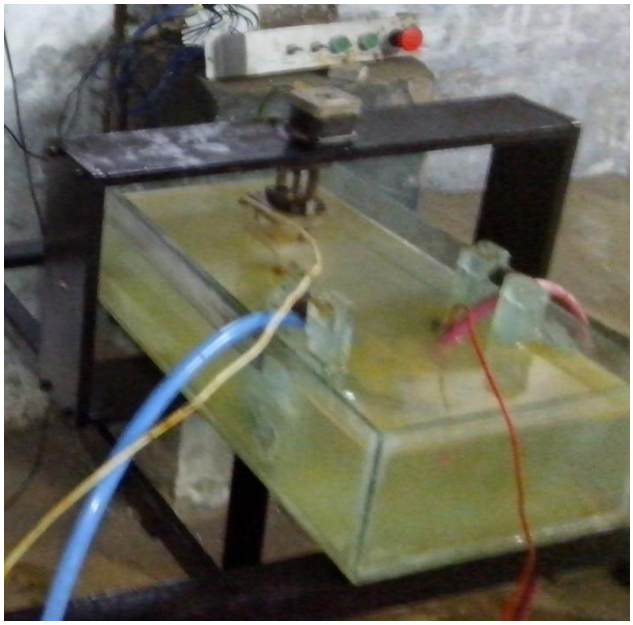

Fig. 3.5 Micro Machining Chamber

3.5 SERVO CONTROL AND ELECTRODE FEED UNIT

A microcontroller unit is used for servo control and electrode feed. This control unit automatically maintain the inter electrode gap (IEG) during machining. At the beginning of machining micro tool moves downward direction and removes the material by electrochemical dissolution of metal. Again, during upwards moment micro tool automatically translate and help to remove the slag by pumping action of electrolyte.

The size of the angle plate fabricated is 250 × 100 × 8 mm. It is used to hold the stepper motor and other associated discrete parts. The other two angle plates support the lead screw with the help of bearings. The lead screw is keyed with the stepper motor shaft and passes through the internally threaded hole of the electrode feeding section made of mild steel. The diameter and the length of the main screw rod are 14 mm and 200 mm respectively. In order to achieve very fine feed of the electrode, 30 threads per inch main screw rod is used. This enables the linear up and downward motion of micro tool to a required level in accordance to the depth of the micro holes to be machined. Other parts used and for feed motion of the micro tool was explained in the above article 3.2.

3.5.1 Microcontroller Unit

The micro movement of tool is achieved through a precision main screw rod's rotation. The main screw rod is rotated by the directly coupled stepper motor. The stepper motor is precisely controlled by the microcontroller unit. A stepper motor with 1.8 /step, 12V, 0.6A, 3 kg-cm torque was used for efficient tool movement during experiments. Different

programmes are stored in the microcontroller unit for (1) forward motion, (2) reverse motion and (3) slow forward. The programmes stored in the microcontroller also help to control the IEG between 20 to 50 µm. The programs and necessary commands can be entered through the keyboard connected to the microcontroller unit. This unit is provided with a reset button for stopping the stepper motor immediately, hence safe from sparking and short-circuiting.

Fig. 3.6 Servo Control and Feed Unit

3.6 MICRO TOOL

The micro tool is act as cathode during micro machining. The tool must match the required shape of the work piece depending on the material and the profile to be produced on workpiece. The high conductive material having high melting point and temperature resistant can be used as tool material and used for ECMM. The diameter of the tool is in the order of 150-200 µm which gives a high current density. A suitable metal includes platinum, tungsten, titanium, molybdenum and copper alloys can be used for micro tools. The tool should be properly insulated for minimizing the stray current effect, for which a specified coating required to be done on the micro tool.

The tools materials used in ECMM must have following properties.

1. Good thermal and electrical conductivity,
2. Corrosion resistance, high machinability
3. Should be stiff enough to withstand the electrolyte pressure without vibrating.
4. High melting point and temperature resistant

3.7 FABRICATION OF MICRO TOOLS ON FABRICATED GRINDING SETUP

To fulfil the requirement of micro tool it is important to fabricate the micro tool as per desire dimension. Keeping in view, a micro tool grinding set-up was designed and fabricated. This fabrication setup was used and fabricated the micro tools. This setup includes micro grinding as well as lapping process. This micro grinding setup has capable to hold precision workspace, high positioning accuracy and resolution, miniature high-speed spindles with maximum 8,000 rpm rotational speed.

An AC motor is used to serve this purpose. The voltage controller is used to control the motor speed by varying voltage. The one end of tool is hold in the motor shaft and another end is free in between adjustable supporting grinding plates. The tool can rotates with the help of motor, free end of tool can rotates between grinder plates.

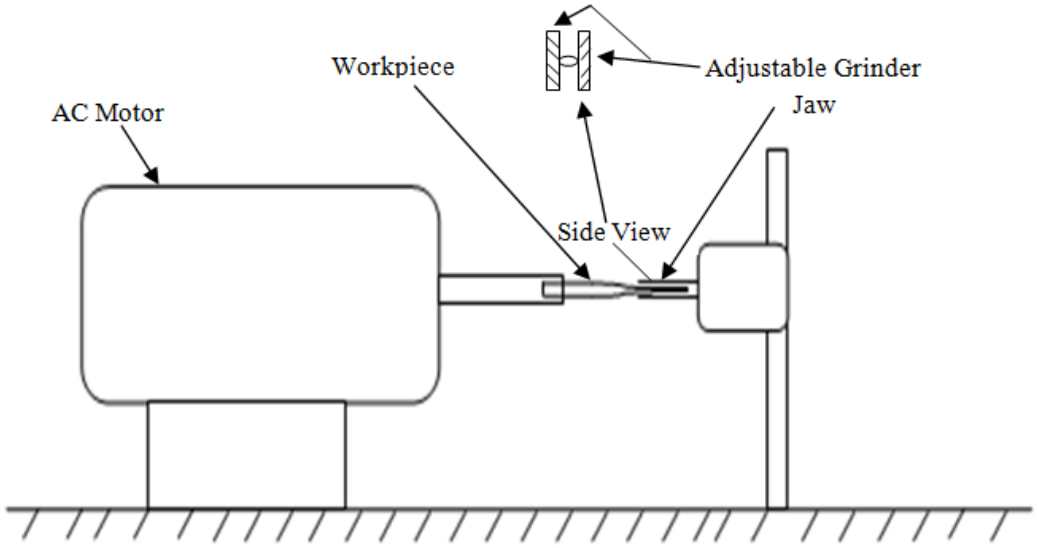

Fig 3.7 Schematic View of Fabricated Micro Grinding Setup

This fabricated set-up is capable to vary the speed such as high speed, moderate speed and low speed which is very much important for micro-grinding of micro tools. Figure 3.7 shows the schematic view of fabricated micro grinding setup.

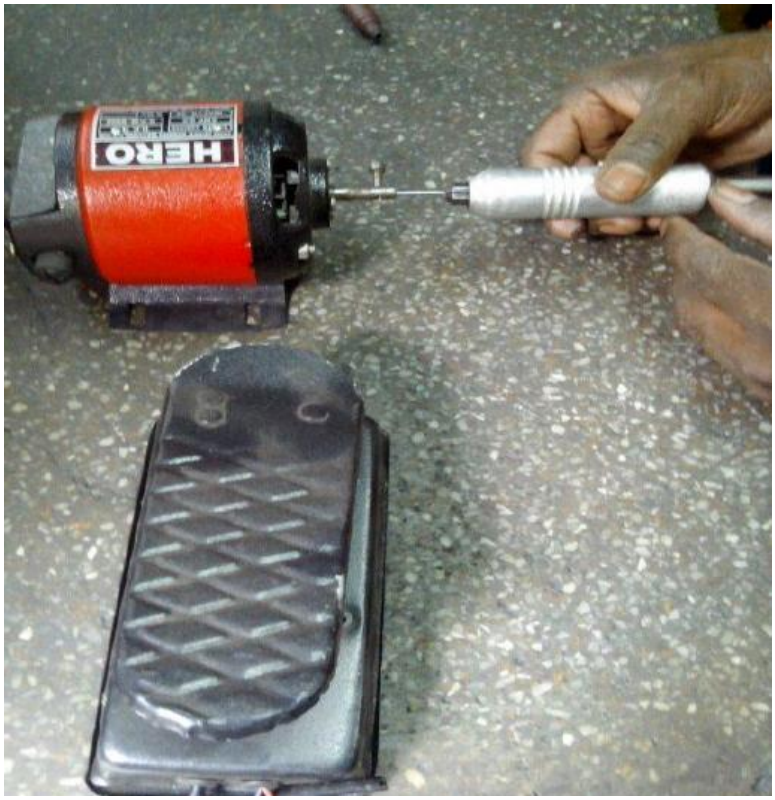

Fig 3.8 A View of Fabricated Micro Grinding Setup

The Tungsten Carbide is used as micro tool i.e. electrode material. Tungsten micro tool has high melting temperature and superior tool life. The raw material used for electrode was 2.0 mm diameters with 300.0 mm length each.

Figure 3.9 shows a fabricated tungsten micro tool. The properties of the Tungsten electrode material as explained in Table 3.1.

Fig 3.9 Fabricated Tungsten Micro Tool

Table 3.1 Properties of Tungsten Micro Tool

Composition	99.9 % W
Density	19.3 g/cm^3
Melting point	3370 ^{0}C
Relative conductivity (to Silver)	14.0
Specific resistance	56.5 μΩ
Thermal expansion coefficient	4.6 × 10-6 K-1

The initial diameter (i.e. 2mm) of tool electrode was reduced up to 300 ±10 μm by utilizing the fabricated grinding set-up. Table 3.2 reported the steps to perform micro tools at different speed, time and gap between adjustable grinding plates.

Table 3.2 Steps of Micro Grinding

Steps	RPM	Machining Time (min)	Accumulated Time (min)	Gap (μm)	Tool Diameters (μm) (±10 μm)	
					Initial	Final
1	6000	8.15	5.15	2100	2000	1200
2	6000	7.10	15.25	1400	1200	800
3	4000	5.15	20.40	1000	800	500
4	3000	5.20	25.60	600	500	300

From Table 3.2 it is clear that step 3 and step 4 were low speed and gap which is desirable for fabrication of 300 ±10 μm diameter micro tool. Figure 3.10 shows the fabricated tool in the different steps.

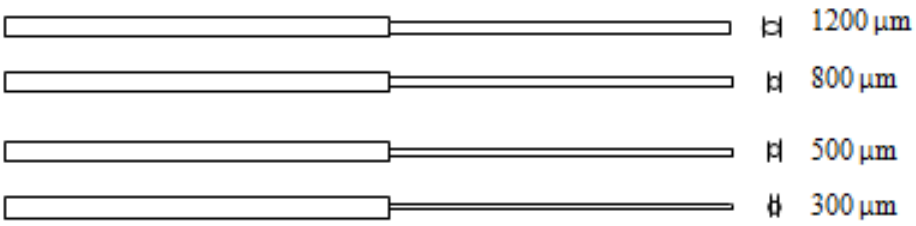

Fig 3.10 Schematic View of Micro Tool during Grinding Steps 1 to 4

In the different steps as mentioned above (Table 3.2) the diameter of tool is reduced and maintained the required length. Table 3.3 represents the micro tool diameter and their length

with aspect ratio of the fabricated tools. Figure 3.11 shows a SEM photograph of a fabricated tool which indicates the conical shape. This conical effect was significantly reduced by lapping process. From Figure 3.11, it clear that there are some burrs is visible on outer surface of the micro tool.

Table 3.3 Generated Micro Tool Specification

S. No.	Tool Length (mm)	Tool diameter (µm)	Aspect Ratio
1	1.8	12	150
2	4	245	16.32
3	4	397	10.07
4	8.53	476	17.92

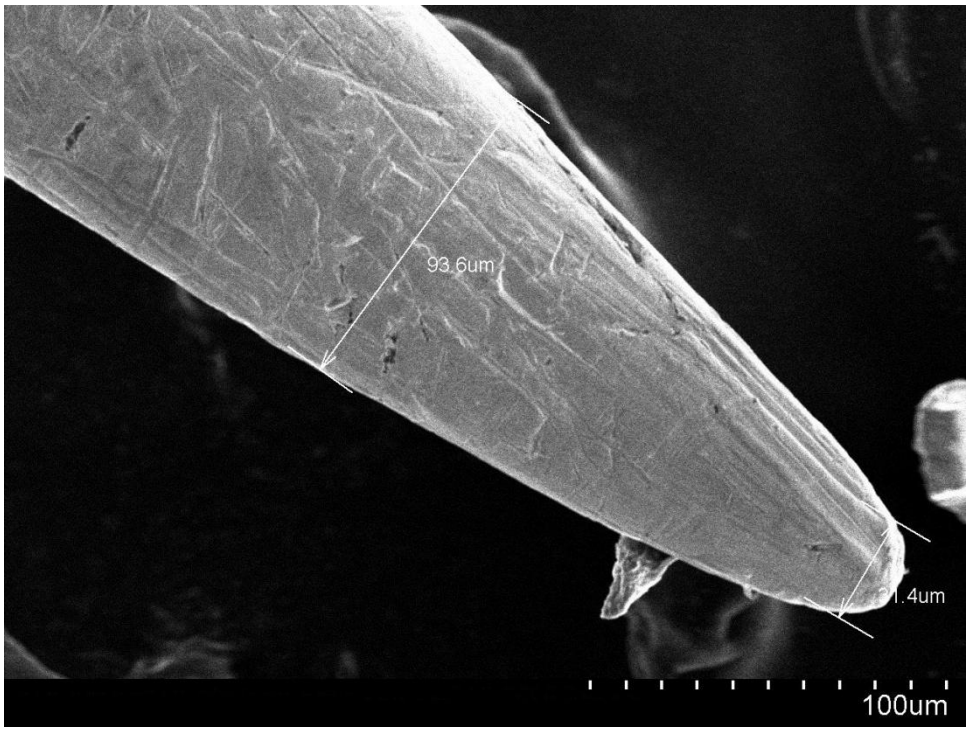

Fig 3.11 SEM View of Micro Tool during Grinding Steps

Figure 3.11 shows the SEM photograph of a micro tool after grinding and before lapping process.

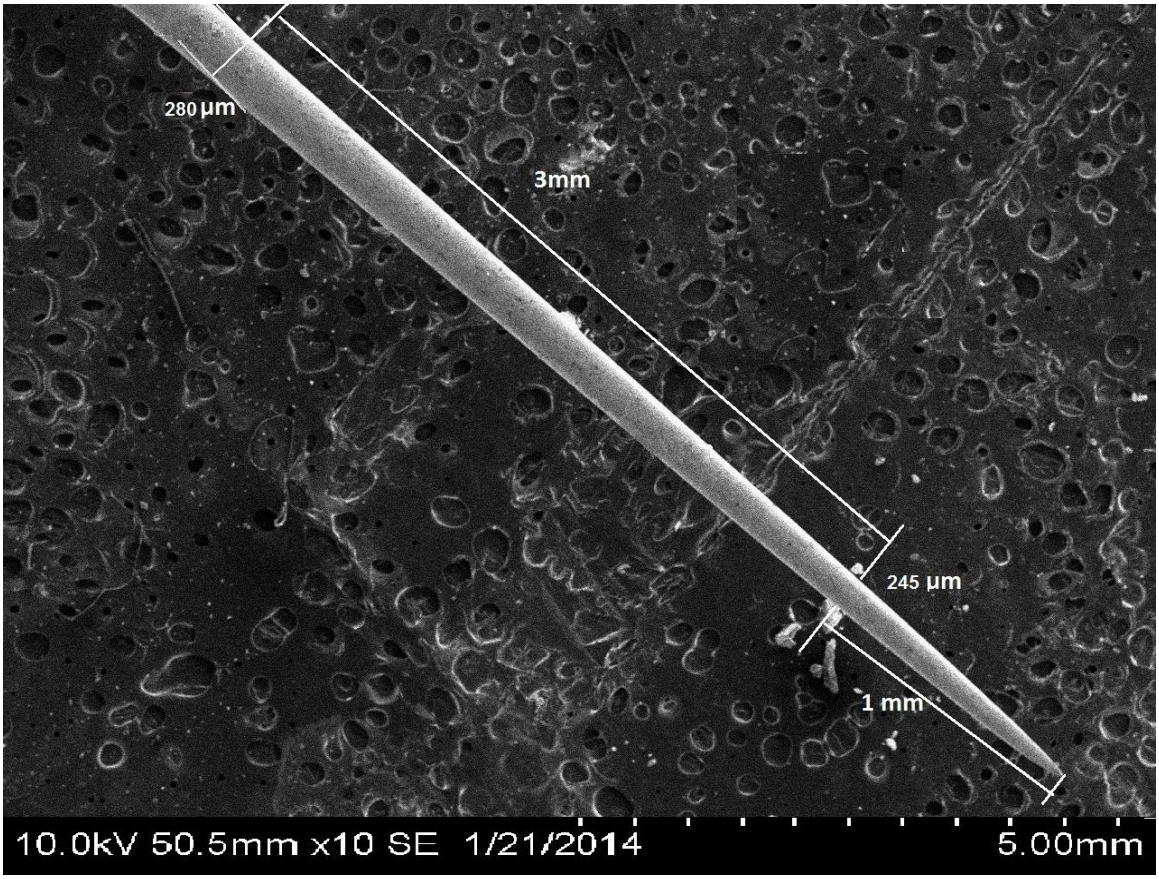

Fig 3.12 SEM View of Micro Tool after Lapping

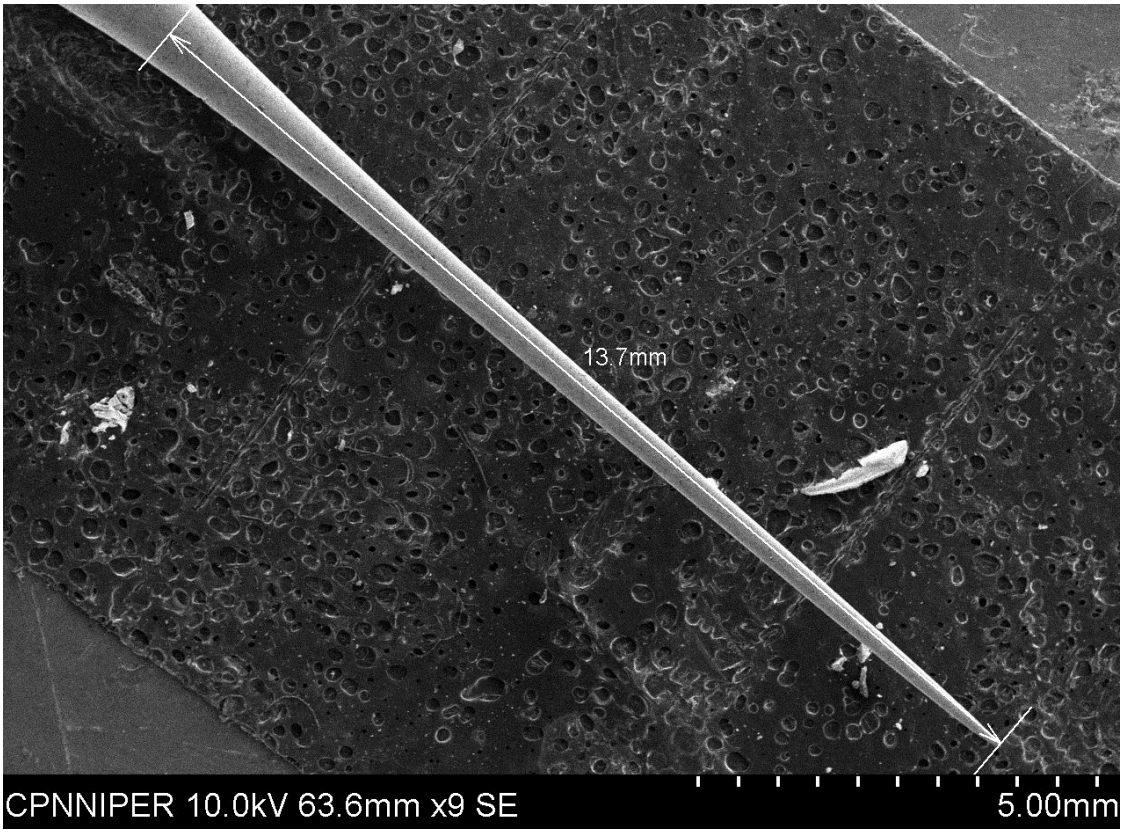

Fig 3.13 SEM View of Micro Tool after Lapping

Figure 3.12 and Figure 3.13 show the SEM photographs of micro tools after lapping. From Figure 3.12 and Figure 3.13, it is clear that the burrs are removed from the outer surface area of micro tool after lapping process.

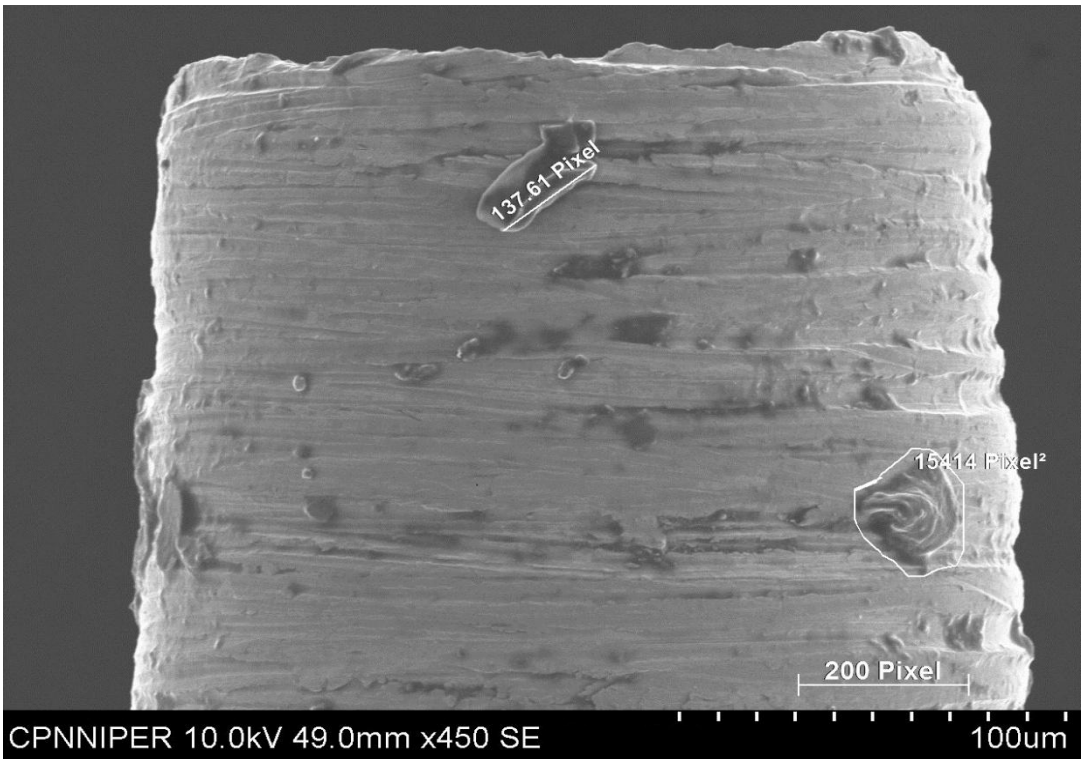

Fig 3.14 SEM View of Tool Tip

Figure 3.14 shows a SEM photograph of micro tool tip. From Figure 3.14, it clearly identified some micro voids and grooves on the tool tip that are generated during grinding. It is because of some particulates are pull out by grinding forces on tool tip.

3.8 FEASIBILITY TEST TO VERIFY THE SUITABILITY OF THE FABRICATED ECMM SETUP

The feasibility tests were carried out during machining of hybrid Al/(Al_2O_3p+SiCp+Cp)-MMC on fabricated electrochemical micro machining (ECMM) set-up to identify the suitability of the fabricated setup for machining of hybrid composites. One factor at a time approach was used i.e. one factor of ECMM process was varied keeping all others constant feasibility tests were carried out. The purpose of these experiments is also to study the variations of the ECMM process responses on variables i.e. machining process parameters. Also, these tests results were utilized and analyzed to identify the range and levels of different parameters for further detail experiments.

The pilot experiments were performed on developed electrochemical micro machining setup. Various input process parameters were varied during the experimentation such as

supply current, supply voltage, pulse on time, pulse off time, electrolyte concentration, and electrolyte flow rate. The following given below were kept constant during the experimentation

1. Work piece : hybrid Al/(Al_2O_3p+SiCp+Cp)-MMC
2. Electrode (micro tool) : Tungsten
3. Work piece height : 2mm
4. Electrolyte : NaCl
5. Electrolyte temperature : 20-24^{0}C

3.8.1 Observations of Feasibility Study

Based on the acquired results during feasibility tests, it is identified that this fabricated ECMM setup can be used for machining of hybrid metal matrix composites. The response characteristics such as material removal rate (MRR), electrode wear rate (EWR), surface roughness, taper cut, over cut and micro spark affected zone (MSAZ) were considered and analyzed the test results.

The material removal was determined by the difference of weight before and after each experiment. The electro wear was determined from the difference of electrode weight before and after machining. The surface roughness measuring instrument Surfcom 130A was utilized to measure the surface roughness heights (SR). The inlet and exit machined hole diameters were measured by utilizing the SEM technique and determined the taper cut, over cut and MSAZ. The condition of the fabricated micro tools and machined holes were analyzed through Scanning Electron Microscope (SEM) photographs. The following relations equations (i) to equation (v) were used for calculation of MRR, EWR, Overcut, taper cut and MSAZ as:

$$\text{MRR} = \frac{\text{Workpiece weight before machining} - \text{workpiece weight after machining}}{\text{Machining Time}} \quad (3.1)$$

$$\text{EWR} = \frac{\text{Electrode weight before machining} - \text{Electrode weight after machining}}{\text{Machining Time}} \quad (3.2)$$

$$\text{Overcut} = \frac{\text{Davg} - \text{d (electrode)}}{2} \quad (3.3)$$

$$\text{Taper cut} = \frac{\text{Di} - \text{De}}{2} \quad (3.4)$$

$$\text{MSAZ} = \frac{\sum_{i}^{N}(\text{Ri} - \text{Ravg})}{\text{N}} \quad (3.5)$$

Where, Davg = average diameter of machined micro hole

d (electrode) = diameter of micro electrode

Di = diameter of machined micro hole at inlet

De = diameter of machined micro hole at exit

Ravg = average radius of machined micro hole

N = Number of radius on the periphery of machined micro hole

3.8.2 Influence of Supply Current on Response Characteristics

Figure 3.15 shows the effect of supply current on response characteristics during micro drilling of hybrid Al/(Al_2O_3p+SiCp+Cp)-MMC. From Figure 3.15, it is clear that the MRR and EWR both increase with increase in supply current. As per Faraday's law, the material removal is proportional to the supply current. The experimentally acquired results satisfy the Faraday's effect. It may be due to the increase of dissolution efficiency. The machining response characteristics such as surface roughness heights (SR), taper cut (TC), over cut (OC) and micro spark affected zone (MSAZ) all increase with increase in supply current. The supply of high current produces non-uniform and irregular machined hole. This may be due to improper cleaning of sludge particles from the inter electrode gap (IEG) during machining. Therefore, surface roughness height, R_a increase with increase in supply current. The trend of taper cut was similar to the overcut and micro spark affected zone; it may be due to the high supply current. It yields higher material removal along the lateral direction. High taper cut, over cut and micro spark affected zone were also observed at high discharge energy density. The large quantity of metal melted when experiment was carried out at high discharge energy density e.g. at 2A or 3A peak current, and thereby formed larger size of discharge craters on workpiece surface. This phenomenon was responsible to make large entrance of micro-hole and poor surface finish. It may reduces the total dissolution time at the exit as compared to inlet of the generated micro hole, enhance generated taper cut and over cut.

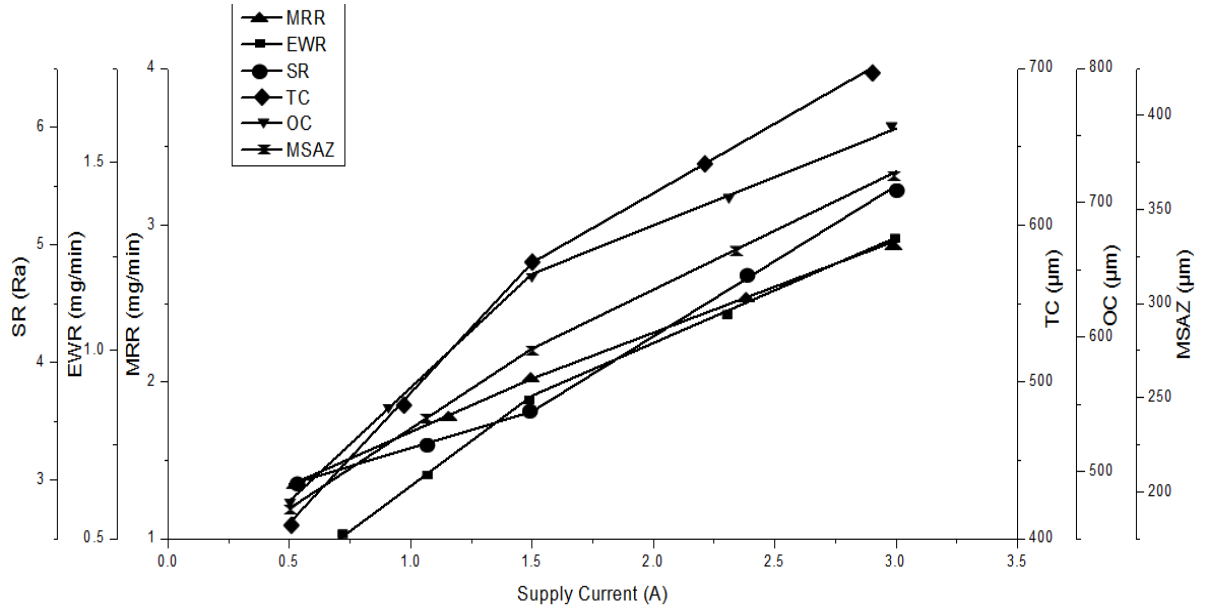

Fig 3.15 Influence of Supply Current on Response Characteristics

3.8.3 Influence of Supply Voltage on Response Characteristics

Figure 3.16 shows the effect of supply voltage on response characteristics during micro drilling of hybrid Al/(Al_2O_3p+SiCp+Cp)-MMC. From Figure 3.16, it is clear that the MRR increases with increase in supply voltage. The electrolyte ionization increases with increase in supply voltage, as a result increase the MRR. Size of micro hole increases with increase in supply voltage. The surface roughness height (Ra) and electrode wear rate (EWR) both increase with increase in supply voltage. From Figure 3.16, it is clear that the over cut, taper cut, and micro spark affected zone all increase with increase in supply voltage. The high-applied voltage may result in breaking of the oxide layer.

At high supply voltage, generated high heat in the inter-electrode gap causing varying local electrolyte conductivity. This phenomenon is responsible for distribution of non-uniform current in the inter-electrode gap. The overcut means larger removal of metal along the lateral direction. It is one of the important causes of high material removal rate as explained above and reduces the total discharge time at the exit as compared to the entrance of the hole.

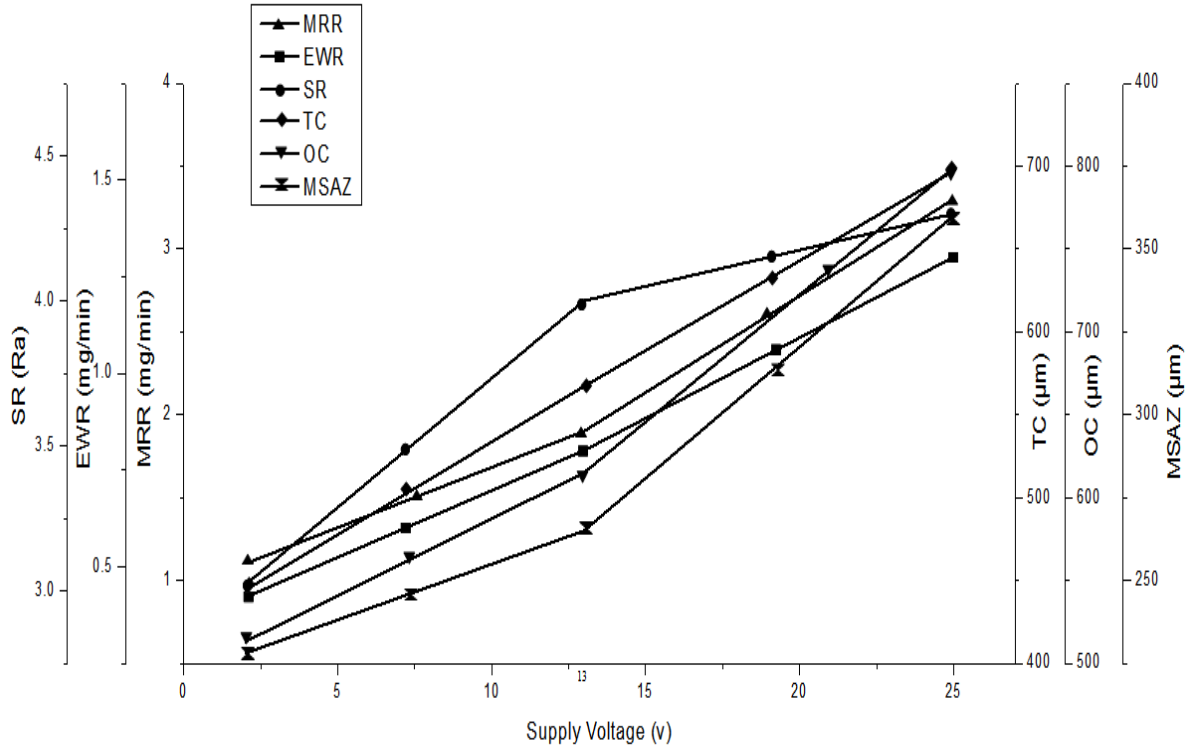

Fig 3.16 Influences of Supply Voltage on Response Characteristics

3.8.4 Influence of Pulse On Time on Response Characteristics

Figure 3.17 shows the effect of pulse on time on response characteristics during micro drilling of hybrid Al/(Al_2O_3p+SiCp+Cp)-MMC. From Figure 3.17, it is clear that the MRR increases with increase in pulse on time. Dissolution efficiency increases as well with increase in pulse on time and thereby decreases actual machining time. The surface roughness height (Ra) decreases with increase in pulse on time. It is also clear that the over cut, taper cut, and micro spark affected zone increase with increase in pulse on time from 0.5µs to 10 µs. With the increase of pulse on time, both supply current as well as period of supply current increases, enhance dissolution of material along the radial direction and thereby increases the overcut. At the same time increases the retention of machined metal particles in the inter electrodes gap. The presence of machined particles in the inter electrode gap may cause of sparking, which may lead to higher overcut. This also leads to increase the electrode wear rate and decrease the machining accuracy.

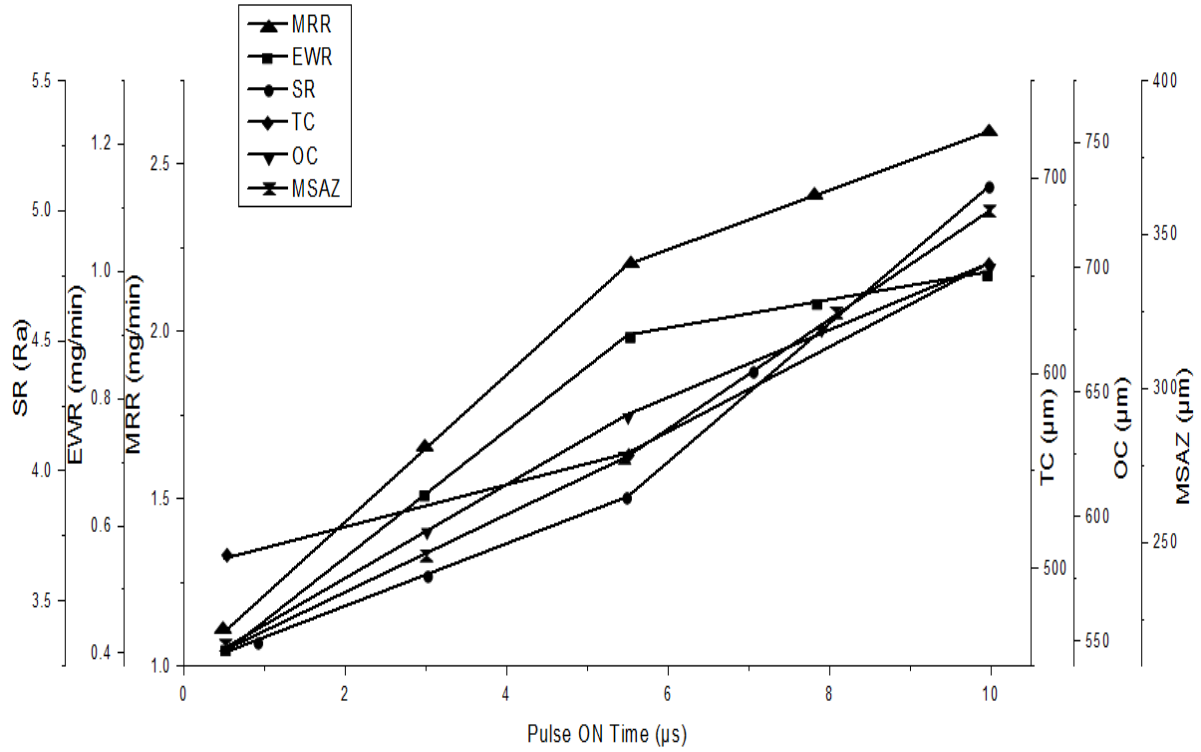

Fig 3.17 Influences of Pulse On Time on Response Characteristics

3.8.5 Influence of Pulse Off Time on Response Characteristics

Figure 3.18 shows the effect of pulse off time on response characteristics during micro drilling of hybrid Al/(Al2O3p+SiCp+Cp)-MMC. Both MRR and EWR decrease with increase in pulse off time. More pulse off time causes less dissolution efficiency resulting in reduction of MRR and EWR. The surface roughness height (Ra) decreases with increase in pulse off time, however it happens up to a certain limit e.g. ranges from 0.5 µs to 5.5 µs. It is because of more time duration allowed for machining that may be sufficient to wash out the sludge from the machining zone. From Figure 3.18, it is clear that over cut, taper cut and micro spark affected zone decrease with increase in pulse off time.

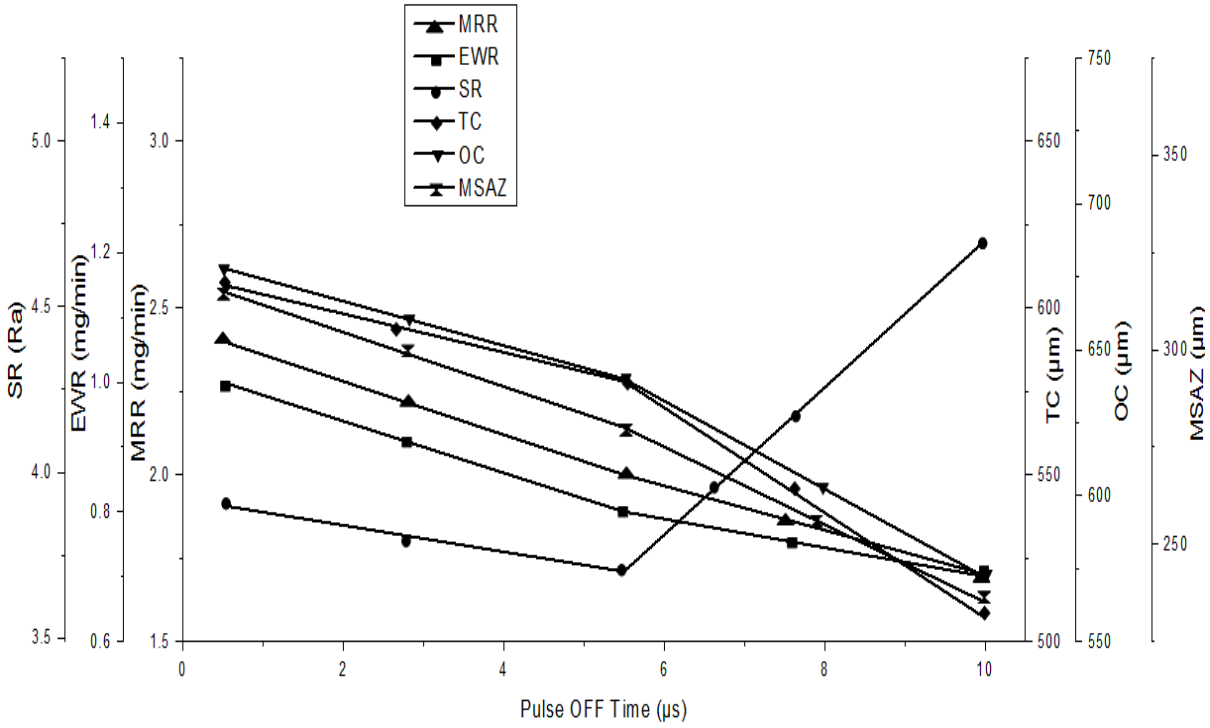

Fig 3.18 Influences of Pulse Off Time on Response Characteristic

3.8.6 Influence of Electrolyte Concentration on Response Characteristics

Figure 3.19 shows the effect of electrolyte concentration on response characteristics during micro drilling of hybrid Al/(Al_2O_3p+SiCp+Cp)-MMC. At higher concentration e.g. 25 (g/l) of electrolyte, a large number of ions are formed during machining, as a result there is an increase in machining current density. It leads to increase the MRR. The overcut, taper cut and micro spark affected zone increase with increase in electrolyte concentration. Both electrolyte conductivity and current density increase with increase in electrolyte concentration and thereby leads to increase the radial and lateral etching, overcut and taper cut.

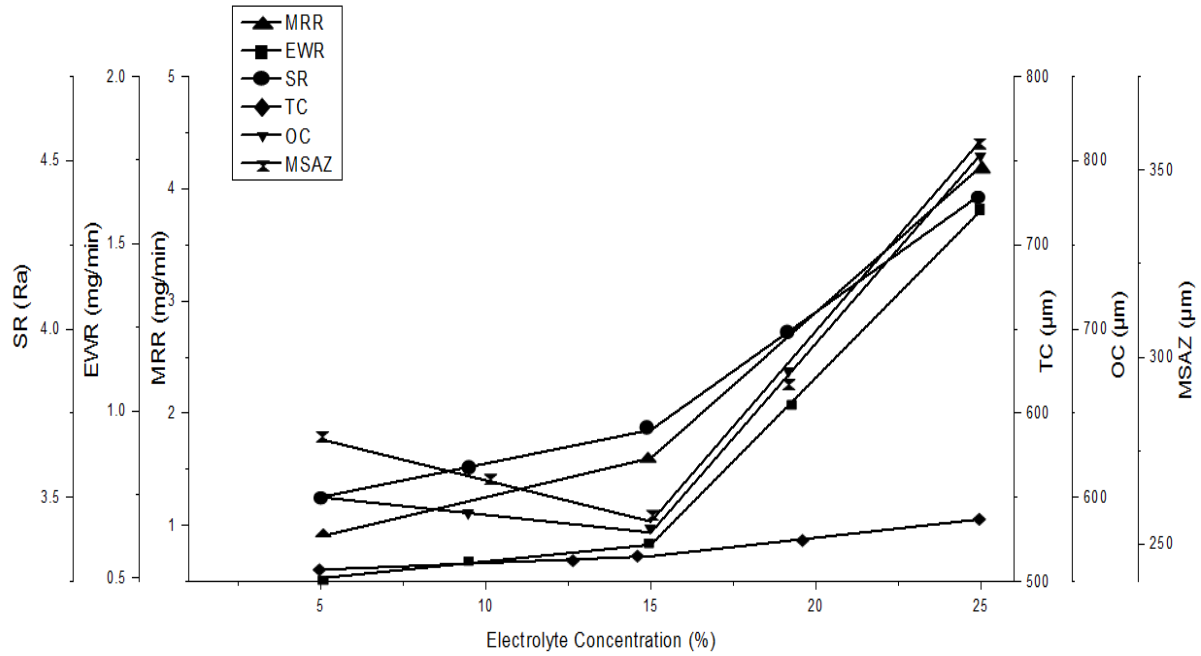

Fig 3.19 Influences of Electrolyte Concentration on Response Characteristics

3.8.7 Influence of Electrolyte Flow Rate on Response Characteristics

Figure 3.20 shows the effect of electrolyte flow rate on response characteristics during micro drilling of hybrid Al/(Al_2O_3p+SiCp+Cp)-MMC. From Figure 3.20, it is clear that the MRR increases with increase in electrolyte flow rate, however it is up to a certain limit e.g. 0.6 l/min of electrolyte flow rate. It is because of easy removal of sludge particles from the inter electrode gap. It was also noticed that the EWR and Ra (SR) decrease with increase in electrolyte flow rate. The high electrolyte flow pressure also introduces vibration, which in turn increases surface roughness height. From Figure 3.20, it is clear that the over cut, taper cut, and micro spark affected zone increase with increase in electrolyte flow rate. At high-pressure of electrolyte flow, the micro tool starts to vibrate and thereby increases the area of metal removal around the tool. It leads to increase the over cut, taper cut, and micro spark affected zone.

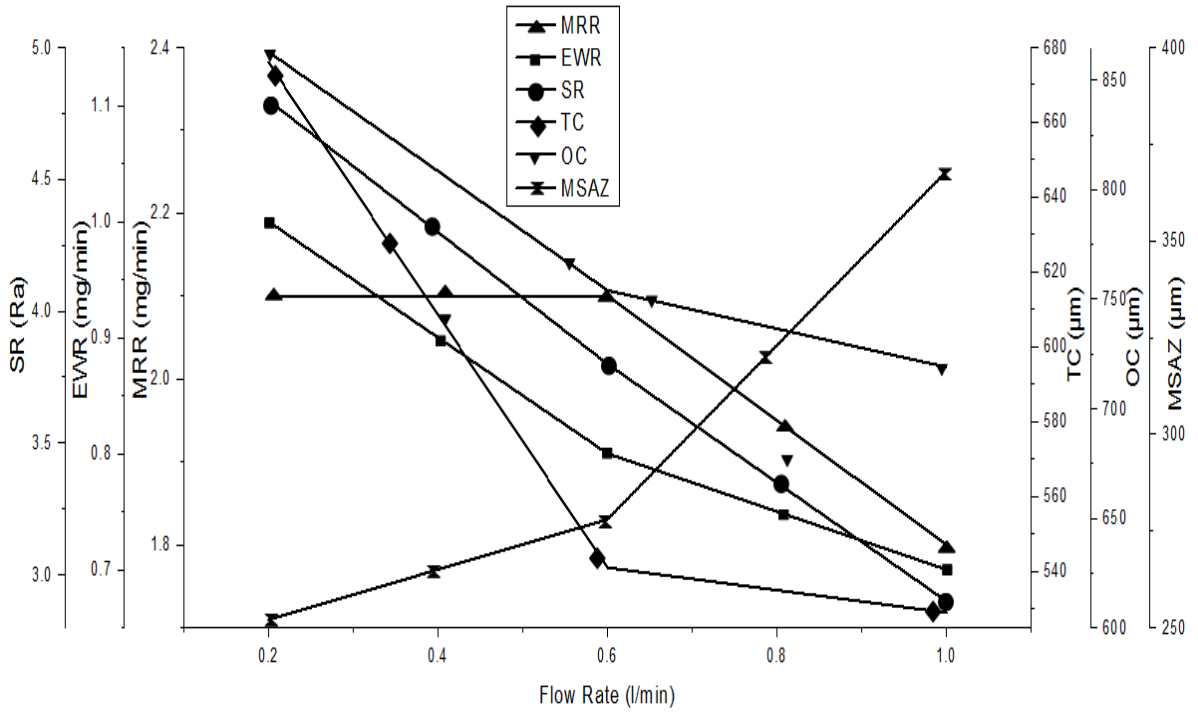

Fig 3.20 Influences of Electrolyte Flow Rate on Response Characteristics

Fig 3.21 Micro Drill Holes Machined on ECMM

Figures 3.21 (a) and Figure 3.21 (b) show the micro holes which are machining on hybrid metal matrix composite by fabricated ECMM setup. Micro hole as shown in Figure 3.21 (a) represents the result of machining at parameters setting i.e. at 1 Amp supply current, 10 V DC supply, 5 µs pulse on, 5 µs pulse off, 15 g/*l* consternation of NaCl electrolyte, 0.4 *l*/min electrolyte flow rate. Micro hole as shown in Figure 3.21 (b) represents the result of machining at parameters setting i.e. at 0.5 Amp supply current, 10 V DC supply, 5 µs pulse on, 5 µs pulse off, 15 g/*l* consternation of NaCl electrolyte, 0.4 *l*/min electrolyte flow rate.

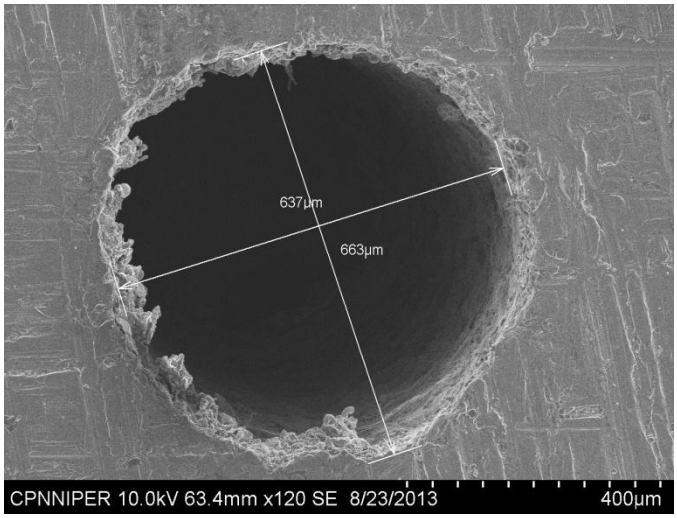

Fig 3.22 SEM Micro-Graph of Micro Hole Produced with 1 Amp Supply Current

Figure 3.22 shows SEM photograph of a micro hole generated at 1 Amp supply current, 10 V DC supply, 5 µs pulse on, 5 µs pulse off, 15 g/*l* consternation of NaCl electrolyte, 0.4 *l*/min electrolyte flow rate. This SEM photograph shows the non-circular micro-hole, it is due to not clean the removed particles from the micro hole surface during machining.

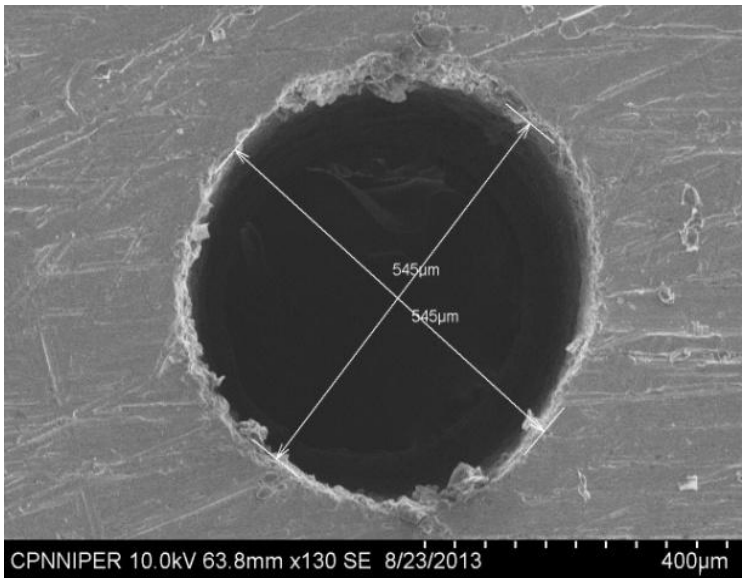

Fig 3.23 SEM Micro-Graph of Micro Hole Produced with 0.5 Amp Supply Current

Figure 3.23 shows SEM photograph of a micro hole generated at 0.5 Amp supply current, 10 V DC supply, 5 µs pulse on, 5 µs pulse off, 15 g/*l* consternation of NaCl electrolyte, 0.4 *l*/min electrolyte flow rate. This SEM photograph shows the better machined circular micro-hole as compared to the micro hole is shown in Figure 3.22.

3.9 CONCLUSION BASED ON FEASIBILITY TESTS RESULTS

From the feasibility tests results, it is clear that this fabricated ECMM setup can be effectively used for machining of hybrid metal matrix composite in micro domain. The effective parameters of the fabricated ECMM setup and their ranges were identified through

this feasibility tests. The developed ECMM setup parameters, their lower and upper limits were identified based on the analysis of the test results acquired during feasibility tests and explained in Table 3.4.

Table 3.4 Range of Process Parameter

Parameters	Symbol	Units	Lower Limit	Upper Limit
Supply Voltage	V	v	2	25
Electrolyte Concentration	EC	(g/*l*)	5	25
Pulse ON Time	Ton	µs	0.5	10
Electrolyte Flow rate	FR	*l*/min	0.2	1

3.10 PLANNING FOR DETAIL EXPERIMENTS

To perform the detail experimental investigation, it is important to make effective planning before carrying out the experiments. The selection of research methodology including planning of experimentation, design of set-up, construction of set-up, fabrication of workpiece specimens from the cast metal matrix composites are utmost important before carrying out the detail experiments and optimization of the process parameters. Keeping in view, a planning was done for detail experiments and analysis the experimental results. The Taguchi method based design of experiments, Response surface methodology, were employed and made out a plan as explained in the successive articles.

3.10.1 Planning for Experimentation as per Taguchi Design of Experiments

The developed ECMM setup and sodium nitrate as electrolyte were used for machining of Al/(Al_2O_3p+SiCp+Cp)-MMC. Based on the feasibility experiments and review of literature sodium nitrate was selected as electrolyte, as it give better machining precision as described by Bhattacharyya et al. (2002) and carried out the detail experiments as per planned as explained in Article 3.10.

The following parameters of developed ECMM setup as explained in Table 3.5 were considered for analyzing the micro machining performance criteria e.g. electrode wear rate, material removal rate, taper cut, over cut, surface roughness and micro spark affected zone. Experiments were carried out based on Taguchi method based design of experiment, $L_{27}(3^{13})$ orthogonal array. The factors were studied and their levels were chosen is represented in Table 3.5.

Table 3.5 ECMM Parameters and Their Levels (for Taguchi)

S. No	Input Parameters	Units	Levels		
			1	2	3
1.	Supply Voltage	v	2	13	25
2.	Electrolyte Concentration	(g/*l*)	5	10	25
3.	Pulse ON Time	µs	0.5	5	10
4.	Electrolyte Flow rate	*l*/min	0.2	0.6	1

Table 3.6 format for L_{27} (3^{13}) orthogonal array has been used for conducting the detail experiments and utilized the acquired results for optimization of ECMM setup parameters as explained in the next Chapter 4.

Table 3.6 L_{27} (3^{13}) Orthogonal Array

Experiment No.	Supply Voltage (V)	Electrolyte Concentration (g/*l*)	Pulse ON Time (µs)	Electrolyte Flow rate (*l*/min)
1.	2	5	0.5	0.2
2.	2	5	5.5	0.2
3.	2	5	10.0	0.2
4.	2	15	0.5	0.6
5.	2	15	5.5	0.6
6.	2	15	10.0	0.6
7.	2	25	0.5	1.0
8.	2	25	5.5	1.0
9.	2	25	10.0	1.0
10.	13	5	0.5	1.0
11.	13	5	5.5	1.0
12.	13	5	10.0	1.0
13.	13	15	0.5	0.2
14.	13	15	5.5	0.2
15.	13	15	10.0	0.2
16.	13	25	0.5	0.6
17.	13	25	5.5	0.6
18.	13	25	10.0	0.6
19.	25	5	0.5	0.6
20.	25	5	5.5	0.6
21.	25	5	10.0	0.6
22.	25	15	0.5	1.0
23.	25	15	5.5	1.0
24.	25	15	10.0	1.0
25.	25	25	0.5	0.2
26.	25	25	5.5	0.2
27.	25	25	10.0	0.2

Twenty-seven experiments were carried out (each experiment is repeated three times) on the fabricated ECMM setup to identify the effect of process parameters on various responses. The experiments were designed based on L_{27} orthogonal array with varying the different parameters at constant electrolyte temperature range i.e. 20^0-24^0 with tungsten micro tool i.e. electrode. The accuracy of the generated micro hole directly depends upon the design of the fabricated micro tool. Tool design includes the tool shape, which is a perfectly negative mirror image of the hole to be drilled on the workpiece. The tools used for ECMM must have high electrical and thermal conductive, high resistance to corrosion and wear, high stiffness to withstand the electrolyte flow pressure as well as the tool material must have very good machinability. Tungsten having high rigidity, toughness and melting point was used as tool electrode for micro ECM. The fabricated micro tool having 298 µm diameter x 8.10 mm long was used for detail experiments.

The work-piece specimens (size: 10 mm x 10 mm x 2 mm each) were prepared from stir cast hybrid Al/(Al_2O_3p+SiCp+Cp)-MMC samples by shaping and surface grinding operations. The different sets of experiments were carried out with varying machining parameters to investigate the influence of ECMM process parameters on various response characteristics such as material removal rate (MRR), surface roughness heights (SR), electrode wear rate (EWR), and taper cut (TC) and explained in the Chapter 4

3. 10.2 Planning for Experimentation as per Box-Behnken Design

In order to reduce the number of experiments to a reasonable number, Box–Behnken design was used to investigate the effect of six parameters on various response characteristics. The acquired test results were analysed based on response surface methodology (RSM). Response surface methodology is a collection of mathematical and statistical techniques that employ regression analysis to provide a relationship between the input process parameters and output performance based on experimental results. Finally, the analysis was done to study the main effects and their interactions to explore the quadratic effects of the influence of parameters on the performances. Table 3.7 represents the scheme of Box–Behnken design. All experiments were performed with three replications. Table 3.8 represents the RSM based design of experiments and average test results for various responses.

Table 3.7 Box–Behnken Design

Factors	M	No. of Blocks	Factorials Pts. Per block	Total with 1 centre point
6	3	6	8	49

Table 3.8 Design of Experiments

S.N	IP (Amp)	V (v)	Ton (µs)	Toff (µs)	EC (g/l)	FR (l/min)
1.	1.5	13	5.5	5.5	15	0.6
2.	0.5	2	5.5	0.5	15	0.6
3.	1.5	25	5.5	5.5	5	0.2
4.	1.5	13	0.5	10.0	15	1.0
5.	1.5	13	10.0	10.0	15	0.2
6.	3.0	2	5.5	0.5	15	0.6
7.	0.5	13	0.5	5.5	15	0.2
8.	1.5	2	5.5	5.5	25	0.2
9.	3.0	25	5.5	10.0	15	0.6
10.	0.5	13	5.5	10.0	25	0.6
11.	1.5	2	5.5	5.5	5	0.2
12.	0.5	13	10.0	5.5	15	1.0
13.	3.0	13	0.5	5.5	15	1.0
14.	1.5	25	0.5	5.5	25	0.6
15.	0.5	13	0.5	5.5	15	1.0
16.	1.5	25	5.5	5.5	5	1.0
17.	1.5	2	5.5	5.5	25	1.0
18.	1.5	13	0.5	0.5	15	1.0
19.	1.5	25	5.5	5.5	25	0.2
20.	3.0	13	10.0	5.5	15	1.0
21.	1.5	2	5.5	5.5	5	1.0
22.	0.5	13	10.0	5.5	15	0.2
23.	1.5	25	0.5	5.5	5	0.6
24.	1.5	25	10.0	5.5	25	0.6
25.	1.5	25	5.5	5.5	25	1.0
26.	0.5	25	5.5	10.0	15	0.6
27.	1.5	2	10.0	5.5	25	0.6
28.	1.5	13	10.0	10.0	15	1.0
29.	3.0	13	5.5	0.5	25	0.6
30.	1.5	25	10.0	5.5	5	0.6
31.	3.0	25	5.5	0.5	15	0.6

S.N	IP (Amp)	V (v)	Ton (µs)	Toff (µs)	EC (g/l)	FR (l/min)
32.	1.5	13	10.0	0.5	15	1.0
33.	1.5	13	0.5	0.5	15	0.2
34.	0.5	13	5.5	10.0	5	0.6
35.	1.5	13	10.0	0.5	15	0.2
36.	1.5	13	0.5	10.0	15	0.2
37.	0.5	2	5.5	10.0	15	0.6
38.	1.5	2	0.5	5.5	5	0.6
39.	3.0	13	0.5	5.5	15	0.2
40.	3.0	13	5.5	0.5	5	0.6
41.	0.5	13	5.5	0.5	25	0.6
42.	3.0	2	5.5	10.0	15	0.6
43.	1.5	2	0.5	5.5	25	0.6
44.	0.5	25	5.5	0.5	15	0.6
45.	3.0	13	5.5	10.0	5	0.6
46.	3.0	13	10.0	5.5	15	0.2
47.	1.5	2	10.0	5.5	5	0.6
48.	3.0	13	5.5	10.0	25	0.6
49.	0.5	13	5.5	0.5	5	0.6

Summary

An electrochemical micro machining (ECMM) set-up is indigenously designed and fabricated for experimental investigation. The various components and parts were used to fabricate the ECMM set-up and their fabrication processes were also explained in the chapter. The feasibility tests were carried out on the fabricated set-up during micro drilling of hybrid Al/(Al_2O_3p+SiCp+Cp)-MMC. A complete planned was done for feasibility study to identify the suitability of the developed ECMM set-up for machining of hybrid Al-MMC specimens. The feasibility test results reveals that the fabricated ECMM set-up can be effectively used for machining of Al/(Al_2O_3p+SiCp+Cp)-MMC in micron domain. Acquired results from the feasibility experiments also directly helped to identify the process parameters which affect the response characteristics such as material removal rate (MRR), electrode wear rate (EWR), surface roughness heights (R_a), taper cut, over cut and micro spark affected zone. In this chapter also explained the planned for carrying out the different sets of experiments to

achieve the objective of research investigation. Taguchi's methods based design of experiments, L_{27} (3^{13}) orthogonal array and response surface methodology (RSM) Box–Behnken design were employed and made out the experimental planned accordingly. Acquired results were analyzed for ANOVA and S/N Ratio to identify the significant process parameters which affect the output performance characteristics and optimize the process parameters for better surface finish with higher MRR and lower EWR respectively during micro drilling of hybrid Al-MMC and explained all these in the successive chapter 4.

Chapter 4

DETAIL EXPERIMENTATIONS, RESULTS AND DISCUSSION

Introduction

This chapter presents the detailed experimental investigation during micro drilling of hybrid Al/(Al_2O_3p+SiCp+Cp)-MMC on developed electrochemical micro machining (ECMM) set-up based on Taguchi's design of experiments, L_{27} (3^{13}) orthogonal array and response surface methodology (RSM) Box–Behnken design method. The experiments were carried out in two stages. In the first stage, feasibility experiments were carried out to check the suitability of the fabricated ECMM set-up for machining of Al-MMCs in micro domain as discussed in chapter 3. In the second stage, detailed experiments were carried out and explained in this chapter. The planning for detail experiments was described in previous chapter 3. The results acquired from the detailed experiments were utilized to construct the Analysis of variance (ANOVA) table to identify the most significant parameters affecting the micro machining performance criteria i.e. electrode wear rate, material removal rate, taper and the surface roughness height, R_a(µm). The main purpose of the ANOVA is to investigate the design parameters and to indicate the parameters that significantly affect the quality characteristics. The effects of different parameters of ECMM set-up on micro machining performance characteristics are explained briefly through various graphs in this chapter. The optimal parametric setting value will help to set the parameters for better perforce characteristics. However, a brief discussion on micro machined surface texture is very important to fulfil the basic aim of this research investigation. Keeping this in view, the current chapter also presents the various SEM photographs of machined surface of hybrid Al-MMC. The selected machined surfaces were analysed through SEM, EDX and XRD and are explained in this chapter.

4.1 EXPERIMENTAL RESULTS AND DISCUSSION

The detailed experiments were carried out based on Taguchi design of experiment L_{27} (3^{13}) orthogonal array and Response Surface Methodology (RSM). The developed ECMM setup parameters such as supply voltage (V), electrolyte concentration (g/l), pulse on time (µs), electrolyte flow rate (l/min) and their level (as explained in Table 3.5, Chapter 3) considered for detail experimentation based on Taguchi design of experiment. Table 4.1 represents Taguchi method based L_{27} (3^{13}) orthogonal array and experimental results. The machining response criteria such as electrode wear rate, material removal rate, taper effect and surface roughness heights were considered for analysis.

Taguchi method, a powerful tool in the design of experiment, is used to optimize the micro electrochemical machining (ECMM) parameters for effective machining of hybrid Al/(Al_2O_3p+SiCp+Cp)-MMC.

Table 4.1 Taguchi Method Based L_{27} (3^{13}) Orthogonal Array and Experimental Results

S. NO	V (V)	EC (g/*l*)	Ton (µs)	FR (*l*/min)	MRR (mg/min)	EWR (mg/min)	SR (Ra)	TC (µm)
1.	2	5	0.5	0.2	1.058	0.487	1.12	288
2.	2	5	5.5	0.2	0.979	0.437	1.01	245
3.	2	5	10.0	0.2	2.059	1.078	4.19	523
4.	2	15	0.5	0.6	0.137	0.068	6.94	736
5.	2	15	5.5	0.6	1.402	0.818	4.92	525
6.	2	15	10.0	0.6	1.168	0.846	4.35	586
7.	2	25	0.5	1.0	0.330	0.169	3.16	435
8.	2	25	5.5	1.0	2.546	1.276	5.43	635
9.	2	25	10.0	1.0	4.150	1.883	7.08	842
10.	13	5	0.5	1.0	1.916	0.764	4.72	512
11.	13	5	5.5	1.0	2.456	1.258	5.11	635
12.	13	5	10.0	1.0	2.426	1.349	5.43	626
13.	13	15	0.5	0.2	2.364	1.844	5.24	631
14.	13	15	5.5	0.2	2.685	1.288	5.32	678
15.	13	15	10.0	0.2	2.364	1.153	5.87	688
16.	13	25	0.5	0.6	4.364	2.419	7.31	845
17.	13	25	5.5	0.6	5.352	2.914	8.15	879
18.	13	25	10.0	0.6	5.456	2.554	8.21	912
19.	25	5	0.5	0.6	2.916	1.524	5.72	635
20.	25	5	5.5	0.6	3.726	1.824	7.58	812
21.	25	5	10.0	0.6	4.231	2.187	7.02	795
22.	25	15	0.5	1.0	2.203	1.587	5.12	635
23.	25	15	5.5	1.0	4.236	2.214	7.51	865
24.	25	15	10.0	1.0	8.923	3.244	9.41	1069
25.	25	25	0.5	0.2	4.136	2.204	7.25	861
26.	25	25	5.5	0.2	5.481	2.535	8.20	945
27.	25	25	10.0	0.2	6.235	3.646	8.39	988

4.1.1 Effect of ECMM Parameters on MRR

The material removal rate (MRR) was determined from the difference of work piece weight before and after each set of machining operations. Figure 4.1(a) shows the S/N ratio (dB) curve by factor level of supply voltage (V) for material removal rate (MRR). From Figure 4.1 (a), it is clear that there is increase in MRR with increase in supply voltage from 2V to 13V. The MRR again increases with increase in supply voltage from 13 V to 25V. The results, plotted in Figure 4.1(a), satisfy the Faraday's effect. As it is stated that the supply current increases with increase in supply voltage, as a result increases dissolution efficiency. Hence, there is an increase in the electrolyte ionization with increase in supply voltage and which in turn

increases MRR. The size of micro holes increases with increase in supply voltage. Figure 4.1 (b) shows the S/N Ratio (dB) curve by factor level of electrolyte concentration for material removal rate (MRR). From graph Figure 4.1(b), it has clear that the S/N ratio for MRR initially decreases with increase in electrolyte concentration from 5 to 15 g/*l*. However, it further increases with increase in electrolyte concentration from 15 to 25 g/*l*. At higher concentration e.g. 25 (g/*l*) of electrolyte, a large number of ions are formed during machining, as a result there is an increase in machining current density which leads to increase the MRR. Figure 4.1 (c) shows the S/N Ratio (dB) curve by factor level of pulse on time for MRR. From graph Figure 4.1 (c), it is clear that the S/N ratio for MRR increases with increase in pulse on time. Dissolution efficiency increases as well with increase in pulse on time and thereby decreases actual machining time. Figure 4.1 (d) shows the S/N Ratio (dB) curve by factor level of flow rate of electrolyte for MRR. From graph Figure 4.1 (d), it is clear that the S/N ratio for MRR initially decreases with increase in flow rate of electrolyte from 0.2 l/min to 0.6 l/min, but further S/N ratio for MRR increases with increase in flow rate of electrolyte from 0.6 l/min to 1 l/min. It is because of easy removal of sludge particles from the inter electrode gap at 1.0 l/min electrolyte flow rate.

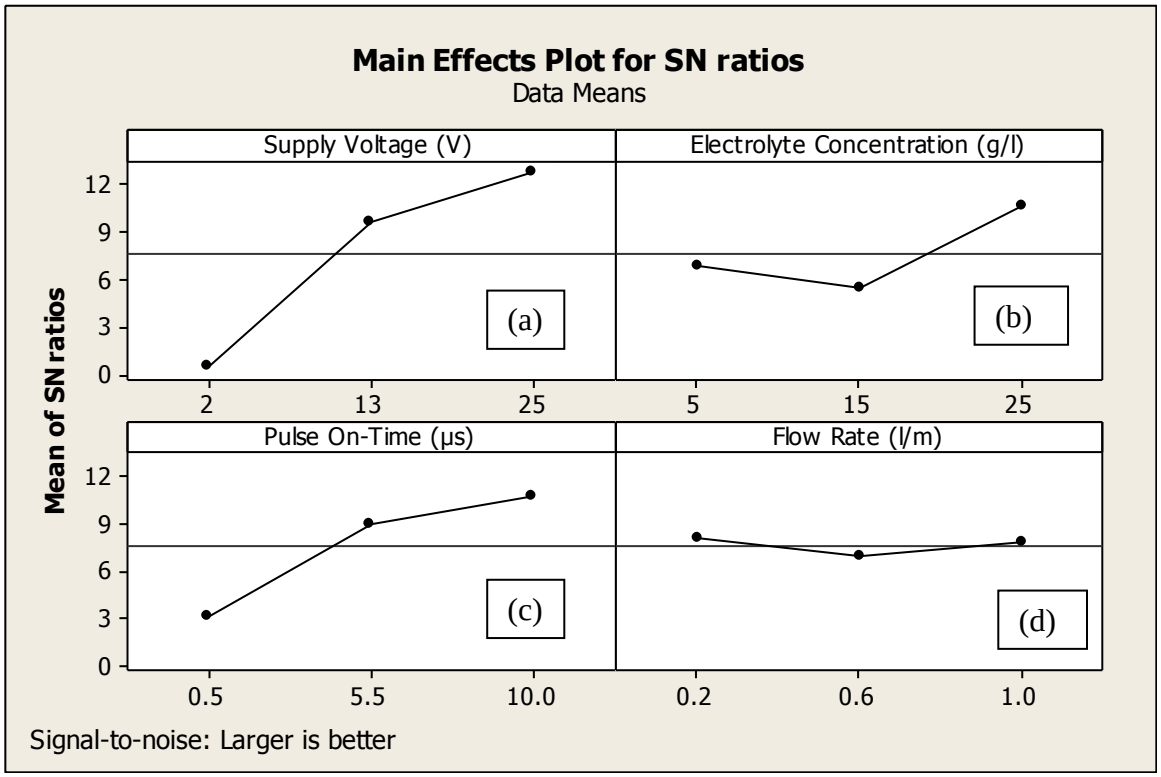

Fig. 4.1 S/N Ratio (dB) Graphs for MRR

Table 4.2 Parameter Wise S/N Ratio for MRR and Their Rank

Level	S/N ratio of Supply Voltage (V)	S/N ratio of Electrolyte Concentration (g/*l*)	S/N ratio of Pulse on-time (µs)	S/N ratio of Flow rate (*l*/min)
1	0.4939	6.7754	3.1112	8.1232
2	9.6423	5.4392	8.9514	6.9304
3	12.7405	10.6622	10.8141	7.8231
Delta	12.2466	5.2230	7.7029	1.1928
Rank	1	3	2	4

Table 4.2 represents the S/N ratio based ranking against each parameters of ECMM set-up for MRR. From Table 4.2, it is clear that for S/N ratio, supply voltage has a great effect on MRR. The flow rate has the least effect on MRR. Therefore, the parameter, supply voltage has 1st rank.

Table 4.3 ANOVA for MRR

Source	DF	Seq SS	Adj SS	Adj MS	F	P	%Contribution	Remarks
Supply Voltage (V)	2	49.512	49.512	24.756	49.314	0.000	47.53	Significant
Electrolyte Concentration (g/l)	2	21.181	21.181	10.59	20.80	0.013	20.33	Significant
Pulse On-Time (µs)	2	22.216	22.216	11.108	22.127	0.010	21.33	Significant
Flow Rate (l/min)	2	2.202	2.202	1.101	2.193	0.933	2.12	Non-Significant
Error	18	09.048	09.048	0.502			8.69	
Total	26	104.159						

R-Sq = 91.31%,

Table 4.3 represents the ANOVA and 'F test' values. The F-value for all the sources i.e. values of Prob >F less than 0.05, which indicates the model terms are significant at 95% confidence level. From ANOVA Table 4.3, it is clear that for MRR, the supply voltage, electrolyte concentration and pulse on-time are the significant model terms.

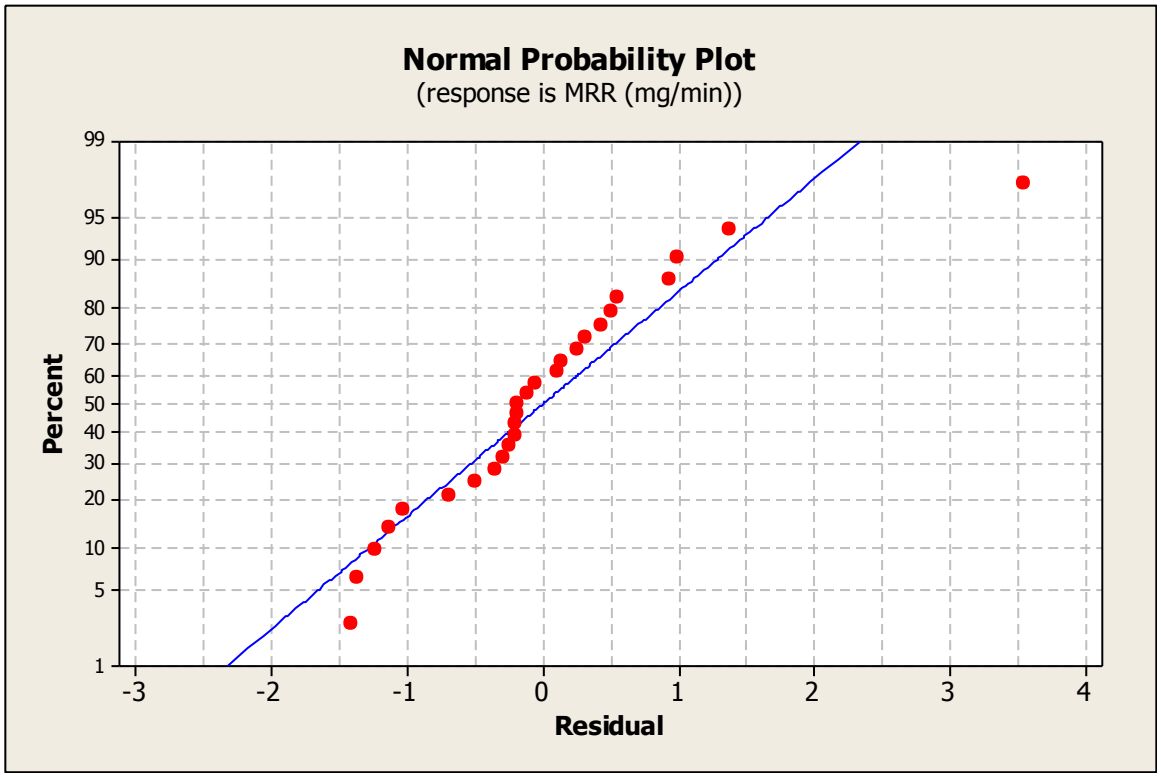

Fig 4.2 Normal Probability Plots for MRR

Figure 4.2 shows the normal probability plots for MRR. Most of residuals are found on a straight line which indicates that errors are normally distributed. This is the normality test to be qualified by the model for checking the model. From Figure 4.2, it has been found that models are significant.

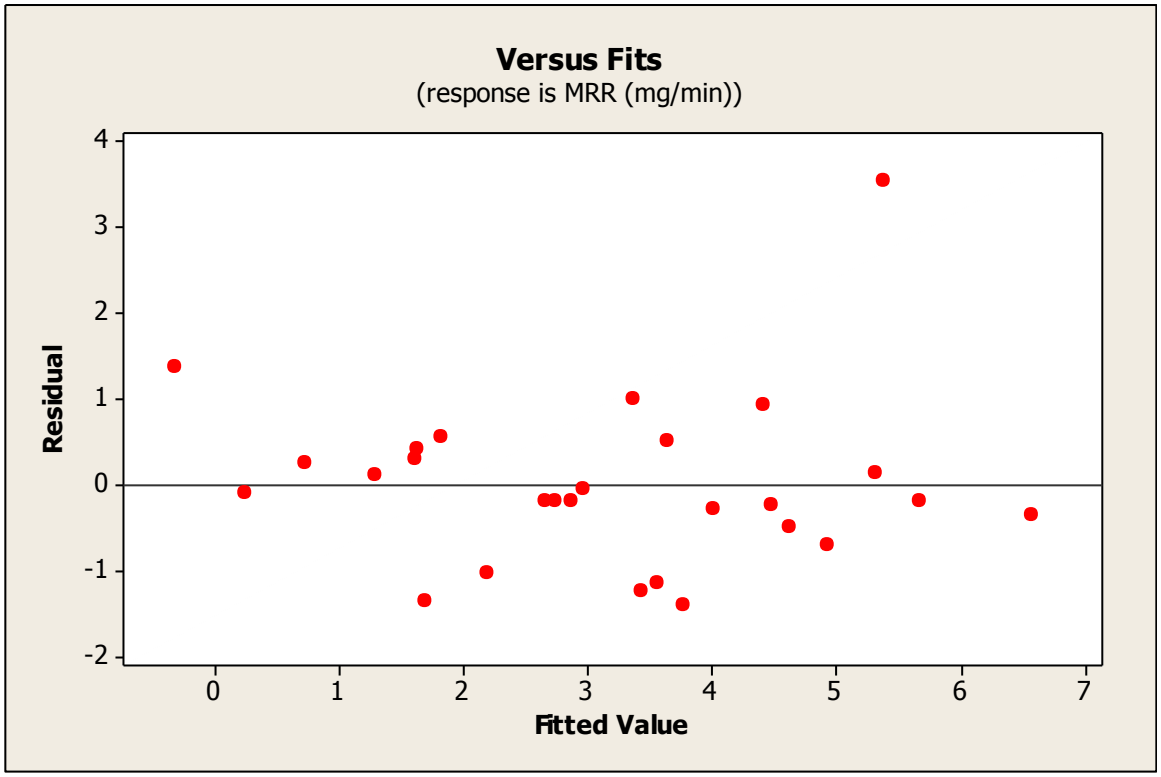

Fig 4.3 Residuals and Fitted Values for MRR

Figure 4.3 shows the residuals vs. fitted plot for material removal rate. The residuals are distributed randomly and are not clustered that indicates model is good.

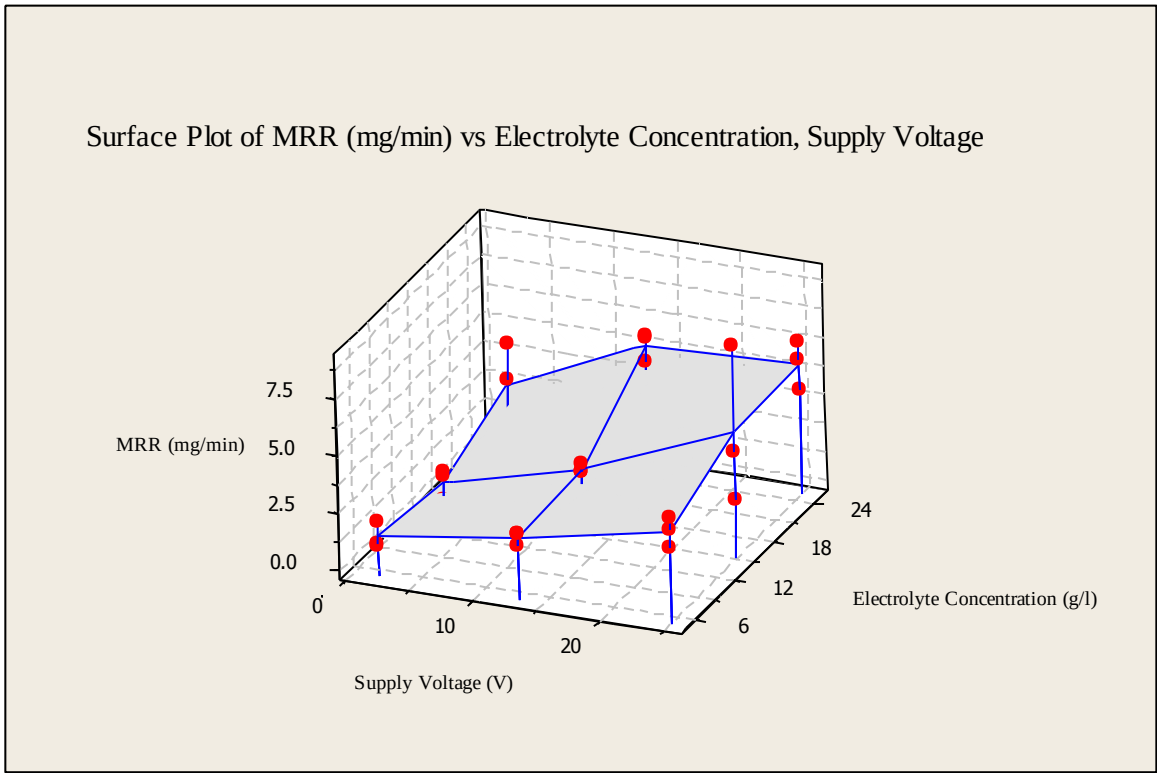

Fig 4.4 Interaction Effect of Supply Voltage and Electrolyte Concentration on MRR

Figure 4.4 shows interaction effect of supply voltage and electrolyte concentration on MRR. From this interaction plot Figure 4.4, it is clear that the MRR increases with increase in both ECMM parameters i.e. supply voltage and electrolyte concentration. With increase in supply voltage there is an increase in potential difference between cathode and anode, which intensively increases electrolyte ionization and current density, which in turn increases the MRR. Therefore, material removal rate increases with increase in dissolution efficiency; it is due to the increase of supply voltage. The MRR also increases with increase in the concentration of electrolyte. This is due to the increase in the conductance of the electrolyte with increase in electrolyte concentration. A large number of ions associated in the IEG at higher concentration of electrolyte results in an increase in the machining current and conductivity; thus increases the material removal rate.

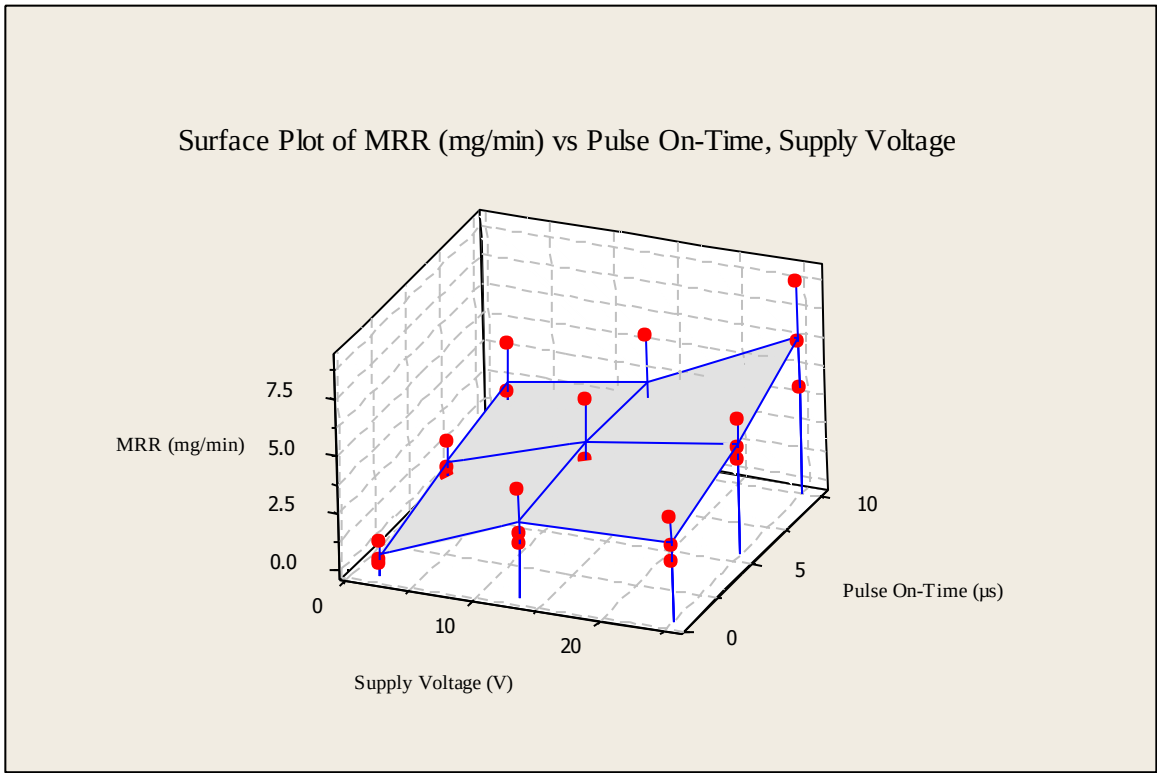

Fig 4.5 Interaction Effect of Supply Voltage and Pulse On Time on MRR

Figure 4.5 shows the interaction effect between pulse on time and supply voltage on MRR. From Figure 4.5, it is clear that the MRR increases with increase in both pulse-on-time and supply voltage. From this graph Figure 4.5, it is noticed that the MRR increases with increase in pulse on time. When the pulse on time is too short, material dissolution is negligible. With the supply of high pulse on time, both faradic current and period of faradic current increases, thereby the amount of faradic effects increases rapidly. The increase in pulse-on-time implies that greater time is allowed for machining and thereby increases dissolution efficiency. Hence, material removal rate is increased and machining time is decreased with increase in pulse-on-time.

Figure 4.6 shows the interaction effect of pulse on time and electrolyte concentration on MRR. From Figure 4.6, it is clear that the MRR increases with increase in both pulse-on-time and electrolyte concentration. From this graph Figure 4.6, it is noticed that the MRR increases with increase in pulse-on-time. When the pulse-on-time is too low, material dissolution is negligible. With the supply of high pulse-on-time, both faradic current and period of faradic current increases, at the same time the amount of faradic effects also increases. Enlarge in pulse on time implies that more time allowed for machining and thereby increases dissolution efficiency. Hence, MRR is increased and machining time decreased with increase in pulse-on-time.

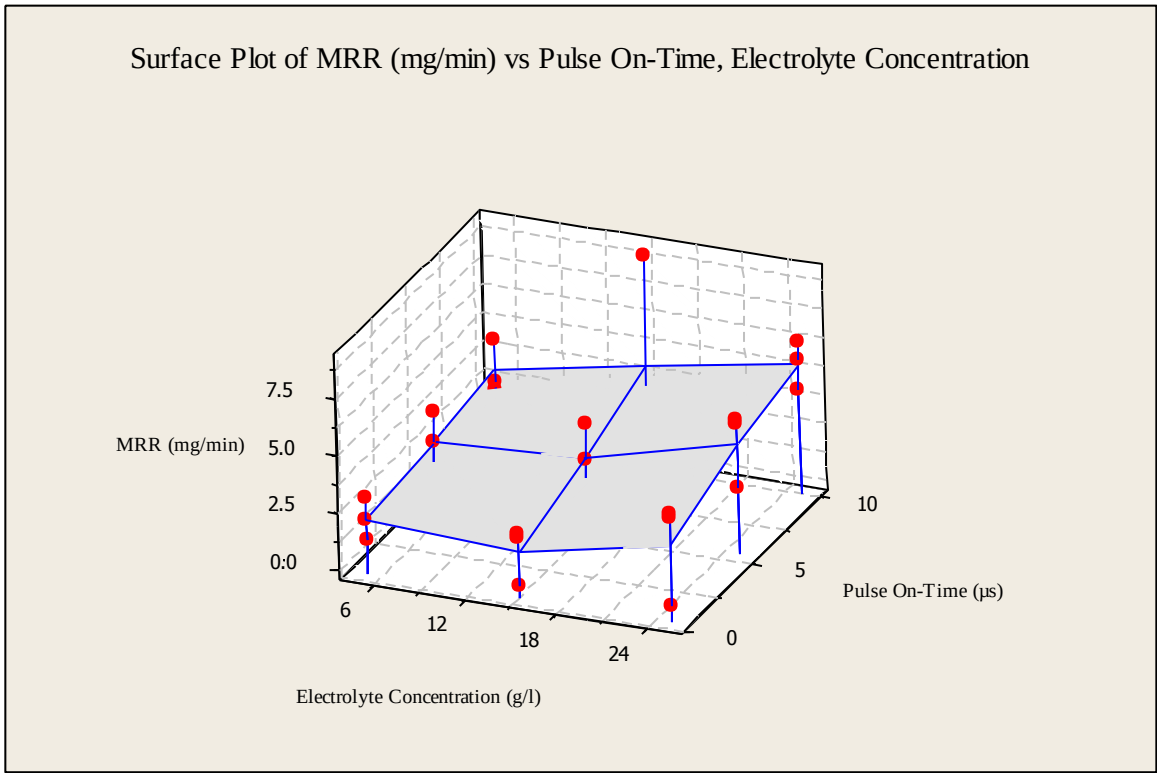

Fig 4.6 Interaction Effect of Electrolyte Concentration and Pulse On Time on MRR

4.1.2 Effect of ECMM Parameters on EWR

The term electrode wear rate (EWR) is the loss of electrode weight during micro drilling of hybrid MMC.

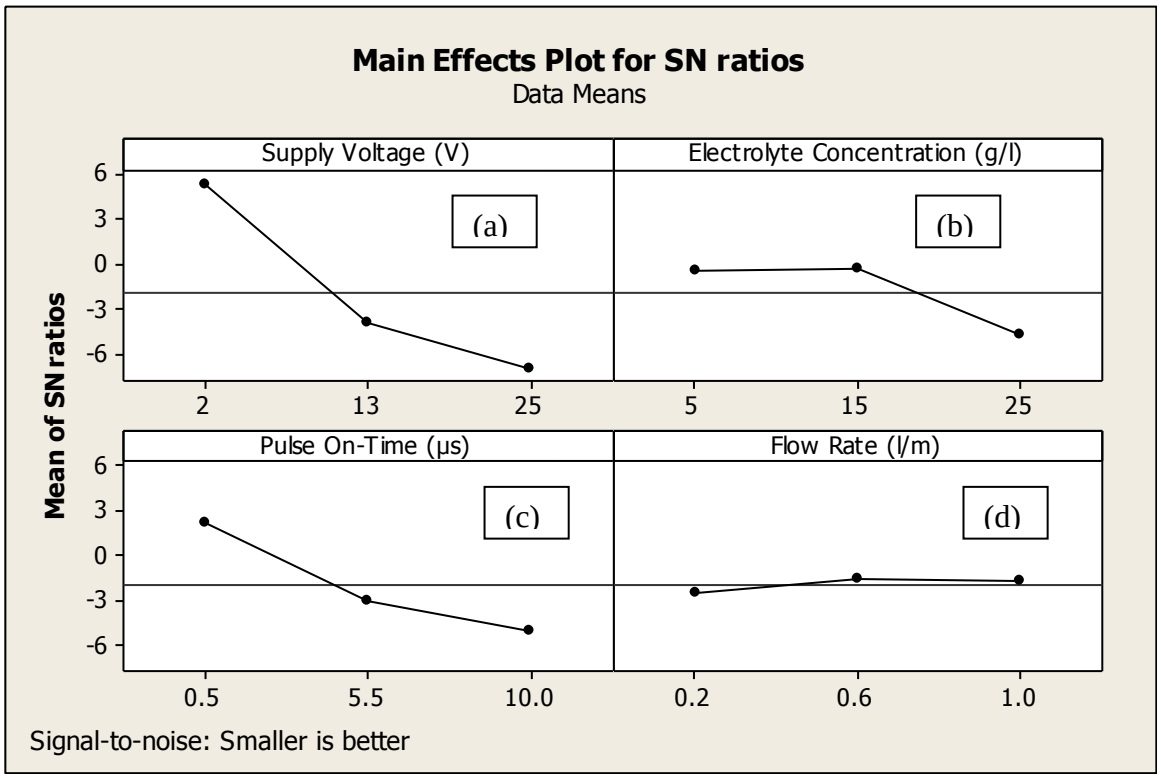

Fig 4.7 S/N Ratio (dB) Graphs for EWR

Figure 4.7 (a) shows the S/N ratio (dB) curve by factor level of supply voltage (V) for electrode wear rate (EWR). Graph is plotted by utilizing the EWR results obtained by variation of ECMM parameters i.e. variation supply voltage (V), electrolyte concentration (g/*l*), pulse on time (µs), and flow rate (l/min) on response factors i.e. electrode wear rate (EWR). It was observed that there is a decrease in S/N ratio for EWR with the increase of supply voltage. Figure 4.7 (b) shows the S/N Ratio (dB) curve by factor level of electrolyte concentration for electrode wear rate (EWR). From graph Figure 4.7 (b), it is observed that S/N ratio of EWR decreases with increase in electrolyte concentrations. At higher concentration i.e. 25 (g/*l*) of electrolyte, a large number of ions are formed during machining, as a result there is an increase in machining current density. It leads to increase the EWR. Figure 4.7 (c) shows the S/N Ratio (dB) curve by factor level of pulse on time for electrode wear rate (EWR). From graph Figure 4.7 (c), it is noticed that S/N ratio for EWR decreases with increase in pulse on time. Figure 4.7 (d) shows the S/N Ratio (dB) curve by factor level of flow rate of electrolyte for electrode wear rate (EWR). From graph Figure 4.7 (d), it is noticed that S/N ratios of EWR first increases slightly with increase in flow rate of electrolyte from 0.2 l/min to 0.6 l/min and by further increase in flow rate of electrolyte from 0.6 l/min to 1 l/min, the S/N ratio for EWR again slightly increases. It is because of easy removal of sludge particles from the inter electrode gap at 1.0 l/min flow rate.

Table 4.4 Parameter Wise S/N Ratio for EWR and Their Rank

Level	**S/N ratio of Supply Voltage (V)**	**S/N ratio of Electrolyte Concentration (g/*l*)**	**S/N ratio of Pulse on-time (µs)**	**S/N ratio of Flow rate (*l*/min)**
1	5.2403	-0.5717	2.2062	-2.4603
2	-4.0125	-0.3711	-2.9852	-1.5819
3	-6.9993	-4.8288	-4.9926	-1.7294
Delta	12.2397	4.4577	7.1988	0.8785
Rank	1	3	2	4

Table 4.4 represents the S/N ratio based ranking against each parameter of ECMM for EWR. From Table 4.4, it is clear that for signal to noise ratio (dB), supply voltage has a great effect on EWR. The flow rate has the least effect on EWR. Therefore, the parameter, supply voltage has 1st rank.

Table 4.5 ANOVA for EWR

Source	DF	Seq SS	Adj SS	Adj MS	F	P	%Contribution	Remarks
Supply Voltage (V)	2	11.4118	11.4118	5.7059	55.12	0.000	51.72	Significant
Electrolyte Concentration (g/l)	2	5.0532	5.0532	2.5266	24.41	0.001	22.89	Significant
Pulse On-Time (µs)	2	3.3254	3.3254	1.6627	16.06	0.009	15.07	Significant
Flow Rate (l/min)	2	0.4141	0.4141	0.2070	2.0	0.769	1.88	Non-Significant
Error	18	1.8627	1.8627	0.1035			8.44	
Total	26	22.0672						

R-Sq = 91.55%,

Table 4.5 represents the ANOVA and 'F test' values. The F-value for all the sources i.e. values of Prob >F less than 0.05, which indicates that the model terms are significant at 95% confidence level. From ANOVA Table 4.5, it is clear that for EWR the sources supply voltage, electrolyte concentration and pulse on-time significant model terms.

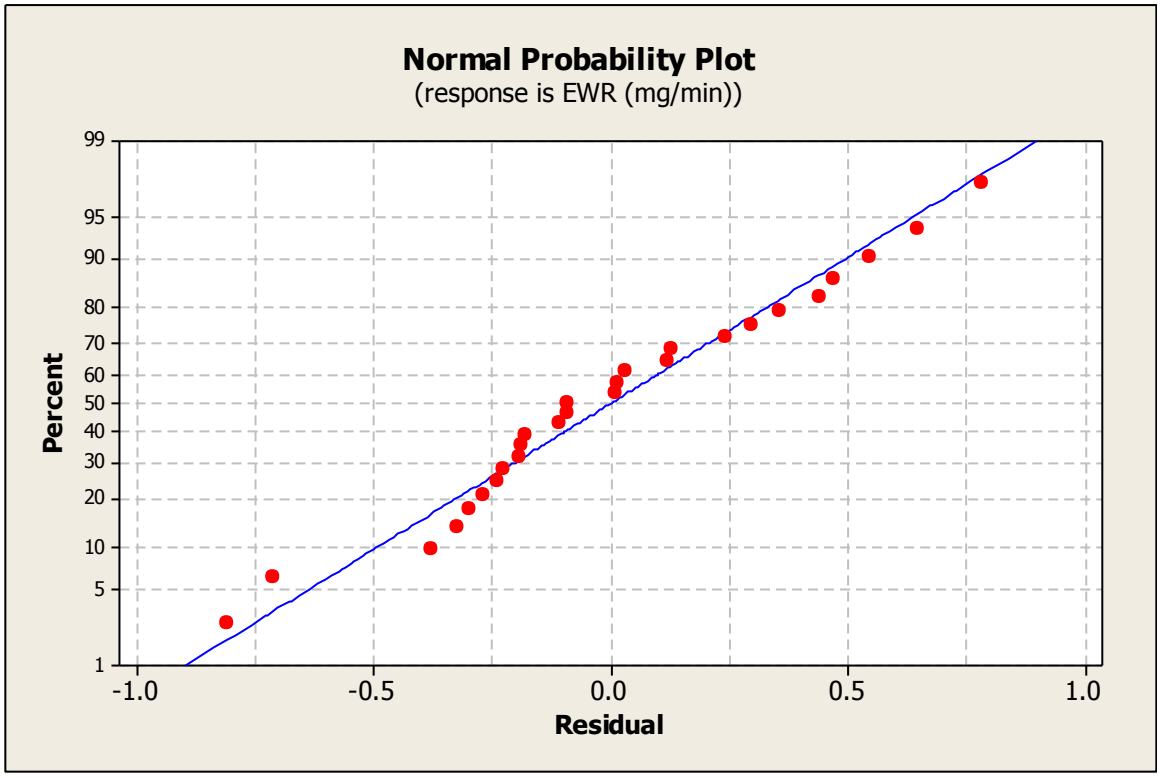

Fig 4.8 Normal Probability Plots for EWR

Figure 4.8 shows the normal probability plots for EWR. Most of residuals are found on a straight line which indicates that errors are normally distributed. This is the normality test to be

qualified by the model for its validation. From Figure 4.8, it has been found that models are significant.

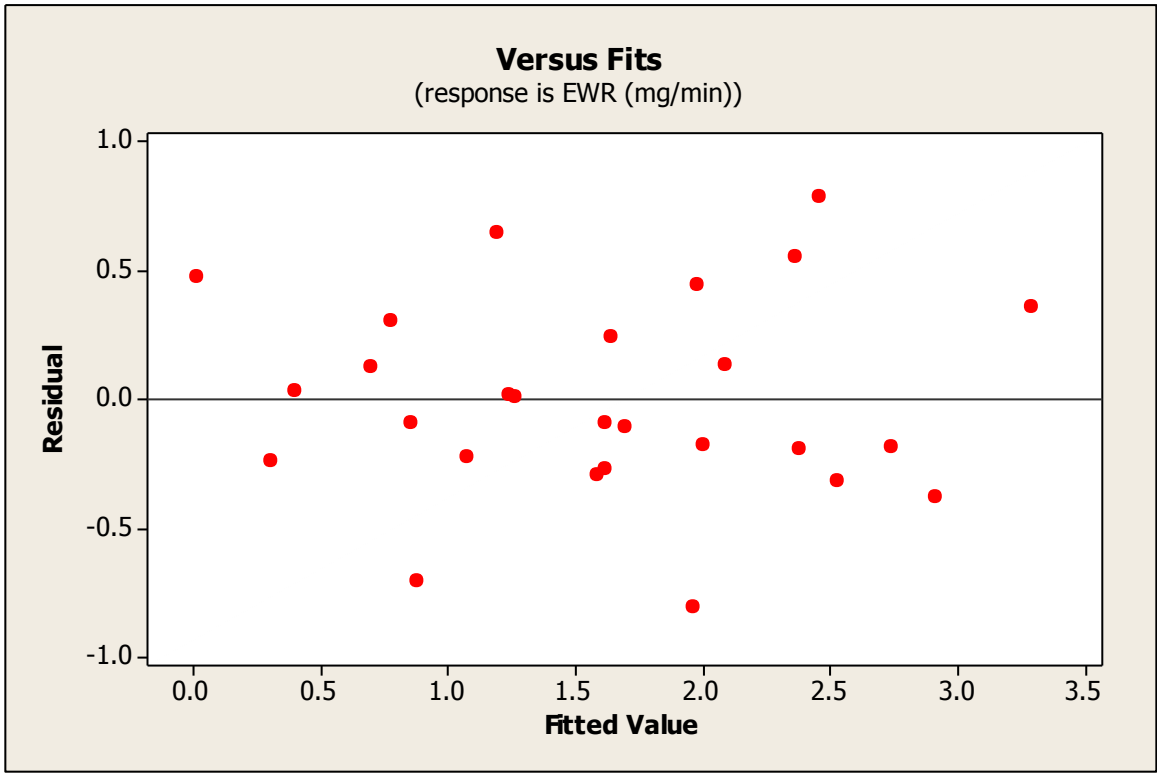

Fig 4.9 Residuals and Fitted Values for EWR

Figure 4.9 shows the residuals and fitted plot for electrode wear rate. The residuals are distributed randomly and are not clustered which indicates that model is good.

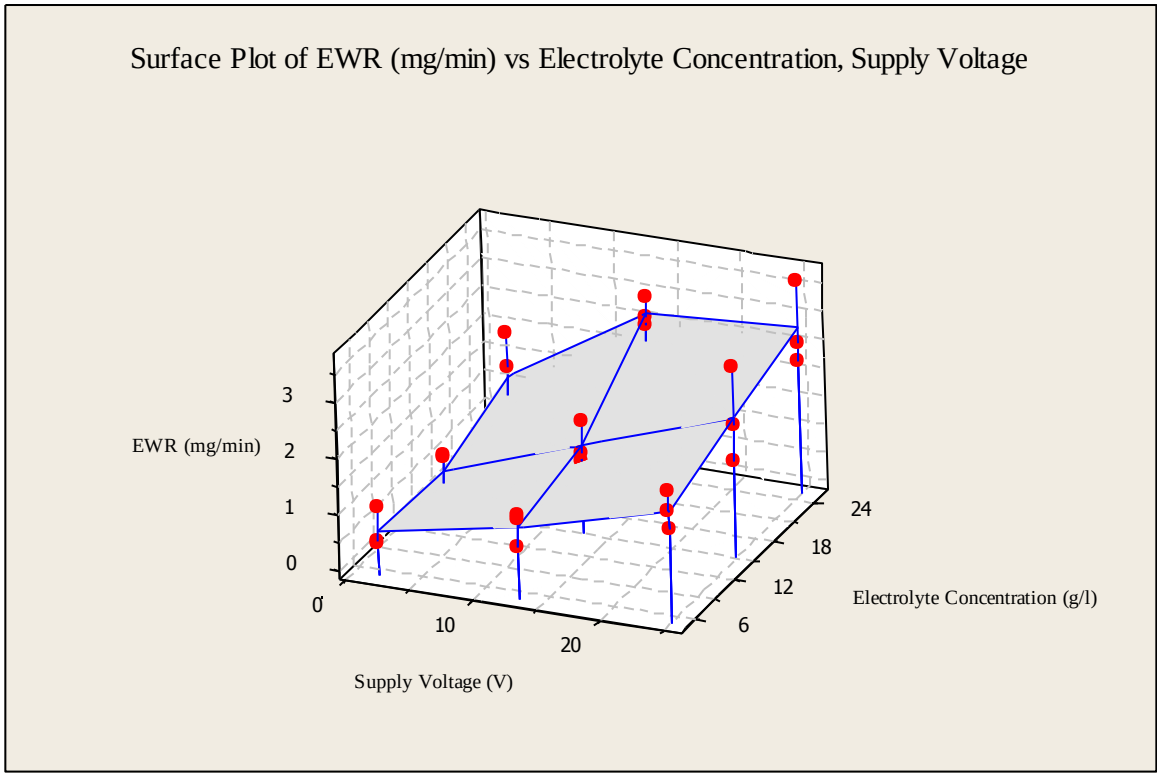

Fig 4.10 Interaction Effect of Supply Voltage and Electrolyte Concentration on EWR

Figure 4.10 shows interaction effect of supply voltage and electrolyte concentration on EWR. From the interaction graph Figure 4.10, it is clear that the EWR increases with increase in both ECMM parameters i.e. supply voltage and electrolyte concentration. With increase in supply voltage there is an increase in potential difference between cathode and anode, which intensively increases electrolyte ionization, and enhances more electrode wear. This is because of the increased number of the hydrogen gas bubbles at higher supply voltage, which gets entrapped in between electrode and workpiece surface at IEG. The presence of machined particles in the micro machining inter electrode gap may cause sparking, which may lead to electrode wear and decrease the machining accuracy. As the electrolyte concentration is increased, the reaction rate in the IEG increases proportionally. The electrolyte conductivity and current density increases due to poor agitation rate. This leads to non-uniform reaction on the surface of the electrode due to increase in the number of hydrogen gas bubbles generated at front end of the electrode, and hence, cylindrical length reduces with increase in electrolyte concentration.

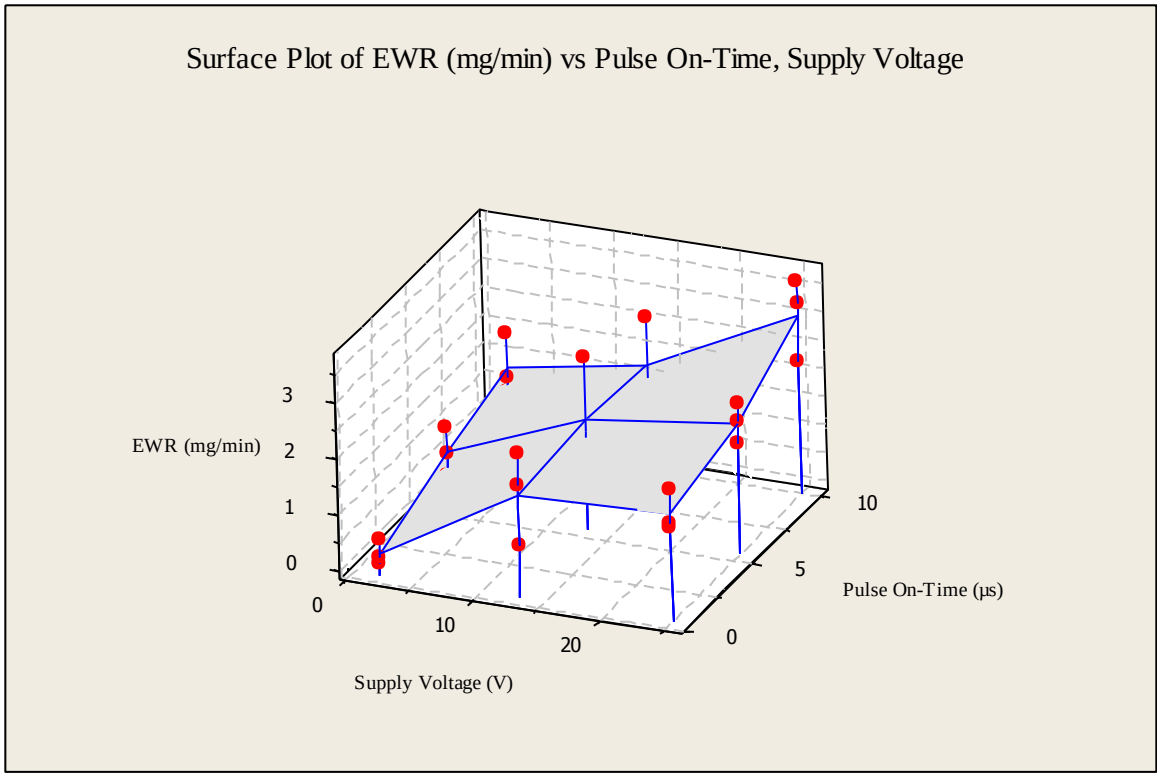

Fig 4.11 Interaction Effect of Supply Voltage and Pulse On Time on EWR

Figure 4.11 shows the interaction effects of pulse on time and supply voltage on EWR. It is clear that EWR increases with increase in both pulse-on-time and supply voltage. From Figure 4.11, it is noticed that the EWR rises with rise in pulse on time. With increase in the supply of pulse on time, both faradic current and period of faradic current increases, and there by the amount of faradic effects increases rapidly. Enlarge in pulse on time implies that more time

allowed for machining and thereby increases dissolution efficiency. Hence, more material dissolved from electrode.

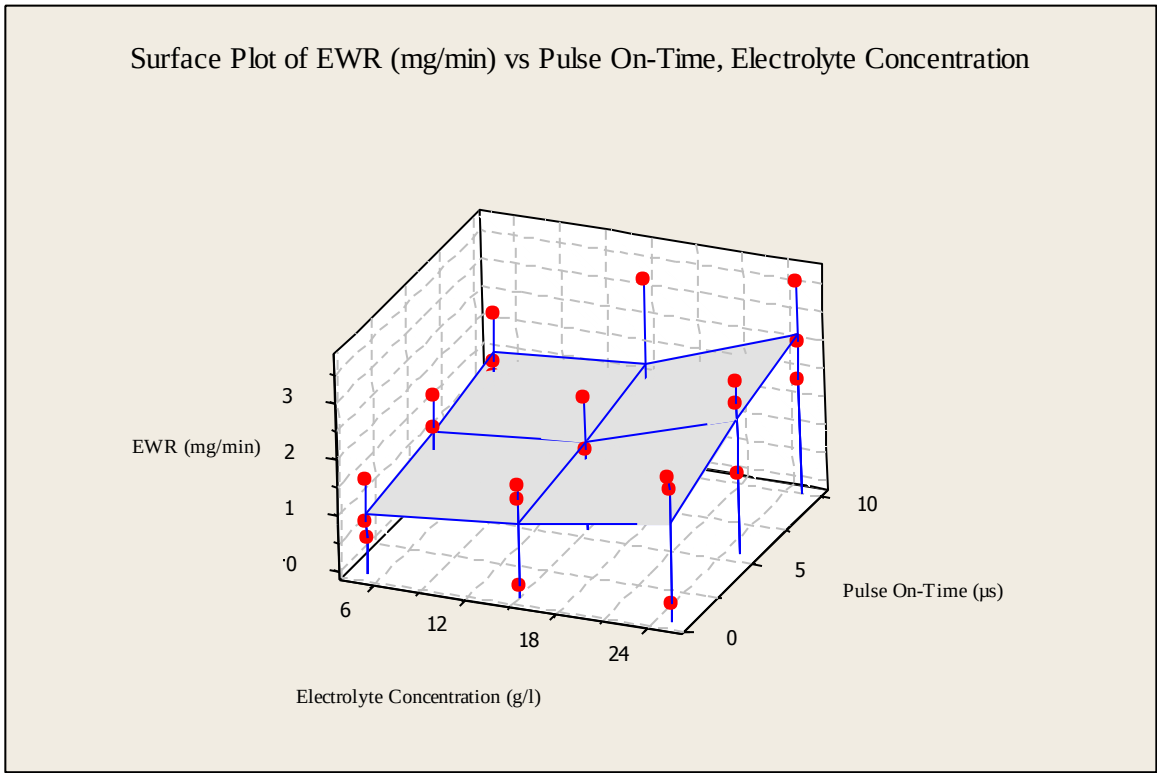

Fig 4.12 Interaction Effect of Electrolyte Concentration and Pulse On Time on EWR

Figure 4.12 shows the interaction effects of pulse on time and electrolyte concentration for EWR. It is clear that EWR increases with increase in both pulse-on-time and electrolyte concentration.

4.1.3 Effect of ECMM Parameters on Surface Roughness

The surface roughness height (Ra) was measured by Surfcom 130A surface roughness measuring instrument, the cut-off length 0.8 mm and evaluation length was 4 mm. Surface roughness height (Ra) has been measured by three times and average value of surface roughness height (Ra) taken for analysis.

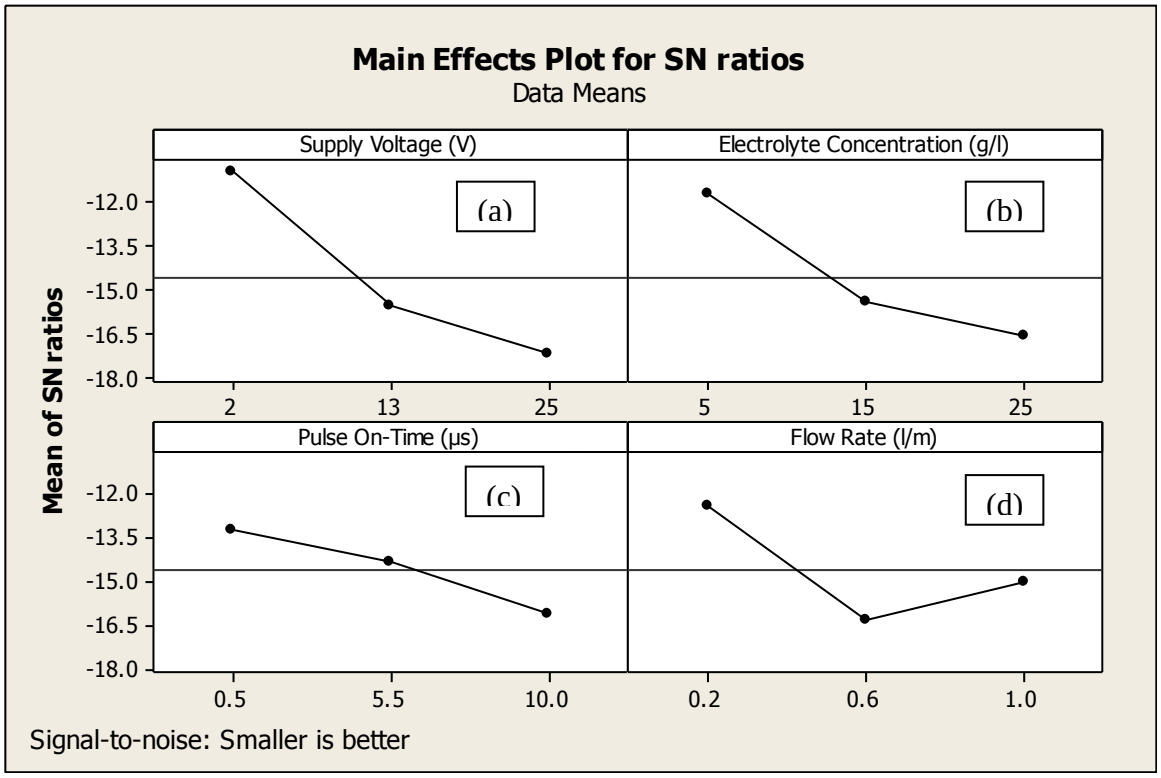

Fig 4.13 S/N Ratio (dB) Graphs for Surface Roughness Height, R_a (µm)

Figure 4.13 (a) shows the S/N ratios (dB) curve by factor level of supply voltage (V) for surface roughness height, R_a (SR). Graph plotted by utilizing the acquired results during experiments with variation of supply voltage (V), and from this curve it is clear that there is decrease in S/N ratio for SR with the increase of supply voltage. Figure 4.13 (b) shows the S/N Ratio (dB) curve by factor level of electrolyte concentration for surface roughness height, R_a (SR). From graph Figure 4.13 (b), it is noticed that the S/N ratio for SR decreases with increase in electrolyte concentrations. At higher concentration i.e. 25 (g/*l*) of electrolyte, a large number of ions are formed during machining, as a result there is an increase in machining current density. It leads to increase in the surface roughness. Figure 4.13 (c) shows the S/N Ratio (dB) curve by factor level of pulse on time for surface roughness height, R_a (SR). From curve Figure 4.13 (c), it is clear that S/N ratio of SR decreases by increase in pulse on time. Figure 4.13 (d) shows the S/N Ratios (dB) curve by factor level of flow rate of electrolyte for surface roughness height, R_a (SR). From curve Figure 4.13 (d), it is clear that S/N ratio of SR first decreases with increase in flow rate of electrolyte from 0.2 *l*/min to 0.6 *l*/min and by further increase in flow rate of electrolyte from 0.6 *l*/min to 1 *l*/min, the S/N ratio of SR increases. It is because of easy removal of sludge particles from the inter electrode gap at 1.0 *l*/min flow rate.

Table 4.6 Parameter Wise S/N Ratio for R_a(µm) and Their Rank

Level	S/N ratio of Supply Voltage (V)	S/N ratio of Electrolyte Concentration (g/*l*)	S/N ratio of Pulse on-time (µs)	S/N ratio of Flow rate (*l*/min)
1	-10.96	-11.73	-13.28	-12.42
2	-15.60	-15.43	-14.32	-16.32
3	-17.20	-16.60	-16.16	-15.02
Delta	6.24	4.88	2.88	3.90
Rank	1	2	4	3

Table 4.6 represents the S/N ratio based ranking against each parameters of ECMM for R_a(µm). From Table 4.6, it is clear that for S/N ratio by factor level of supply voltage has a greatest effect for R_a. The pulse on time has the least effect on SR. Therefore, the parameter, supply voltage has 1st rank.

Table 4.7 ANOVA for Surface Roughness Height, R_a (µm)

Source	DF	Seq SS	Adj SS	Adj MS	F	P	%Contribution	Remarks
Supply Voltage (V)	2	49.295	49.295	24.6475	42.04	0.000	44.18	Significant
Electrolyte Concentration (g/l)	2	29.497	29.497	14.7485	25.155	0.001	26.44	Significant
Pulse On-Time (µs)	2	10.931	10.931	5.4655	9.322	0.033	9.79	Significant
Flow Rate (l/min)	2	11.304	11.304	5.652	9.64	0.030	10.13	Significant
Error	18	10.554	10.554	0.5863			9.46	
Total	26	111.582						

R-Sq = 90.54%,

Table 4.7 shows the ANOVA and 'F test' values. The F-value for all the sources i.e. values of Prob >F less than 0.05, which indicates that the model terms are significant at 95% confidence level. From ANOVA table 4.7, it is clear that for R_a (µm) the sources supply voltage, electrolyte concentration, pulse on-time and flow rate are significant model terms.

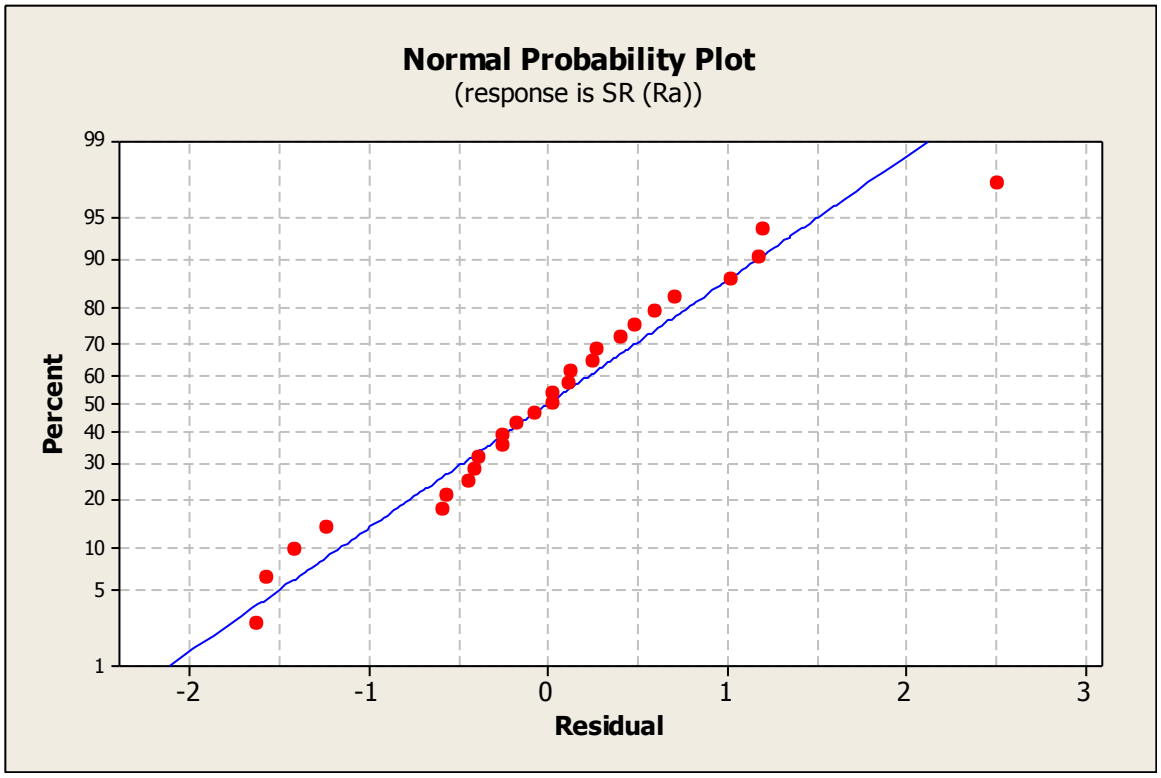

Fig 4.14 Normal Probability Plots for SR

Figure 4.14 show the normal probability plots for SR (R_a, µm). Most of the residuals are found on a straight line which indicates that errors are normally distributed. This is the normality test to be qualified by the model for checking the model. Form Figure 4.14, it has been found that models are significant.

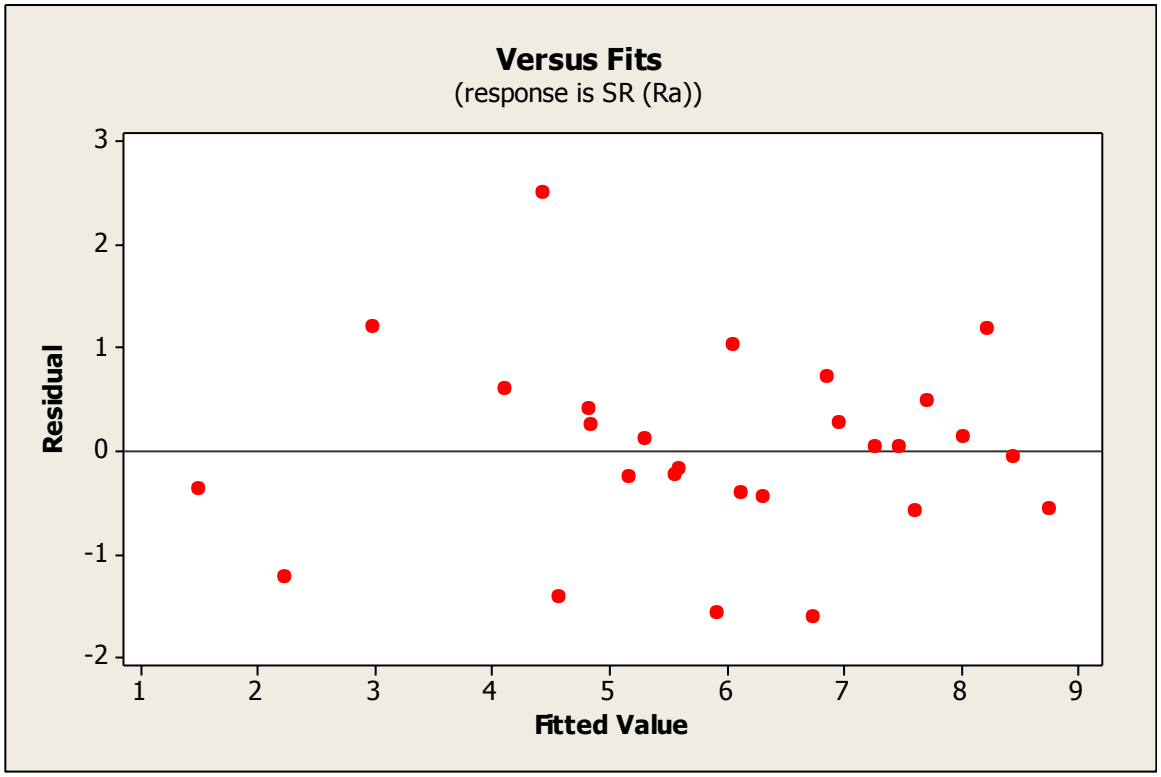

Fig 4.15 Residuals and Fitted Values for SR

Figure 4.15 shows the residuals and fitted values for surface roughness height, R_a(µm). The residuals are distributed randomly and are not clustered. This indicates a good model.

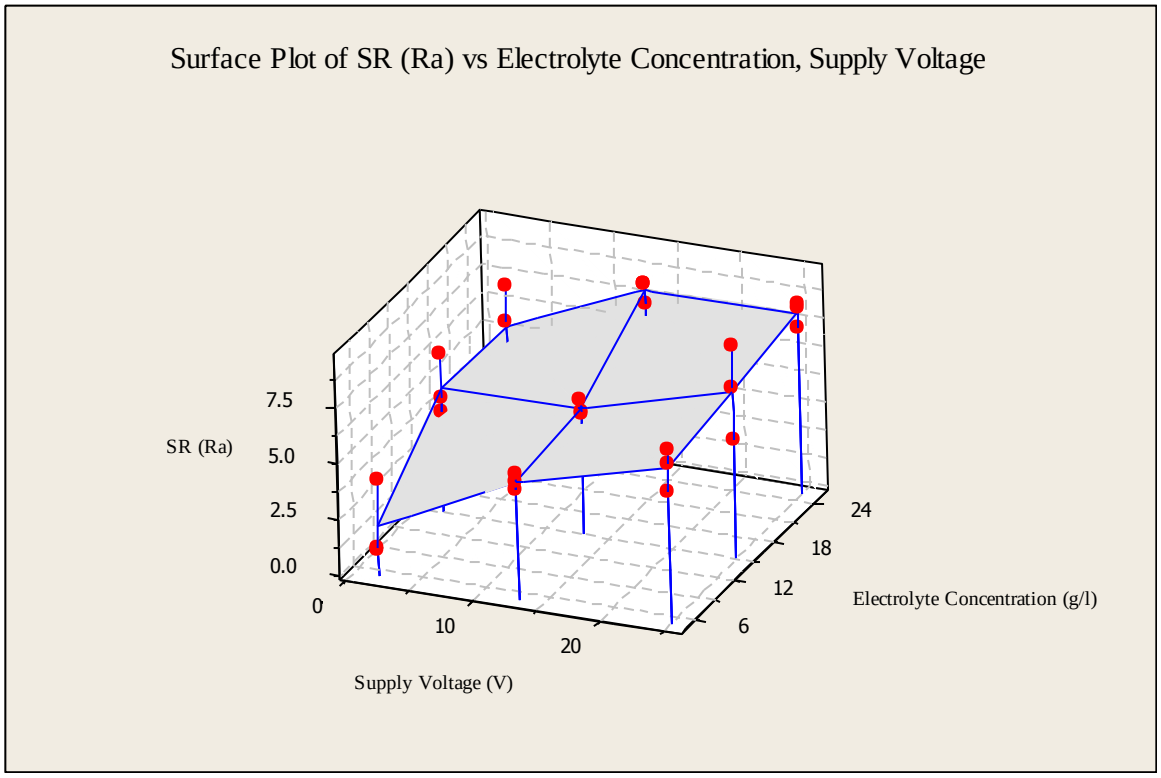

Fig 4.16 Interaction Effect of Supply Voltage and Electrolyte Concentration on SR

Figure 4.16 shows interaction effect of supply voltage and electrolyte concentration on surface roughness height, R_a(µm). It is clear from the interaction graph, that the SR increases with increase in both ECMM parameters i.e. supply voltage and electrolyte concentration. An increase in the supply voltage results in an increase in the produced heat and current density between the inter electrodes gap (IEG). The higher current density in the IEG generates high rate of dissolution of metal with non-uniform dissolution, as a result in deep grain boundary attack of the metal surface. Sometimes pitting on metal surfaces are occurs, results in increases of surface roughness height (Ra). The surface roughness height, Ra (µm) increases with increase in concentration of electrolyte. The large number of ions associated in the IEG at higher concentration of electrolyte means increase the machining current density and conductivity. A high current density increases the tendency of pitting and thus results in the generation of rough surfaces. At higher electrolyte concentration, machined holes are non-uniform and irregular. This irregularity on micro hole may be caused due to improper cleaning of sludge particles from the inter electrode gap (IEG). Hence, surface roughness height increases with increase in electrolyte concentration due to higher quantity of melted material being removed, and larger discharge craters induced in the workpiece surface. In addition, the dissolution product can stack up easily and unusual dissolution of materials can induced

further. This is because of unsteady and non-uniform metallic dissolution, which causes uneven microstructure, and etch pits. This phenomenon causes the entrance of micro-hole to be larger and so the surface finish becomes worse.

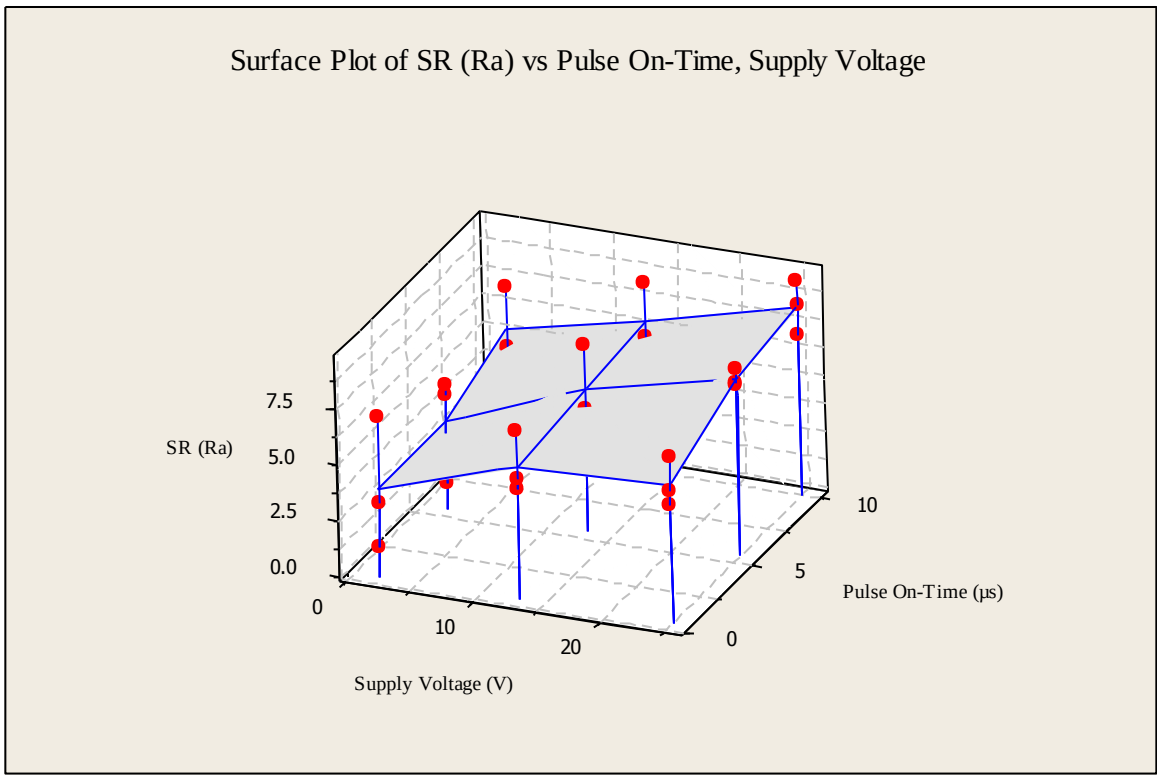

Fig 4.17 Interaction Effects of Supply Voltage and Pulse On Time on SR

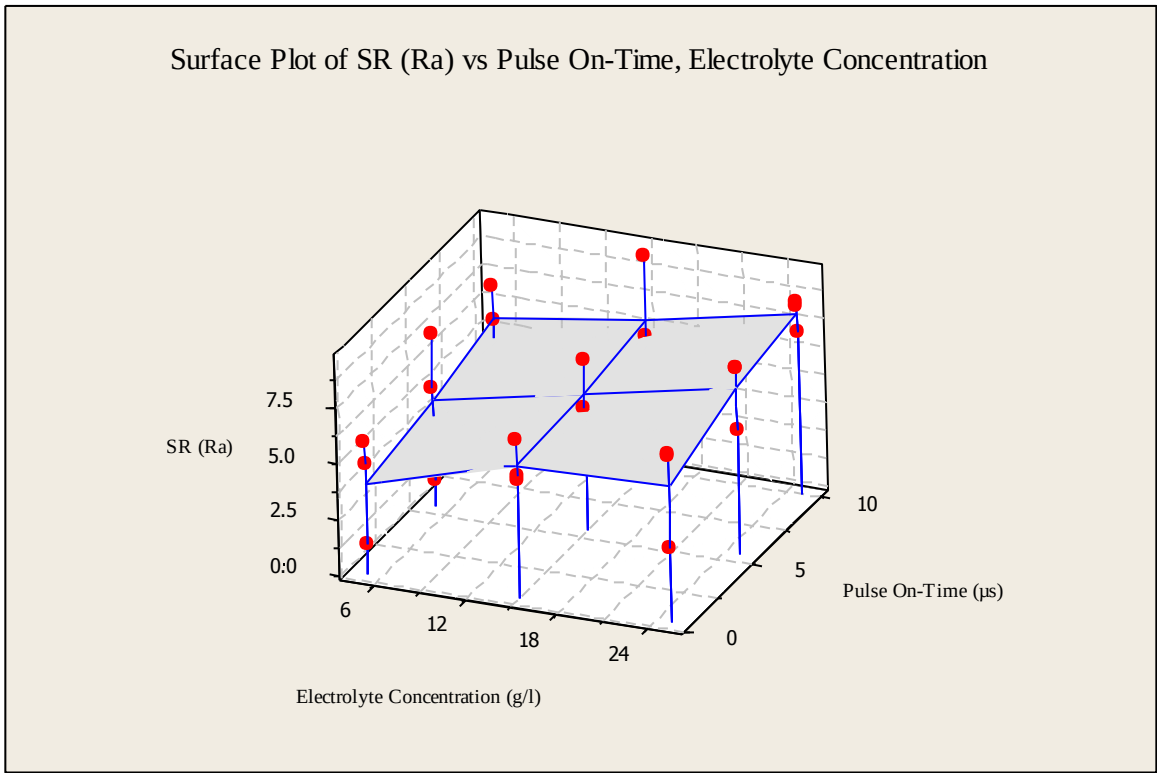

Fig 4.18 Interaction Effects of Electrolyte Concentration and Pulse On Time on SR

Figure 4.17 shows the interaction effects of pulse on time and supply voltage on surface roughness height, R_a (µm). It is clear that the R_a increases with increase in both pulse on time and supply voltage. Figure 4.18 shows the interaction effects of pulse on time and electrolyte concentration on surface roughness height, R_a. It is clear that the R_a increases with increase in both pulse-on-time and electrolyte concentration. At higher pulse-on-time, generation of sparks starts and the localization effect reduces due to the improper flushing of electrolyte, the debris cannot be fully flushed out from the IEG. Thus, increases surface roughness due to the non-uniform metallic dissolution of material.

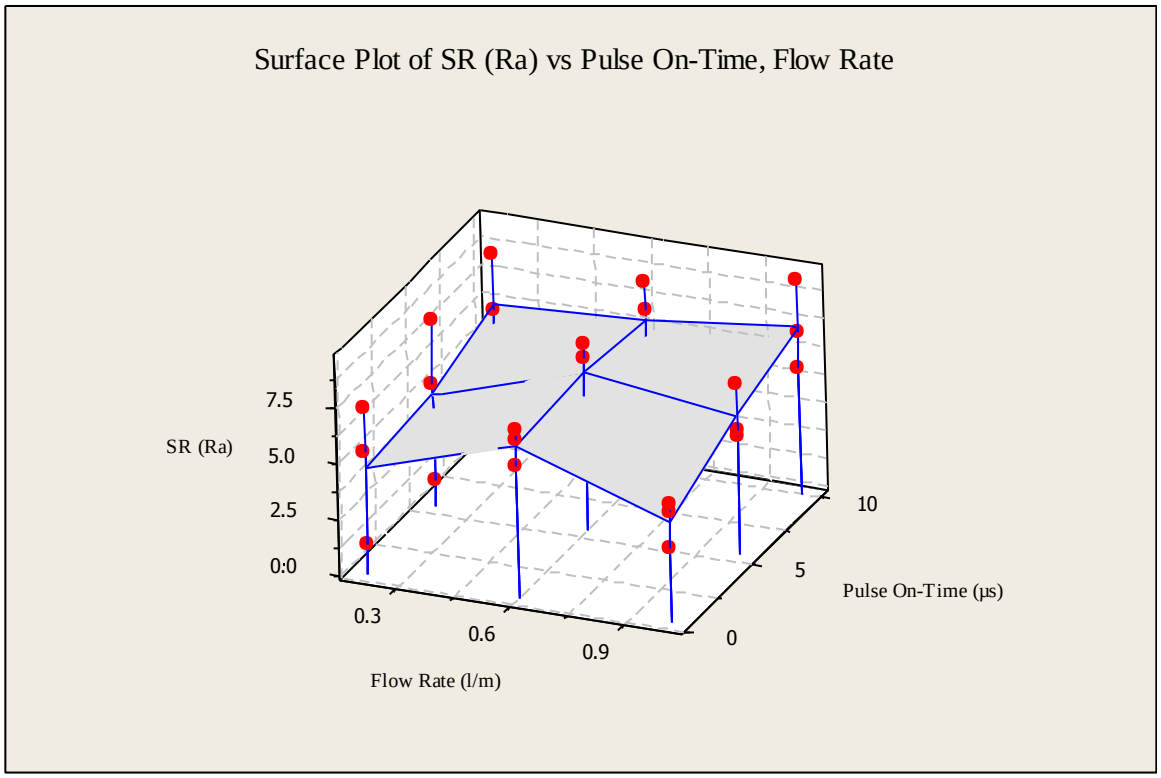

Fig 4.19 Interaction Effects of Electrolyte Flow Rate and Pulse On Time on SR

Figure 4.19 shows the interaction effects of electrolyte flow rate and pulse on time on surface roughness height (R_a, µm). It is clear that the R_a increases with increase in pulse on time. The surface roughness height (R_a) also decreases with increasing the electrolyte flow, it is because of large flushing pressure that helps to remove the debris from the machining zone. Increased electrolyte flow rate, which means the turbulence being high, the effect of rotating eddies will be reduced and no flow streak appears on the surface, as a result generates better surface finish.

4.1.4 Effect of ECMM Parameters on Taper Cut

The taper cut was determined from the difference of inlet diameter and exit diameter of each machined hole. Figure 4.20 (a) shows the S/N ratio (dB) curve by factor level of supply voltage (V) for taper cut (TC). From Figure 4.20 (a), it is clear that there is decrease in S/N ratio with

increase in supply voltage. The high-applied voltage may cause in breaking of the oxide layer. The high heat generated in the inter-electrode gap causes varying local electrolyte conductivity. This phenomenon is responsible for distribution of non-uniform current in the inter-electrode gap. Figure 4.20 (b) shows the S/N Ratios (dB) curve by factor level of electrolyte concentration for taper cut (TC). From graph Figure 4.20 (b), it is noticed that the S/N ratios for TC decreases with increase in electrolyte concentration. Both electrolyte conductivity and current density increase with increase in electrolyte concentration and thereby leads to increase in radial and lateral etching, therefore, increases taper cut. Figure 4.20 (c) shows the S/N Ratio (dB) curve by factor level of pulse on time for taper cut (TC). From graph Figure 4.20 (c), it is clear that the S/N ratio for TC decreases with increase in pulse on time. With the increase of pulse on time, both current as well as period of supply current increase, enhance dissolution of material along the radial direction and thereby increases taper cut. Figure 4.20 (d) shows the S/N Ratio (dB) curve by factor level of flow rate of electrolyte for taper cut (TC). From graph Figure 4.20 (d), it is clear that S/N ratio for TC decreases with increase in flow rate of electrolyte from 0.2 *l*/min to 0.6 *l*/min and by further increase of flow rate of electrolyte from 0.6 *l*/min to 1.0 *l*/min, the S/N ratio for TC increases.

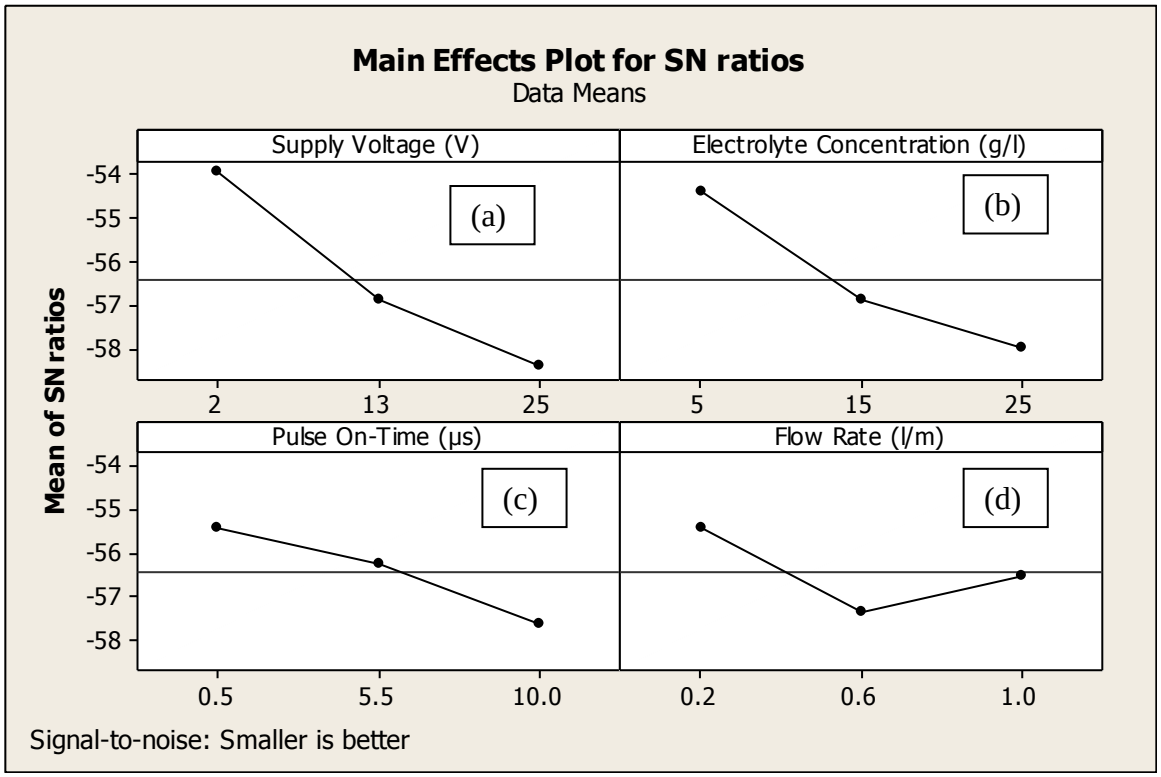

Fig 4.20 S/N Ratio (dB) Graphs for Taper Cut (TC)

Table 4.8 Parameter Wise S/N Ratio for TC and Their Rank

Level	S/N ratio of Supply Voltage (V)	S/N ratio of Electrolyte Concentration (g/*l*)	S/N ratio of Pulse on-time (µs)	S/N ratio of Flow rate (*l*/min)
1	-53.97	-54.42	-55.43	-55.42
2	-56.91	-56.87	-56.25	-57.33
3	-58.41	-58.01	-57.62	-56.54
Delta	4.44	3.59	2.20	1.91
Rank	1	2	3	4

Table 4.8 represents the S/N ratio based ranking against each parameters of ECMM for TC. From Table 4.8, it is clear that for S/N ratio, supply voltage has the great effect on TC. The flow rate has the small effect on S/N ratio for TC. Therefore, the parameter, supply voltage has 1st rank.

Table 4.9 ANOVA for TC

Source	DF	Seq SS	Adj SS	Adj MS	F	P	%Contribution	Remarks
Supply Voltage (V)	2	450296	450296	225148	43.676	0.000	42.56	Significant
Electrolyte Concentration (g/l)	2	319683	319683	159841.5	31.00	0.000	30.21	Significant
Pulse On-Time (µs)	2	142496	142496	71248	13.821	0.009	13.48	Significant
Flow Rate (l/min)	2	52903	52903	26451.5	5.131	0.136	4.99	Non-Significant
Error	18	92788	92788	5154.88			8.76	
Total	26	1058166						

R-Sq = 91.23%,

Table 4.9 represents the ANOVA and 'F test' values. The F-value for all the sources i.e. values of Prob >F less than 0.05, which indicates the model terms are significant at 95% confidence level. From ANOVA table 4.9, it is clear that for taper cut, the sources supply voltage, electrolyte concentration, pulse on-time and flow rate are significant model terms.

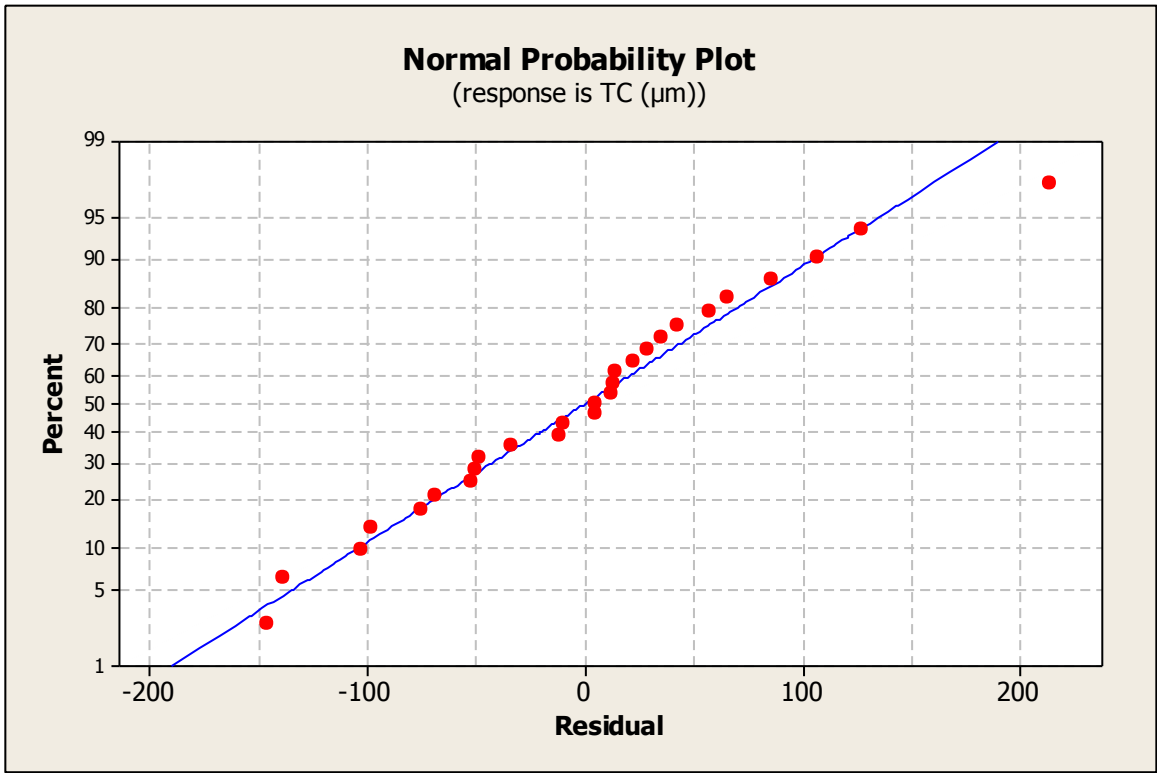

Fig 4.21 Normal Probability Plots for TC

Figure 4.21 show the normal probability plots for TC. Most of residuals are found on a straight line which indicates that errors are normally distributed. This is the normality test required to be qualified by the model for checking the model. From figure 4.21, it has been found that models are significant.

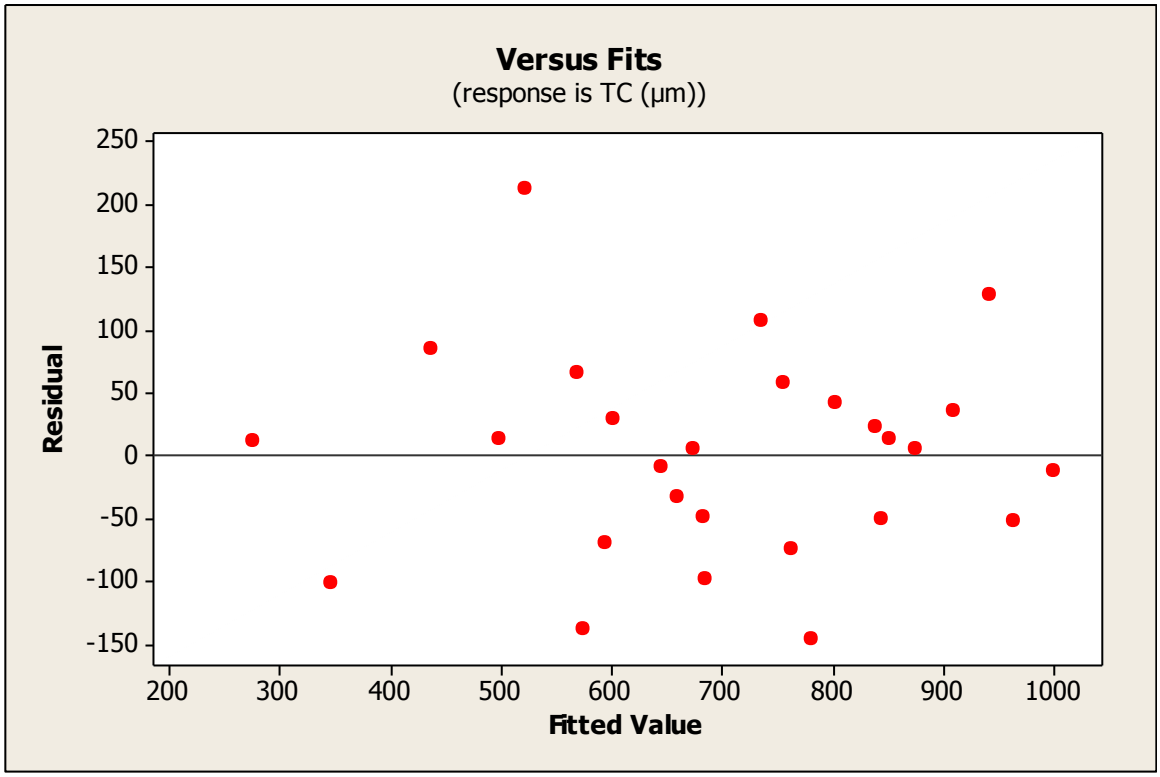

Fig 4.22 Residuals and Fitted Values for TC

Figure 4.22 shows the residuals and fitted plot for surface roughness height, R_a (µm). The residuals are distributed randomly and are not clustered. This indicates the model is good.

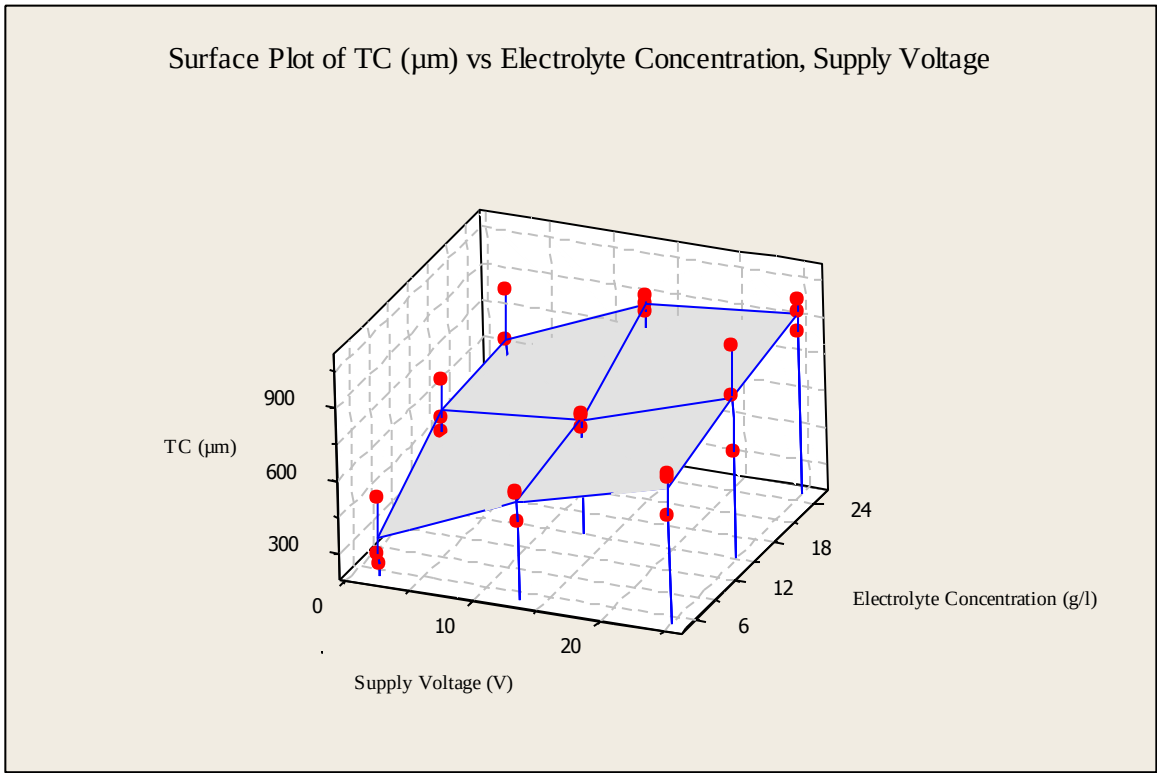

Fig 4.23 Interaction Effects of Supply Voltage and Electrolyte Concentration on TC

Figure 4.23 shows the interaction effect of supply voltage and electrolyte concentration on taper cut. From the interaction graph Figure 4.23, it is clear that the TC increases with increase in both the ECMM parameters i.e. supply voltage and electrolyte concentration. The heat produced and current density between the inter electrodes gap (IEG) increases by increasing the supply voltage. High current density in the IEG leads to non-uniform and higher dissolution of metal, as a result in deep grain boundary attack of the metal surface. Sometimes pitting on metal surfaces also occurs, resulting in increase of surface roughness height (Ra). The taper cut increases with increase in concentration of electrolyte. The large number of ions associated in the IEG at higher concentration of electrolyte cause an increase in the machining current density and conductivity. At higher electrolyte concentration, machined holes produced were non-uniform and irregular. This irregularity in micro hole may be caused due to the improper cleaning of sludge particles by the flow of electrolyte from the inter electrode gap (IEG). Hence, taper cut increases with increase in electrolyte concentration, it is because of high material removal rate, thereby large discharge craters were generated on the workpiece surface.

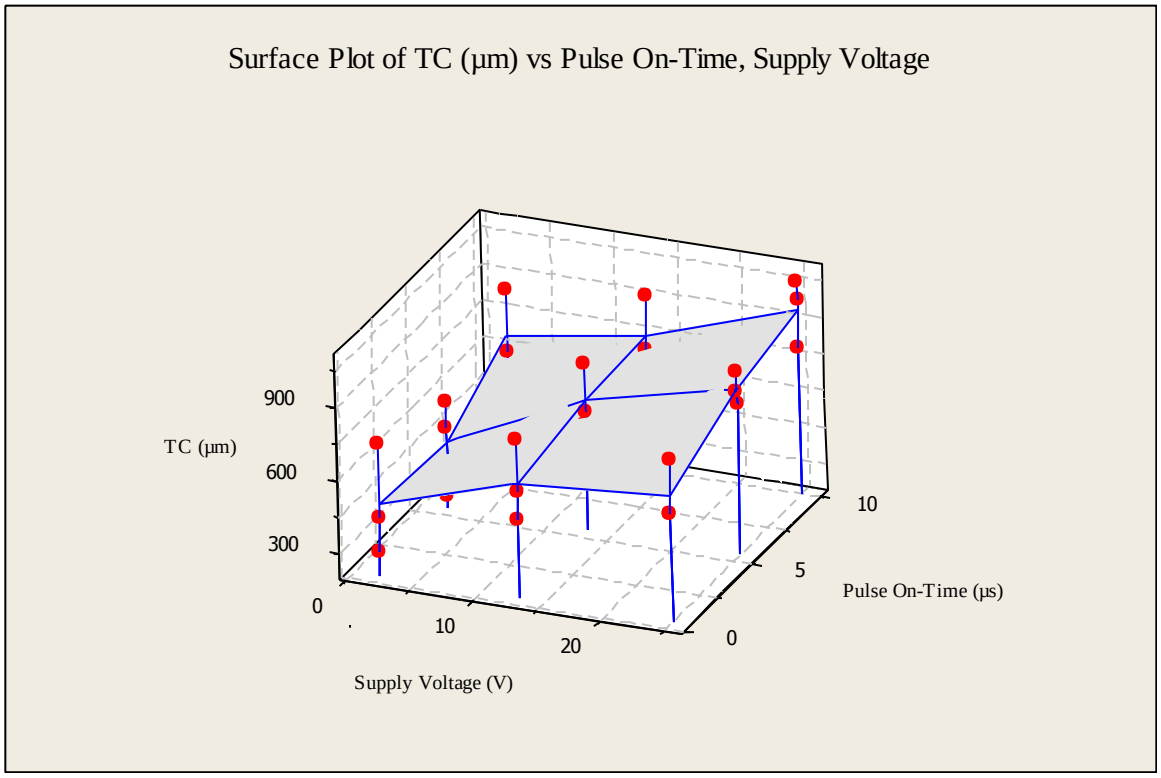

Fig 4.24 Interaction Effects of Supply Voltage and Pulse On Time on TC

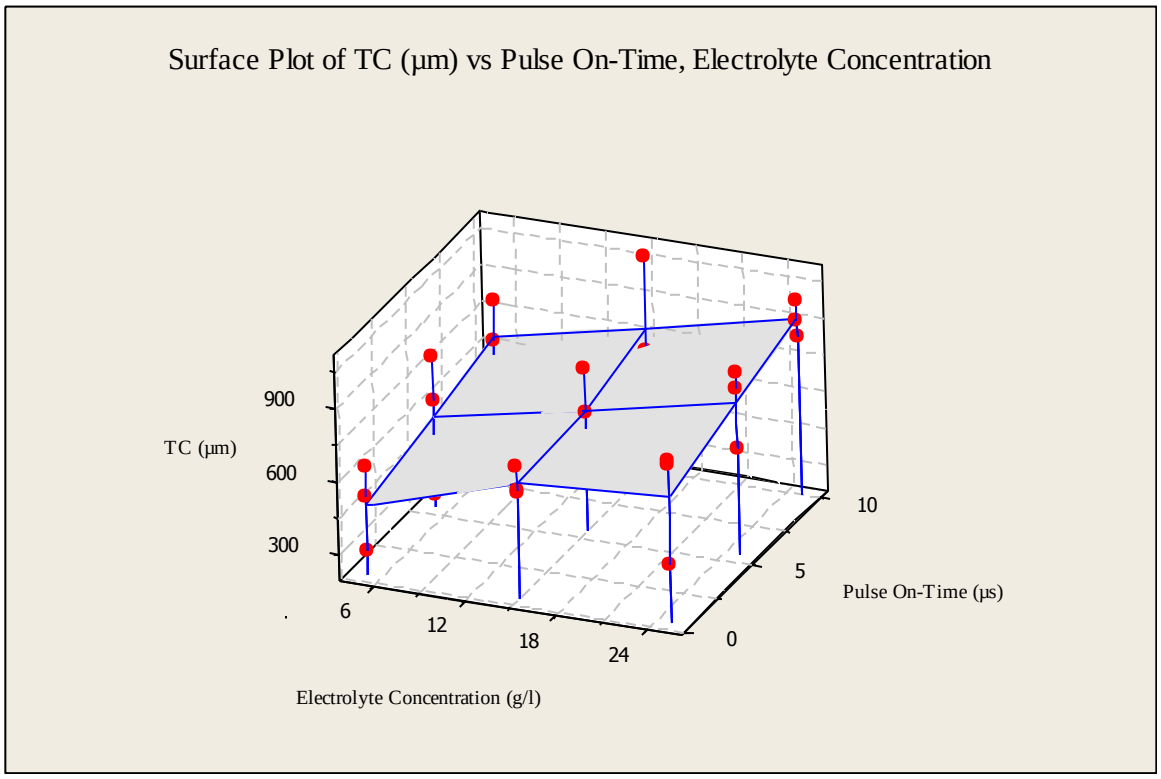

Fig 4.25 Interaction Effects of Electrolyte Concentration and Pulse On Time on TC

Figure 4.24 shows the interaction effects of pulse-on-time and supply voltage on taper cut. It is clear that TC increases with increase in both pulse-on-time and supply voltage. The supply of high voltage produces non-uniform and irregular machined hole. This may be due to improper cleaning of sludge particles from the inter electrode gap (IEG) during machining. At the same

time removal of machined metal particles increases in between the inter electrodes gap. The presence of machined particles in the inter electrode gap may cause sparking, which may lead to higher taper cut. Figure 4.25 shows the interaction effects of pulse-on-time and electrolyte concentration on taper cut. It is clear that the TC increases with increase in both pulse-on-time and electrolyte concentration. At higher pulse on time, generation of sparks starts and the localization effect reduces due to improper flushing of electrolyte due to which the debris are not fully flushed out from the IEG. Thus, increases taper cut due to non-uniform metallic dissolution of material. At higher electrolyte concentration, a large number of ions are formed during machining. As a result there is an increase in machining current density and this leads to increase the taper cut.

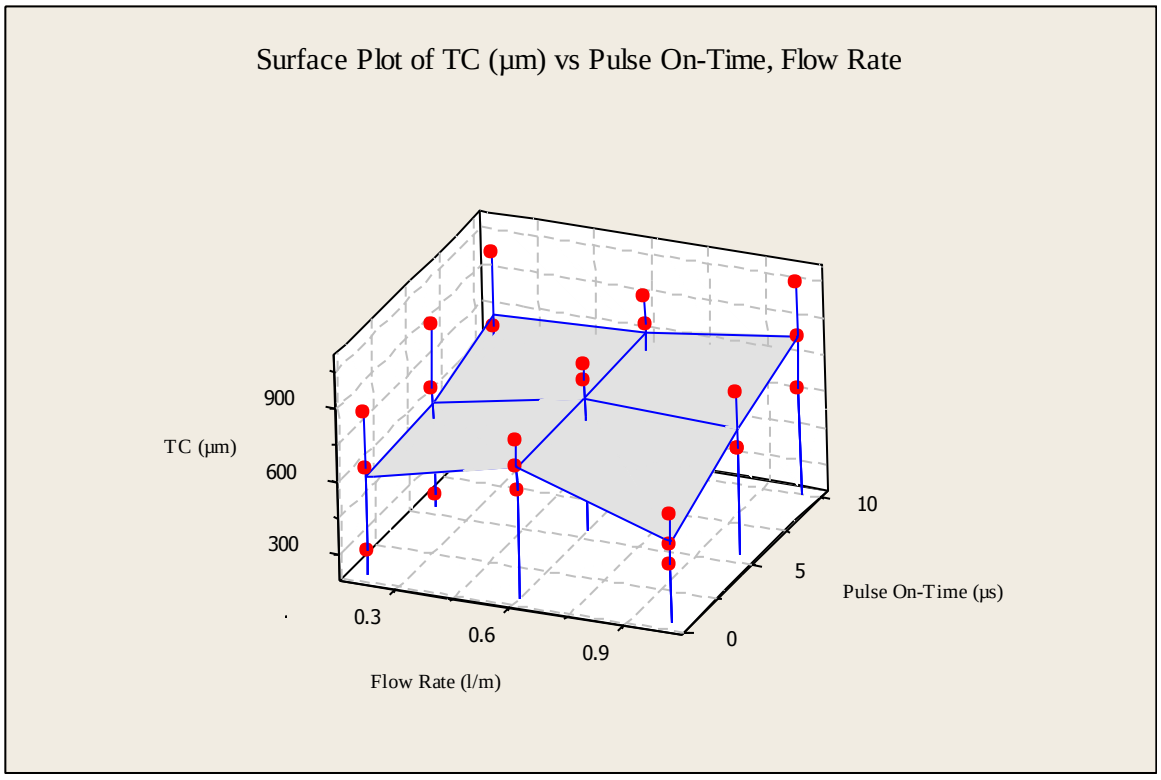

Fig 4.26 Interaction Effects of Electrolyte Flow Rate and Pulse On Time on TC

Figure 4.26 shows the interaction effects of electrolyte flow rate and pulse-on-time on taper cut. It is clear that the TC increases with increase in pulse on time. With the increase in pulse on time, both the current as well as the period of supply current increase, which enhances dissolution of material along the radial direction and thereby increase in taper cut. The taper cut decreases by increasing the electrolyte flow rate because of large flushing pressure, which helps in removing the debris from the machining zone.

4.2 SINGLE RESPONSE OPTIMIZATION USING TAGUCHI DESIGN OF EXPERIMENT

According to Taguchi's design of experiments, the summary statistics i.e. S/N ratio is utilized to optimize the parametric combinations for maximum material removal rate, minimum electrode wear rate, minimum surface roughness height, and minimum taper cut during electrochemical micro machining of hybrid Al/MMC.

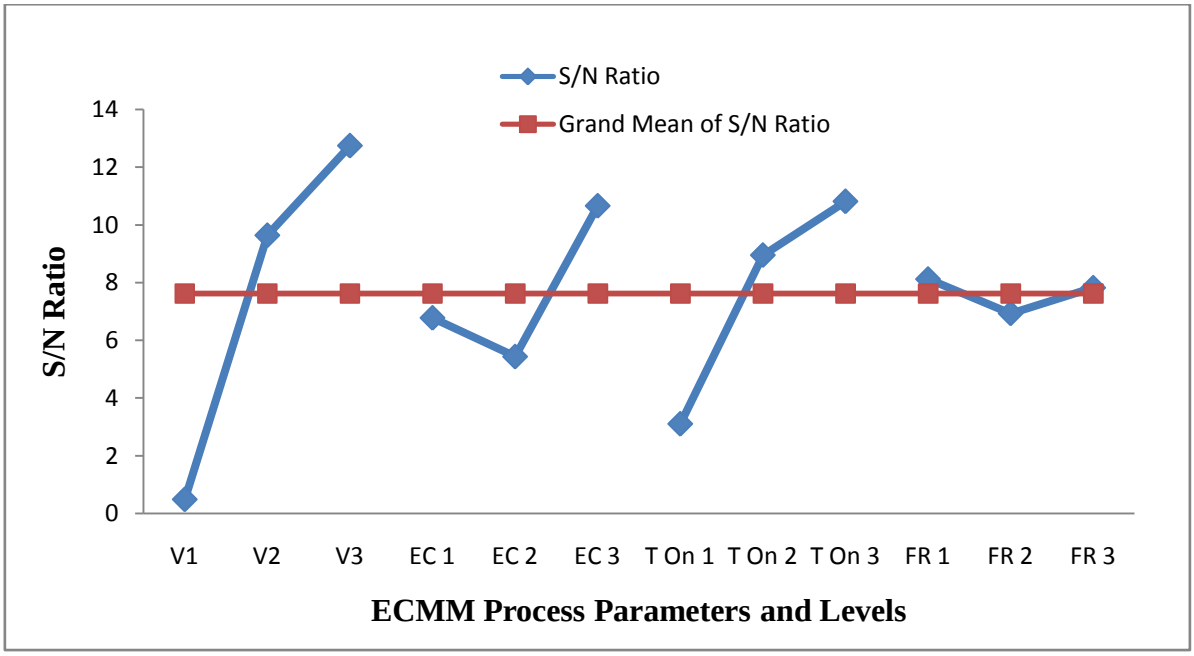

Fig 4.27 Average S/N Ratio for MRR

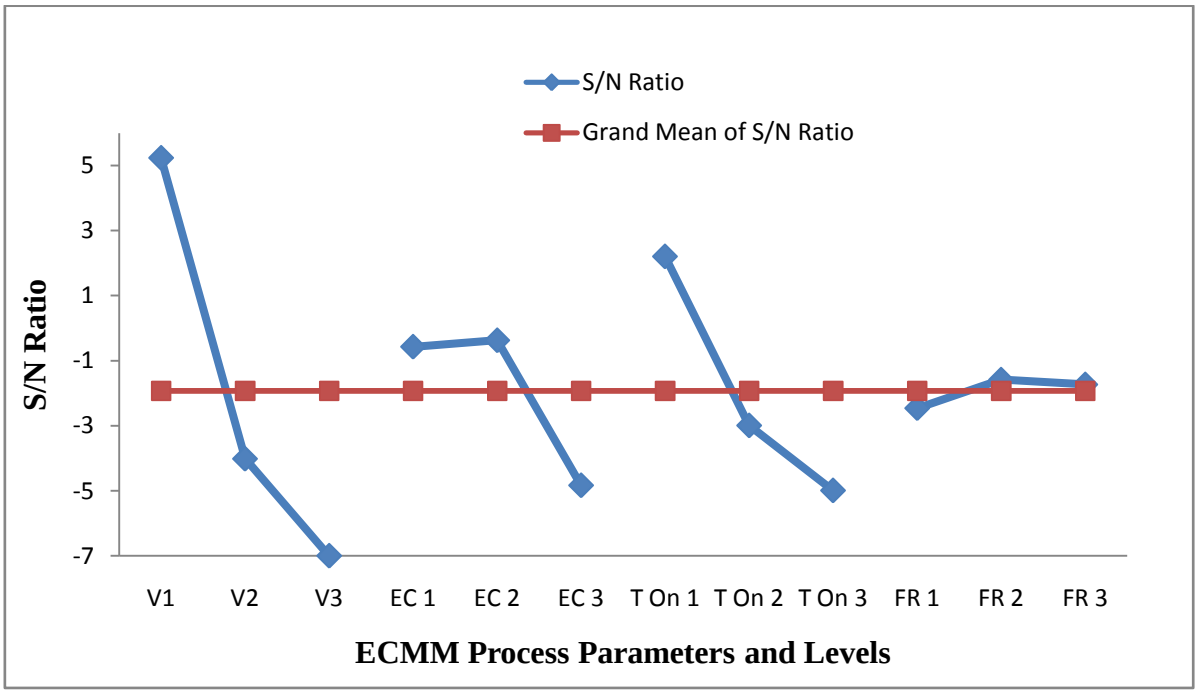

Fig 4.28 Average S/N Ratio for EWR

The average S/N ratio (dB) curves for each factor level for MRR are displayed in Figure 4.27. From Figure 4.27, it is concluded that for maximum MRR the parametric combination is V_3, EC_3, Ton_3 and FR_1. The average S/N ratio (dB) curves for each factor level for electrode wear rate (EWR) are displayed in Figure 4.28. From Figure 4.28, it is concluded that for minimum electrode wear rate (EWR) the parametric combination is V_1, EC_2, Ton_1 and FR_2.

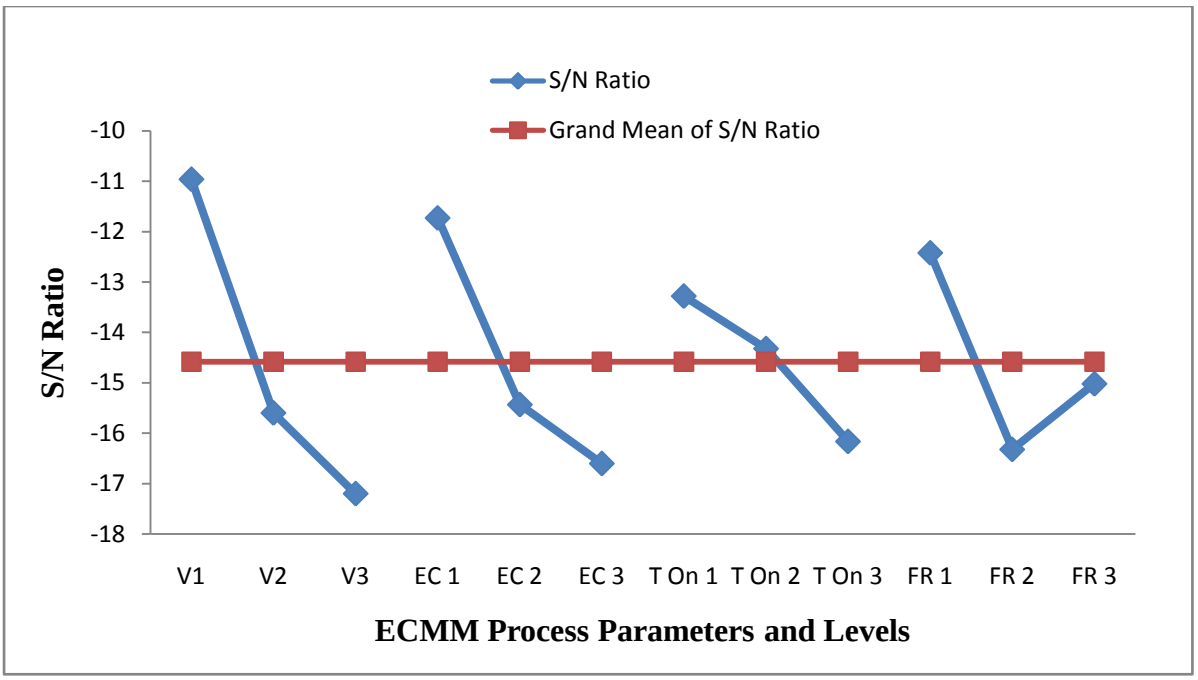

Fig 4.29 Average S/N Ratio for SR

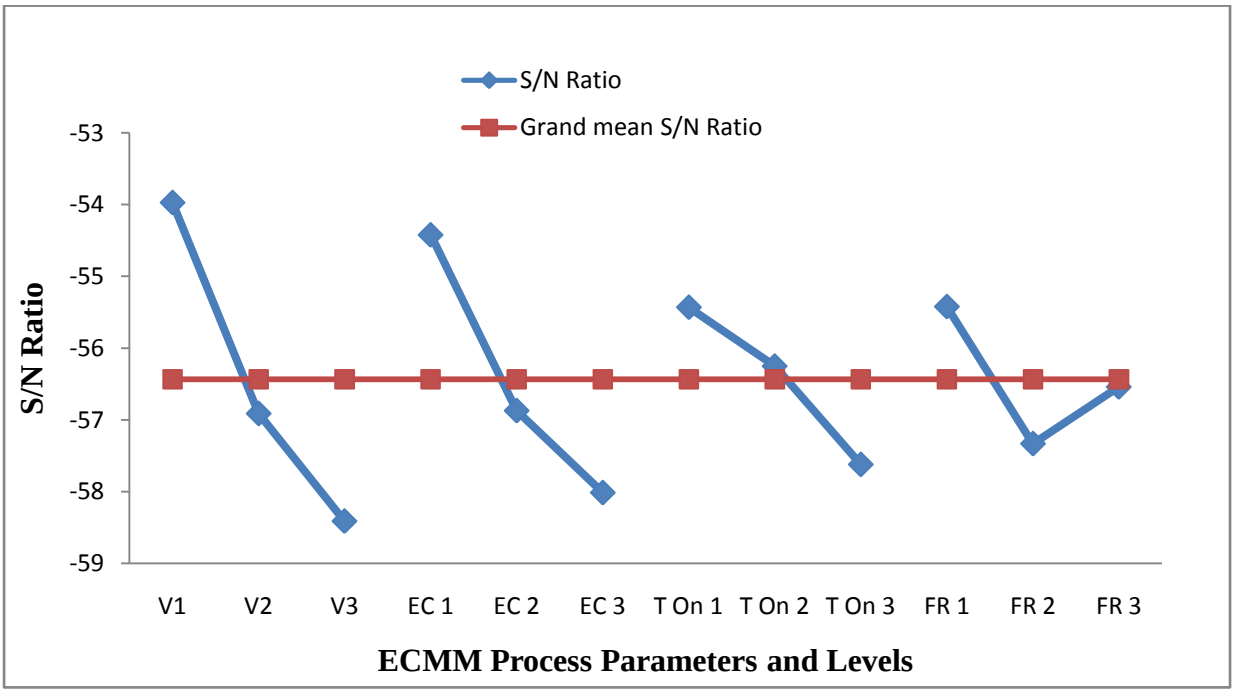

Fig 4.30 Average S/N Ratio for TC

The average S/N ratio (dB) curves for each factor level for surface roughness height, R_a (µm) are displayed in Figure 4.29. From Figure 4.29, it is concluded that for minimum surface

roughness height, R_a the parametric combination is V_1, EC_1, Ton_1 and FR_1. The average S/N ratio (dB) curves for each factor level for taper cut (TC) are displayed in Figure 4.30. From Figure 4.30, it is concluded that for minimum taper cut (TC) the parametric combination is V_1, EC_1, Ton_1 and FR_1.

4.3 MULTI RESPONSE OPTIMIZATION USING DESIRABILITY

Box Behnkan design was used to establish the mathematical relations of the response surface methodology (RSM). RSM is a powerful tool in the design of experiment which has been used in multi response optimization of the ECMM parameters for effective machining of hybrid Al metal matrix composite. Multi response optimization was done using desirability function in conjunction with RSM to overcome the problem of contradictory of single response optimization.

Table 4.10 Design of Experiments as per RSM and Test Results

S. NO	Ip (Amp)	V (v)	Ton (µs)	Toff (µs)	EC (g/*l*)	FR (*l*/min)	MRR (mg/min)	EWR (mg/min)	SR (Ra)	TC (µm)	OC (µm)	MSAZ (µm)
1	1.5	13	5.5	5.5	15	0.6	1.058	0.487	1.12	545	617	129
2	0.5	2	5.5	0.5	15	0.6	0.979	0.437	1.01	288	273	101
3	1.5	25	5.5	5.5	5	0.2	2.059	1.078	4.19	468	593	281
4	1.5	13	0.5	10.0	15	1.0	0.137	0.068	6.94	585	617	238
5	1.5	13	10.0	10.0	15	0.2	1.402	0.818	5.92	525	586	243
6	3.0	2	5.5	0.5	15	0.6	1.168	0.446	4.35	586	668	382
7	0.5	13	0.5	5.5	15	0.2	0.330	0.169	3.16	254	395	94
8	1.5	2	5.5	5.5	25	0.2	2.546	1.276	3.43	556	621	319
9	3.0	25	5.5	10.0	15	0.6	4.150	1.883	6.08	585	658	221
10	0.5	13	5.5	10.0	25	0.6	2.916	0.564	3.72	480	535	214
11	1.5	2	5.5	5.5	5	0.2	0.317	0.258	2.11	354	381	175
12	0.5	13	10.0	5.5	15	1.0	0.887	0.349	2.43	626	626	335

S. NO	Ip (Amp)	V (v)	Ton (µs)	Toff (µs)	EC (g/*l*)	FR (*l*/min)	MRR (mg/min)	EWR (mg/min)	SR (Ra)	TC (µm)	OC (µm)	MSAZ (µm)
13	3.0	13	0.5	5.5	15	1.0	2.435	0.844	5.24	784	627	362
14	1.5	25	0.5	5.5	25	0.6	2.685	1.288	7.32	817	961	417
15	0.5	13	0.5	5.5	15	1.0	0.303	0.153	1.87	386	493	177
16	1.5	25	5.5	5.5	5	1.0	0.827	0.419	1.31	724	830	490
17	1.5	2	5.5	5.5	25	1.0	2.352	0.914	1.15	612	729	395
18	1.5	13	0.5	0.5	15	1.0	1.158	0.554	2.21	562	616	256
19	1.5	25	5.5	5.5	25	0.2	6.916	2.924	5.72	828	915	358
20	3.0	13	10.0	5.5	15	1.0	2.726	1.824	4.58	662	787	428
21	1.5	2	5.5	5.5	5	1.0	0.349	0.187	1.02	538	655	268
22	0.5	13	10.0	5.5	15	0.2	1.203	0.587	5.12	615	544	285
23	1.5	25	0.5	5.5	5	0.6	0.444	0.214	2.51	410	482	182
24	1.5	25	10.0	5.5	25	0.6	8.923	2.244	5.41	995	1145	410
25	1.5	25	5.5	5.5	25	1.0	5.544	2.704	2.70	1069	1104	574
26	0.5	25	5.5	10.0	15	0.6	1.481	0.535	3.70	405	542	247
27	1.5	2	10.0	5.5	25	0.6	2.937	0.646	3.39	476	566	225
28	1.5	13	10.0	10.0	15	1.0	1.416	0.716	3.31	743	689	414
29	3.0	13	5.5	0.5	25	0.6	6.605	3.246	6.56	1028	1210	582
30	1.5	25	10.0	5.5	5	0.6	1.610	0.950	6.21	663	776	495
31	3.0	25	5.5	0.5	15	0.6	4.566	1.896	4.28	974	1071	533

S. NO	Ip (Amp)	V (v)	Ton (µs)	Toff (µs)	EC (g/*l*)	FR (*l*/min)	MRR (mg/min)	EWR (mg/min)	SR (Ra)	TC (µm)	OC (µm)	MSAZ (µm)
32	1.5	13	10.0	0.5	15	1.0	3.489	0.856	2.28	828	866	481
33	1.5	13	0.5	0.5	15	0.2	1.093	0.566	3.36	344	445	121
34	0.5	13	5.5	10.0	5	0.6	1.286	0.645	2.75	387	587	178
35	1.5	13	10.0	0.5	15	0.2	2.767	1.289	8.56	688	669	345
36	1.5	13	0.5	10.0	15	0.2	0.998	0.478	3.90	360	402	126
37	0.5	2	5.5	10.0	15	0.6	0.289	0.155	3.06	240	268	121
38	1.5	2	0.5	5.5	5	0.6	0.456	0.241	2.71	375	488	96
39	3.0	13	0.5	5.5	15	0.2	2.159	1.074	3.81	786	586	328
40	3.0	13	5.5	0.5	5	0.6	1.241	0.621	4.62	744	846	436
41	0.5	13	5.5	0.5	25	0.6	3.923	0.945	3.30	469	509	264
42	3.0	2	5.5	10.0	15	0.6	0.964	0.086	4.87	422	515	180
43	1.5	2	0.5	5.5	25	0.6	1.233	0.126	4.20	398	456	184
44	0.5	25	5.5	0.5	15	0.6	0.467	0.245	2.17	427	518	119
45	3.0	13	5.5	10.0	5	0.6	0.656	0.146	6.33	585	570	281
46	3.0	13	10.0	5.5	15	0.2	4.143	2.047	8.86	576	625	352
47	1.5	2	10.0	5.5	5	0.6	0.582	0.461	5.35	490	546	294
48	3.0	13	5.5	10.0	25	0.6	4.956	2.467	6.49	778	897	359
49	0.5	13	5.5	0.5	5	0.6	2.032	1.141	3.26	346	455	167

4.4 ANALYSIS OF ECMM PARAMETERS ON MRR

To decide about the adequacy of the model, three different tests viz. sequential model sum of squares, lack of fit tests and model summary statistics were analyzed for material removal rate. Table 4.11 displays the selection of adequate model to fit MRR characteristics.

Table 4.11 Selection of Adequate Model for MRR

Sequential Model Sum of Squares						
Source	**Sum of Squares**	**Df**	**Mean Square**	**F Value**	**p-Value Prob>F**	
Mean	231.74	1	231.74			
Linear	128.34	6	21.39	17.85	<0.0001	
2FI	29.25	15	1.95	2.31	0.0232	
Quadratic	15.52	6	2.59	5.82	0.0006	suggested
Cubic	9.10	18	0.51	1.65	0.2384	Aliased
Residual	2.45	8	0.31			
Total	416.39	54	7.71			
Lack of Fit Tests						
Source	Sum of Squares	Df	Mean Square	F Value	p-Value Prob>F	
Linear	54.63	42	1.30	3.83	0.0681	
2FI	25.37	27	0.94	2.77	0.1295	
Quadratic	9.85	21	0.47	1.38	0.3864	Suggested
Cubic	0.75	3	0.25	0.74	0.5722	Aliased
Pure Error	1.70	5	0.34			
Model Summary Statistics						
Source	Std. Dev.	R-Squared	Adjusted R-Squared	Predicted R-Squared	PRESS	
Linear	1.09	0.6950	0.6561	0.5934	75.08	
2FI	0.92	0.8534	0.7572	0.5833	76.96	
Quadratic	0.67	0.9375	0.8725	0.7033	54.79	Suggested
Cubic	0.55	0.9867	0.9121	-0.1394	210.39	Aliased

From Table 4.11, it can be observed that for all the responses, the quadratic model is appropriate. The “lack of fit” test compares the residual error to the pure error from the replicated design points. The results indicate that the quadratic model in all the characteristics

does not show significant lack of fit, the adequacy of quadratic model is confirmed as the p-value is less than 0.5 hence quadratic model is suggested for the entire test.

4.4.1 Pooled Analysis of Variance (ANOVA) for MRR

To construct the pool ANOVA design expert 6.0 software was used. The aim of construction of pooled ANOVA is to pool the different factors together and test the significance. Table 4.12 represents Pooled ANOVA for MRR.

Table 4.12 Pooled ANOVA for MRR

Source	Sum of Squares	DF	Mean Square	F Value	p-value Prob>F	Status
Model	168.68	11	15.33	40.31	< 0.0001	Significant
A	18.13	1	18.13	47.67	< 0.0001	Significant
B	28.89	1	28.89	75.94	< 0.0001	Significant
C	15.28	1	15.28	40.17	< 0.0001	Significant
D	3.34	1	3.34	8.77	0.0050	Significant
E	68.37	1	68.37	179.73	< 0.0001	Significant
E^2	14.38	1	14.38	37.81	< 0.0001	Significant
AB	3.92	1	3.92	10.32	0.0025	Significant
AE	4.60	1	4.60	12.09	0.0012	Significant
BC	4.04	1	4.04	10.61	0.0022	Significant
BE	8.71	1	8.71	22.88	< 0.0001	Significant
CE	5.54	1	5.54	14.56	0.0004	Significant

The insignificant parameters were pooled using backward elimination method. The model F-value is 40.31, which implies that model is significant. The F-value for all the sources i.e. values of Prob >F less than 0.05, which indicates that the model terms are significant at 95% confidence level. From pooled ANOVA Table 4.12, it is clear that for MRR the sources A, B, C, D, E and interactions AB, AE, BC, BE, CE as well as quadratic terms E^2 are significant model terms. The ‘Lack of Fit’ corresponding F-value is 1.14, which reveals that the ‘Lack of Fit’ is not significant. The "Pred R-Squared" is 0.8338 that makes a reasonable agreement with the “Adj R-Squared” which is 0.8908.

4.4.2 Final Equation in Terms of Actual Factors of MRR

By using Table 4.12, the regression equation for MRR as a function of input process variable was developed using the software (RSM) and is mentioned below. The coefficients (insignificant identified from ANOVA) of some terms of the quadratic equation have been omitted. The developed mathematical model based on RSM for MRR is

$$MRR = 4.759 - 0.857\ I_P - 0.150\ V - 0.269\ T_{on} - 0.078\ T_{off} - 0.421\ E_c + 0.010\ E_c^2 + 0.048\ I_P.V + 0.059\ I_P.E_c + 0.012\ V.T_{on} + 0.00642\ V.E_c + 0.017\ T_{on}.E_c \quad (4.1)$$

Figure 4.31 shows the normal probability plots of residuals for MRR. Most of residuals are found on a straight line which indicates that errors are normally distributed. This is the normality test to be qualified by the model for confirming its validity. After this test it has been found that models are significant.

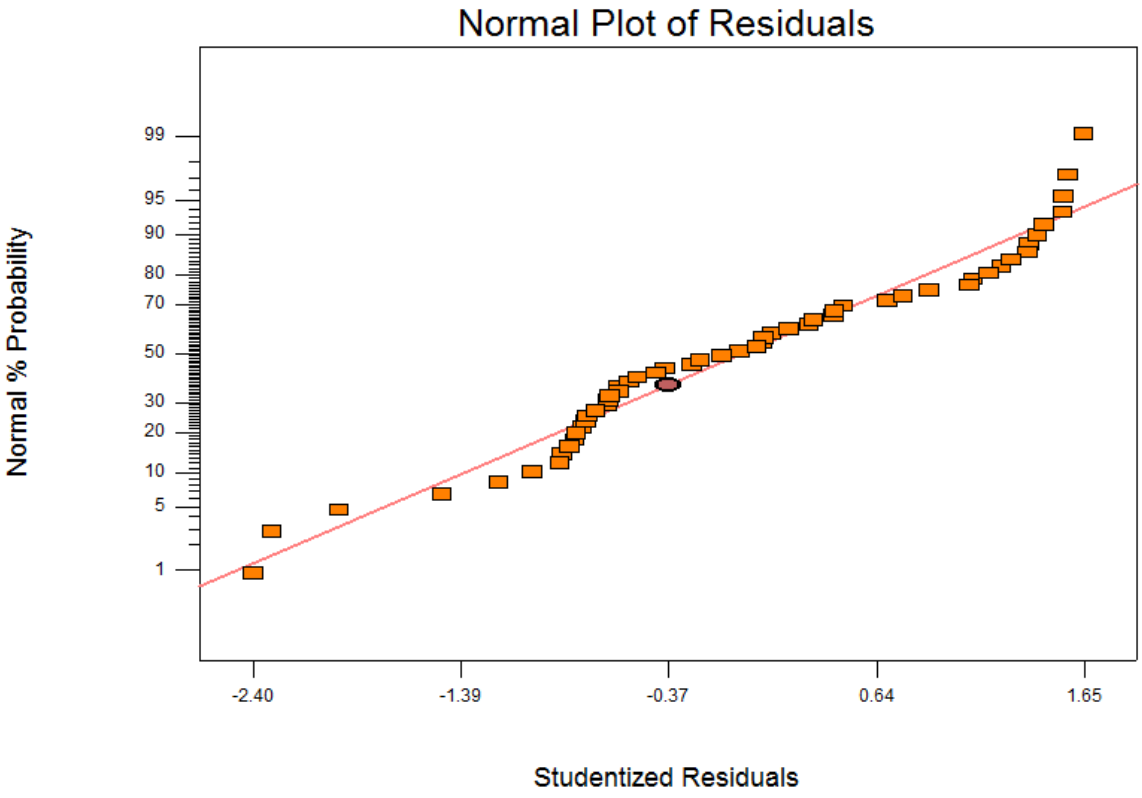

Fig 4.31 Normal Probability Plots for MRR

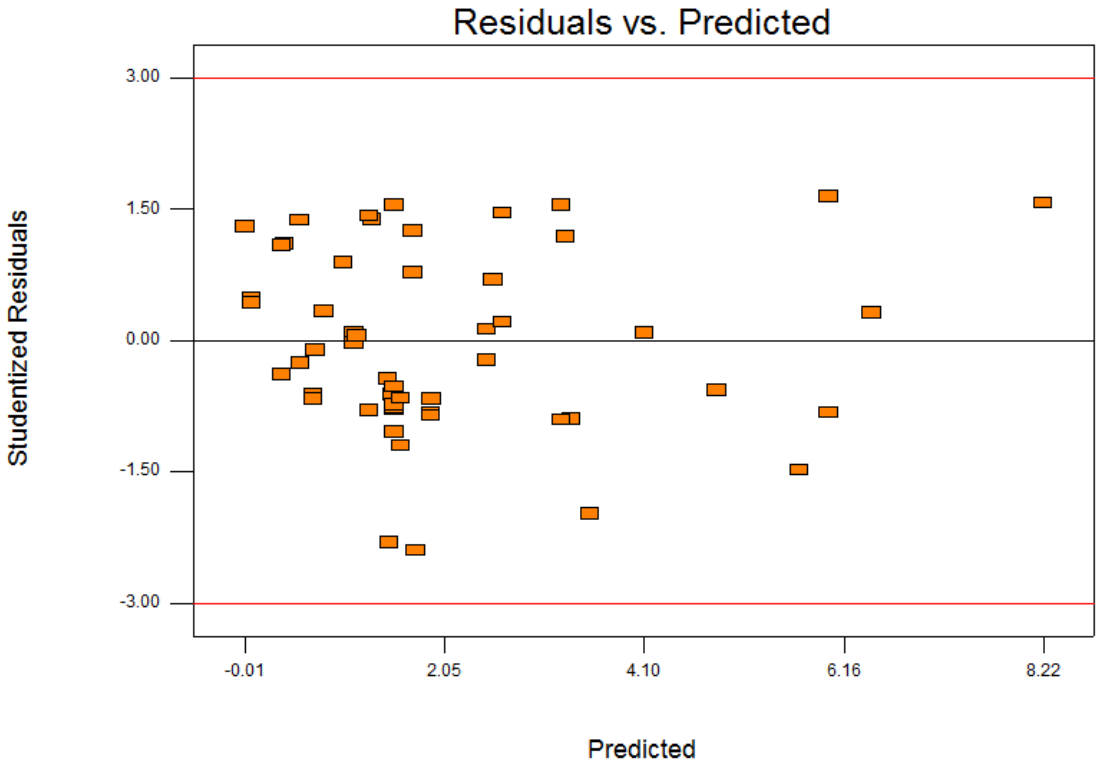

Fig 4.32 Residuals and Predicted Values for MRR

Figure 4.32 shows the residuals and predicted plot for material removal rate. The residuals are distributed randomly and are not clustered that indicates model is good.

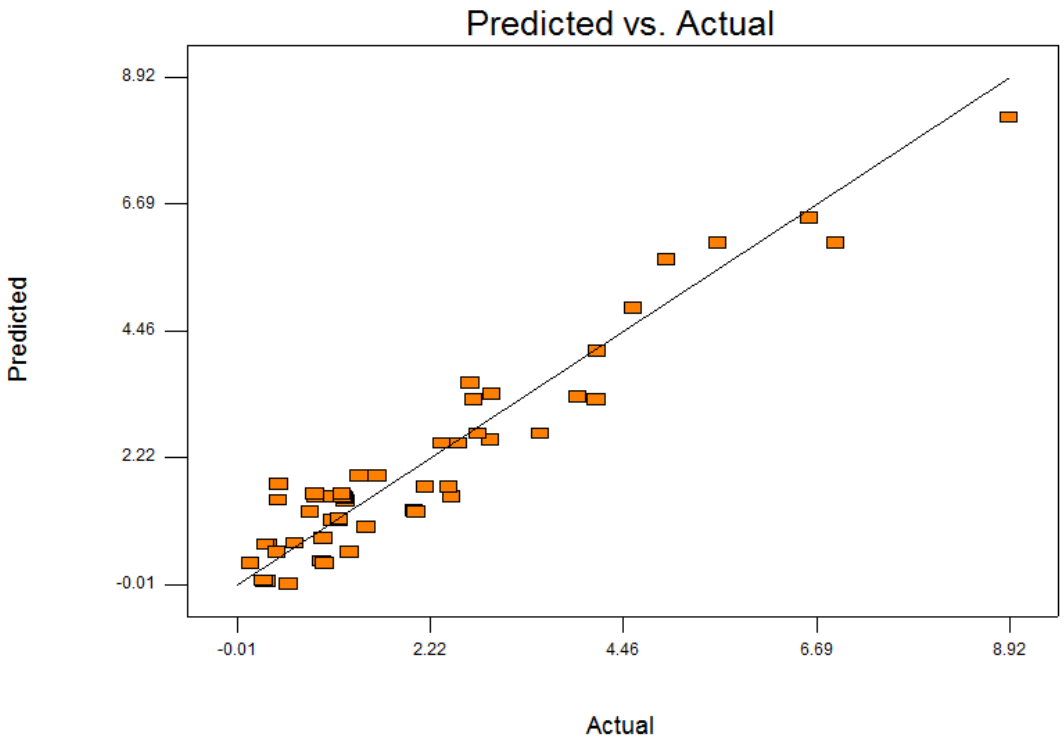

Fig 4.33 Actual and Predicted Values for MRR

Figure 4.33 shows the Predicted and Actual plot for material removal rate. Most of the results were found on a straight line which indicates that errors are normally distributed. This is test to be qualified by the model for checking its validity. From Figure 4.33, it has been found that models are significant.

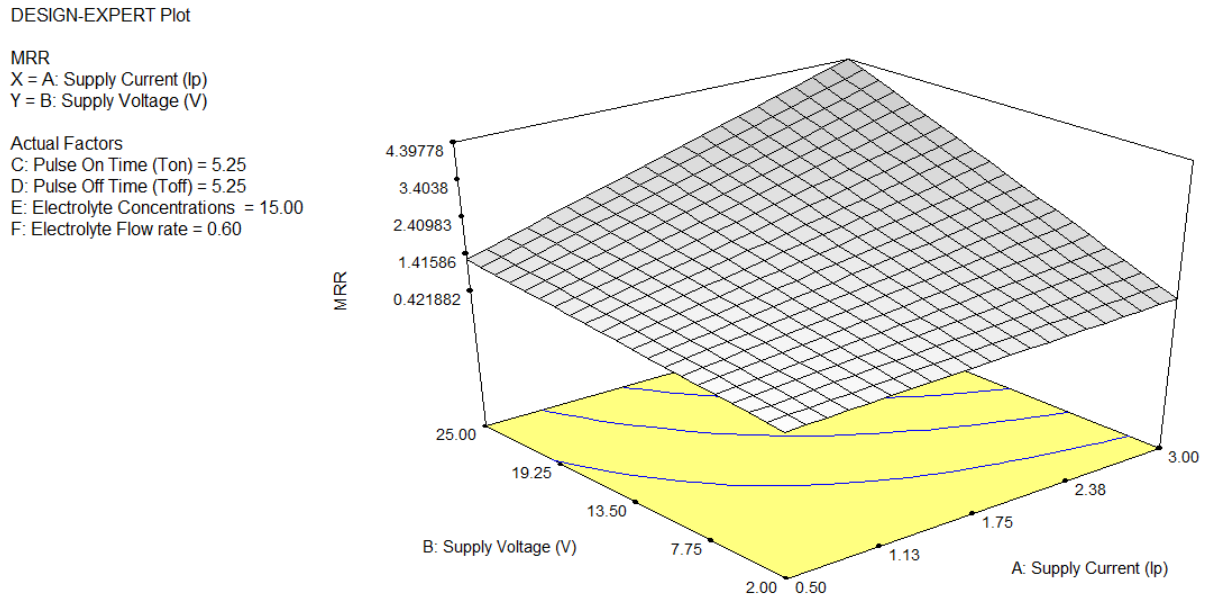

Fig 4.34 Interaction Effects of Supply Current and Supply Voltage on MRR

Figure 4.34 shows the interaction effects of supply current and supply voltage on MRR. From Figure 4.34, it is clear that MRR increases with increase in both supply current and the supply voltage. As per Faraday's law, the material dissolution is proportional to the supply current. The material removal rate rises with supplying more current and as a result dissolution efficiency increases. The machining current increases in the IEG with the increase in supply voltage. This results in higher MRR with raise in voltage. During experiments, it was observed that very less material could be removed when experiments were performed below 10 V supply voltage. This was because the ECM energy was not enough to decompose the workpiece material. Again, with increase in supply voltage there was an increase in potential difference between cathode and anode, which intensively increased electrolyte ionization, and current density, which in turn increased MRR. Therefore, material removal rate increases with increase in dissolution efficiency.

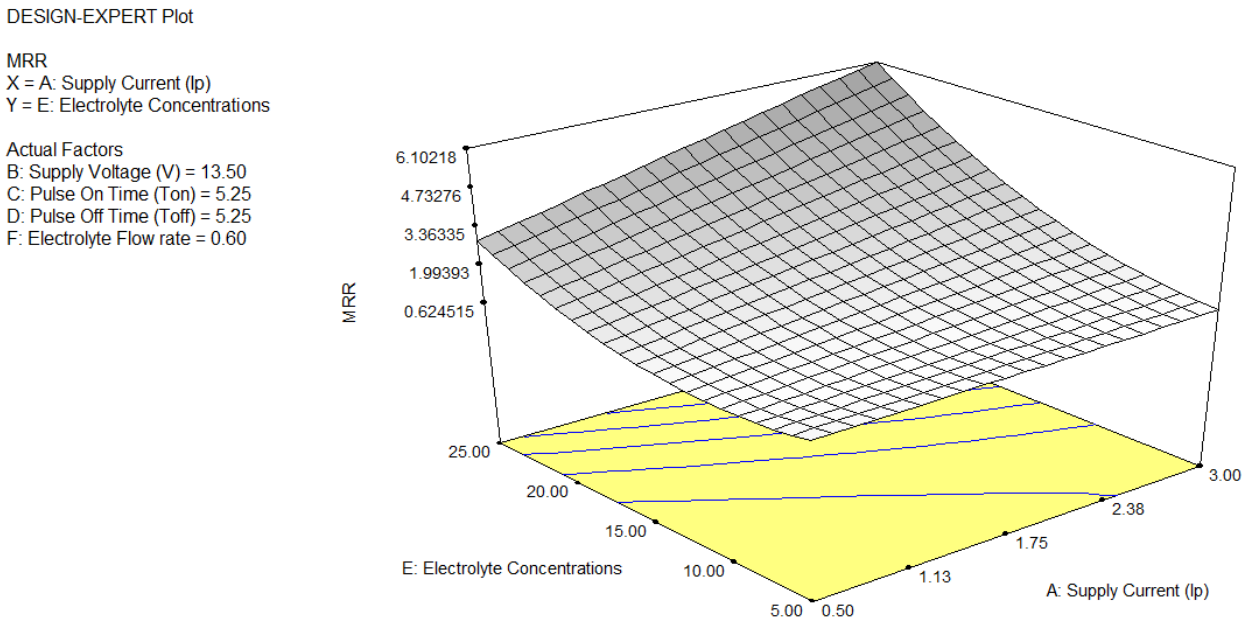

Fig 4.35 Interaction Effects of Electrolyte Concentration and Supply Current on MRR

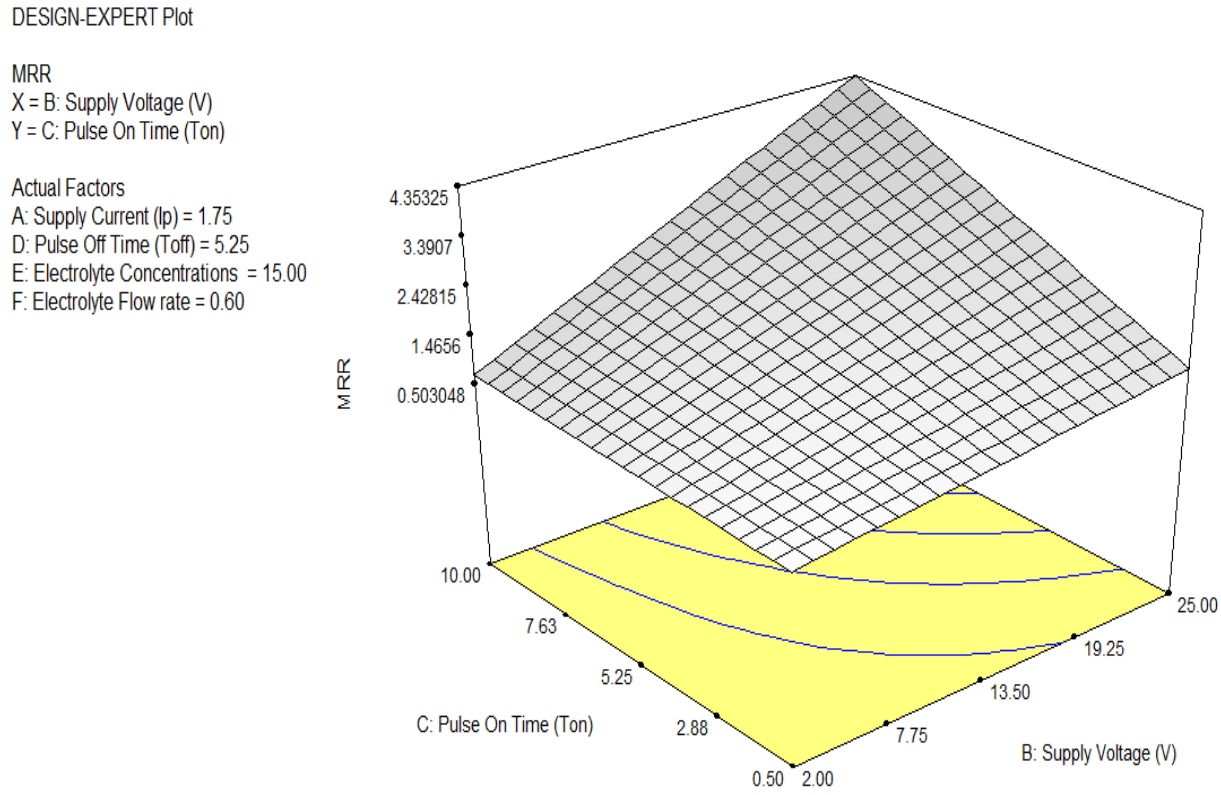

Fig 4.36 Interaction Effects of Pulse On Time and Supply Voltage on MRR

Figure 4.35 shows the interaction effects of electrolyte concentration and supply current on MRR. From Figure 4.35, it is noticed that the MRR increases with increase in both electrolyte concentration and supply current. By increasing the concentration of electrolyte, the MRR increases. This is due to increase of the conductance of electrolyte with the increase in

electrolyte concentration. The large number of ions associated in the IEG at higher concentration of electrolyte means increase the machining current and conductivity; thus increase the material removal rate. Figure 4.36 shows the interaction effects of pulse on time and supply voltage on MRR. From Figure 4.36, it is noticed that the MRR increases with increase in both the pulse on time and the supply voltage. It is also noticed that the MRR rises with rise in pulse on time. When the pulse on time is too short, material dissolution is negligible. With increase in the supply of pulse on time, both the faradic current and the period of faradic current increases, and there by the amount of faradic effect increases rapidly. Enlarge in pulse on time implies that more time allowed for machining and thereby increases dissolution efficiency. Hence the Material removal rate increases and machining time decreases with increase in pulse-on-time.

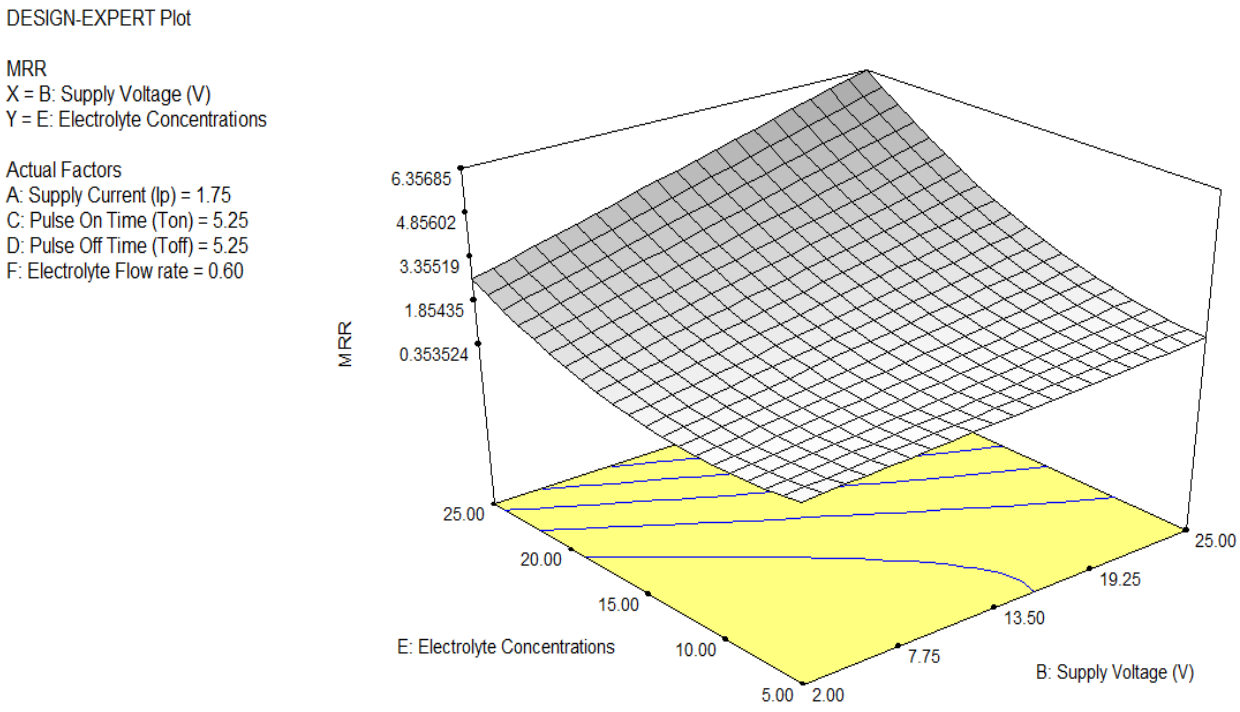

Fig 4.37 Interaction Effects of Electrolyte Concentration and Supply Voltage on MRR

Figure 4.37 shows the interaction effects of electrolyte concentration and supply voltage on MRR. From Figure 4.37, it is clear that the MRR increases with increase in both electrolyte concentration and supply voltage. Figure 4.38 shows the interaction effects of electrolyte concentration and pulse on time on MRR. From Figure 4.38, it is clear that the MRR increases with increase in both the electrolyte concentration and the pulse on time.

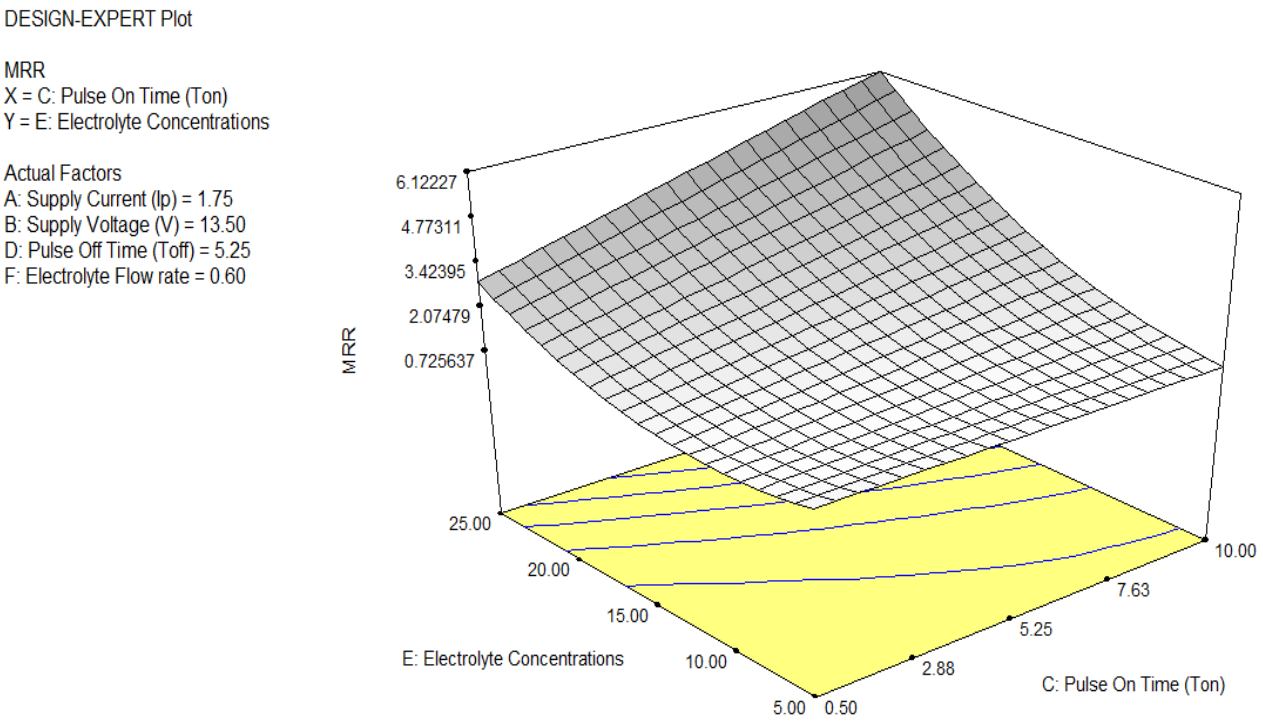

Fig 4.38 Interaction Effects of Electrolyte Concentration and Pulse On Time on MRR

4.5 EFFECT OF ECMM PARAMETERS ON EWR

The term electrode wear rate (EWR) is the loss of electrode weight during micro drilling of hybrid MMC. To decide about the adequacy of the model, three different tests viz. sequential model sum of squares, lack of fit tests and model summary statistics were done for electrode wear rate.

Table 4.13 Selection of Adequate Model for EWR

Sequential Model Sum of Squares						
Source	**Sum of Squares**	**Df**	**Mean Square**	**F Value**	**p-Value Prob>F**	
Mean	40.30	1	40.30			
Linear	20.21	6	3.37	13.85	<0.0001	
2FI	6.43	15	0.43	2.74	0.0081	
Quadratic	3.21	6	0.54	7.79	<0.0001	suggested
Cubic	1.53	18	0.085	2.66	0.0799	Aliased
Residual	0.26	8	0.032			
Total	71.94	54	1.33			
Lack of Fit Tests						
Source	Sum of Squares	Df	Mean Square	F Value	p-Value Prob>F	
Linear	11.18	42	0.27	5.26	0.0353	
2FI	4.75	27	0.18	3.48	0.0844	
Quadratic	1.53	21	0.073	1.44	0.3651	Suggested
Cubic	2.654E-003	3	8.45E-004	0.017	0.9964	Aliased
Pure Error	0.25	5	0.051			
Model Summary Statistics						
Source	Std. Dev.	R-Squared	Adjusted R-Squared	Predicted R-Squared	PRESS	
Linear	0.49	0.6388	0.5927	0.5166	15.29	
2FI	0.40	0.8420	0.7383	0.5194	15.21	
Quadratic	0.26	0.9435	0.8848	0.7322	8.47	Suggested
Cubic	0.18	0.9919	0.9465	0.9656	1.09	Aliased

Table 4.13 display the selection of adequate model to fit EWR characteristics. It is also clear that for all the responses, the quadratic model is appropriate. The “lack of fit” test compares the residual error to the pure error from the replicated design points. The results indicate that the quadratic model in all the characteristics does not show significant lack of fit, hence, the adequacy of quadratic model is confirmed as the p-value is less than 0.5 hence quadratic model is suggested for the entire test.

4.5.1 Pooled Analysis of Variance (ANOVA) for EWR

To construct the pool ANOVA design expert 6.0 software was used. The aim of construction of pooled ANOVA is to pool the different factors together and test for significance. Table 4.14 represents the Pooled ANOVA for EWR.

Table 4.14 Pooled ANOVA for EWR

Source	Sum of Squares	DF	Mean Square	F – Value	p-value Prob>F	Status
Model	29.07	12	2.42	38.66	<0.0001	Significant
A	4.94	1	4.94	78.91	<0.0001	Significant
B	5.98	1	5.98	95.48	<0.0001	Significant
C	2.09	1	2.09	33.38	<0.0001	Significant
D	0.57	1	0.57	9.14	0.0043	Significant
E	9.09	1	9.09	145.07	<0.0001	Significant
F	0.37	1	0.37	5.89	0.0197	Significant
A^2	0.43	1	0.43	6.78	0.0128	Significant
E^2	2.69	1	2.69	43.00	<0.0001	Significant
F^2	0.87	1	0.87	13.87	0.0006	Significant
AB	1.08	1	1.08	17.20	0.0002	Significant
AE	3.43	1	3.43	54.68	<0.0001	Significant
BE	1.38	1	1.38	22.01	<0.0001	Significant

The insignificant parameters were pooled using backward elimination method. The model F-value is 38.66, which implies that model is significant. The F-value for all the sources i.e. values of Prob >F less than 0.05, which indicates the model terms are significant at 95% confidence level. From pooled ANOVA Table 4.14, it is clear that for EWR the sources A, B, C, D, E, F, the interaction terms AB, AE, BE and the quadratic terms A^2, E^2, F^2 were identified as significant parameters affecting EWR. The 'Lack of Fit' corresponding F-value is 1.27, which reveals the 'Lack of Fit' is not significant. The "Pred R-Squared" of 0.8552 is in reasonable agreement with the "Adj R-Squared" of 0.8950.

4.5.2 Final Equation in Terms of Actual Factors of EWR

By using Table 4.14, the regression equation for the EWR as a function of input process variable was developed utilized design expert 8.0 software and is given below. The coefficients

(insignificant identified from ANOVA) of some terms of the quadratic equation have been omitted. The developed mathematical model based on RSM for EWR is

$$EWR = 2.873 - 1.195\,I_p - 0.037\,V + 0.062\,T_{on} - 0.032\,T_{off} - 0.203\,E_c - 2.328\,F_r + 0.126\,I_p^2 + 0.00474\,E_c^2 + 1.682\,F_r^2 + 0.025\,I_p.V + 0.051\,I_p.E_c + 0.0025\,V.E_c \quad (4.2)$$

Figure 4.39 shows the normal probability plots of residuals for EWR. Most of residuals are found to be on a straight line which indicates that errors are normally distributed. This is the normality test to be qualified by the model for checking its validity. After this test it has been found that models are significant.

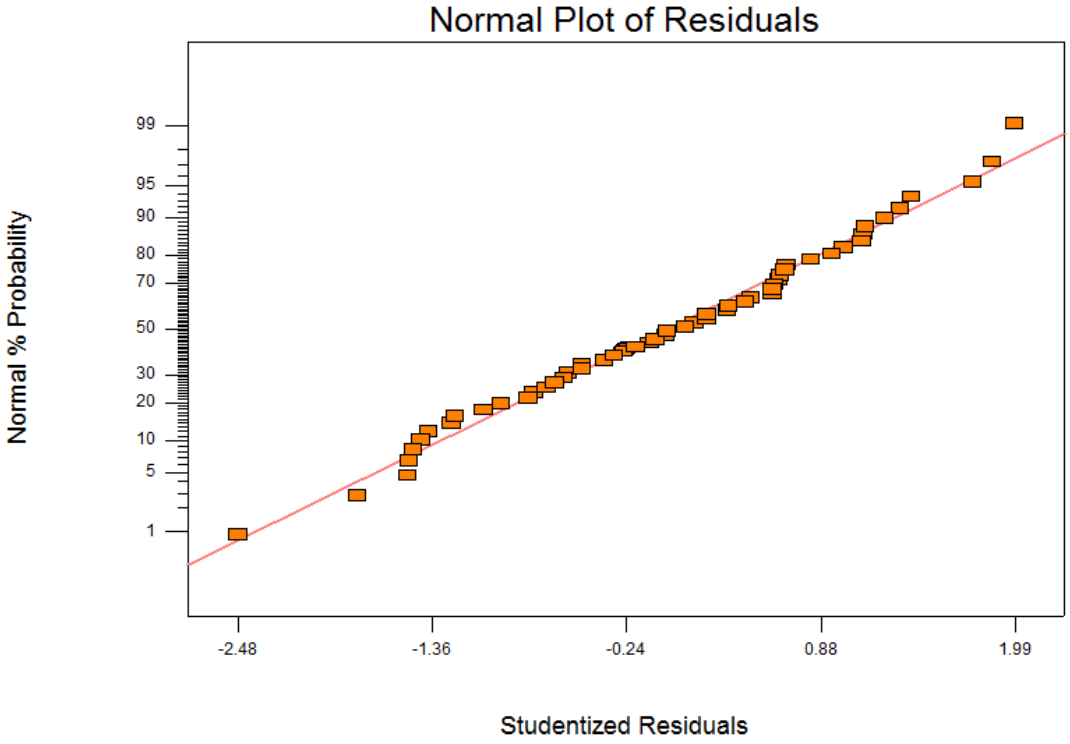

Fig 4.39 Normal Probability Plots for EWR

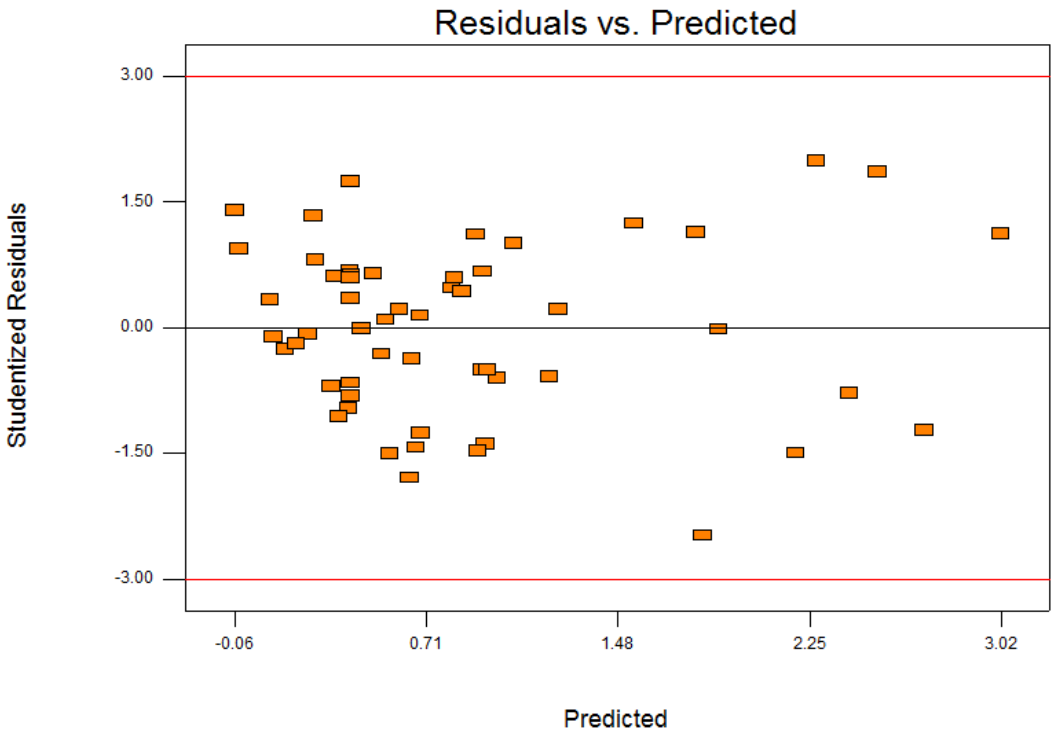

Fig 4.40 Residuals and Predicted Values for EWR

Figure 4.10 shows the residuals and predicted plot for electrode wear rate. The residuals are distributed randomly and are not clustered which indicates that model is good.

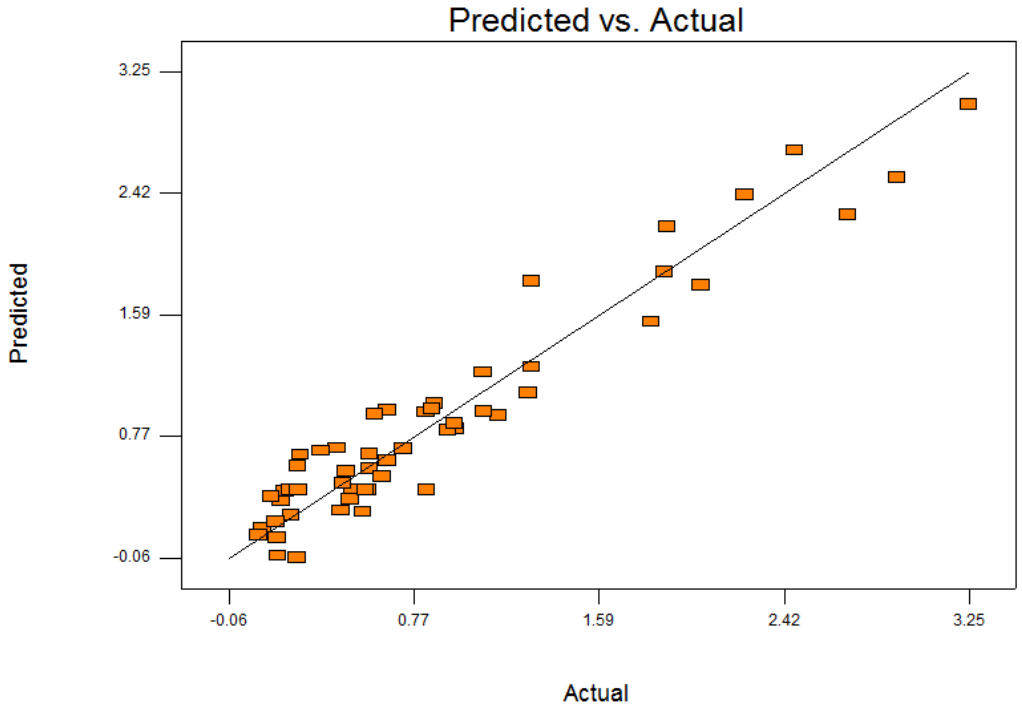

Fig 4.41 Actual and Predicted Values for EWR

Figure 4.41 shows the Predicted and Actual plot for electrode wear rate. Most of results are found to be on a straight line which indicates that errors are normally distributed. This is test to

be qualified by the model for checking its validity. From Figure 4.41, it has been found that models are significant.

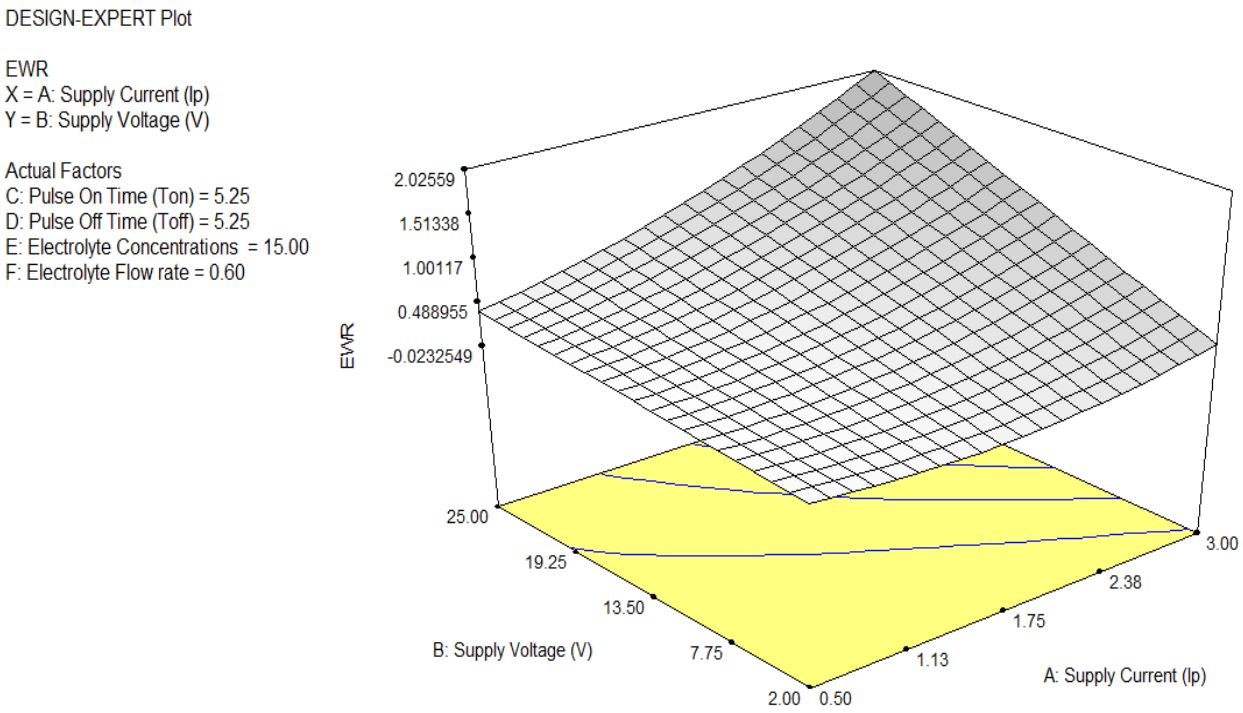

Fig 4.42 Interaction Effects of Supply Voltage and Supply Current on EWR

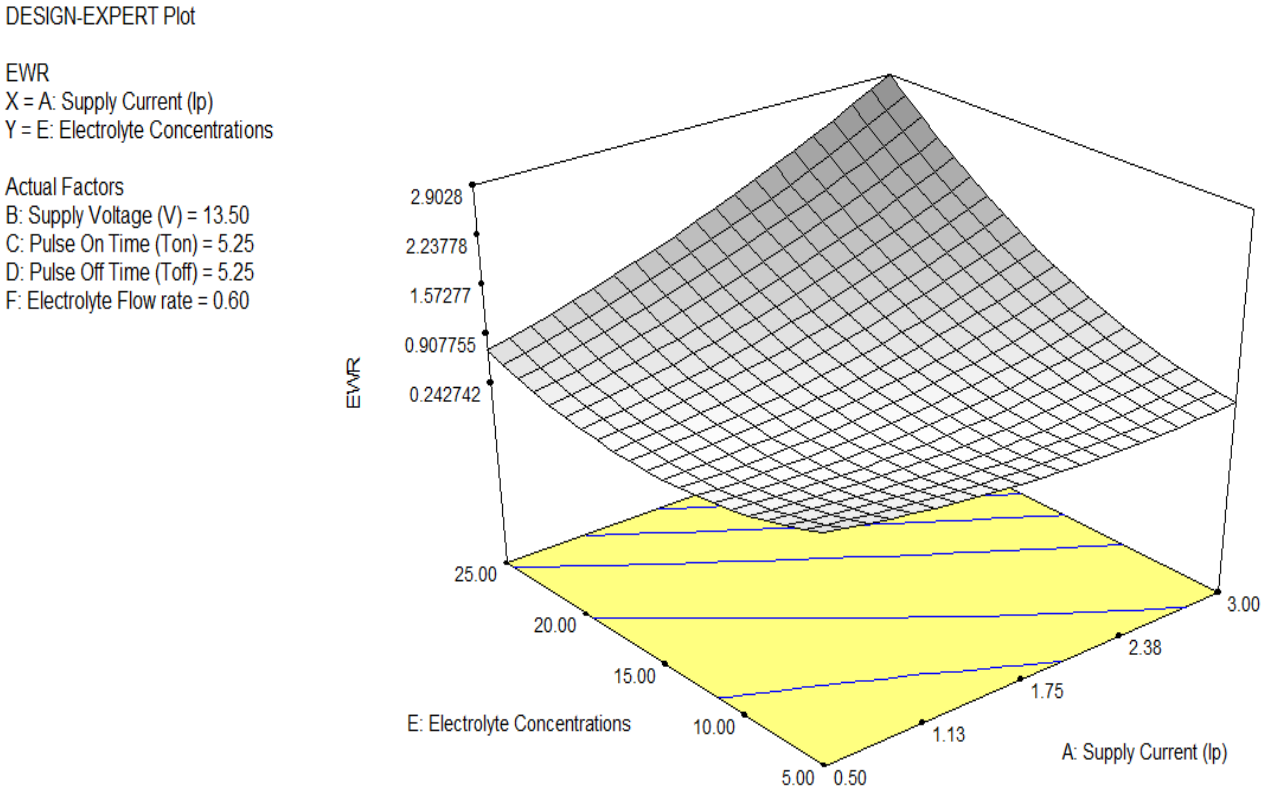

Fig 4.43 Interaction Effects of Electrolyte Concentration and Supply Current on EWR

Figure 4.42 shows the interaction effects of supply voltage and supply current on EWR. From Figure 4.42, it is noticed that the EWR increases with increase in both the supply voltage and the supply current. With increase in supply voltage there is an increase in potential difference between cathode and anode, which intensively increases electrolyte ionization, and enhances electrode wear. This is because of the increased number of the hydrogen gas bubbles at higher supply voltage, which gets entrapped between electrode and workpiece surface at IEG. Figure 4.43 shows the interaction effects of electrolyte concentration and supply current on EWR. It is observed that EWR increases with increase in both the electrolyte concentration and the supply current. The presence of machined particles in the micro machining inter electrode gap may cause sparking, which may lead to electrode wear and decreases the machining accuracy. As the electrolyte concentration is increased, the reaction rate in the IEG increases proportionally. The electrolyte conductivity and current density increases due to poor agitation rate. This leads to non-uniform reaction on the surface of the electrode due to increased number of hydrogen gas bubbles generated and reduces the length of electrode with increase in electrolyte concentration.

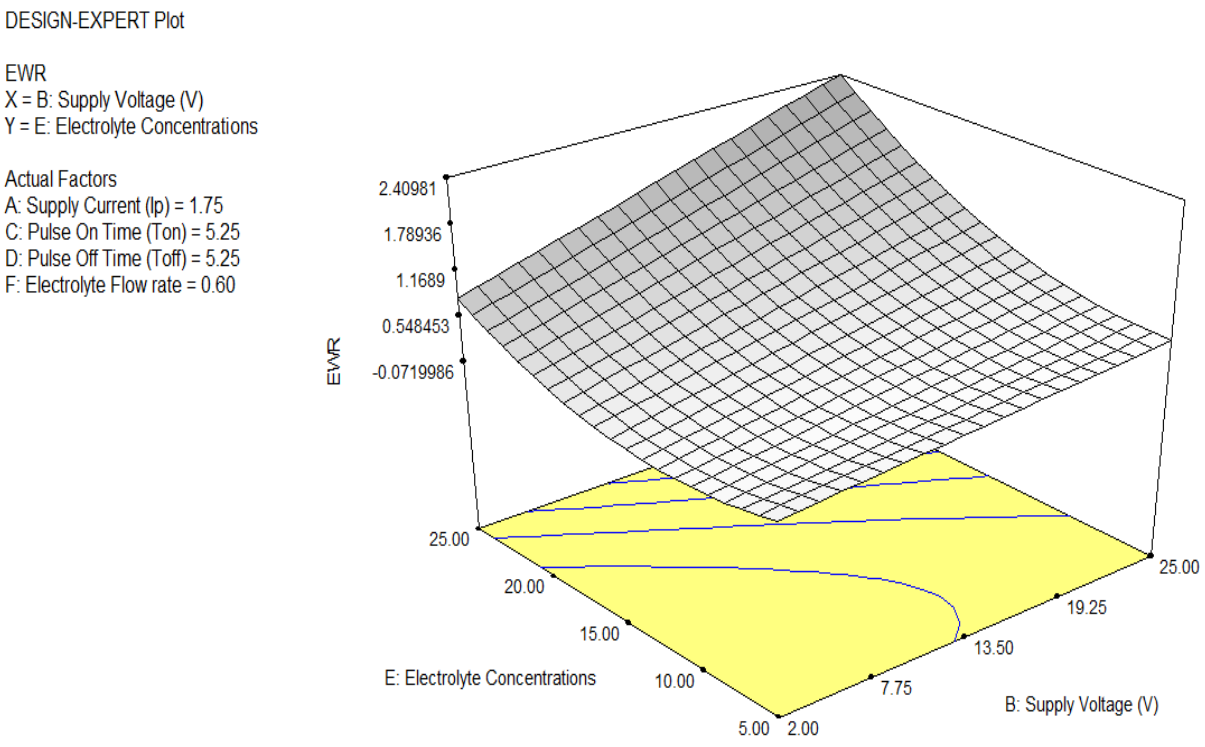

Fig 4.44 Interaction Effects of Electrolyte Concentration and Supply Voltage on EWR

Figure 4.44 shows the interaction effects of electrolyte concentration and supply voltage on EWR. It is observed that EWR increases with increase in both electrolyte concentration and supply voltage.

4.6 EFFECT OF ECMM PARAMETERS ON SURFACE ROUGHNESS

The surface roughness height (Ra) was measured by Surfcom 130A surface roughness measuring instrument whose cut-off and measuring length are 0.8 and 4 mm respectively. Three readings were during measuring of surface roughness height (R_a, µm) and average value was taken for analysis. To decide about the adequacy of the model, three different tests viz. sequential model sum of squares, lack of fit tests and model summary statistics were performed for R_a.

Table 4.15 Selection of Adequate model for SR

Sequential Model Sum of Squares						
Source	**Sum of Squares**	**Df**	**Mean Square**	**F Value**	**p-Value Prob>F**	
Mean	812.24	1	812.24			
Linear	90.83	6	15.14	6.88	<0.0001	
2FI	48.52	15	3.23	1.88	0.0650	
Quadratic	43.24	6	7.21	16.05	<0.0001	Suggested
Cubic	7.18	18	0.40	0.71	0.2384	Aliased
Residual	4.49	8	0.56			
Total	1006.51	54	18.64			
Lack of Fit Tests						
Source	Sum of Squares	Df	Mean Square	F Value	p-Value Prob>F	
Linear	101.33	42	2.41	5.72	0.0294	
2FI	52.81	27	1.96	4.64	0.0472	
Quadratic	9.57	21	0.46	1.08	0.5159	Suggested
Cubic	2.38	3	0.79	1.88	0.2500	Aliased
Pure Error	2.11	5	0.42			
Model Summary Statistics						
Source	Std. Dev.	R-Squared	Adjusted R-Squared	Predicted R-Squared	PRESS	
Linear	1.48	0.4676	0.3996	0.3035	135.31	
2FI	1.31	0.7173	0.5318	0.2718	141.47	
Quadratic	0.67	0.9399	0.8775	0.7468	49.18	Suggested
Cubic	0.75	0.9769	0.8468	-2.3162	644.23	Aliased

The Table 4.15 represents the adequate model to fit surface roughness height, R_a. From Table 4.15, it is noticed that for all the responses, the quadratic model is appropriate. The "lack of fit" test compares the residual error to the pure error from the replicated design points. The results indicate that the quadratic model in all the characteristics does not show significant lack of fit, hence the adequacy of quadratic model is confirmed as value of p is less than 0.5.

4.6.1 Pooled Analysis of Variance (ANOVA) for SR

To construct the pool ANOVA design expert 6.0 software was used. The aim of construction of pooled ANOVA is to pool the different factors together and test for significance. Table 4.16 represents Pooled ANOVA for SR.

Table 4.16 Pooled ANOVA for SR

Source	Sum of Squares	DF	Mean Square	F Value	p-value Prob>F	Status
Model	179.75	15	11.98	31.36	<0.0001	Significant
A	38.81	1	38.81	101.57	<0.0001	Significant
B	9.28	1	9.28	24.29	<0.0001	Significant
C	9.22	1	9.22	24.14	<0.0001	Significant
D	5.81	1	5.81	15.19	0.0004	Significant
E	6.08	1	6.08	15.90	0.0003	Significant
F	22.82	1	22.82	59.71	<0.0001	Significant
A^2	2.86	1	2.86	7.50	0.0094	Significant
C^2	34.61	1	34.61	90.58	<0.0001	Significant
D^2	10.22	1	10.22	26.74	<0.0001	Significant
E^2	8.91	1	8.91	23.33	<0.0001	Significant
BE	2.22	1	2.22	5.82	0.0002	Significant
CD	5.80	1	5.80	15.17	0.0208	Significant
CE	10.22	1	10.22	26.75	0.0004	Significant
CF	20.19	1	20.19	52.83	<0.0001	Significant
DF	7.65	1	7.65	20.03	<0.0001	Significant

The insignificant parameters were pooled using backward elimination method. The model F-value is 31.36, which implies that model is significant. The values of Prob >F less than 0.05 for model, which indicates the model terms are significant at 95% confidence level. From pooled ANOVA Table 4.16, it is clear that for R_a the sources i.e. parameters A, B, C, D, E, F; the

interaction terms of parameters i.e. BE, CD, CE, CF, DF and the quadratic terms parameters i.e. A^2, C^2, D^2, E^2 were significant parameters affecting the R_a (µm). The F-value corresponding 'Lack of Fit' is 0.89, it reveals the 'Lack of Fit' is not significant. The "Pred R-Squared" is 0.8524 which makes a reasonable agreement with the "Adj R-Squared" of 0.8958.

4.6.2 Final Equation in Terms of Actual Factors of SR

By using Table 4.16, the regression equation for R_a as a function of input process variable was developed using the Design expert 8.0 software. The coefficients (insignificant identified from ANOVA) of some terms of the quadratic equation have been omitted. The developed mathematical model based for R_a (µm) is

$$SR = 2.973 - 0.202\ I_p + 0.00543\ V + 0.234\ T_{on} - 0.464\ T_{off} - 0.131\ E_c - 2.040\ F_r + 0.348\ I_p^2 + 0.076\ T_{on}^2 + 0.043\ T_{off}^2 + 0.00875\ E_c^2 + 0.00324\ I_p\ E_c - 0.037\ T_{on}\ .T_{off} - 0.023\ T_{on}.E_c - 0.590\ T_{on}.F_r + 0.514\ T_{off}.F_r \quad (4.3)$$

Figure 4.45 shows the normal probability plots of residuals for SR (R_a, µm). Most of residuals are found to be on a straight line which indicates that errors are normally distributed. From Figure 4.45, it has been found that models are significant.

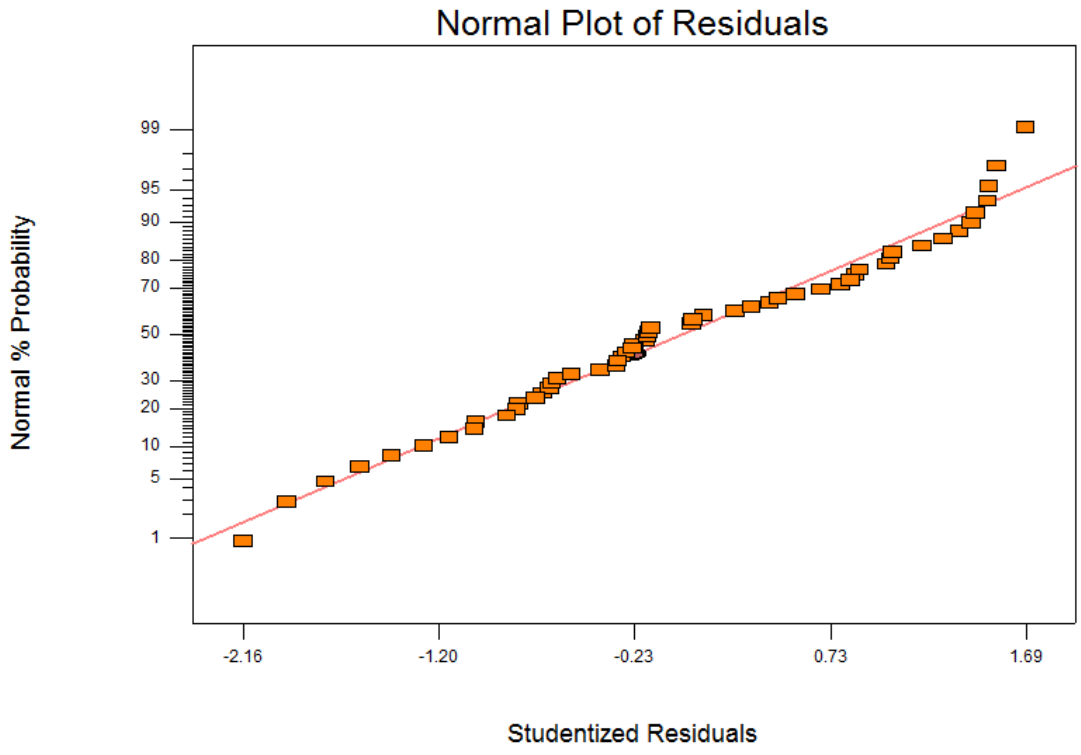

Fig 4.45 Normal Probability Plots for SR (R_a, µm)

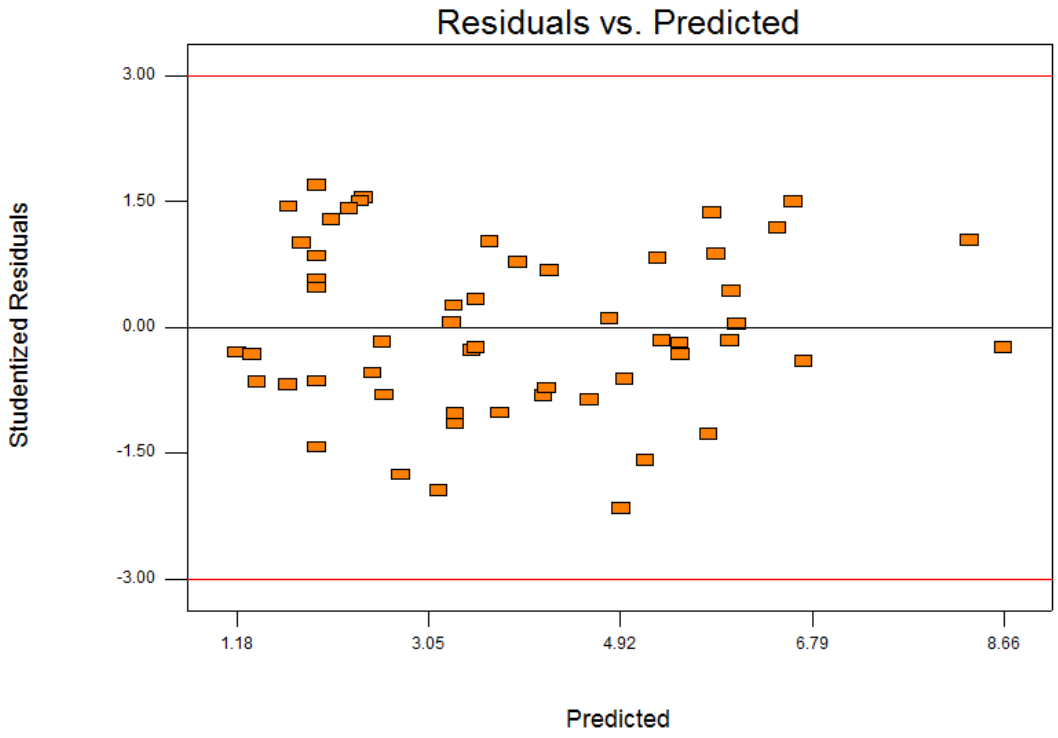

Fig 4.46 Residuals and Predicted Values for SR (R_a, µm)

Figure 4.46 shows the residuals and predicted plot for SR (R_a, µm). The residuals are distributed randomly and are not clustered which indicates that model is good.

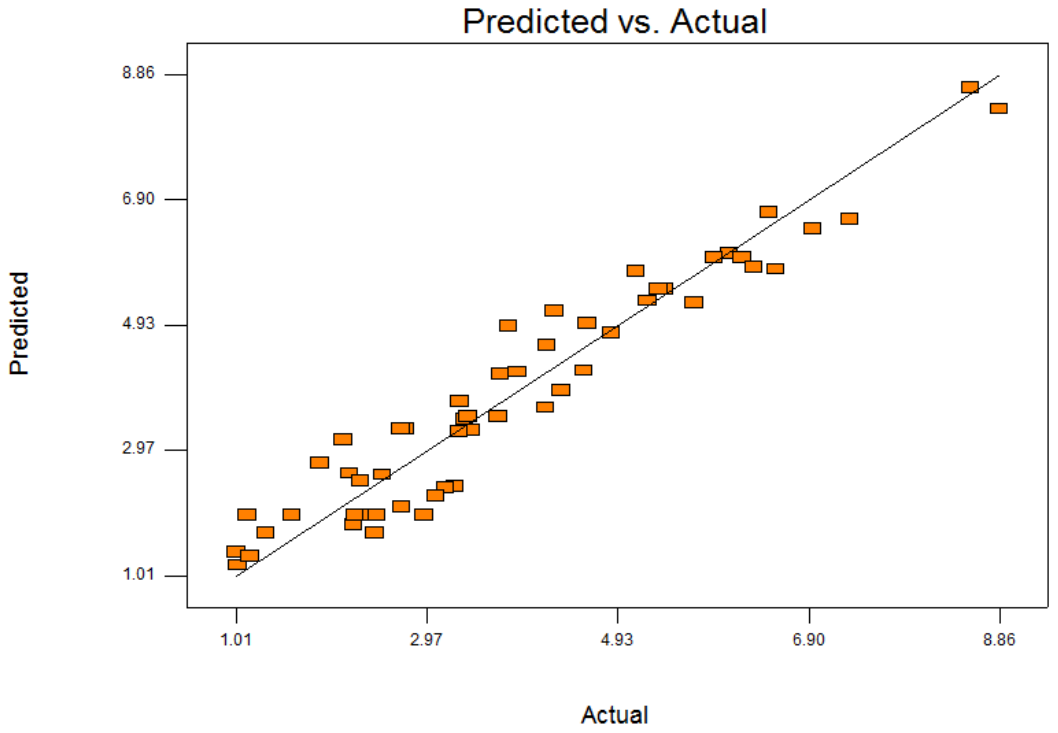

Fig 4.47 Actual and Predicted Values for SR (R_a, µm)

Figure 4.47 shows the Predicted and Actual plot for SR (R_a, µm). Most of results are found to be on a straight line which indicates that errors are normally distributed. This is test to be

qualified by the model for checking its valid it. From Figure 4.47, it is found that models are significant. Figure 4.48 shows the interaction effects of electrolyte concentration and supply voltage on SR (R_a, µm). It is observed that SR increases with increase in both electrolyte concentration and supply voltage. By increasing the concentration of electrolyte, the surface roughness height (R_a, µm) was increased. The large number of ions associated in the IEG at higher concentration of electrolyte means increase the current density and conductivity. Due to increase of current density increases the tendency of pitting, it leads to the generation of rough surface. A higher electrolyte concentration produces non-uniform and irregular machined holes. This irregularity on micro hole may be due to improper cleaning of sludge particles with the flow of electrolyte from the inter electrode gap (IEG). Hence, surface roughness height (R_a, µm) increases with increase in electrolyte concentration, because of more quantity of melted material are removed and larger discharge craters are induced in the workpiece surface. In addition, the dissolution product can stack up easily and unusual dissolution of materials can be induced further. This is because of unsteady and non-uniform metallic dissolution. This phenomenon causes the entrance of micro-hole to be larger and so the surface finish becomes worse.

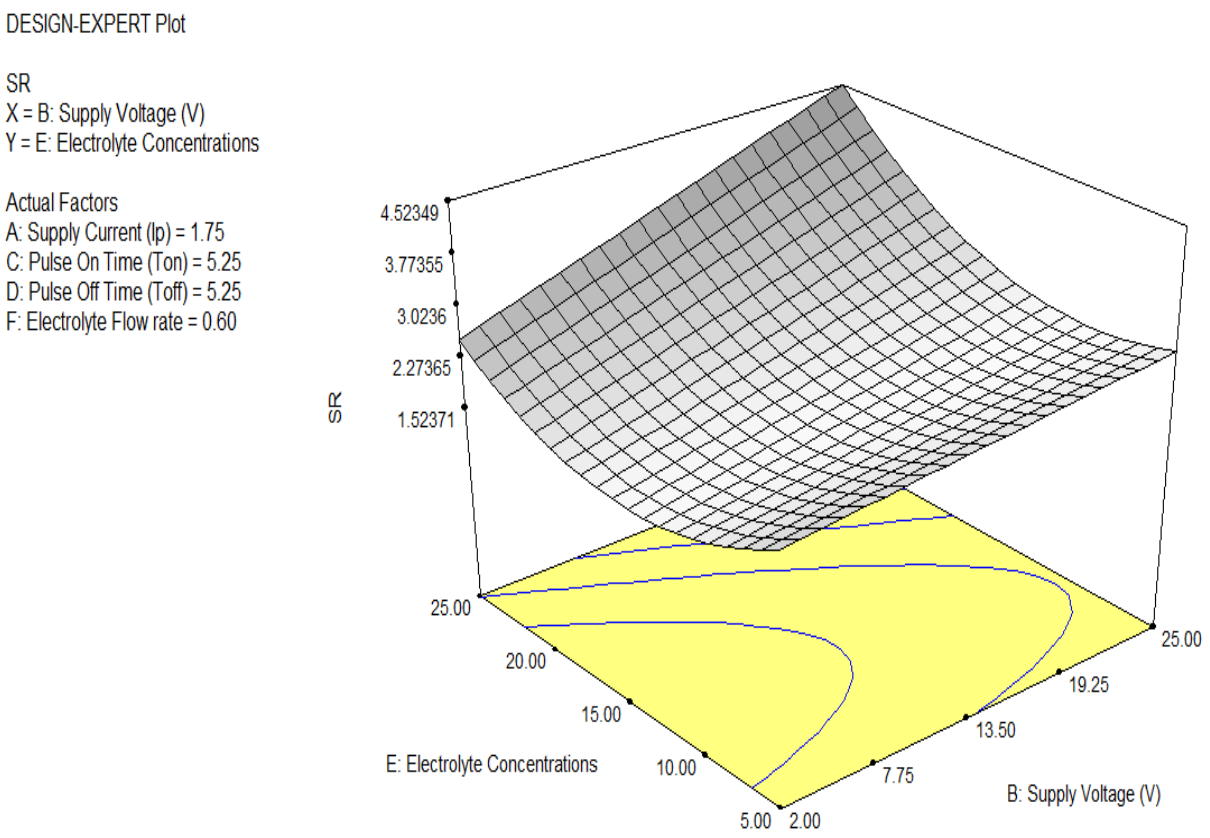

Fig 4.48 Interaction Effects of Electrolyte Concentration and Supply Voltage on SR

The surface roughness height (Ra) increases with increase in supply voltage. The heat produced and the current density between the inter electrodes gap (IEG) increases by

increasing the supply voltage. The higher current density in the IEG generates non-uniform and higher dissolution of metal, as a result in deep grain boundary attack identified on the metal surface. Sometimes pitting on metal surfaces also occurs, thereby increases surface roughness height (R_a, µm).

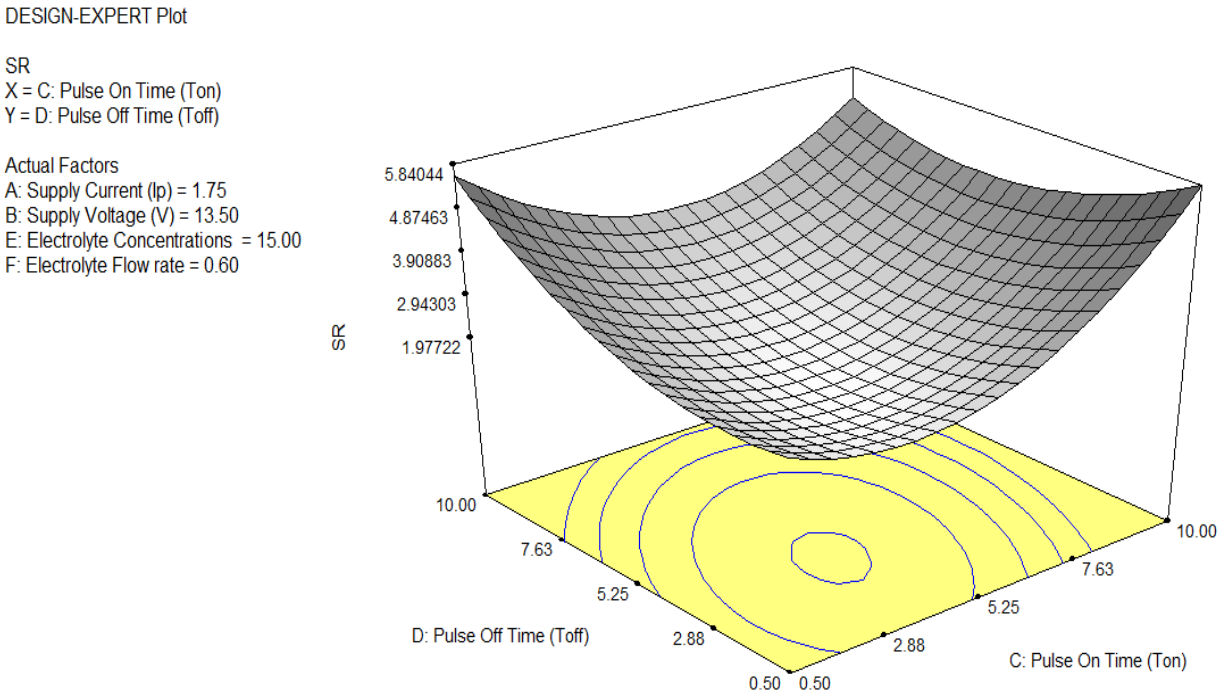

Fig 4.49 Interaction Effects of Pulse Off Time and Pulse On Time on SR (R_a, µm)

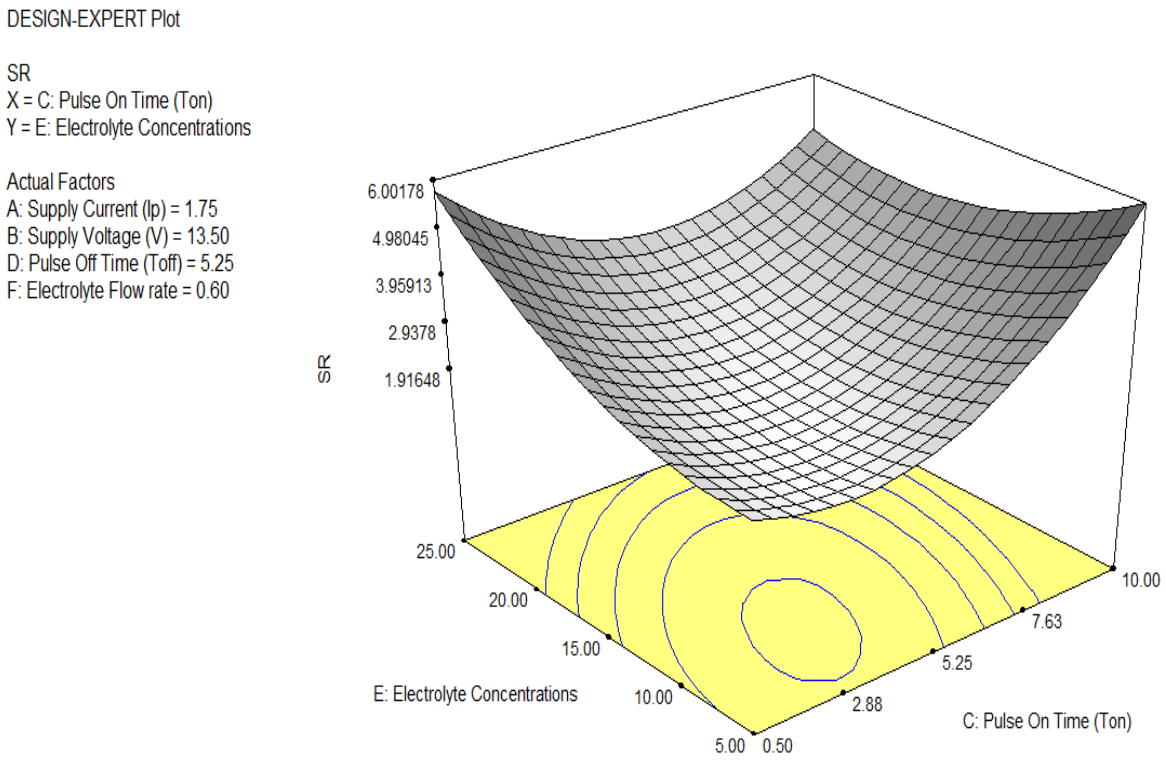

Fig 4.50 Interaction Effects of Electrolyte Concentration and Pulse On Time on SR (R_a, µm)

Figure 4.49 shows the interaction effects of pulse off time and pulse-on-time on SR **(R_a, µm)**. It is observed that SR increases with increase in pulse-on-time and with decrease in pulse off time. Figure 4.50 shows the interaction effects of electrolyte concentration and pulse-on-time on SR (R_a, µm). From Figure 4.50, it is noticed that the SR increases with increase in both electrolyte concentration and pulse on time. The surface roughness height (Ra) decreases with rise in pulse-on-time. At higher pulse on time, generation of sparks starts and the localization effect reduces due to the improper flushing of electrolyte, thereby the debris cannot be fully flushed out from the IEG. Thus, the surface roughness height (R_a, µm) increases due to non-uniform metallic dissolution of material. The surface roughness height, Ra decreases due to rise in pulse off time, but it is up to a certain limit. Again, because of increase the time duration of machining that allows flushing and removes sludge particles from the machining zone.

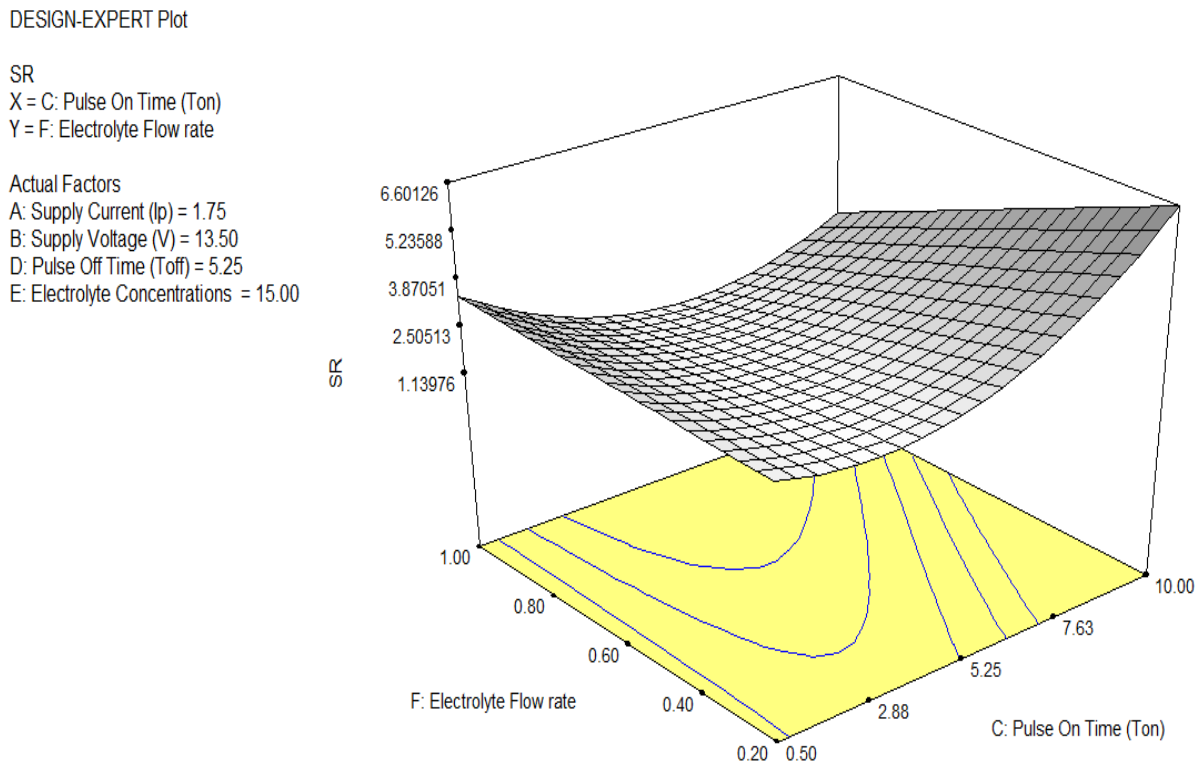

Fig 4.51 Interaction Effects of Electrolyte Flow Rate and Pulse On Time on SR (R_a, µm)

Figure 4.51 shows the interaction effects of electrolyte flow rate and pulse on time on SR (R_a, µm). It is observed that SR increases with increase in pulse on time. The surface roughness height (Ra) decreases by increasing the electrolyte flow rate. It is because of large flushing pressure, which helps to remove the debris from the machining zone. Increased electrolyte flow rate, the turbulence being high, the effect of rotating eddies will be reduced and no flow streak appears on the surface results in better surface finish.

4.7 EFFECT OF ECMM PARAMETERS ON TAPER CUT

The taper cut was determined from the difference of inlet diameter and exit diameter of each machined hole. To decide about the adequacy of the model, three different tests viz. sequential model sum of squares, lack of fit test and model summary statistics were performed for taper cut (TC). Table 4.17 display the adequate model for taper cut.

Table 4.17 Selection of Adequate Model for TC

Sequential Model Sum of Squares						
Source	**Sum of Squares**	**Df**	**Mean Square**	**F Value**	**p-Value Prob>F**	
Mean	1.748E+007	1	1.748E+007			
Linear	1.462E+006	6	2.436E+005	18.43	<0.0001	
2FI	3.180E+005	15	21199.16	2.24	0.0275	
Quadratic	1.828E+005	6	30474.53	6.57	0.0003	suggested
Cubic	93638.19	18	5202.12	1.55	0.2698	Aliased
Residual	26880.90	8	3360.11			
Total	1.956E+007	54	3.622E+005			
Lack of Fit Tests						
Source	Sum of Squares	Df	Mean Square	F Value	p-Value Prob>F	
Linear	6.001E+005	42	14287.21	3.36	0.0888	
2FI	2.821E+005	27	10447.24	2.47	0.1608	
Quadratic	99228.25	21	4725.15	1.11	0.5014	Suggested
Cubic	5590.07	3	1863.36	0.44	0.7360	Aliased
Pure Error	21290.83	5	4258.17			
Model Summary Statistics						
Source	Std. Dev.	R-Squared	Adjusted R-Squared	Predicted R-Squared	PRESS	
Linear	114.98	0.7017	0.6636	0.6003	8.325E+005	
2FI	97.37	0.8544	0.7588	0.5662	9.036E+005	
Quadratic	68.08	0.9421	0.8821	0.7342	5.536E+005	Suggested
Cubic	57.97	0.9871	0.9145	0.2944	1.470E+006	Aliased

From Table 4.17, it is noticed that for all the responses, the quadratic model is appropriate. The "lack of fit" test compares the residual error to the pure error from the replicated design points.

The results indicate that the quadratic model in all the characteristics does not show significant lack of fit, hence the adequacy of quadratic model is confirmed as value of p is less than 0.5.

4.7.1 Pooled Analysis of Variance (ANOVA) for Taper cut (TC)

To construct the pool ANOVA design expert 8.0 software was used. The aim of construction of pooled ANOVA is to pool the different factors together and test for significance. Table 4.18 represents Pooled ANOVA for TC.

Table 4.18 Pooled ANOVA for Taper Cut

Source	Sum of Squares	DF	Mean Square	F Value	p-value Prob>F	Status
Model	1.899E+006	11	1.726E+005	39.40	< 0.0001	Significant
A	5.748E+005	1	5.748E+005	131.18	< 0.0001	Significant
B	3.806E+005	1	3.806E+005	86.88	< 0.0001	Significant
C	81154.52	1	81154.52	18.52	< 0.0001	Significant
D	68829.26	1	68829.26	15.71	0.0003	Significant
E	2.495E+005	1	2.495E+005	56.94	< 0.0001	Significant
F	1.298E+005	1	1.298E+005	29.63	< 0.0001	Significant
E^2	1.068E+005	1	1.068E+005	24.38	< 0.0001	Significant
F^2	1.006E+005	1	1.006E+005	22.96	< 0.0001	Significant
AC	1.185E+005	1	1.185E+005	27.04	< 0.0001	Significant
AD	61241.59	1	61241.59	13.98	0.0006	Significant
BE	84623.46	1	84623.46	19.31	< 0.0001	Significant

Table 4.18 represents the Pooled ANOVA for Taper Cut. From Table 4.18, it is clear that the model is significant for taper cut. The model corresponding F-value is 39.40, which reveals that the model is significant. Values of "Prob > F" less than 0.05, which indicates model terms are also significant. In this case, parameters A, B, C, D, E, F and interactions AC, AD, BE as well as quadratic terms E^2, F^2 are significant model terms. The "Lack of Fit F-value" is 1.03 that implies the Lack of Fit is not significant relative to the pure error. The "Pred R-Squared" is 0.8495 that makes a reasonable agreement with the "Adj R-Squared" (0.8885).

4.7.2 Final Equation in Terms of Actual Factors of TC

By using Table 4.18, the regression equation for the taper cut as a function of input process variable was developed using the software (RSM) and is given below.

$$\text{Taper Cut} = 128.261 + 283.243\ \text{Ip} + 1.463\ \text{V} + 47.911\ \text{Ton} + 6.802\ \text{Toff} - 25.762\ \text{EC} - 481.640\ \text{FR} + 0.914\ \text{EC}^2 + 554.578\ \text{FR}^2 - 20.207\ \text{Ip . Ton} - 10.346\ \text{Ip. Toff} + 0.632\ \text{V. EC} \quad (4.4)$$

Figure 4.52 show the normal probability plots for TC. Most of residuals are found to be on a straight line which indicates that errors are normally distributed. This is the normality test to be qualified by the model for checking its validity. From Figure 4.52 and Table 4.20, it is clear that the models are significant.

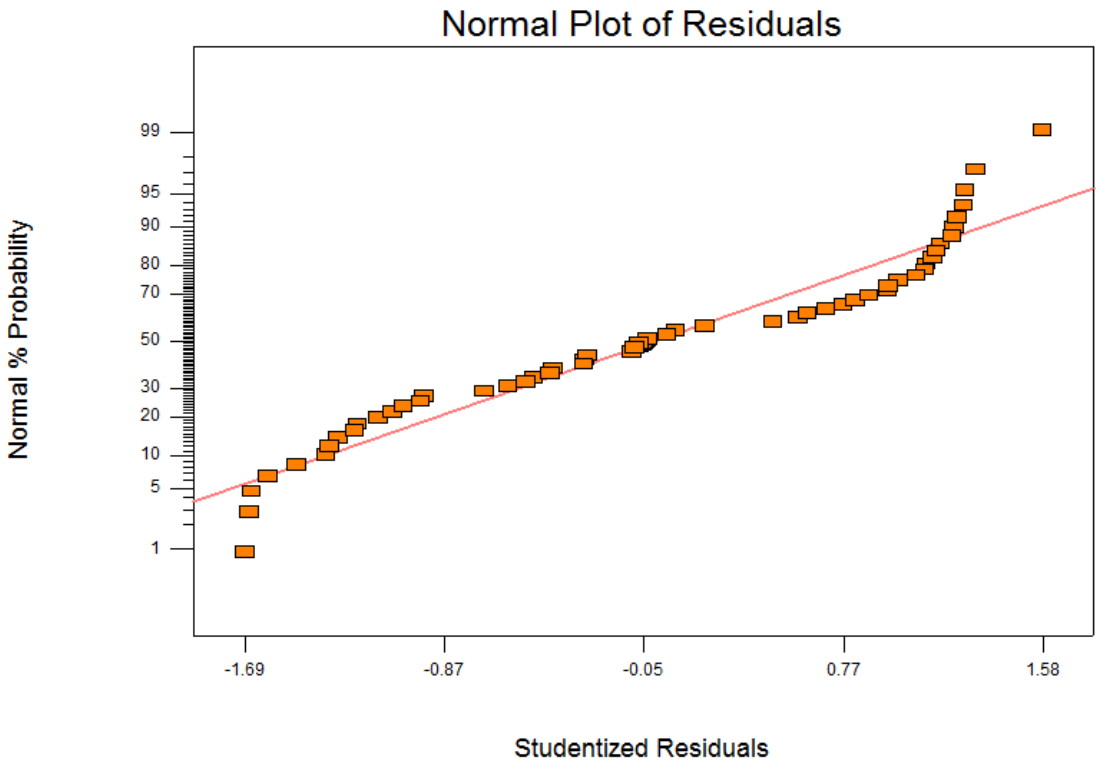

Fig 4.52 Normal Probability Plots for TC

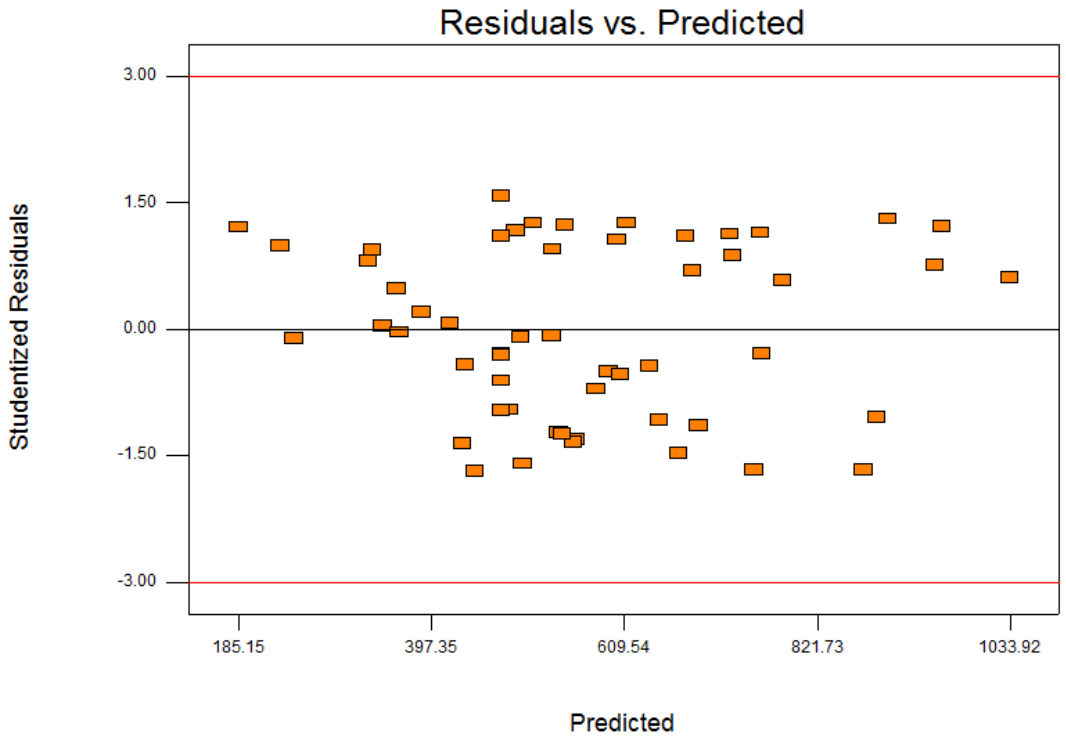

Fig 4.53 Residuals and Predicted Values for TC

Figure 4.53 shows the residuals and predicted plot for taper cut. The residuals are distributed randomly and are not clustered which indicates that model is good.

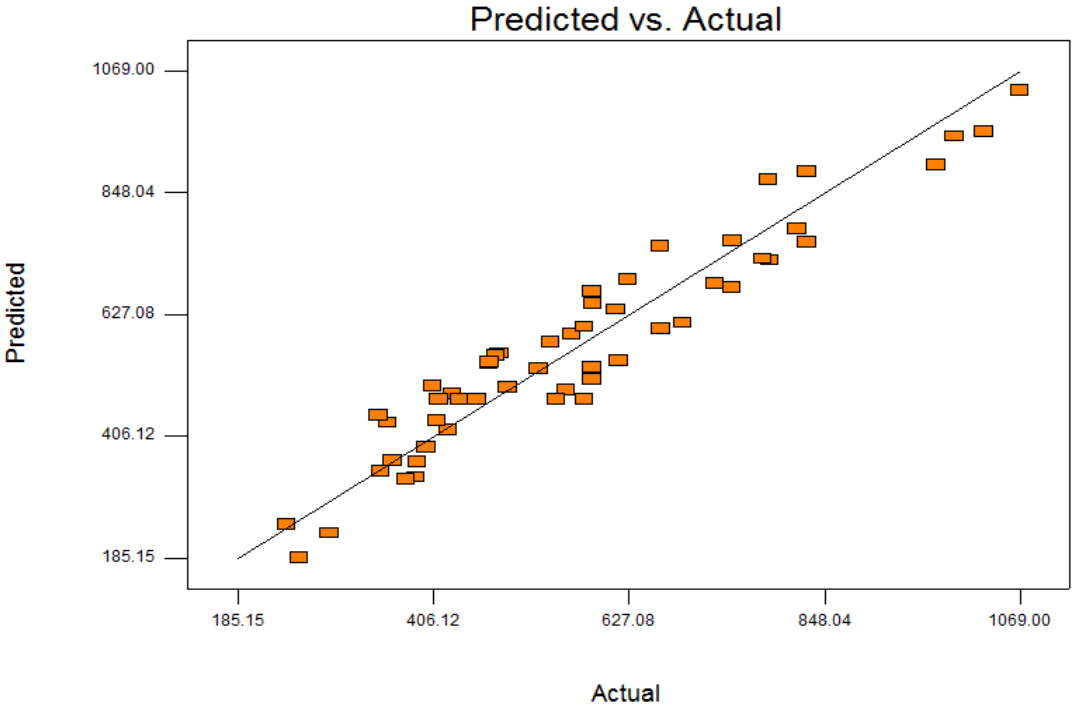

Fig 4.54 Actual and Predicted Values for TC

Figure 4.54 shows the predicted and actual plot for taper cut. Most of the results are found to be on a straight line, which indicates that errors are normally distributed. This is test to be

qualified by the model for checking its validity. From Figure 4.54, it is found that models are significant.

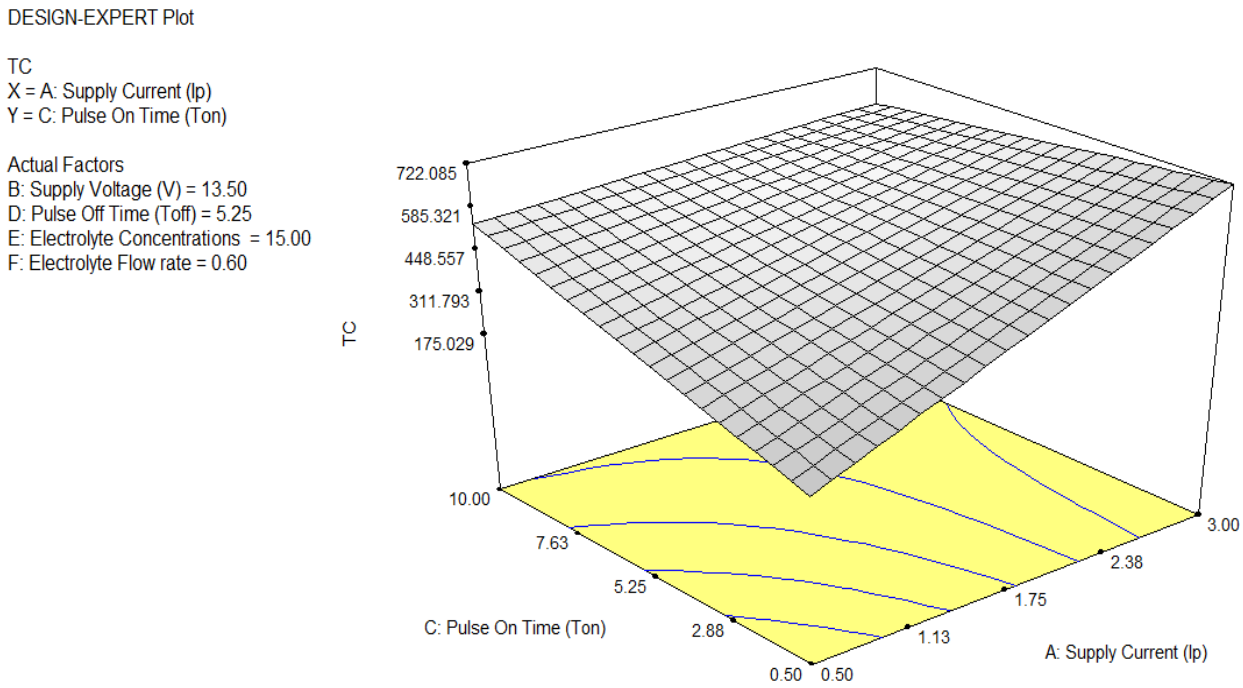

Fig 4.55 Interaction Effects of Pulse On Time and Supply Current on TC

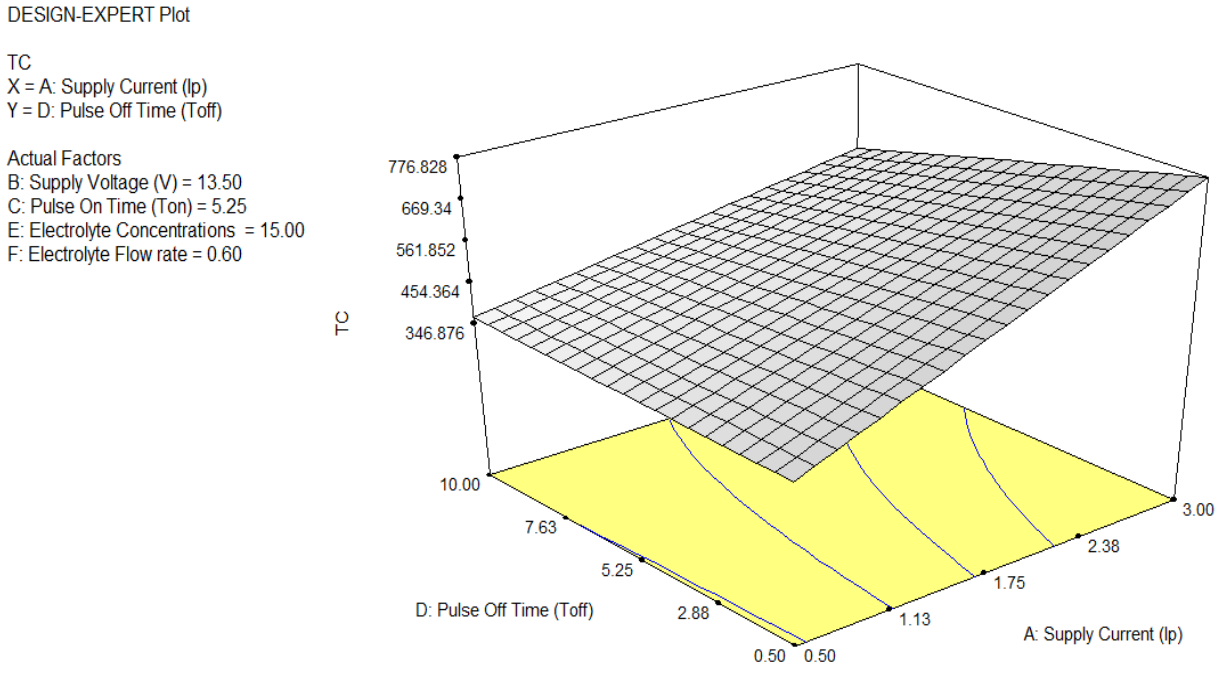

Fig 4.56 Interaction Effects of Pulse Off Time and Supply Current on TC

Figure 4.55 shows the interaction effects of pulse on time and supply current on TC. It is observed that TC increases with increase in both pulse on time and supply current. The supply of high current produces non-uniform and irregular machined hole. This may be due to

improper cleaning of sludge particles from the inter electrode gap (IEG) during machining. Therefore, taper cut increases with increase in supply current. Both supply current and time period increase with increase in pulse on time, thereby enhance dissolution of material along the radial direction and increases taper cut. Figure 4.56 shows the interaction effects of pulse off time and supply current on TC. From Figure 4.56, it is clear that TC increases with increase in supply current. Figure 4.57 shows the interaction effects of electrolyte concentration and supply voltage on TC. It is observed that TC increases with increase in both electrolyte concentration and supply voltage. At higher electrolyte concentration, a large number of ions are formed during machining as a result increases machining current density. Due to higher current density, the taper cut is increased. The taper cut decreases with an increase in pulse off time. It is because of more time duration allowed for machining that may be sufficient to flush out the sludge from the machining zone.

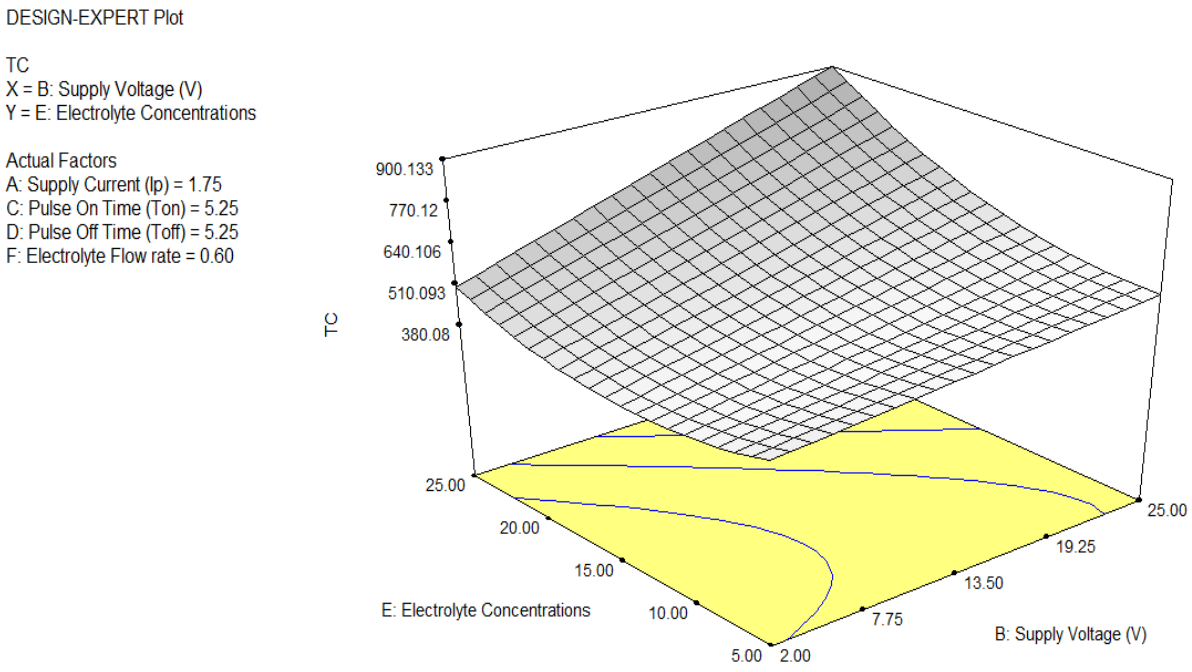

Fig 4.57 Interaction Effects of Electrolyte Concentration and Supply Voltage on TC

4.8 EFFECT OF ECMM PARAMETERS ON OVER CUT (OC)

The over cut was determined from the difference of average diameter of machined micro hole and the average diameter of micro tool. To decide about the adequacy of the model, three different tests viz. sequential model sum of squares, lack of fit tests and model summary statistics were done for over cut. Table 4.19 displays the adequate model for over cut characteristics. The sequential model sum of squares test and model summary statistics are also explained in 4.19. It can be observed that for all the responses, the quadratic model is

appropriate. The “lack of fit” test compares the residual error to the pure error from the replicated design points. The results indicate that the quadratic model in all the characteristics does not show significant lack of fit, hence the adequacy of quadratic model is confirmed as p-value is less than 0.5.

Table 4.19 Selection of Adequate Model for OC

Sequential Model Sum of Squares						
Source	**Sum of Squares**	**Df**	**Mean Square**	**F Value**	**p-Value Prob>F**	
Mean	2.170E+007	1	2.170E+007			
Linear	1.529E+006	6	2.548E+005	17.21	<0.0001	
2FI	2.898E+005	15	19320.58	1.52	0.1551	
Quadratic	2.547E+005	6	42446.16	7.30	0.0001	suggested
Cubic	1.022E+005	18	5679.75	0.93	0.5803	Aliased
Residual	49031.43	8	6128.93			
Total	2.392E+007	54	4.430E+005			
Lack of Fit Tests						
Source	Sum of Squares	Df	Mean Square	F Value	p-Value Prob>F	
Linear	6.707E+005	42	15967.88	3.18	0.0984	
2FI	3.808E+005	27	14105.28	2.81	0.1261	
Quadratic	1.262E+005	21	6007.88	1.20	0.4608	Suggested
Cubic	23929.93	3	7976.64	1.59	0.3032	Aliased
Pure Error	25101.50	5	5020.30			
Model Summary Statistics						
Source	Std. Dev.	R-Squared	Adjusted R-Squared	Predicted R-Squared	PRESS	
Linear	121.67	0.6872	0.6473	0.5805	9.331E+005	
2FI	112.63	0.8175	0.6978	0.4127	1.306E+006	
Quadratic	76.28	0.9320	0.8614	0.6795	7.129E+005	Suggested
Cubic	78.29	0.9780	0.8540	-1.8027	6.235E+006	Aliased

4.8.1 Pooled Analysis of Variance (ANOVA) for OC

To construct the pool ANOVA design expert 8.0 software was used. Table 4.20 represents Pooled ANOVA for OC. The aim of construction of the pooled ANOVA Table 4.20 is to pool the different factors together and test for significance.

Table 4.20 Pooled ANOVA for Over Cut

Source	Sum of Squares	DF	Mean Square	F Value	p-value Prob>F	Status
Model	2.027E+006	11	1.843E+005	39.25	< 0.0001	Significant
A	4.612E+005	1	4.612E+005	98.22	< 0.0001	Significant
B	4.896E+005	1	4.896E+005	104.26	< 0.0001	Significant
C	1.436E+005	1	1.436E+005	30.59	< 0.0001	Significant
D	83941.27	1	83941.27	17.87	0.0001	Significant
E	2.939E+005	1	2.939E+005	62.58	< 0.0001	Significant
F	1.468E+005	1	1.468E+005	31.26	< 0.0001	Significant
E^2	2.358E+005	1	2.358E+005	50.20	< 0.0001	Significant
F^2	32476.01	1	32476.01	6.92	0.0119	Significant
AD	1.183E+005	1	1.183E+005	25.19	< 0.0001	Significant
AE	54382.69	1	54382.69	11.58	0.0015	Significant
BE	82745.30	1	82745.30	17.62	0.0001	Significant

The adequacy of model and effects of process parameters with their interactions for over cut were shown in Table 4.20. The Model F-value is 39.25, it implies that the model is significant. There is only a 0.01% chance that a "Model F-Value" this large could occur due to noise. Values of "Prob > F" less than 0.0500 indicate model terms are significant. In this case parameters and their interactions A, B, C, D, E, F, E^2, F^2, AD, AE, BE are significant model terms. The "Lack of Fit F-value" is 0.93; it implies that the Lack of Fit is not significant relative to the pure error. There is a 61.22% chance for "Lack of Fit F-value". It could be due to noise. The "Pred R-Squared" is 0.8525; that makes a reasonable agreement with the "Adj R-Squared" of 0.8881.

4.8.2 Final Equation in Terms of Actual Factors of OC

By using table 4.20, the regression equation for the over cut as a function of input process variable was developed using the design expert 8.0 software and is given below.

$$\text{Over Cut} = 485.969 + 87.681\ \text{Ip} + 3.037\ \text{V} + 16.276\ \text{Ton} + 12.680\ \text{Toff} - 49.227\ \text{EC} - 182.564\ \text{FR} + 1.358\ \text{EC}^2 + 315.071\ \text{FR}^2 - 14.379\ \text{Ip. Toff} + 6.509\ \text{Ip. EC} + 0.625\ \text{V. EC} \quad (4.5)$$

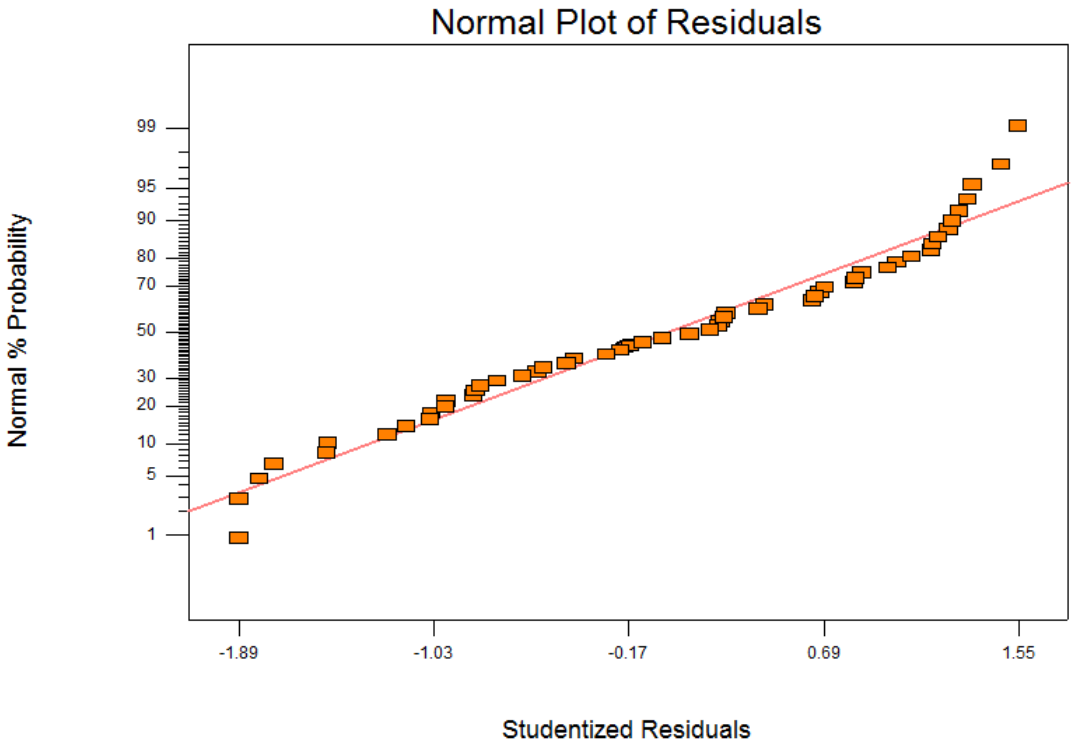

Fig 4.58 Normal Probability Plots for OC

Figure 4.58 shows the normal probability plots for OC. Most of residuals are found to be on a straight line which indicates that errors are normally distributed. This is the normality test to be qualified by the model for checking its validity. After this test it was found that the models are significant.

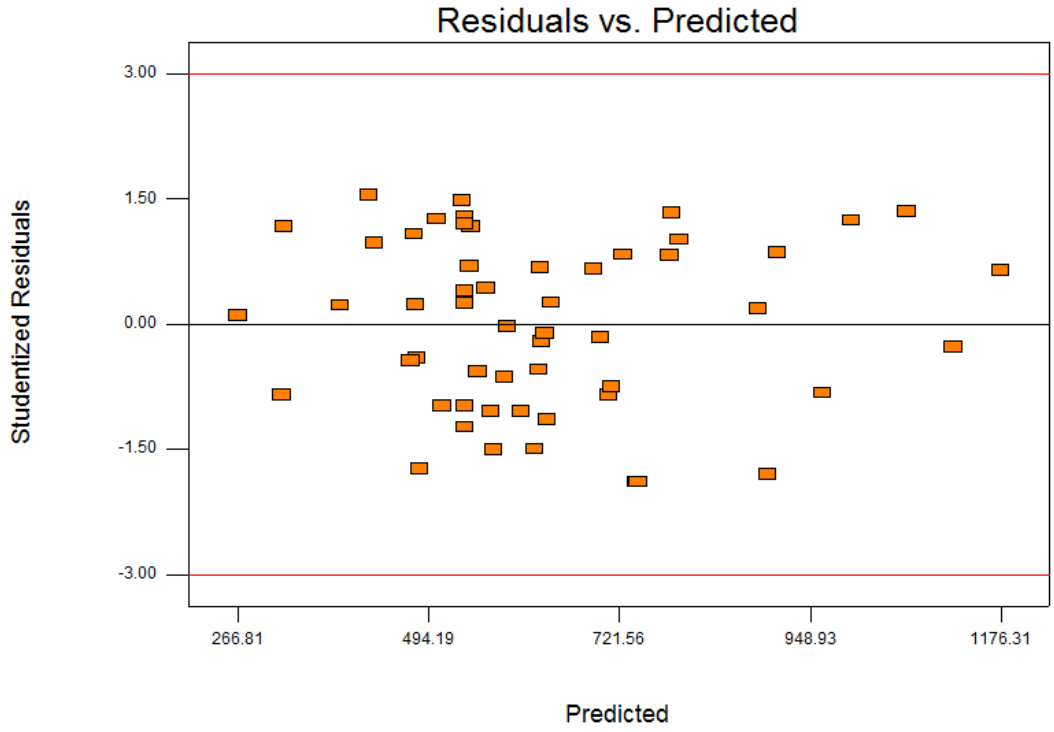

Fig 4.59 Residuals and Predicted Values for OC

Figure 4.59 shows the residuals and predicted plot for over cut. The residuals are distributed randomly and are not clustered which indicates that model is good.

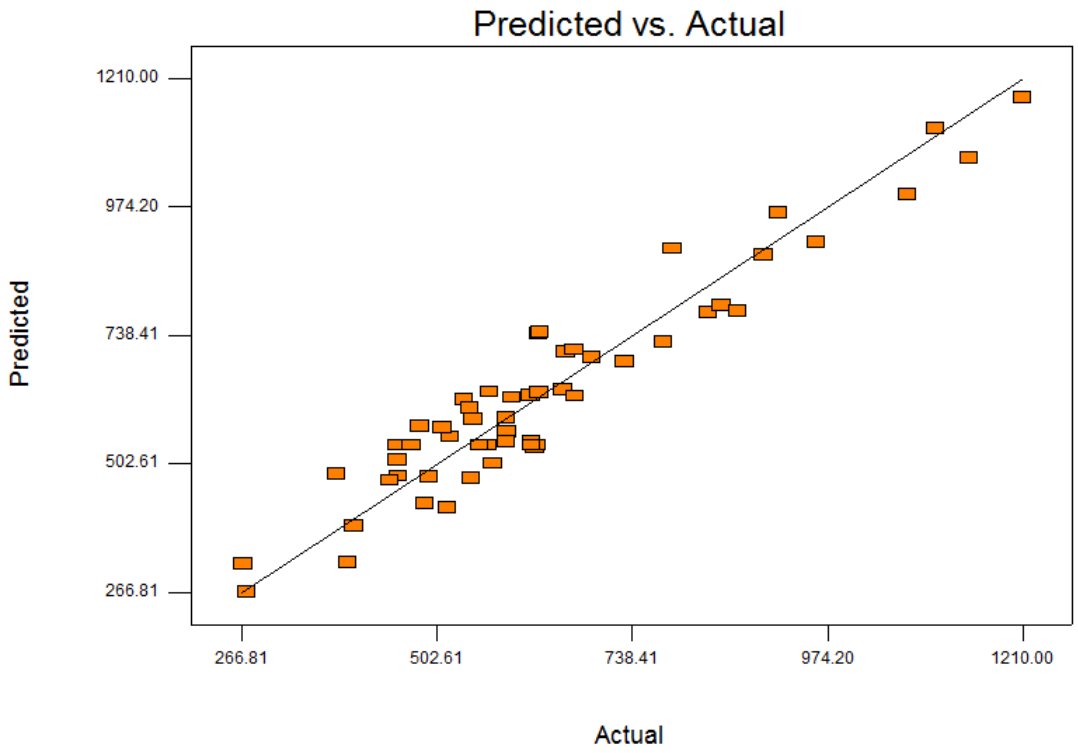

Fig 4.60 Actual and Predicted Values for OC

Figure 4.60 shows the Predicted and Actual plot for over cut. Most of results are found to be on a straight line which indicates that errors are normally distributed. This is the test to be

qualified by the model for checking its validity. From Figure 4.60, it is found that the models are significant. Figure 4.61 shows the interaction effects of pulse off time and supply current on OC. From Figure 4.61, it is noticed that the OC increases with increase in supply current. A large quantity of metal was melted when experiment was carried out at high discharge energy density at 3A peak current, and thereby formed larger size of discharge craters on workpiece surface. This phenomenon was responsible in making large entrance of micro-hole and poor surface finish. It may reduce the total dissolution time at the exit as compared to inlet of the generated micro hole and thus enhance the generated over cut.

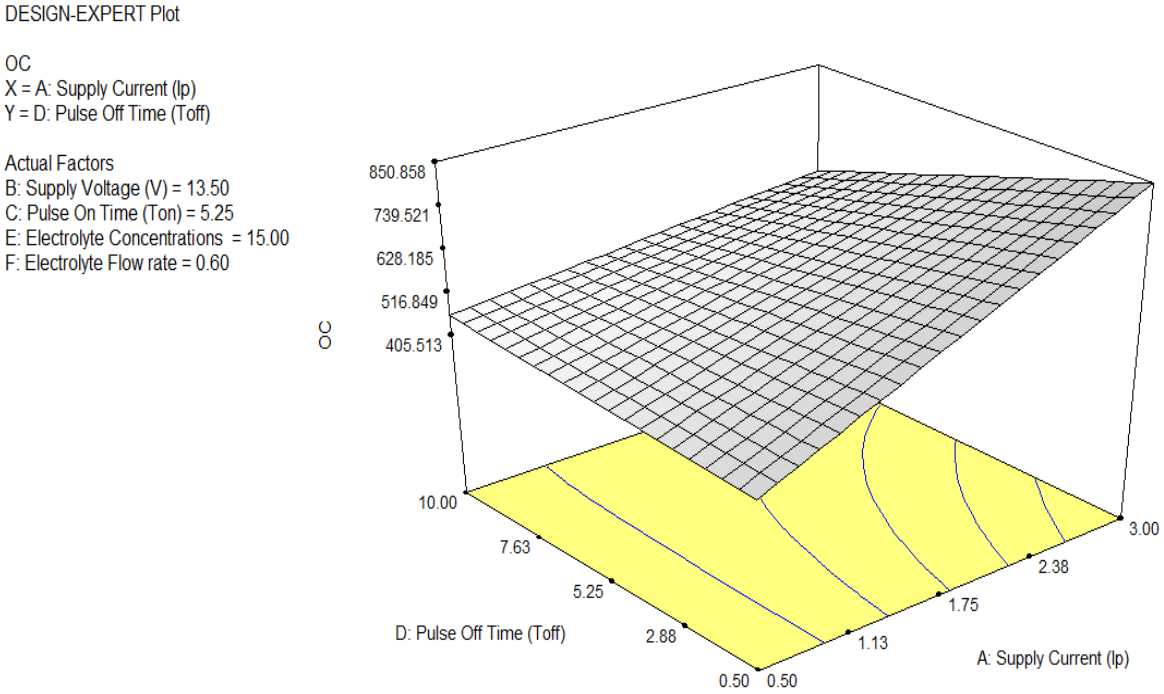

Fig 4.61 Interaction Effects of Pulse Off Time and Supply Current on OC

Figure 4.62 shows the interaction effects of electrolyte concentration and supply current on OC. From Figure 4.62, it is noticed that the OC increases with increase in both electrolyte concentration and supply current. Both electrolyte conductivity and current density increases with increase in electrolyte concentration, it leads to an increase in radial and lateral etching, hence increases the overcut. It is clear that the over cut decreases with increase in pulse off time. At the low pulse off time, the removal of machined metal particles between the inter electrodes gap increases. The presence of machined particles in the inter electrode gap may cause of sparking and it leads to higher overcut.

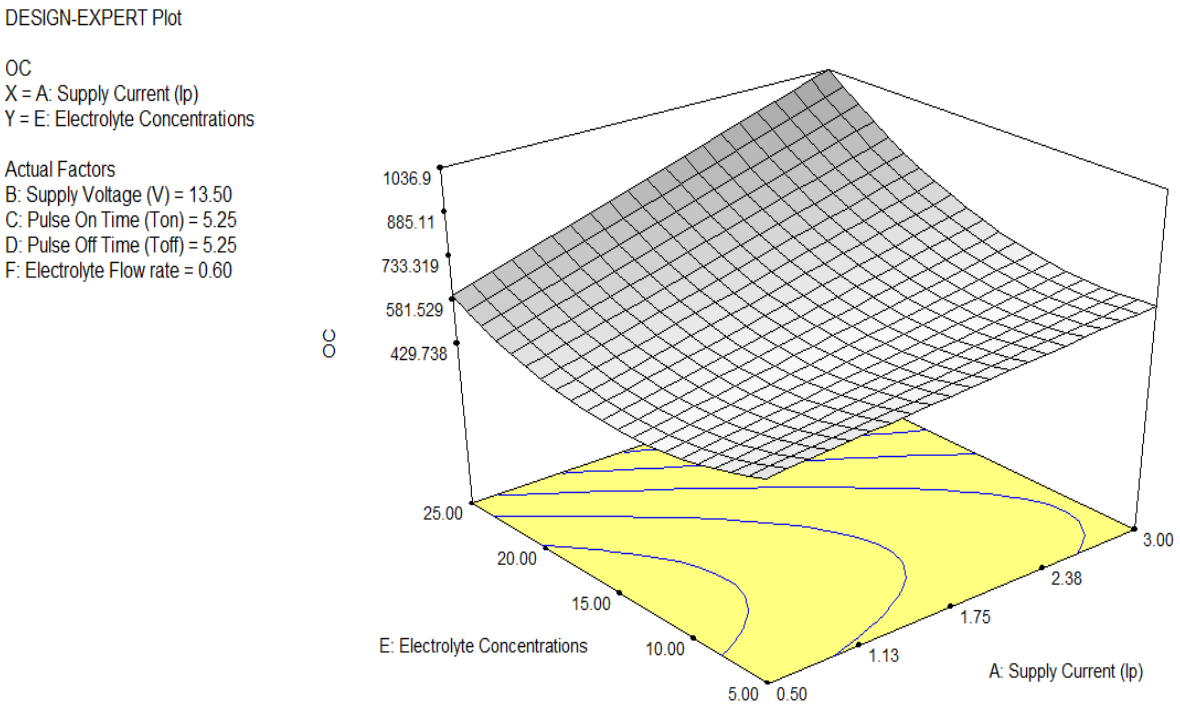

Fig 4.62 Interaction Effects of Electrolyte Concentration and Supply Current on OC

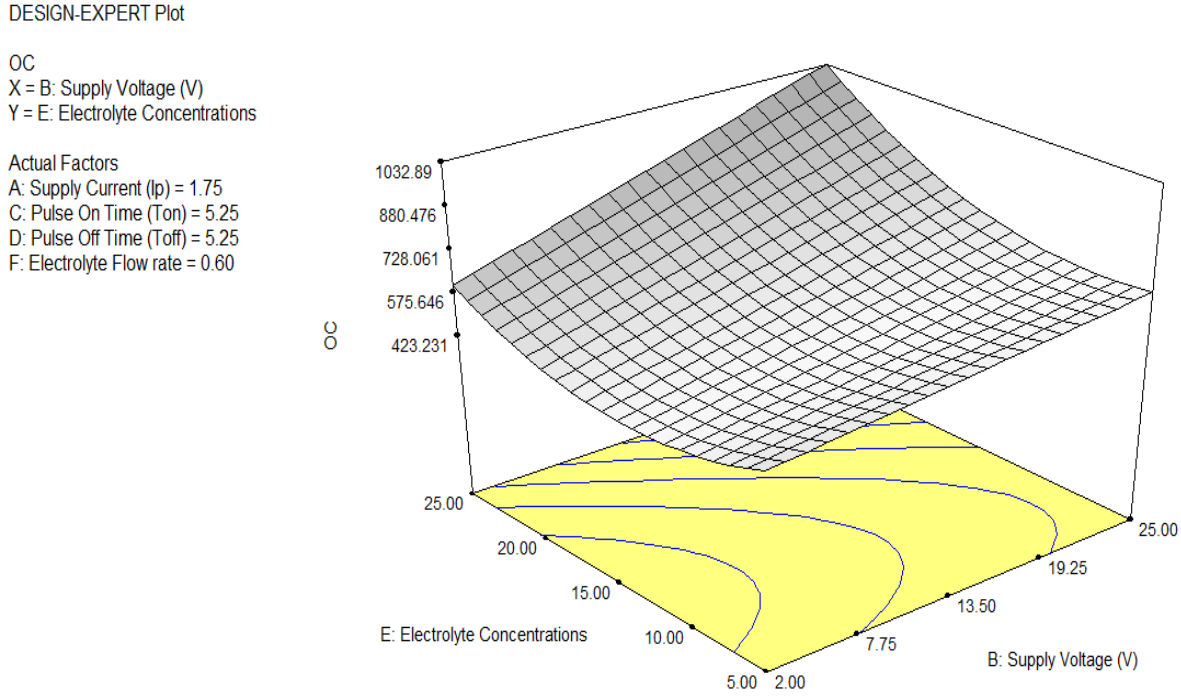

Fig 4.63 Interaction Effects of Electrolyte Concentration and Supply Voltage on OC

Figure 4.63 shows the interaction effects of the electrolyte concentration and the supply voltage on OC. It is observed that OC increases with increase in both electrolyte concentration and supply voltage.

4.9 EFFECTS OF PROCESS PARAMETERS ON MICRO SPARK AFFECTED ZONE (MSAZ)

To decide about the adequacy of the model, three different tests viz. sequential model sum of squares, lack of fit tests and model summary statistics were performed for micro spark affected zone. Table 4.21 displays the tests to select the adequate model to fit MSAZ characteristics. The sequential model sum of squares test in this table shows the contribution of the terms of increasing complexity to the model.

Table 4.21 Selection of Adequate Model for MSAZ

Sequential Model Sum of Squares						
Source	**Sum of Squares**	**Df**	**Mean Square**	**F Value**	**p-Value Prob>F**	
Mean	4.183E+006	1	4.183E+006			
Linear	5.755E+005	6	95921.14	12.74	<0.0001	
2FI	1.199E+005	15	7991.16	1.09	0.3999	
Quadratic	1.762E+005	6	29365.63	13.22	<0.0001	suggested
Cubic	42421.39	18	2356.74	1.23	0.3992	Aliased
Residual	15324.52	8	1915.57			
Total	5.113E+006	54	94679.33			
Lack of Fit Tests						
Source	Sum of Squares	Df	Mean Square	F Value	p-Value Prob>F	
Linear	3.483E+005	42	8292.47	7.51	0.0162	
2FI	2.284E+005	27	8459.86	7.66	0.0160	
Quadratic	52222.41	21	2486.78	2.25	0.1874	Suggested
Cubic	9801.02	3	3267.01	2.96	0.1367	Aliased
Pure Error	5523.50	5	1104.70			
Model Summary Statistics						
Source	Std. Dev.	R-Squared	Adjusted R-Squared	Predicted R-Squared	PRESS	
Linear	86.76	0.6193	0.5707	0.5119	4.536E+005	
2FI	85.50	0.7483	0.5831	0.3752	5.807E+005	
Quadratic	47.13	0.9379	0.8733	06985	2.802E+005	Suggested
Cubic	43.77	09835	0.8908	-1.7273	2.535E+006	Aliased

It can be observed that for all the responses, the quadratic model is appropriate. The “lack of fit” test compares the residual error to the pure error from the replicated design points. The results indicate that the quadratic model in all the characteristics does not show significant lack of fit, hence the adequacy of quadratic model is confirmed as p- value is less than 0.5. Hence, quadratic model is suggested.

4.9.1 Pooled Analysis of Variance (ANOVA) for MSAZ

To construct the pool ANOVA design expert 8.0 software was used. Table 4.22 represents Pooled ANOVA for MSAZ. The aim of construction of pooled ANOVA is to pool the different factors together and test the significance of the parameters and their interactions.

Table 4.22 Pooled ANOVA for Micro Spark Affected Zone

Source	Sum of Squares	DF	Mean Square	F Value	p-value Prob>F	Status
Model	8.460E+005	12	70501.84	34.70	< 0.0001	Significant
A	2.145E+005	1	2.145E+005	105.58	< 0.0001	Significant
B	1.058E+005	1	1.058E+005	52.04	< 0.0001	Significant
C	1.029E+005	1	1.029E+005	50.63	< 0.0001	Significant
D	48434.47	1	48434.47	23.84	< 0.0001	Significant
E	42120.81	1	42120.81	20.73	< 0.0001	Significant
F	83066.66	1	83066.66	40.88	< 0.0001	Significant
E^2	1.050E+005	1	1.050E+005	51.69	< 0.0001	Significant
F^2	85434.63	1	85434.63	42.04	< 0.0001	Significant
AC	9474.43	1	9474.43	4.66	0.0367	Significant
AD	66028.74	1	66028.74	32.49	< 0.0001	Significant
BF	8547.91	1	8547.91	4.21	0.0467	Significant
CE	27454.71	1	27454.71	13.51	0.0007	Significant

The adequacy of model and effects of process parameters with their interactions for micro spark affected zone are shown in Table 4.22. The Model F-value is 34.70, it implies that the model is significant. There is only a 0.01% chance for "Model F-Value" it could be due to noise. Values of "Prob > F" less than 0.0500 indicates that the model terms are significant. In this case parameters and their interactions A, B, C, D, E, F, E^2, F^2, AC, AD, BF, CE are the significant model terms. The "Lack of Fit F-value" is 1.96 which implies that the Lack of Fit is not significant relative to the pure error. There is a 23.41% chance for "Lack of Fit F-value";

this large could occur due to noise. The "Pred R-Squared" is 0.8467 that makes a reasonable agreement with the "Adj R-Squared" (0.8841).

4.9.2 Final Equation in Terms of Actual Factors of MSAZ

By using Table 4.22, the regression equation for the over cut as a function of input process variable was developed using the software design expert 8.0 and is given below.

$$\begin{aligned}\text{MSAZ} &= 25.01 + 161.45\ \text{Ip} + 1.508\ \text{V} + 42.61\ \text{Ton} + 9.31\ \text{Toff} - 16.53\ \text{EC} - 561.84\ \text{FR} \\ &+ 0.90\ \text{EC}^2 + 511.03\ \text{FR}^2 - 5.715\ \text{Ip.Ton} - 10.74\ \text{Ip .Toff} + 7.10\ \text{V.FR} \\ &- 1.23\ \text{Ton.EC}\end{aligned} \tag{4.6}$$

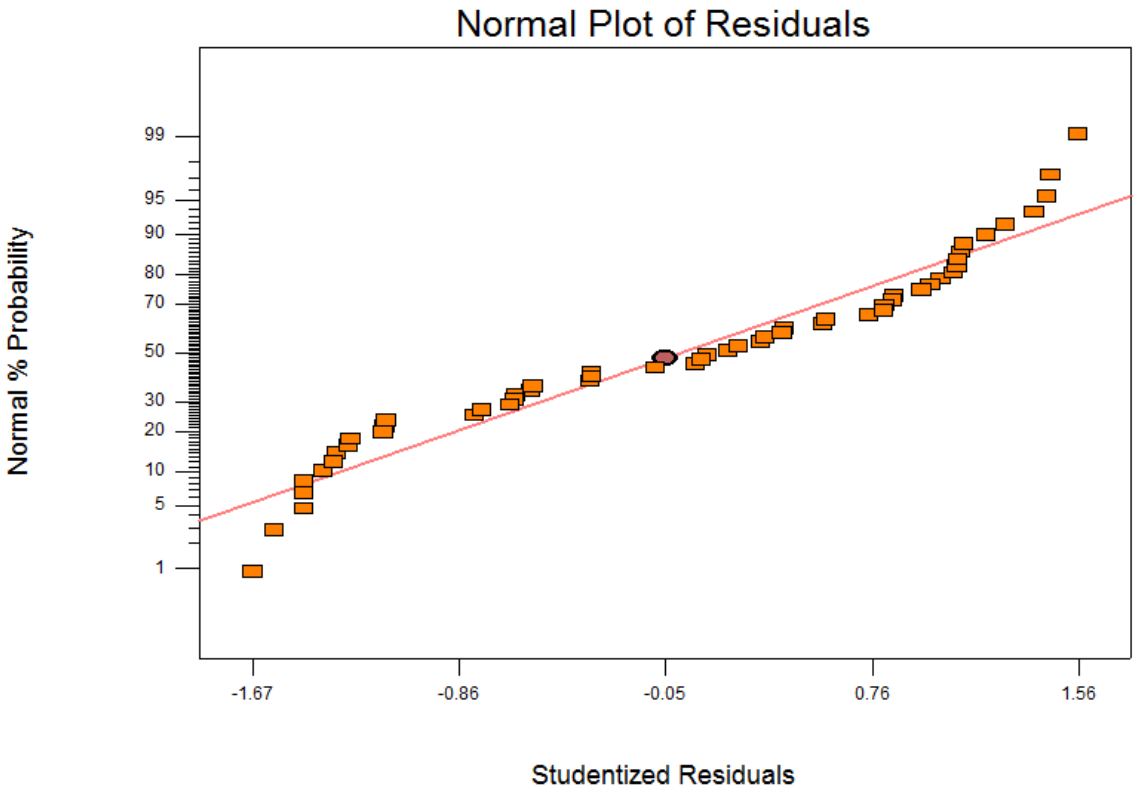

Fig 4.64 Normal Probability Plots for MSAZ

Figure 4.64 shows the normal probability plots for MSAZ. Most of the residuals are found to be on a straight line which indicates that errors are normally distributed. This is the normality test to be qualified by the model for checking its validity. After this test it is found that models are significant.

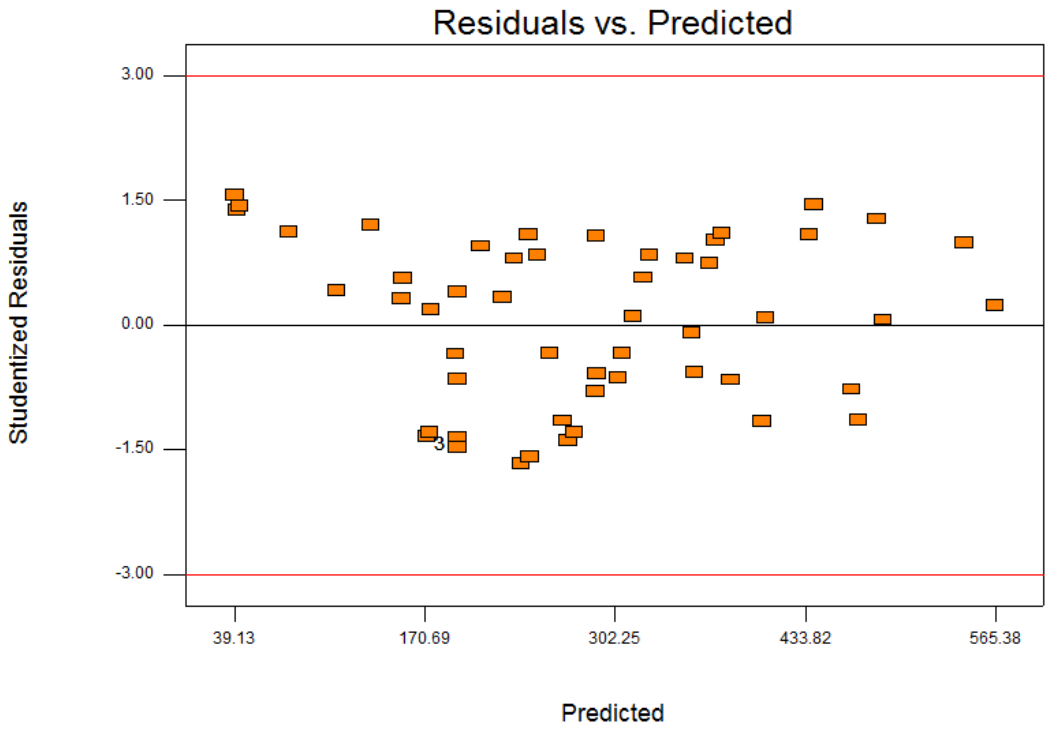

Fig 4.65 Residuals and Predicted Values for MSAZ

Figure 4.65 shows the residuals and predicted plot for micro spark affected zone. The residuals are distributed randomly and are not clustered which indicates that model is good.

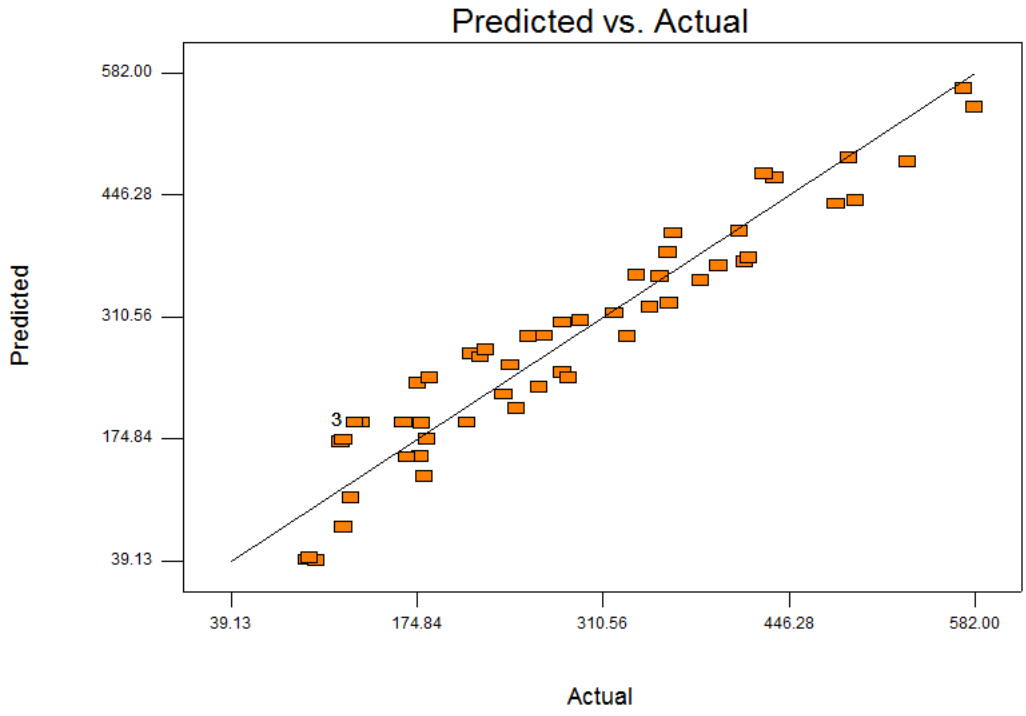

Fig 4.66 Actual and Predicted Values for MSAZ

Figure 4.66 shows the Predicted and Actual plot for micro spark affected zone. Most of the results are found to be on a straight line which indicates that errors are normally distributed. From Figure 4.66, it is found that models are significant.

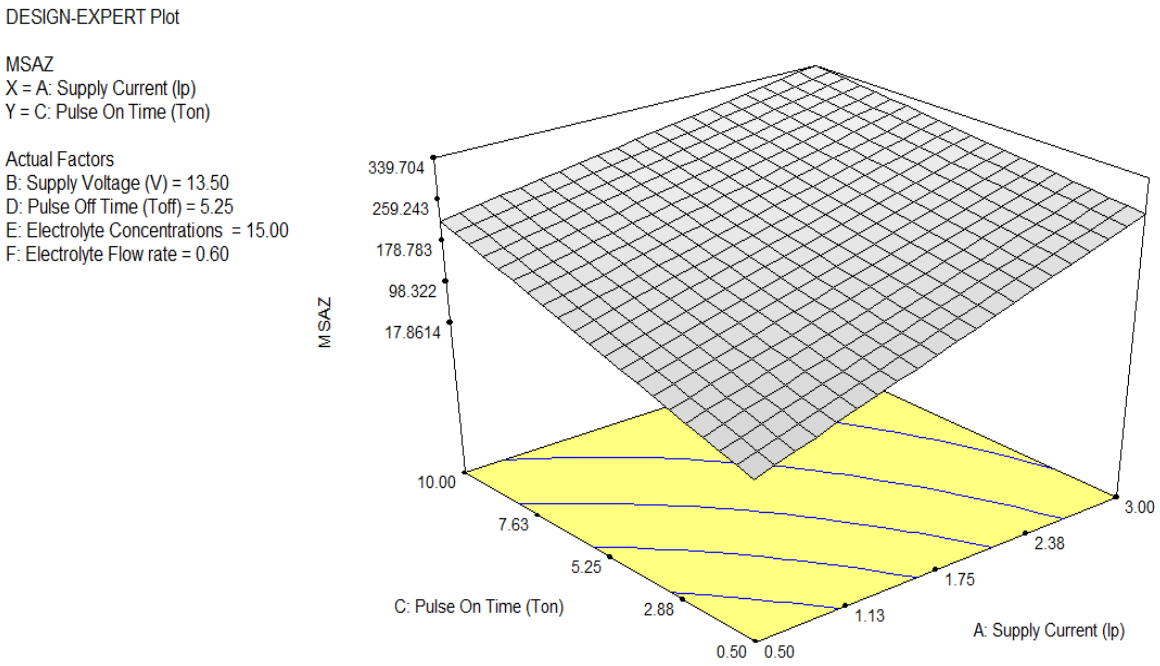

Fig 4.67 Interaction Effects of Pulse On Time and Supply Current on MSAZ

Figure 4.67 shows the interaction effects of pulse on time and supply current on MSAZ. From Figure 4.67, it is clear that the MSAZ increases with increase in both pulse on time and supply current. The more micro spark affected zone means larger removal of metal along the lateral direction. Both electrolyte conductivity and current density increases with increase in supply current and pulse on time, thereby increases radial and lateral etching, results in increase of micro spark affected zone. Figure 4.68 shows the interaction effects of pulse off time and supply current. It is noticed that MSAZ increases with increase in supply current. Figure 4.69 shows the interaction effects of electrolyte flow rate and supply voltage on MSAZ. From Figure 4.69, it is noticed that the MSAZ increases with an increase in both the electrolyte flow rate and the supply voltage. At high-pressure of electrolyte flow, the micro tool starts to vibrate and thereby increases the area of metal removal around the tool. It leads to increase the micro spark affected zone. It is clear that the micro spark affected zone is increase with increase in supply voltage. The high applied voltage may break the oxide layer. At high supply voltage and high current, generates high heat in the inter-electrode gap causing varying the local electrolyte conductivity. This phenomenon is responsible for distribution of non-uniform current in the inter-electrode gap.

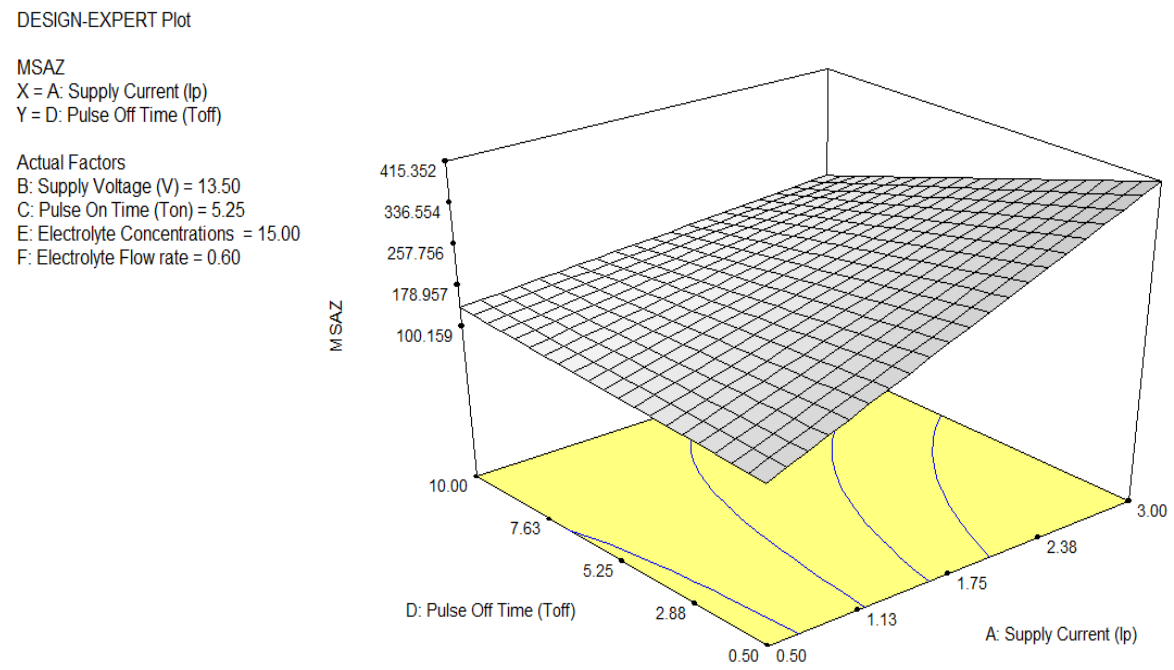

Fig 4.68 Interaction Effects of Pulse Off Time and Supply Current on MSAZ

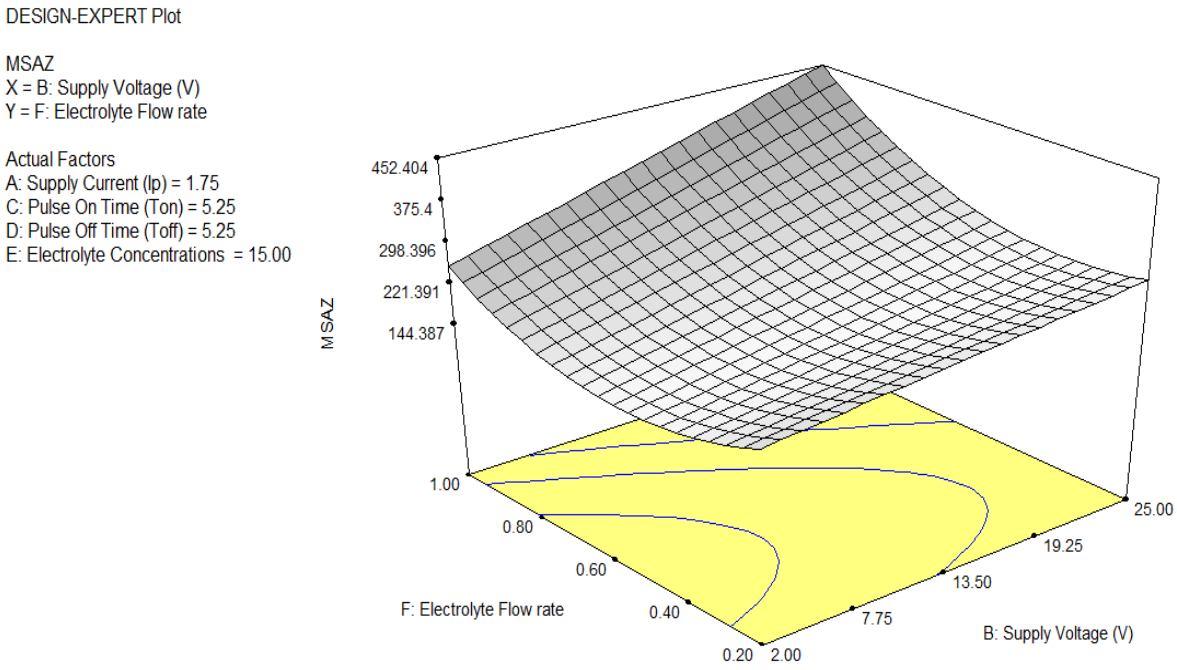

Fig 4.69 Interaction Effects of Electrolyte Flow Rate and Supply Voltage on MSAZ

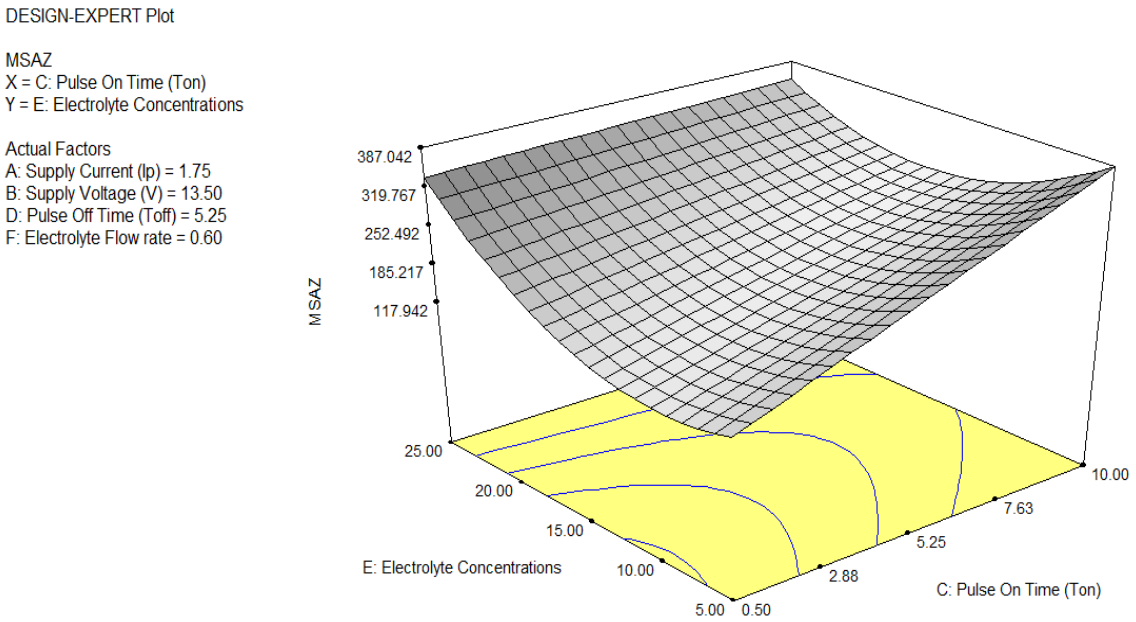

Fig 4.70 Interaction Effects of Electrolyte Concentrations and Pulse On Time on MSAZ

Figure 4.70 shows the interaction effects of electrolyte concentrations and pulse on time on MSAZ. It is observed that MSAZ increases with increase in both electrolyte concentrations and pulse on time.

4.10 MULTI RESPONSE OPTIMIZATION USING DESIRABILITY

Multi response optimization was done using desirability function in conjunction with RSM to overcome the problem of contradictory responses of single response optimization. All possible multi characteristics models have been developed. Goals and limits were established for each response in order to accurately determine their impact on overall desirability. Table 4.23 represents the parameters and their range for multi responses such as MRR, EWR, SR, TC, OC, and MSAZ optimization.

Table 4.23 Range of Input Parameters for Multi Response Optimization

Name	Goal	Lower Limit	Upper Limit	Lower Weight	Upper Weight	Importance
Supply current (Ip)	is in range	0.5	3	1	1	3
Supply Voltage (V)	is in range	2	25	1	1	3
Pulse On Time (Ton)	is in range	0.5	10	1	1	3
Pulse Off Time (Toff)	is in range	0.5	10	1	1	3
Electrolyte Concentration (EC)	is in range	5	25	1	1	3
Electrolyte Flow rate (Fr)	is in range	0.2	1	1	1	3
MRR	Maximize	0.137	8.923	1	1	3
EWR	Minimize	0.068	3.245	1	1	3
SR	Minimize	1.01	8.86	1	1	3
TC	Minimize	240	1069	1	1	3
OC	Minimize	268	1210	1	1	3
MSAZ	Minimize	94	582	1	1	3

The goal of optimization is to maximize the MRR, and minimize EWR, SR, TC, OC and MSAZ for the given set of conditions that will meet all the goals. It is not necessary that the value of desirability is always 1.0 as the value is completely dependent on how closely the lower and upper limits are set relative to the actual optimum. A set of 10 optimal solutions is derived for the specified design space constraints for multi response characteristics using Design of Expert 8.0 software. Table 4.24 reports the set of conditions possessing highest desirability value for the desired response. The optimal set of conditions with higher desirability function required for obtaining desired response characteristics under selected specified constraints.

Table 4.24 Set of Multi Response Optimal Solutions

S.No	Ip (Amp)	V (v)	Ton (µs)	Toff (µs)	EC (g/*l*)	FR (*l*/min)	MRR (mg/min)	EWR (mg/min)	SR (Ra)	TC (µm)	OC (µm)	MSAZ (µm)	Desirability
1	0.50	2.03	3.38	6.26	14.38	0.60	0.316	0.03	1.00	159.22	267.96	13.49	0.997
2	0.51	2.00	2.44	5.23	15.70	0.71	0.360	0.11	1.00	154.23	267.74	13.14	0.996
3	0.56	2.00	3.54	6.12	13.17	0.51	0.368	0.05	1.00	160.33	267.97	13.91	0.996
4	0.50	2.00	1.24	2.92	16.51	0.86	0.484	0.08	1.01	163.70	278.95	24.53	0.991
5	0.50	2.12	2.72	1.43	16.74	0.60	0.673	0.02	1.00	135.46	224.78	0.48	0.990
6	0.58	2.00	1.35	0.56	17.27	0.81	0.694	0.04	1.01	168.29	267.98	24.37	0.989
7	0.81	2.00	2.99	6.85	12.95	0.35	0.331	0.06	1.35	178.51	267.99	38.87	0.989
8	0.50	2.00	5.16	6.35	16.07	0.44	0.370	0.11	1.27	216.21	268	62.85	0.988
9	0.50	17.7	0.50	2.80	11.15	0.70	0.141	0.10	1.69	203.71	415.19	28.73	0.956
10	0.53	2.00	8.94	9.67	17.28	0.71	0.411	0.11	2.64	413.88	398.31	166.00	0.872

The setting of ECMM parameters for multi response optimization for machining of hybrid Al/MMC is IP: 0.5 A, V: 2.03 V, Ton: 3.38 µs, Toff : 6.26 µs, EC: 14.38 g/l, and Fr: 0.60 l/sec. The ramp function graph and bar graph were drawn using Design Expert 8.0, these graphs show the desirability for multi response optimization. Figure 4.71 shows the ramp function graph of desirability for multi response optimization. The dot on each ramp reflects the factor setting or response prediction for those response characteristics. The height of the dot shows how much desirable it is, a linear ramp function is created the low value and the goal or the high value and the goal as the weight for each parameter was set equal to one.

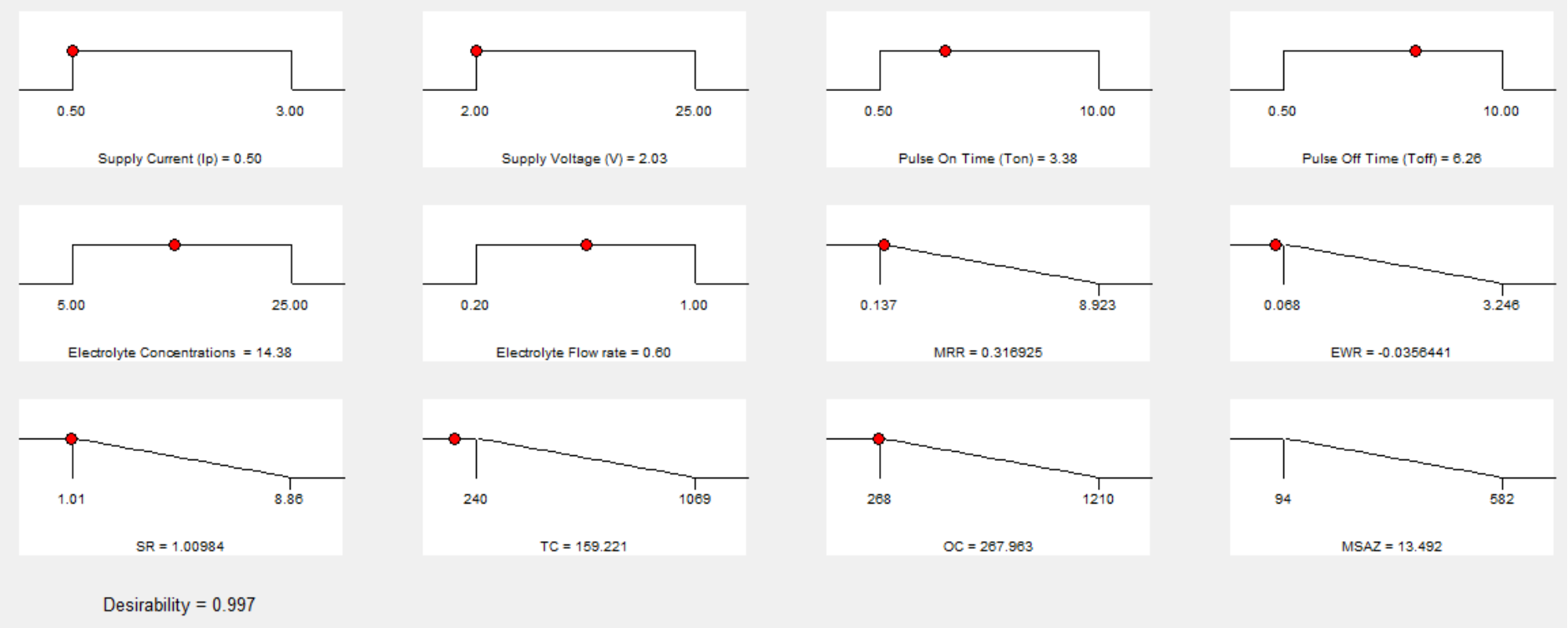

Fig 4.71 Ramp Function Graph of Desirability for Multi Response Optimization

The Figure 4.72 shows the bar graph of overall desirability function of the input parameters and responses for multi response optimization. Desirability varies from 0 to 1 depending upon the closeness of the response towards target. The bar graph shows how well each variable satisfies the criterion.

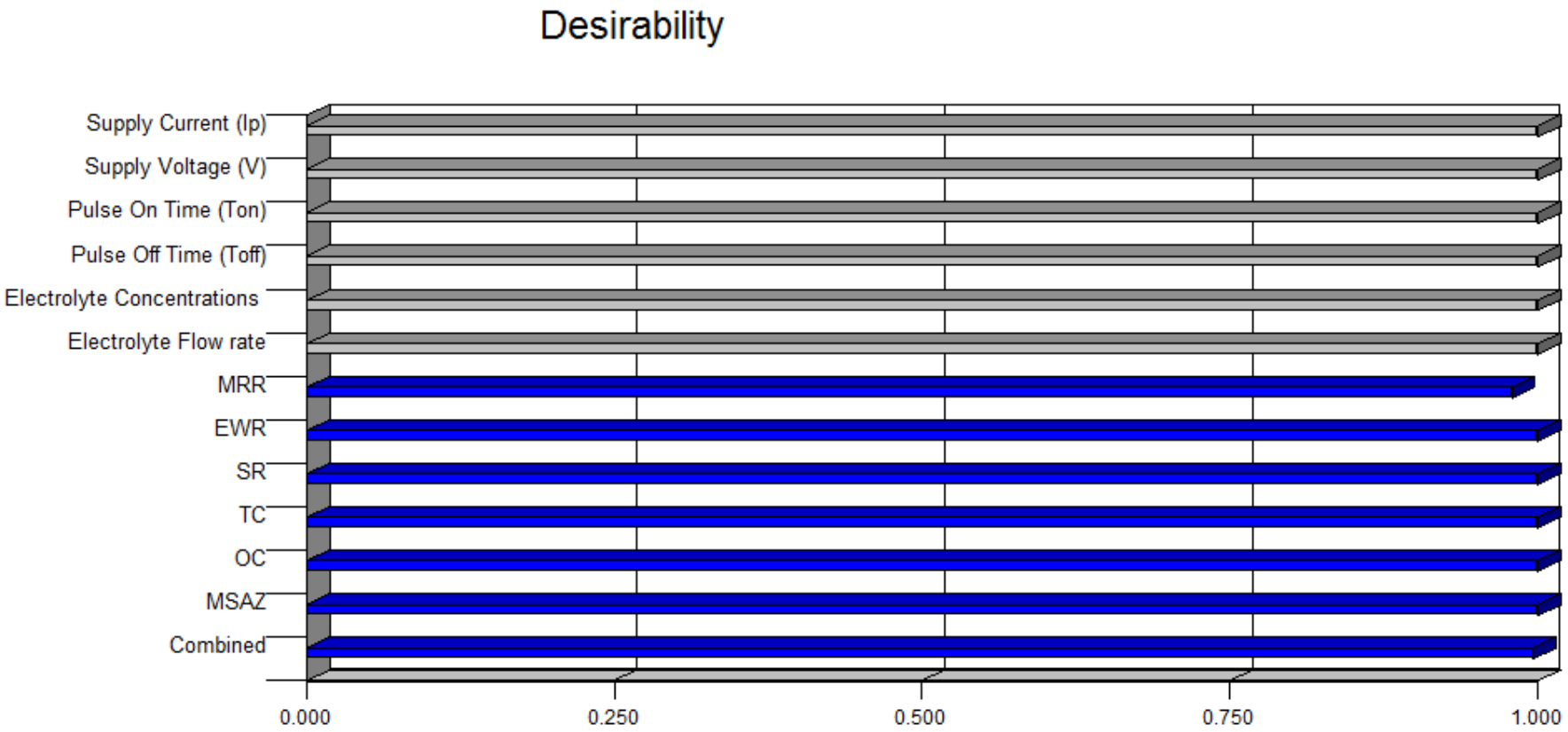

Fig 4.72 Desirability Bar Graph for Multi Response Optimization

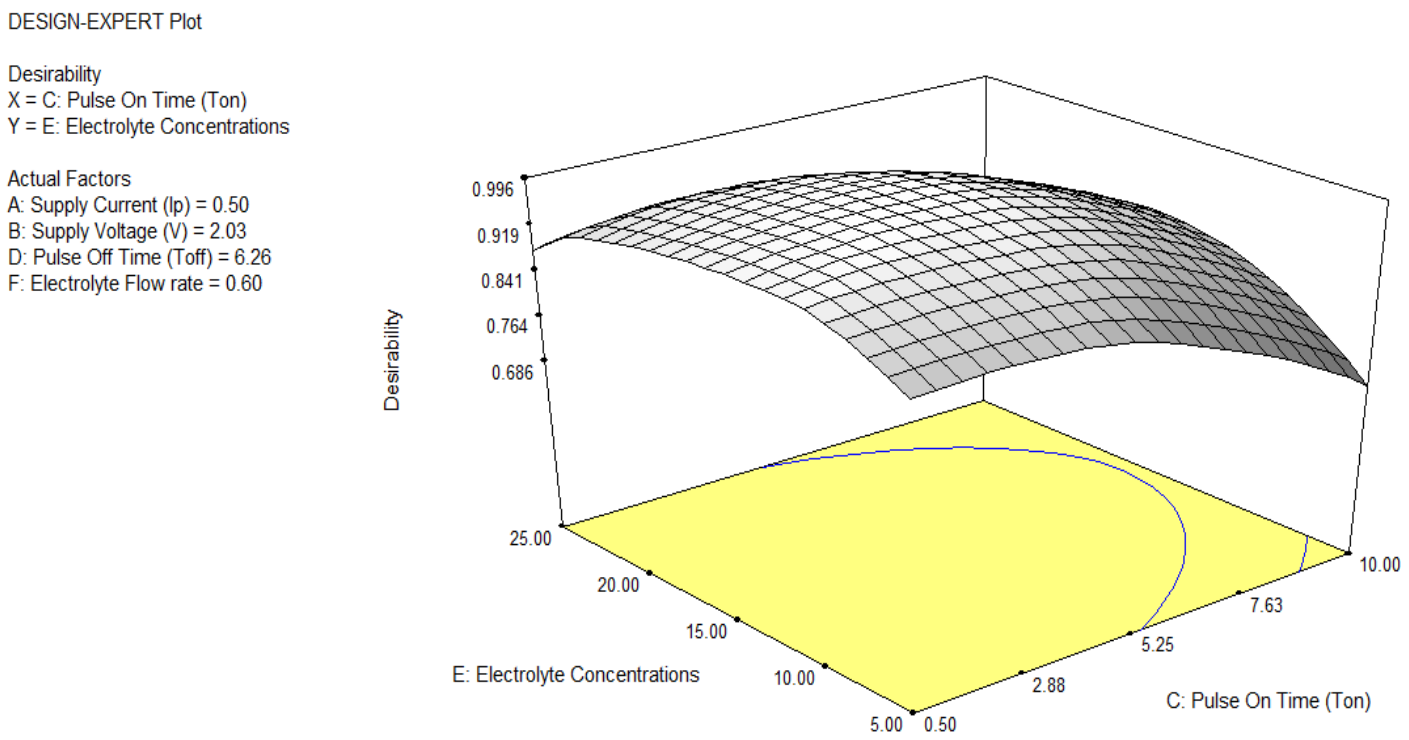

Fig 4.73 Interaction Effects of Electrolyte Concentration and Pulse On Time on Desirability

Figure 4.73 shows interaction effects of pulse on time and electrolyte concentration on desirability function distribution for multi response optimization. It can be visualized that low level of pulse on time and low level of electrolyte concentration is favourable to meet all the goals.

4.11 CONFIRMATION EXPERIMENTS

The validity experiments were carried out to validate the multi-optimization of electrochemical micro machining parameters for MRR, EWR, SR, TC, OC, and MSAZ. The acquired results reveal that the experimental values make a good agreement with the predicted model values, therefore model is

adequate. The error between experimental and model values for MRR, EWR, SR, TC, OC, MSAZ are within 8.21%, 7.80%, 7.40%, 3.57%, 3.91% and 5.26% respectively.

Table 4.25 Confirmation Experiments

S. NO	Parameters and Their Units						Responses and Their Units																	
	IP (A)	V (v)	Ton (µs)	Toff (µs)	EC (g/*l*)	FR (*l*/min)	MRR (mg/min)			EWR (mg/min)			SR (Ra)			TC (µm)			OC (µm)			MSAZ (µm)		
							From Model	From Exp.	Error (%)	From Model	From Exp.	Error (%)	From Model	From Exp.	Error (%)	From Model	From Exp.	Error (%)	From Model	From Exp.	Error (%)	From Model	From Exp.	Error (%)
1	0.5	2.0	3.5	6.5	14	0.60	0.316	0.292	8.21	0.035	0.038	7.80	1.00	1.08	7.40	159.22	165.12	3.57	267.96	278.87	3.91	13.49	14.24	5.26
2	0.5	2.5	2.5	5.5	16	0.70	0.360	0.332	8.43	0.114	0.118	3.38	1.00	1.11	9.9	154.23	158.23	2.52	267.74	277.42	3.48	13.14	14.32	8.24
3	0.5	2.5	3.5	6.0	13	0.50	0.368	0.349	5.44	0.056	0.061	8.19	1.00	1.05	4.76	160.33	168.43	4.80	267.97	278.56	3.80	13.91	15.12	8.00

The optimal combination from multi response optimization of ECMM parameters for effective machining of hybrid Al/MMC is found as supply current (IP) 0.5 A, supply voltage (V) 2.0 V, Pulse on time (Ton) 3.5 µs, Pulse off time (Toff) 6.5 µs, Electrolyte Concentration (EC) 14 g/*l*, and Electrolyte flow rate (Fr) 0.60 *l*/sec.

4.12 SEM, EDS AND XRD OF MICRO HOLES

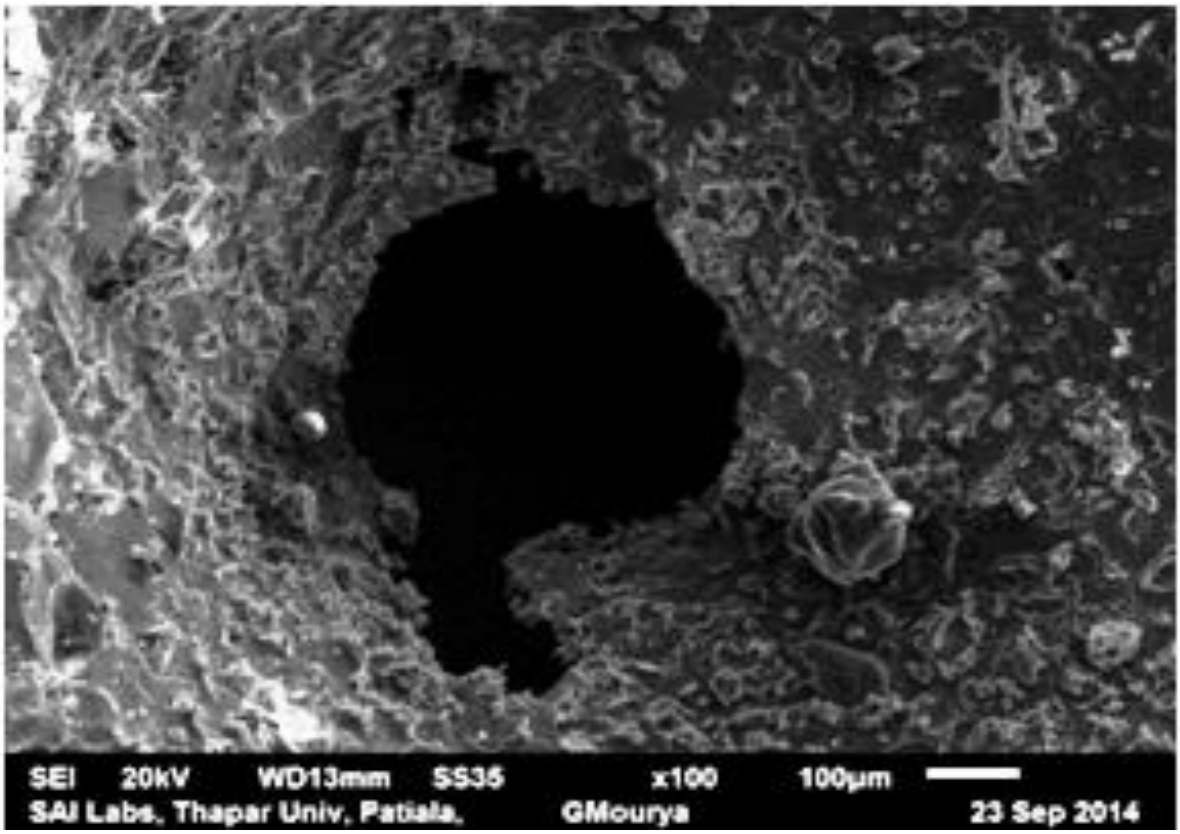

Fig. 4.74 SEM Photograph of A Micro Hole Machined at 1 A Supply Current, 25 V Supply Voltage, 10 µs Pulse On Time, 5 µs Pulse Off Time, 5 g/*l* electrolyte concentration, and 0.6 *l*/min electrolyte flow rate.

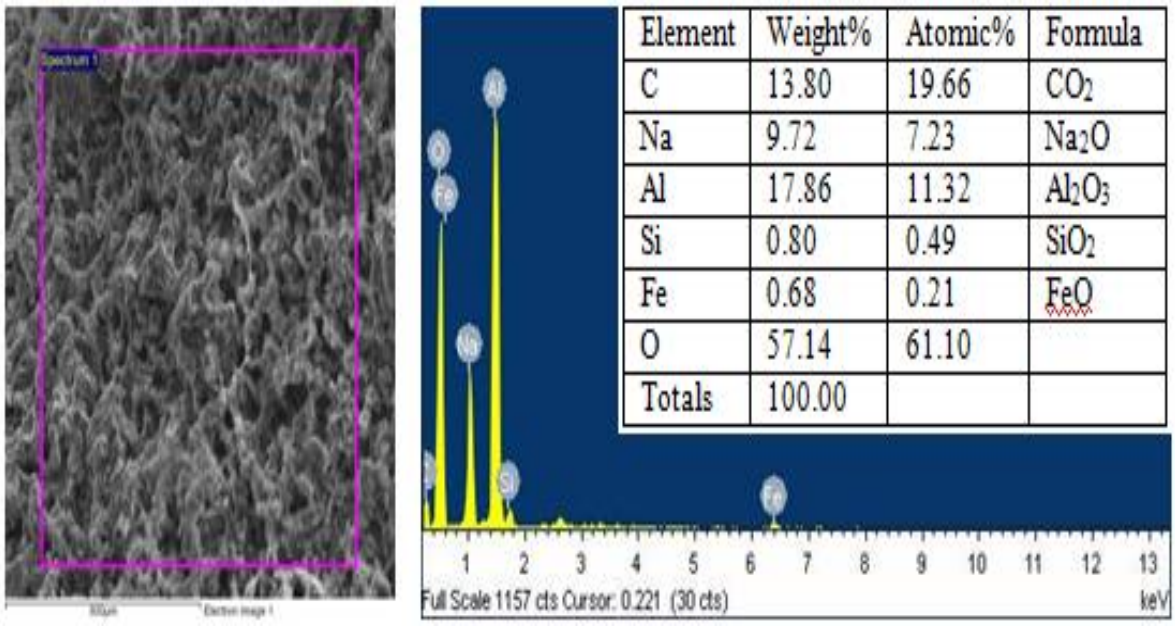

Element	Weight%	Atomic%	Formula
C	13.80	19.66	CO_2
Na	9.72	7.23	Na_2O
Al	17.86	11.32	Al_2O_3
Si	0.80	0.49	SiO_2
Fe	0.68	0.21	FeO
O	57.14	61.10	
Totals	100.00		

Fig. 4.75 EDS Reveals the Presence of Different Elements of Machined Hole (Fig 4.74)

Figure 4.74 shows the SEM photograph of a machined micro hole machined by developed ECMM setup at 1 A supply current, 25 V supply voltage, 10 µs pulse on time, 5 µs pulse off time 5 g/*l* electrolyte concentration, and 0.6 *l*/min electrolyte flow rate. At this setting of

parameters, high heat was generated in between the IEG as a result varying the electrolyte conductivity thereby a non-uniform current distribution in the gap was identified. As the electrolyte flow rate becomes low, it may not be enough to clean the machined product i.e. sludge completely from the IEG, thereby causing micro sparking. These micro sparks may generate uncontrolled MRR phenomenon, which in turn results in large overcut, taper cut and generation of micro spark affected zone.

Figure 4.75 shows the EDS of the generated micro hole (Figure 4.74). From Figure 4.75, it is clear that there are small particles of sodium and chloride on the periphery of machined hole, it is may be due to the reaction product of anode with electrolyte NaCl. From EDS analysis (Figure 4.74), the percentage of residuals such as sodium (Na), carbon (C), silicon (Si), aluminium (Al), iron (Fe) and oxygen (O) are detected on surface of micro holes. The micro hole surface was distorted because of sodium chloride, which was generated because of hybrid MMC machining and removal of material due to the electrochemical dissolution.

Figure 4.76 shows SEM photograph of a machined micro hole generated at 1 A supply current, 25 V supply voltage, 5.5 µs pulse on time, 5 µs pulse off time, 15 g/*l* electrolyte concentration, and 1.0 *l*/min electrolyte flow rate. From Figure 4.76, some irregularities in the shape of small grooves and pitting are identified; it is may be the cause of developing the micro sparks due to the presence of sludge at high voltage and high electrolyte concentration. These micro sparks cause uncontrolled material removal, resulting in improper generation of shape of micro hole.

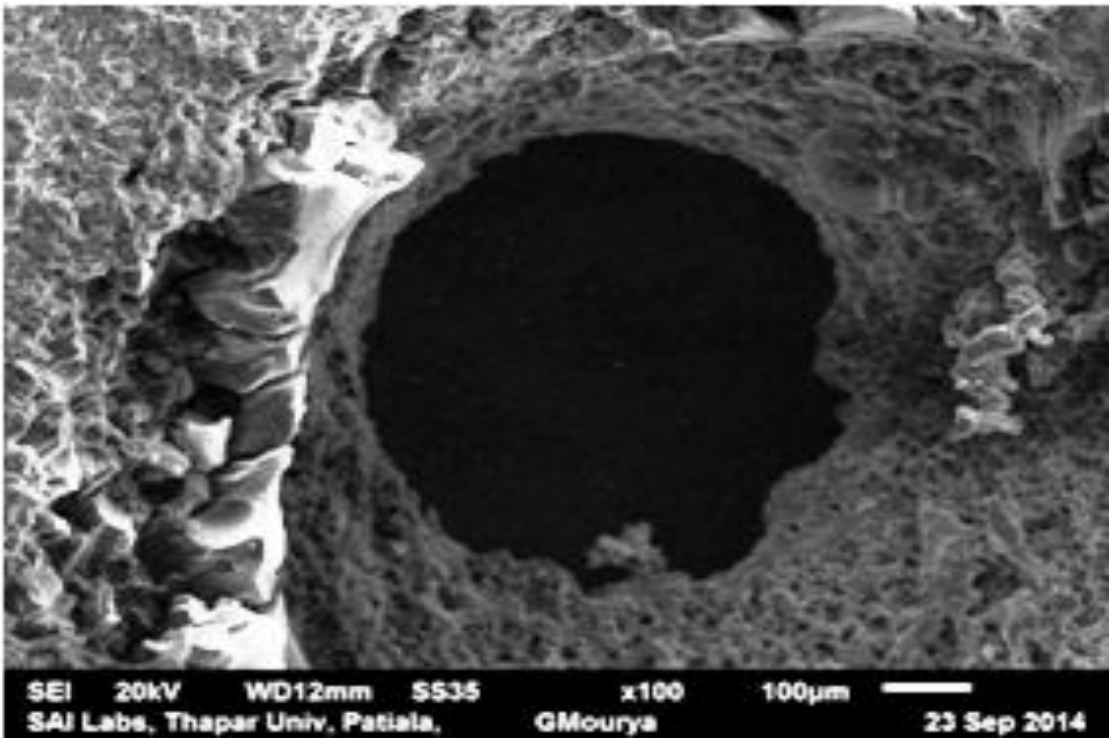

Fig. 4.76 SEM Photograph of A Machined Micro Hole at 1 A Supply Current, 25 V Supply Voltage, 5.5 µs Pulse On Time, 5 µs Pulse Off Time 15 g/*l* Electrolyte Concentration, and 1.0 *l*/min Electrolyte Flow Rate.

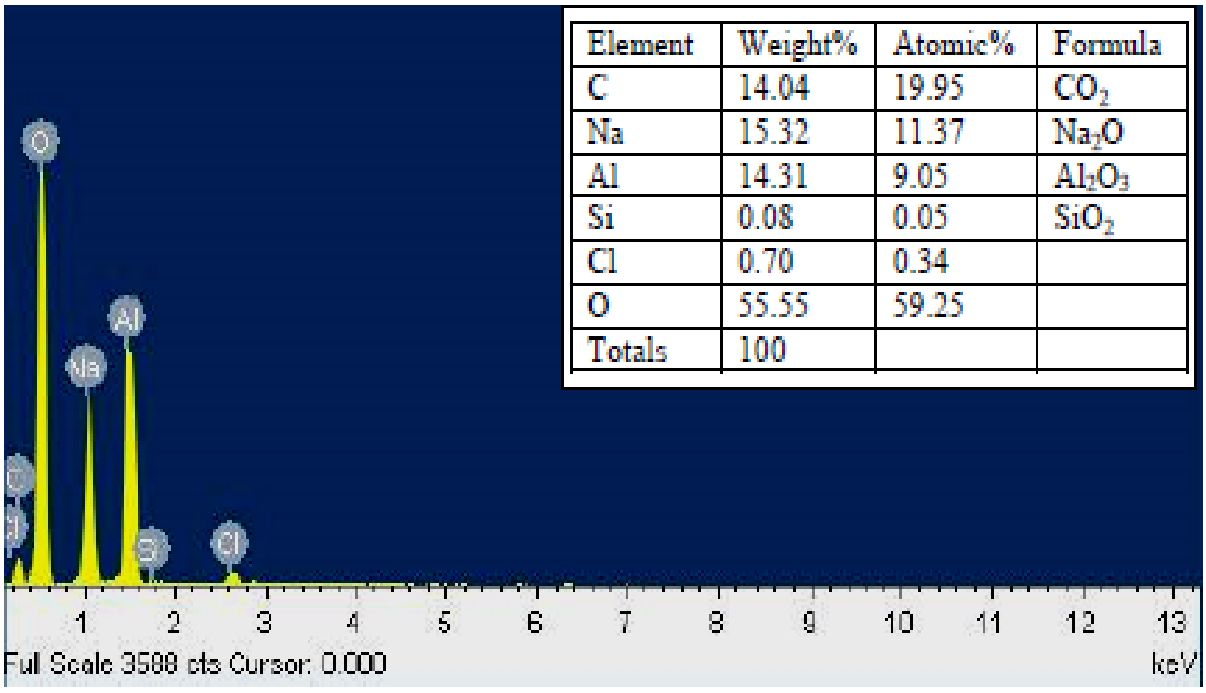

Element	Weight%	Atomic%	Formula
C	14.04	19.95	CO_2
Na	15.32	11.37	Na_2O
Al	14.31	9.05	Al_2O_3
Si	0.08	0.05	SiO_2
Cl	0.70	0.34	
O	55.55	59.25	
Totals	100		

Fig. 4.77 EDS Reveals the Presence of Different Elements of Machined Hole (Fig 4.76)

Figure 4.77 shows the EDS of micro machined hole (Figure 4.76). From Figure 4.77, it is clear that there were small particles of sodium and chloride on the periphery of machined hole, it is

may be due to the reaction product of anode with electrolyte NaCl. From EDS analysis Figure 4.77, the residuals such as sodium (Na), carbon (C), silicon (Si), aluminium (Al), and oxygen (O) are detected on surface of micro holes. The micro hole surface was distorted because the sodium chloride, which was generated from the workpiece specimen hybrid Al/MMC and hamper the electrochemical dissolution.

Figure 4.78 shows SEM photograph of a machined micro hole generated at 1.5 A supply current, 25 V supply voltage, 10 µs pulse on time, 5.5 µs pulse off time, 25 g/*l* electrolyte concentration, and 0.6 *l*/min electrolyte flow rate. At high supply voltage, high heat is generated in between the IEG, as a result varying the electrolyte conductivity and hence a non-uniform current distribution in the gap is formed. As the pulse off time become shorter, it may not be enough to clean the machined product i.e. sludge completely from the IEG, thereby causing micro sparking. From Figure 4.78, some irregularities are identified in the shape of small grooves and pitting; it is may be the cause of developing the micro sparks during machining because of the presence of sludge and high voltage supply. These micro sparks may generate uncontrolled MRR phenomenon, which in turn generates large overcut, taper cut and as well as generates micro spark affected zone.

Figure 4.79 shows SEM micrograph of a machined micro hole machined at 0.5 A supply current, 25 V supply voltage, 5.5 µs pulse on time, 10 µs pulse off time, 15 g/*l* electrolyte concentration, and 0.6 *l*/min electrolyte flow rate. At high machining voltage, high heat generated in between the IEG, results varying the electrolyte conductivity and hence a non-uniform current distribution in the gap is formed. This irregularity is identified in the shape of small groove; it may be a cause of developing micro sparks due to the presence of sludge at high voltage.

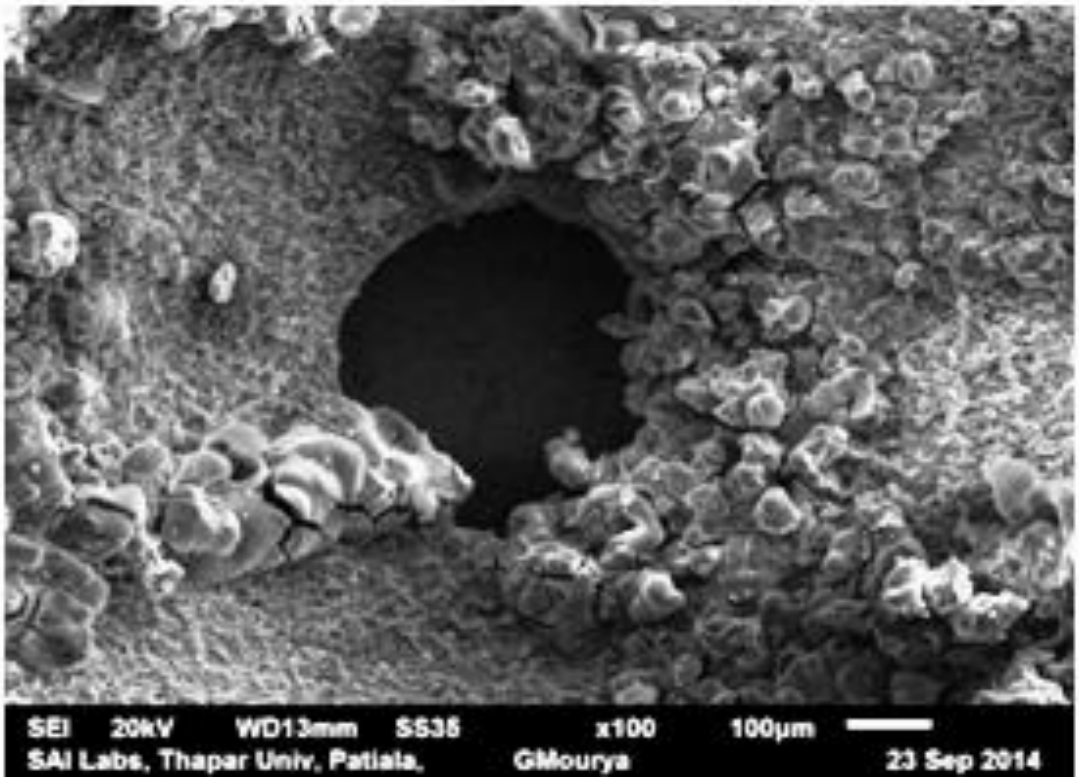

Fig. 4.78 SEM Photograph of Micro Hole Machined at 1.5 A Supply Current, 25 V Supply Voltage, 10 µs Pulse On Time, 5.5 µs Pulse Off Time, 25 g/*l* Electrolyte Concentration, and 0.6 *l*/min Electrolyte Flow Rate.

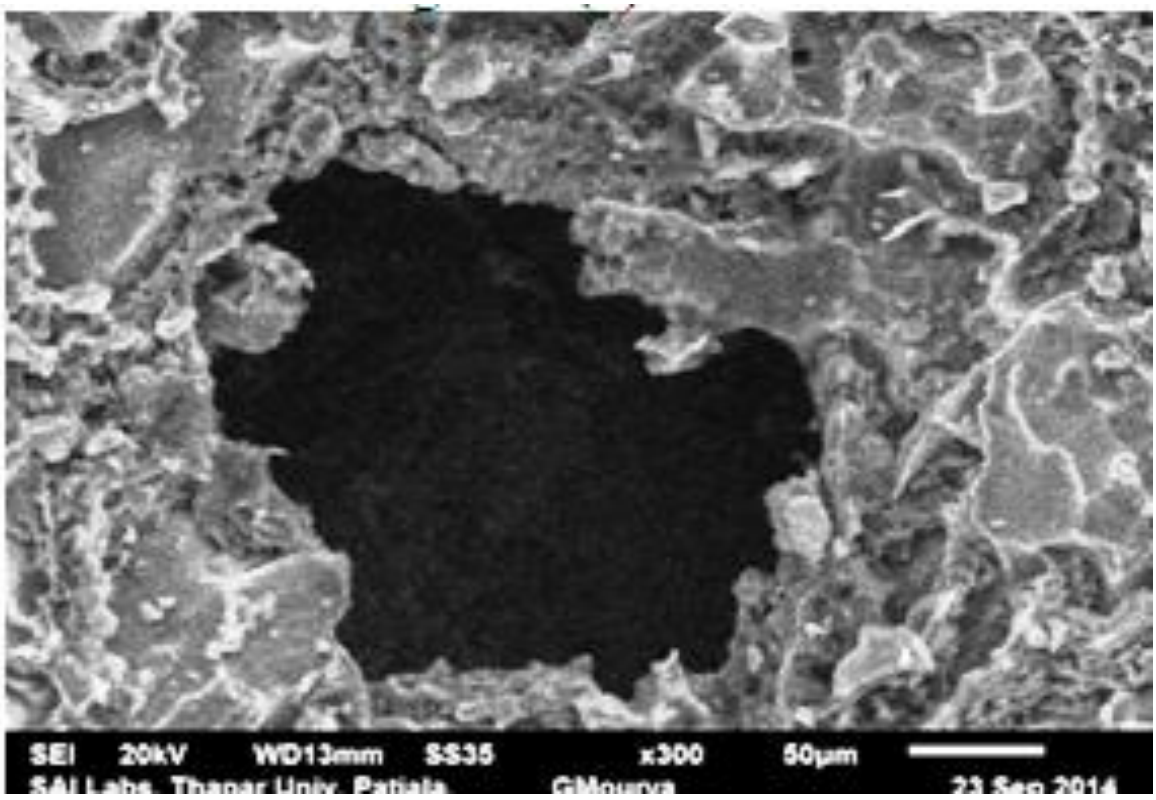

Fig. 4.79 SEM Photograph of A Micro Hole Machined at 0.5 A Supply Current, 25 V Supply Voltage, 5.5 µs Pulse On Time, 10 µs Pulse Off Time, 15 g/*l* Electrolyte Concentration, and 0.6 *l*/min Electrolyte Flow Rate.

Figure 4.80 shows SEM micrograph of a machined micro hole machined at 1.5 A supply current, 13 V supply voltage, 0.5 µs pulse on time, 10 µs pulse off time, 15 g/*l* electrolyte concentration, and 0.2 *l*/min electrolyte flow rate. Figure 4.81 shows the EDS of an extended part of micro hole as shown in Figure 4.80. From Figure 4.80, it is clear that the small particles of sodium and chloride on the periphery of machined hole may be due to the reaction product of anode with electrolyte NaCl. In EDS analysis, the percentage of residuals such as sodium (Na), carbon (C), silicon (Si), aluminium (Al), and oxygen (O) are detected on surface of micro holes. The micro hole surface was distorted because the sodium chloride, which was generated from the hybrid Al/MMC, interfered during electrochemical dissolution. The presence of oxygen in the workpiece probably was due to the fact the electrolyte normally contains water.

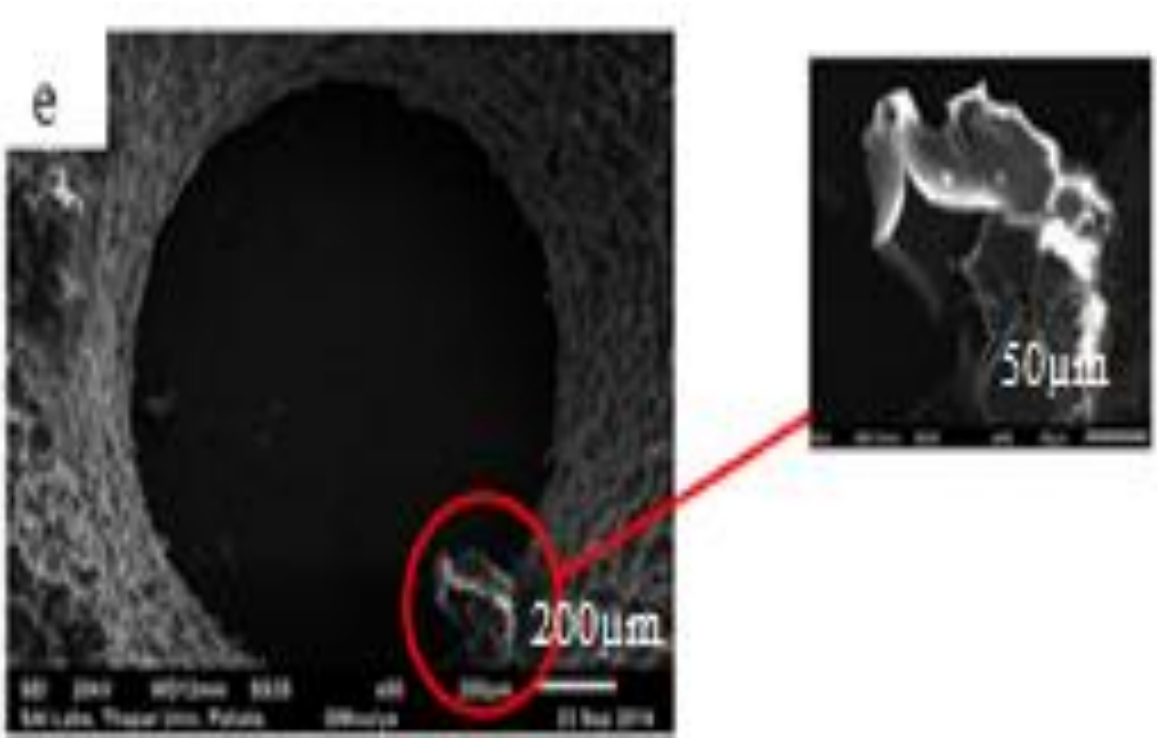

Fig. 4.80 SEM Photograph of Micro Holes Machined at 1.5 A Supply Current, 13 V Supply Voltage, 0.5 µs Pulse On Time, 10 µs Pulse Off Time, 15 g/*l* Electrolyte Concentration, and 0.2 *l*/min Electrolyte Flow Rate.

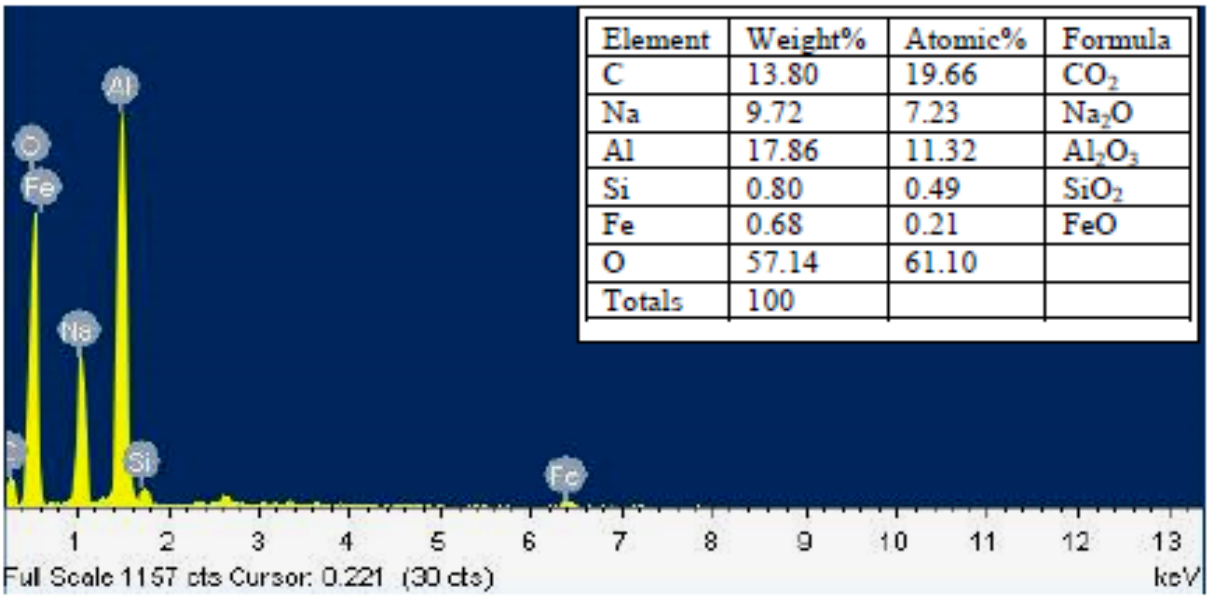

Element	Weight%	Atomic%	Formula
C	13.80	19.66	CO_2
Na	9.72	7.23	Na_2O
Al	17.86	11.32	Al_2O_3
Si	0.80	0.49	SiO_2
Fe	0.68	0.21	FeO
O	57.14	61.10	
Totals	100		

Fig. 4.81 EDS Reveals the Presence of Different Elements of Micro Machined Hole (Fig 4.80)

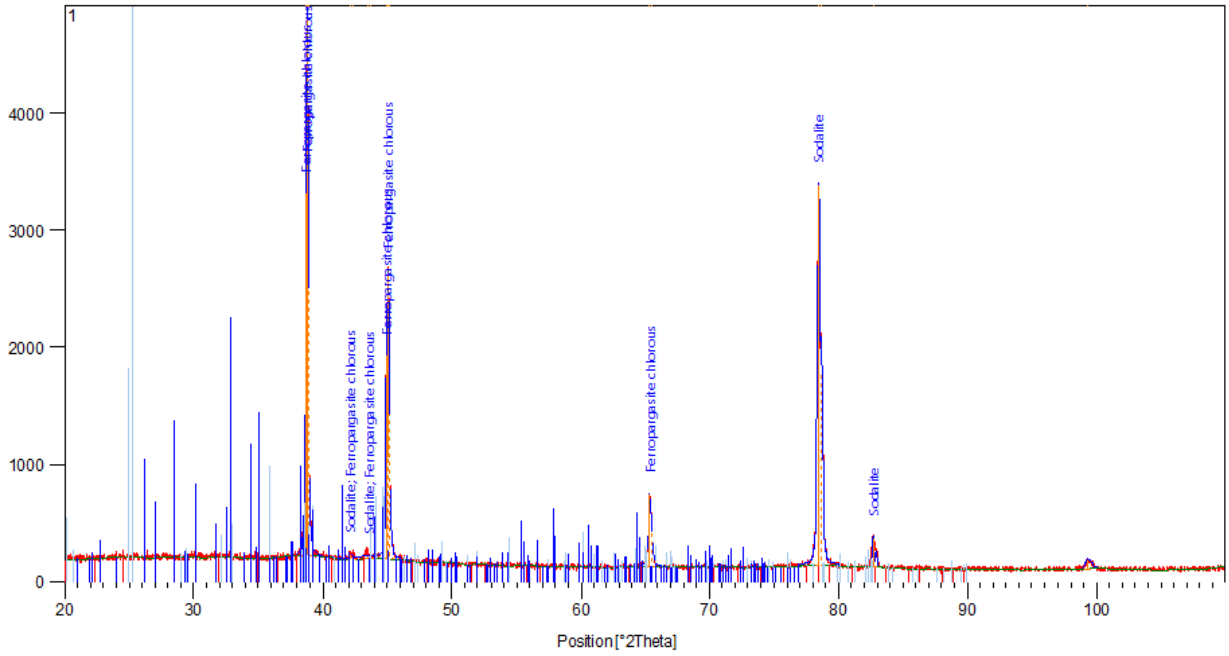

Fig. 4.82 XRD Pattern Micro Holes Machined at 0.5 A Supply Current, 13 V Supply Voltage, 10 µs Pulse On Time, 5.5 µs Pulse Off Time, 15 g/*l* Electrolyte Concentration, and 1.0 *l*/min Electrolyte Flow Rate.

The X-Ray diffraction technique is important to examine the presence of elements and formation of new compounds during machining by thermal process of any material. Figure 4.82 shows the element pattern of workpiece specimen when it was micro machined at 0.5 A supply current, 13 V supply voltage, 10 µs pulse on time, 5.5 µs pulse off time, 15 g/*l* electrolyte concentration, and 1 *l*/min electrolyte flow rate. The presence of Al_2O_3, C, SiC

particles, sodium chloride and formation of new compound sodalite and ferropargasite chlorous was confirmed by XRD plot. The formation of new compound sodalite may be due to reaction between sodium chloride content of workpiece Al_2O_3, SiC element, and aluminium itself due to excessive temperature into machining zone. The formation of compound ferropargasite chlorous may be due to chemical dissolution of ferrous material of workpiece holding device and reaction of workpiece with sodium chloride.

Figure 4.83 show the SEM of the micro machined holes machined at 1.5 A supply current, 13 V supply voltage, 10 µs pulse on time, 10 µs pulse off time, 15 g/*l* electrolyte concentration and 0.2 *l*/min electrolyte flow rate. At high machining voltage, high heat generated in between the IEG, results varying the electrolyte conductivity and hence a non-uniform current distribution in the gap is formed. As the electrolyte flow rate become shorter, it may not be enough to clean the machined product i.e. sludge partially blockage the IEG, thereby causing micro sparking. This irregularity is identified in the shape of small groove and pitting; it may be a cause of developing micro sparks due to the presence of sludge at high voltage and more electrolyte concentration. These micro sparks may generate uncontrolled MRR phenomenon, which in turn results in large overcut, taper cut and generation of micro spark affected zone.

Figure 4.84 show the SEM of the micro machined holes generated at 1.0 A supply current, 13 V supply voltage, 10 µs pulse on time, 5 µs pulse off time 5 g/*l* electrolyte concentration and 1.0 *l*/min electrolyte flow rate. At high pulse on time and supply current, the discharge energy per pulse increases, which produces deeper and wider overlapping craters, pockmarks, and micro cracks on the machined surface. Hence, at high supply current, the impact of discharge energy on workpiece surface becomes high, it leads to increase dissolution rate, thereby increases deterioration in surface roughness.

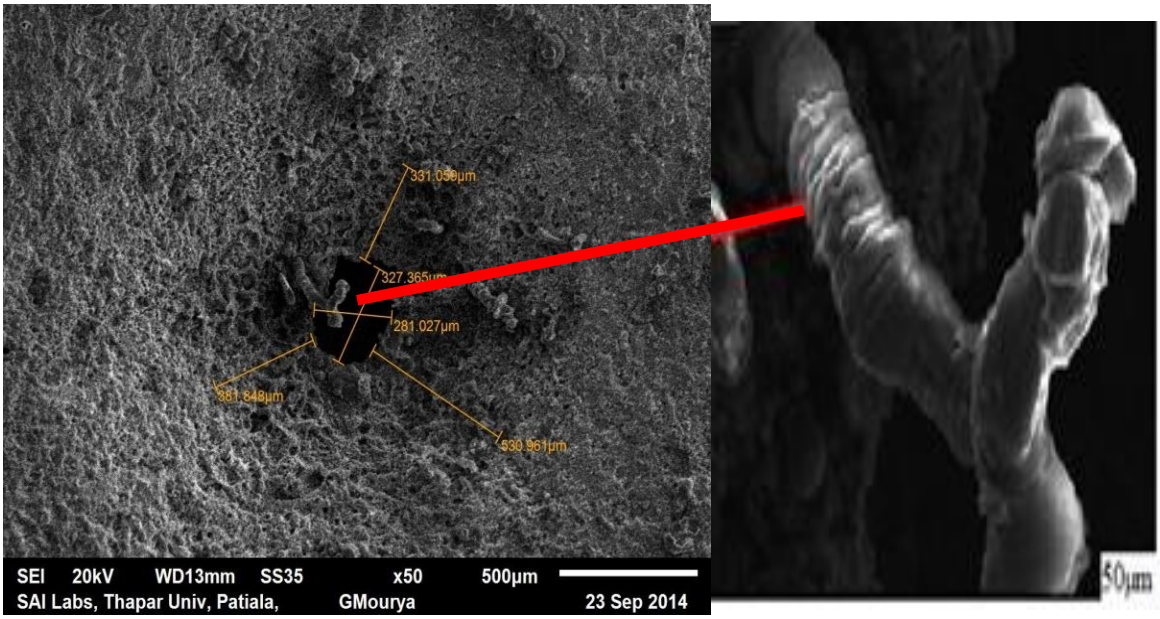

Fig. 4.83 SEM Photograph of Micro Machined Hole Machined at 1.5 A Supply Current, 13 V Supply Voltage, 10 µs Pulse On Time, 10 µs Pulse Off Time, 15 g/*l* Electrolyte Concentration and 0.2 *l*/min Electrolyte Flow Rate.

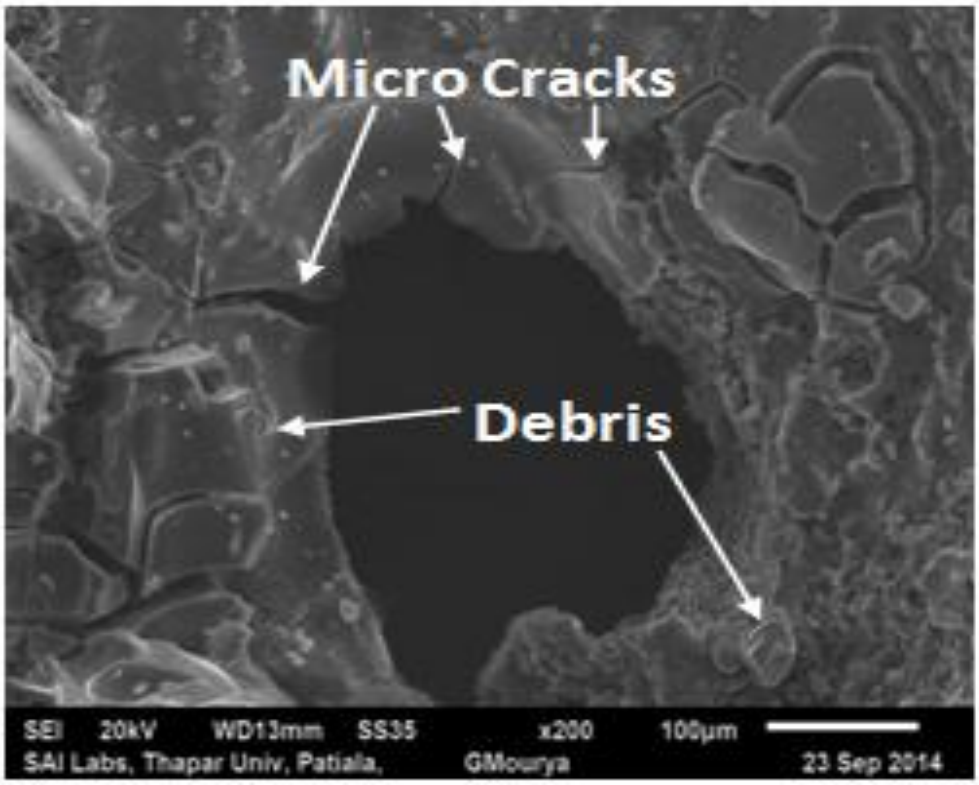

Fig. 4.84 SEM Photograph of Micro Machined Hole Machined at 1.0 A Supply Current 13 V Supply Voltage, 10 µs Pulse On Time, 5 µs Pulse Off Time, 5 g/*l* Electrolyte Concentration and 1.0 *l*/min Electrolyte Flow Rate.

Figure 4.85 (a) shows the SEM photograph of the machined hole machined at parametric settings i.e. 3 A supply current, 25 V supply voltage, 5.5 µs pulse on time, 10 µs pulse off time, 15 g/*l* electrolyte concentration and 0.6 *l*/min electrolyte flow rate. From Figure 4.85, it is noticed that the some of the material was deposited on micro machined surface and not removed from the inter electrode gap. The solidification of micro machined material also has been observed on the machined surface in the form of debris. The supply of high current produces non-uniform and irregular machined hole. This may be due to improper cleaning of sludge particles from the inter electrode gap (IEG) during machining. The high-applied voltage may result in breaking of the oxide layer. At high supply voltage, high heat in the inter-electrode gap is generated causing varying local electrolyte conductivity. This phenomenon is responsible for distribution of non-uniform current in the inter-electrode gap. The accuracy of micro hole was poor generated at parametric settings i.e. 3 A supply current, 13 V supply voltage, 0.5 µs pulse on time, 5.5 µs pulse off time, 15 g/*l* electrolyte concentration and 1 *l*/min electrolyte flow rate is shown in SEM photograph Figure 4.85 (b). Fig 4.85 (c) shows the micro cracks, micro debris and overlap craters have been identified on machined micro hole generated at parametric settings i.e. 3 A supply current, 13 V supply voltage, 10 µs pulse on time, 5.5 µs pulse off time, 15 g/*l* electrolyte concentration and 1 *l*/min electrolyte flow rate. Fig. 4.85 (d) shows the SEM photograph of the machined hole machined at 3 A supply current, 13 V supply voltage, 5.5 µs pulse on time, 0.5 µs pulse off time, 25 g/*l* electrolyte concentration and 0.6 *l*/min electrolyte flow rate. The overlapping craters, cracks and pockmarks have been observed on the machined micro surface. This may be due to supply of higher current and high pulse on time. The formation of deep and wide craters was observed at high supply current and pulse on time.

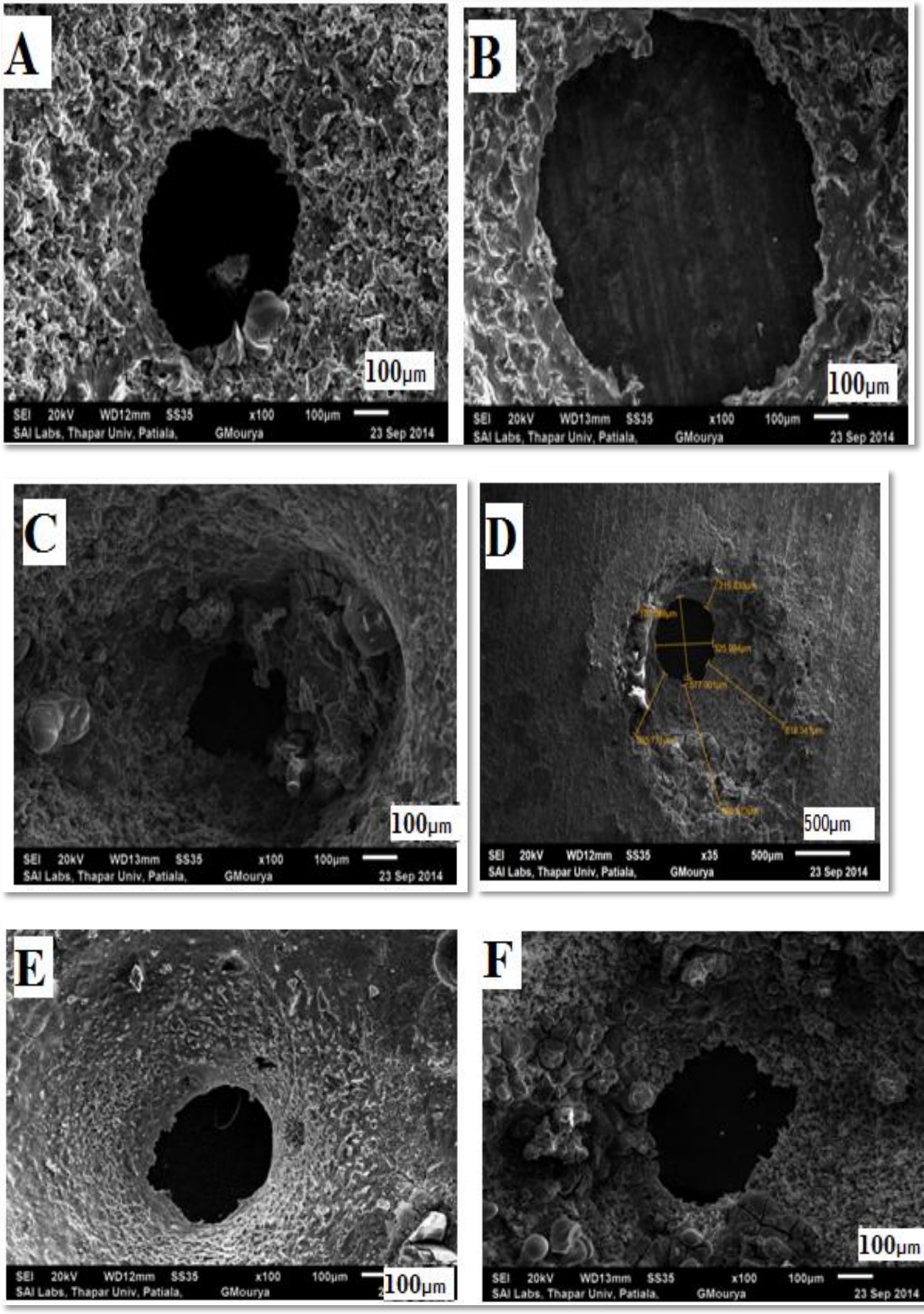

Fig. 4.85 SEM Photographs of Micro Machined Holes Machined at Higher Level of ECMM Machining Parameters

Fig. 4.85 (e) shows the SEM image of the machined hole machined at 3 A supply current, 25 V supply voltage, 5.5 µs pulse on time, 0.5 µs pulse off time, 15 g/*l* electrolyte concentration and 0.6 *l*/min electrolyte flow rate. Fig. 4.85 (f) shows the SEM image of the machined hole machined at parametric settings i.e. 1.5 A supply current, 25 V supply voltage, 5.5 µs pulse on time, 5.5 µs pulse off time, 25 g/*l* electrolyte concentration and 0.2 *l*/min electrolyte flow rate. With the increase of pulse-on time, both current and period of supply current increased. As a result increase the dissolution of material along the radial direction and thereby increases the overcut. At the same time removal of machined metal particles increases in between the inter electrodes gap. The presence of machined particles in the inter electrode gap may cause of sparking, which may lead to higher overcut.

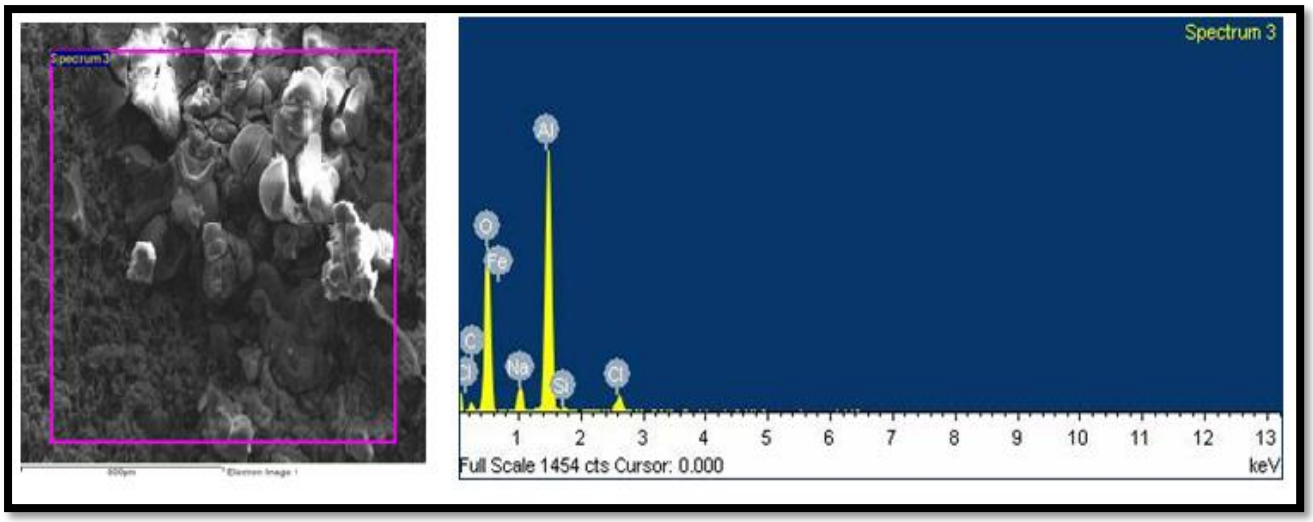

Fig. 4.86 EDS Analysis of Micro Machined Surface at Higher Level of ECMM Machining Parameters (Fig. 4.85 (f))

Figure 4.86 shows the EDS analysis of the micro machined surface of hybrid Al/MMC machined at 1.5 A supply current, 25 V supply voltage, 5.5 µs pulse on time, 5.5 µs pulse off time, 25 g/*l* electrolyte concentration and 0.2 *l*/min electrolyte flow rate. The deposition of compounds on the periphery of micro machined surface was identified. It may be due to supply of high voltage resulting in generation of high temperature and heat. The formation of small particles of sodium and chloride on the periphery of machined hole was observed. This may be due to the reaction of work piece with NaCl electrolyte solution. In addition, the presence of residuals such as sodium (Na), carbon (C), silicon (Si), aluminium (Al) and oxygen (O) were identified on the surface of micro holes. It reveals that there is migration of Fe from micro tool to the micro machined surface. Further, the presence of oxygen is due to formation of oxides and break down of electrolyte.

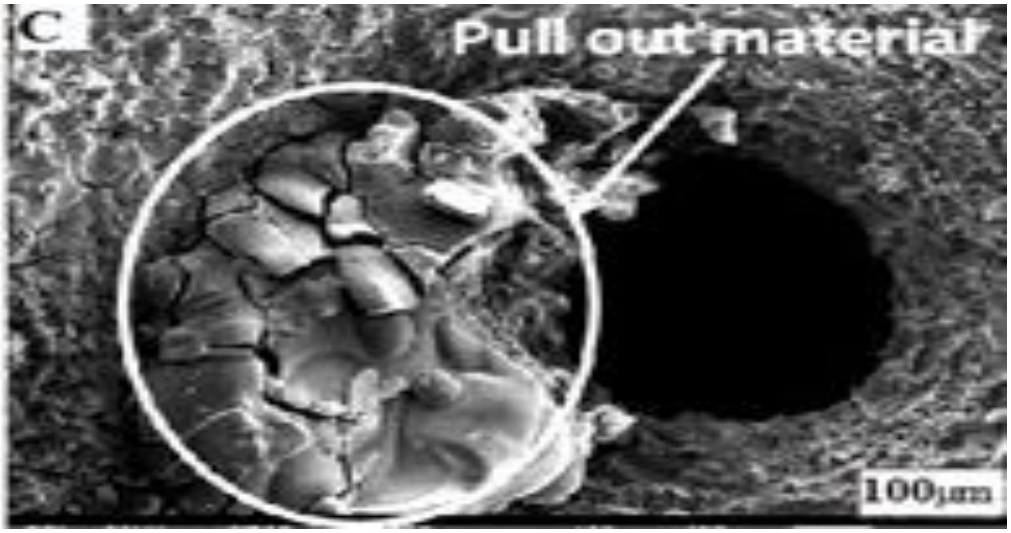

Fig. 4.87 SEM Photograph of Micro Machined Hole Machined at 1.5 A Supply Current, 13 V Supply Voltage, 10 µs Pulse On Time, 0.5 µs Pulse Off Time, 15 g/*l* Electrolyte Concentration and 0.2 *l*/min Electrolyte Flow Rate.

Figure 4.87 shows the SEM analysis for micro machined surface of hybrid Al/MMC machined at 1.5 A supply current, 13 V supply voltage, 10 µs pulse on time, 0.5 µs pulse off time, 15 g/*l* electrolyte concentration and 0.2 *l*/min electrolyte flow rate. From Figure 4.87, it is clear that the few part of the molten material was deposited in the form of globules i.e. debris. From the detail studies, it is also clear that the molten metal is not removed from the gap and some part of the molten metal's are pullouts and solidifies on the surface of the machine zone in the form of debris.

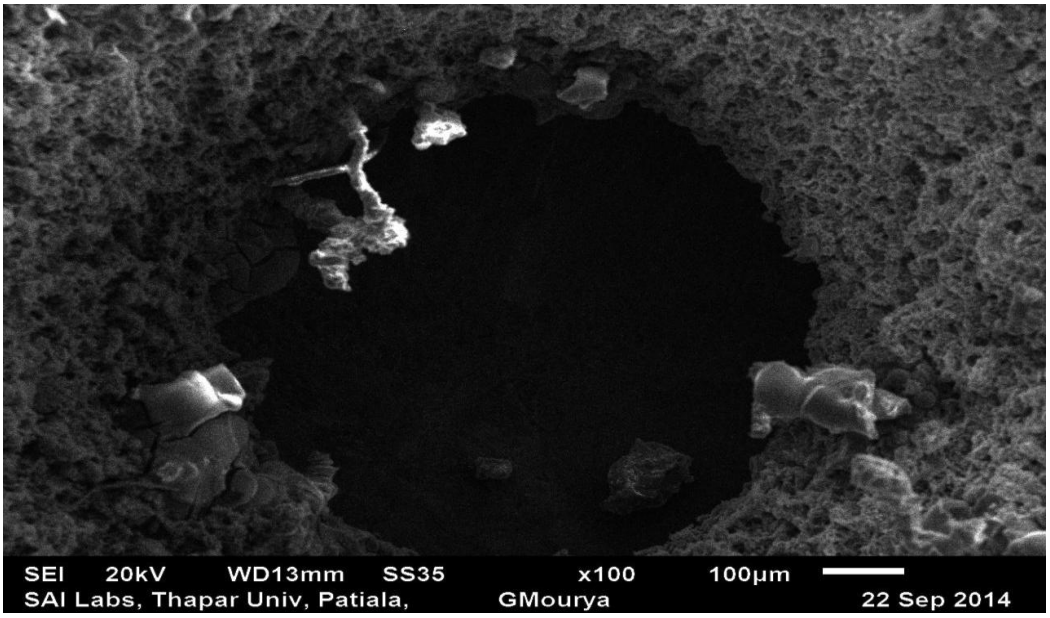

Fig. 4.88 SEM Photograph of Micro Machined Hole Machined at 3 A Supply Current, 13 V Supply Voltage, 5.5 µs Pulse On Time, 10 µs Pulse Off Time, 25 g/*l* Electrolyte Concentration and 0.6 *l*/min Electrolyte Flow Rate.

Figure 4.88 shows the SEM analysis for micro machined surface of hybrid MMC obtained at 3 A supply current, 13 V supply voltage, 5.5 µs pulse on time, 10 µs pulse off time, 25 g/*l* electrolyte concentration and 0.6 *l*/min electrolyte flow rate. From Figure 4.88, it is clear that the few part of the molten material was deposited in the form of globules as debris.

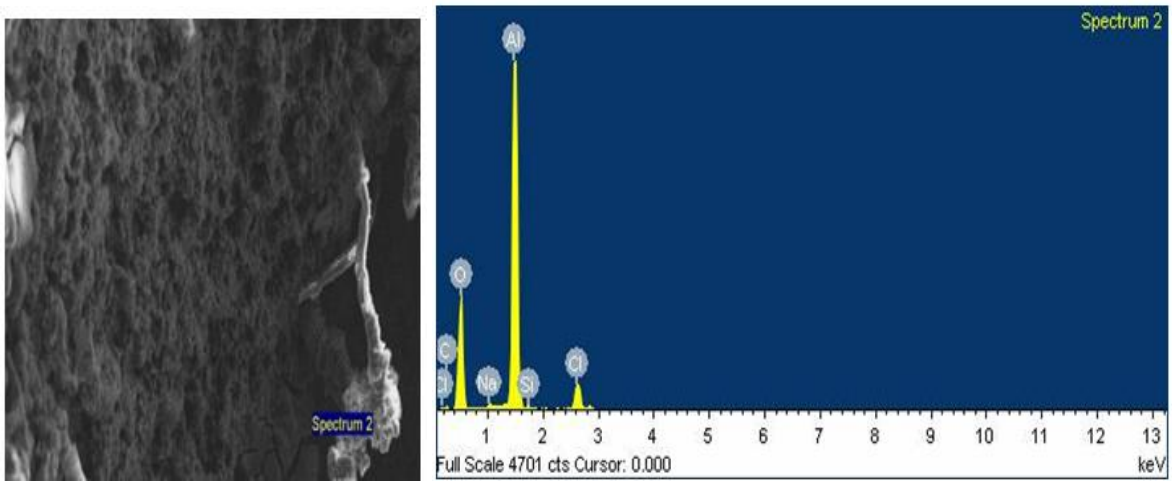

Fig. 4.89 EDS Analysis of Micro Machined Surface of Hybrid Al/MMC (Fig. 4.88)

Figure 4.89 shows the EDS of micro machined surface of hybrid MMC machined at 3 A supply current, 13 V supply voltage, 5.5 µs pulse on time, 10 µs pulse off time, 25 g/*l* electrolyte concentration and 0.6 *l*/min electrolyte flow rate. From Figure 4.89, it is clear that there is some irregularity and deposition of some reaction products surrounding the micro machined surface. It may be due to supply of high voltage and large amount of heat generated in between the inter electrode gap (IEG), causes variation of the electrolyte conductivity and non-uniform distribution of current in the gap. The percentage of residuals such as sodium (Na), carbon (C), silicon (Si), aluminium (Al), and oxygen (O) were detected on machined surface of the micro holes. The micro machined surface was slightly distorted because of the sodium chloride, and it reduces the electrochemical dissolution. The presence of oxygen in the workpiece probably was due to the fact of the electrolyte normally contains water.

Figure 4.90 shows the SEM analysis for micro machined surface of hybrid Al/MMC machined at 1.5 A supply current, 25 V supply voltage, 5.5 µs pulse on time, 5.5 µs pulse off time, 25 g/*l* electrolyte concentration and 1 *l*/min electrolyte flow rate. At higher voltage and higher electrolyte concentration, the dissolution energy per pulse increases, which produces the deeper and wider overlapping craters, and pockmarks on the machined surface. The rapid cooling and heating effect the generate gas bubbles that explode when discharge ceases.

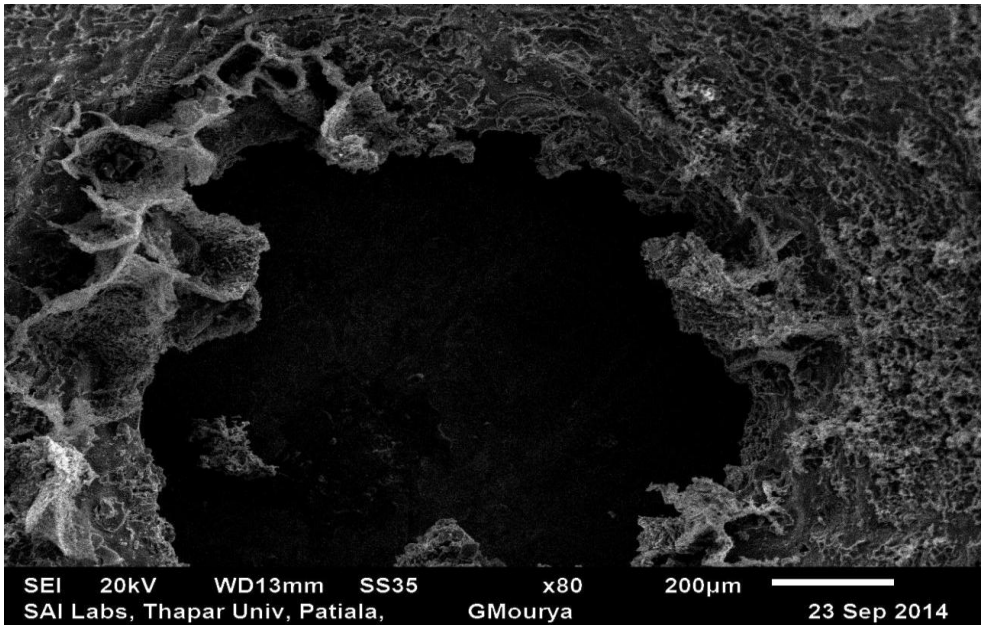

Fig. 4.90 SEM Photograph of Micro Machined Hole Machined at 1.5 A Supply Current, 25 V Supply Voltage, 5.5 µs Pulse On Time, 5.5 µs Pulse Off Time, 25 g/*l* Electrolyte Concentration and 1 *l*/min Electrolyte Flow Rate.

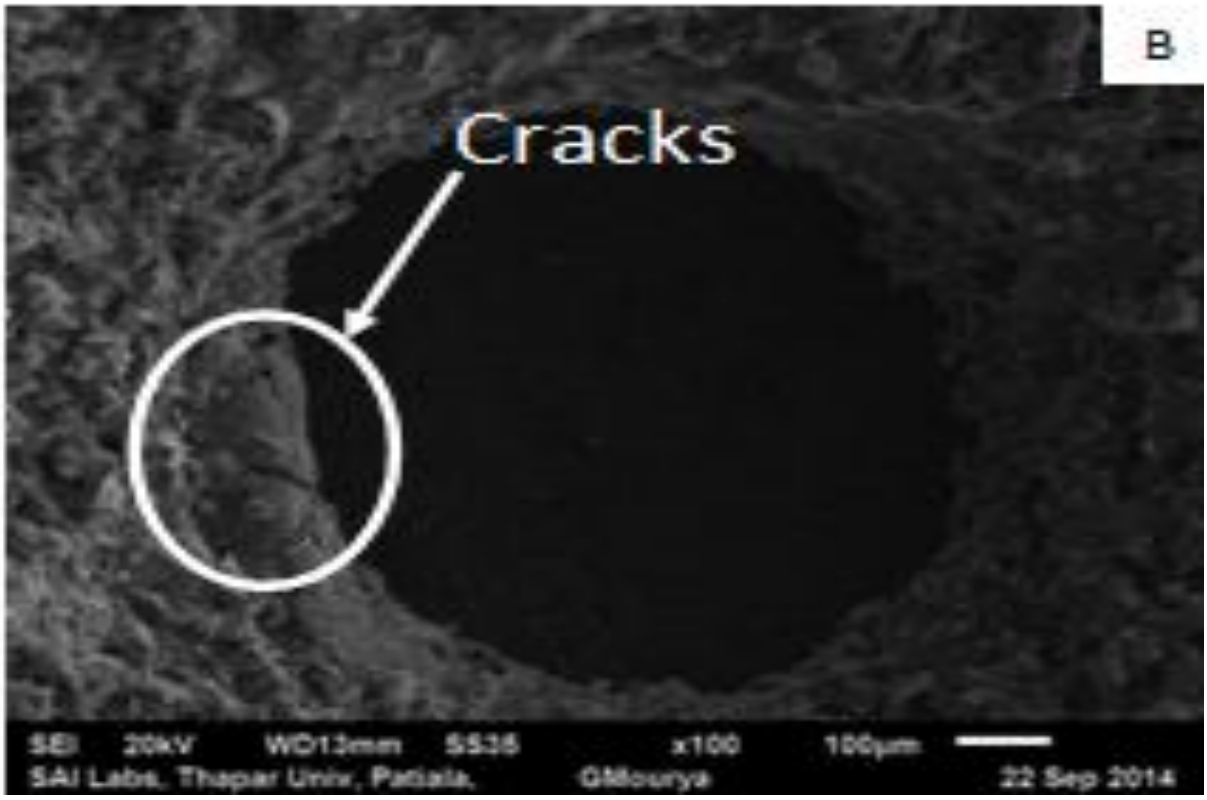

Fig. 4.91 SEM Photograph of Micro Machined Hole Machined at 1 A Supply Current, 13 V Supply Voltage, 0.5 µs Pulse On Time, 5 µs Pulse Off Time, 25 g/*l* Electrolyte Concentration and 0.6 *l*/min Electrolyte Flow Rate.

Figure 4.91 shows the SEM analysis of the micro machined surface of hybrid Al/MMC machined at 1 A supply current, 13 V supply voltage, 0.5 µs pulse on time, 5 µs pulse off time, 25 g/*l* electrolyte concentration and 0.6 *l*/min electrolyte flow rate. The rapid cooling and heating effect at in IEG generates the gas bubbles that explode when discharge ceases. The deeper and wider cracks were identified when experiments were carried out at high voltage and high electrolyte concentration. The impact of discharge energy increases in the machining zone, as a result dissolution rate of metal increases that leads to deterioration of the machined surface.

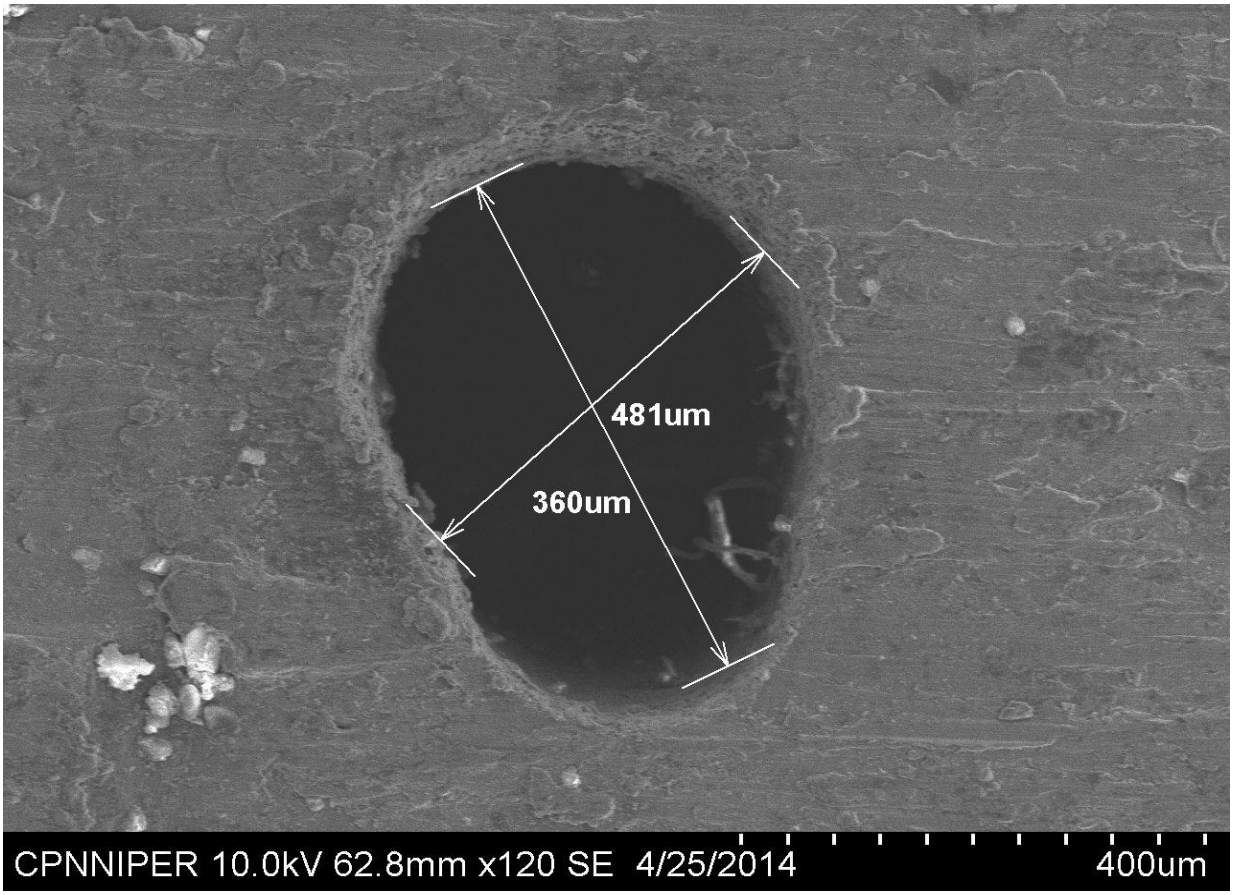

Fig. 4.92 SEM Photograph of Micro Machined Hole Machined at 1 A Supply Current, 25 V Supply Voltage, 10 µs Pulse On Time, 5 µs Pulse Off Time, 15 g/*l* Electrolyte Concentration and 1.0 *l*/min Electrolyte Flow Rate.

Figure 4.92 shows the SEM photograph for micro machined surface of hybrid Al/MMC machined at 1 A supply current, 25 V supply voltage, 10 µs pulse on time, 0.5 µs pulse off time, 15 g/*l* electrolyte concentration and 1.0 *l*/min electrolyte flow rate. From Figure 4.92, it is clear that the micro machined hole is oval in shape, which due to micro machined of hybrid MMC at higher voltage and higher electrolyte flow rate. The micro tool become vibrates so

that more materials have dissolved in lateral direction of hole, hence increases taper cut and more overcut.

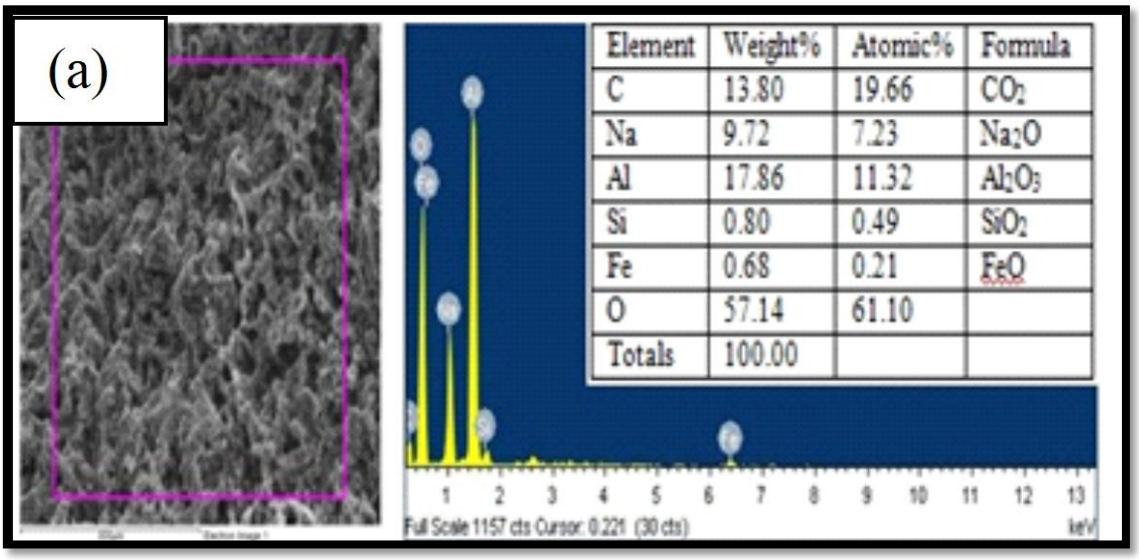

Fig. 4.93 EDS Reveals the Presence of Different Elements from the Machined Hole as Shown in Fig. 4.92

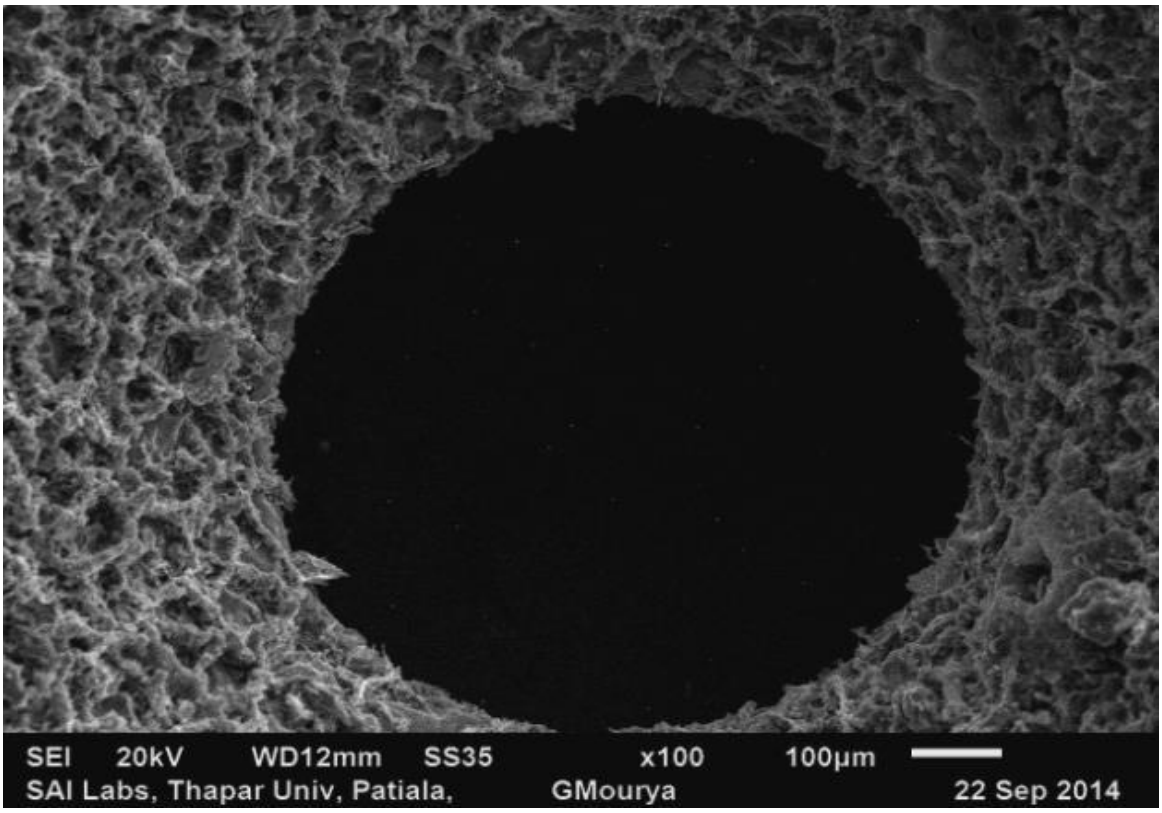

Fig. 4.94 SEM Photograph of Micro Machined Hole Machined at 0.5 A Supply Current, 2 V Supply Voltage, 5.5 µs Pulse On Time, 10 µs Pulse Off Time, 15 g/*l* Electrolyte Concentration and 0.6 *l*/min Electrolyte Flow Rate.

Figure 4.93 EDS shows the different elements present even after micro machined of the stir cast hybrid Al/MMC. EDS shows the presence of small particles of sodium and chloride on the periphery of machined hole, it may be due to the reaction product at anode with NaCl electrolyte. In EDS also identified the percentage of residuals such as Na, Carbon, Si, Al, and Oxygen on the surface of micro holes. The micro machined surface distorted due to sodium chloride impedes during electrochemical dissolution. The oxygen is present in the workpiece due to the fact the electrolyte normally contains water.

Figure 4.94 shows the SEM photograph of the micro machined surface of machine at 0.5 A supply current, 2 V supply voltage, 5.5 µs pulse on time, 10 µs pulse off time, 15 g/*l* electrolyte concentration and 0.6 *l*/min electrolyte flow rate. From Figure 4.94, it clear that the hole is circular due to machining of hybrid Al/MMC at low power supply at higher pulse off time.

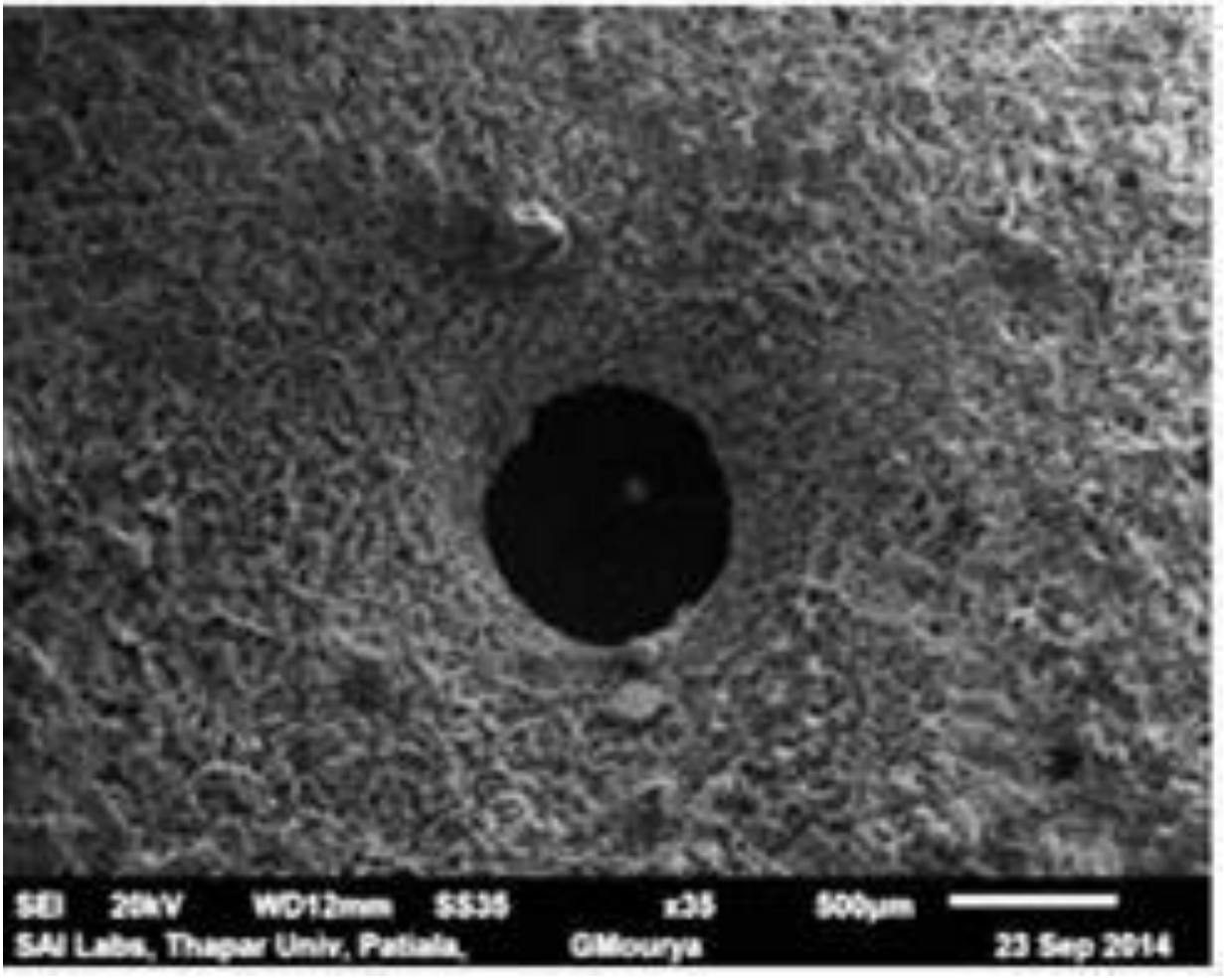

Fig. 4.95 SEM Photograph of Micro Machined Hole Machined at 1.5 A Supply Current, 2 V Supply Voltage, 0.5 µs Pulse On Time, 5.5 µs Pulse Off Time, 25 g/*l* Electrolyte Concentration and 0.6 *l*/min Electrolyte Flow Rate.

Figure 4.95 shows SEM photograph of the micro hole machined at 1.5 A supply current, 2 V supply voltage, 0.5 µs pulse on time, 5.5 µs pulse off time, 25 g/*l* electrolyte concentration and 0.6 *l*/min electrolyte flow rate. From Figure 4.95, it clear that the hole is circular. This machining condition i.e. parametric setting gives better performance i.e. high MRR as well as low taper cut, low over cut, low micro spark affected zone. From the examination of surface texture, it is noticed that during micro electrochemical machining, sodium chloride is deposited in the form of debris.

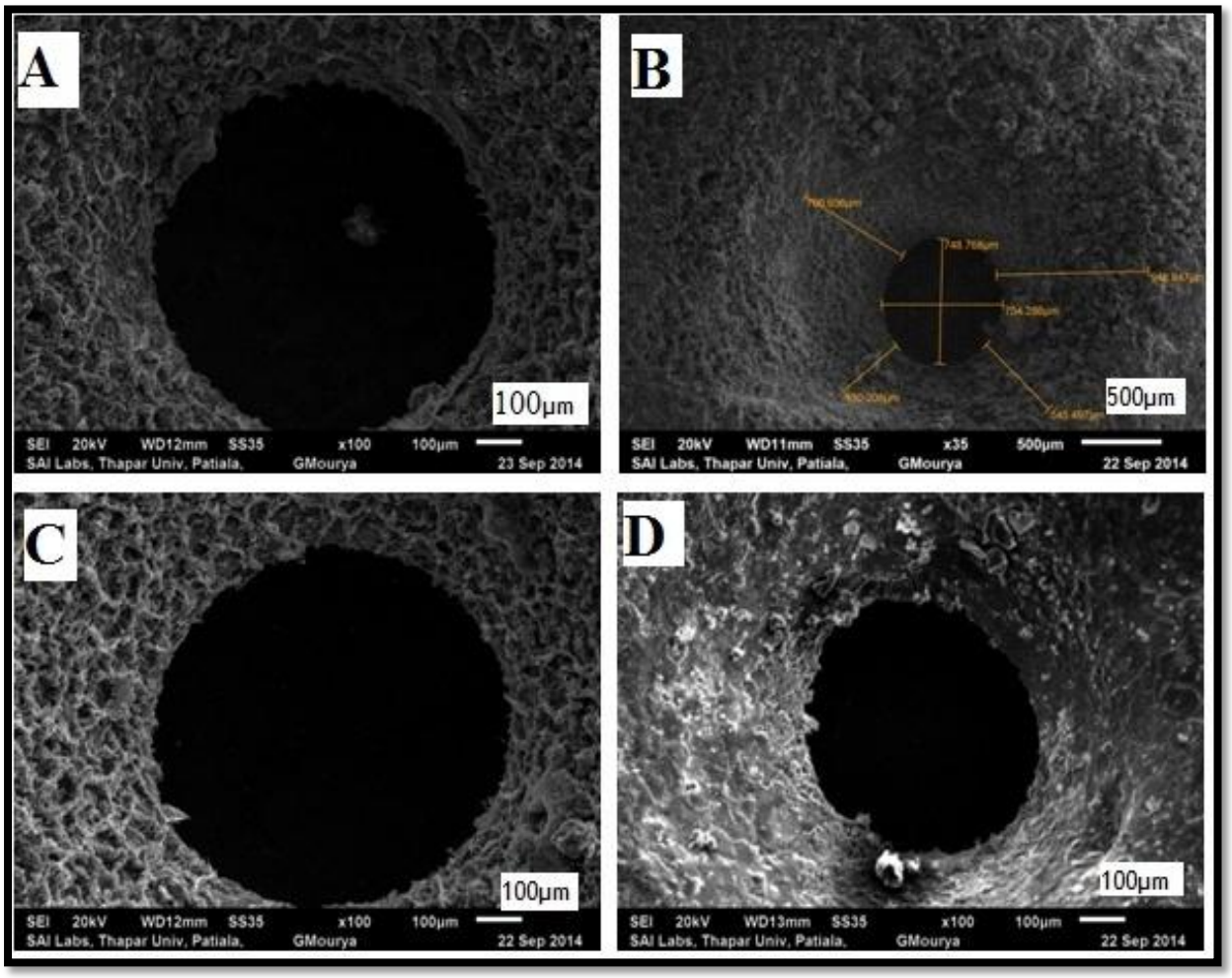

Fig. 4.96 SEM Photographs of Micro Machined Hole Machined at Lower Level of ECMM Machining Parameters

Fig. 4.96 (a) shows SEM photograph of machined holes machined at 0.5 A supply current, 2 V supply voltage, 5.5 µs pulse on time, 0.5 µs pulse off time, 15 g/*l* electrolyte concentration, and 0.6 *l*/min electrolyte flow rate. At this parametric setting, low taper cut, low over cut and low micro spark affected zone were identified. Fig. 4.96 (b) shows SEM photograph of micro machined hole machined at 1.5 A supply current, 2 V supply voltage, 5.5 µs pulse on time, 5.5 µs pulse off time, 5 g/*l* electrolyte concentration and 1 *l*/min electrolyte flow rate. Fig. 4.96 (c)

shows SEM image of the micro machined hole generated at 0.5 A supply current, 2 V supply voltage, 5.5 µs pulse on time, 10 µs pulse off time, 15 g/*l* electrolyte concentration and 0.6 *l*/min electrolyte flow rate. Fig. 4.96 (d) shows another SEM image of the micro machined hole machined at 1.5 A supply current, 2 V supply voltage, 0.5 µs pulse on time, 5.5 µs pulse off time, 25 g/*l* electrolyte concentration and 0.6 *l*/min electrolyte flow rate.

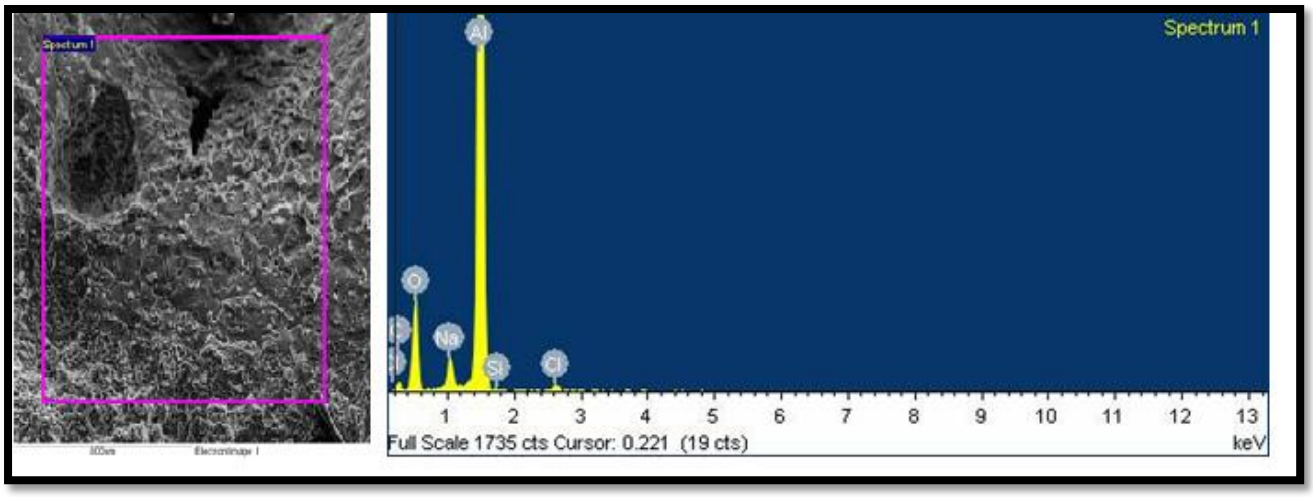

Fig. 4.97 EDS Analysis of The Micro Machined Surface Machined at 1.5 A Supply Current, 2 V Supply Voltage, 0.5 µs Pulse On Time, 5.5 µs Pulse Off Time, 25 g/*l* Electrolyte Concentration and 0.6 *l*/min Electrolyte Flow Rate

Figure 4.97 shows EDS of the micro hole surface machined at parameters setting i.e. 1.5 A supply current, 2 V supply voltage, 0.5 µs pulse on time, 5.5 µs pulse off time, 25 g/*l* electrolyte concentration and 0.6 *l*/min electrolyte flow rate. The formation of small particles of sodium and chloride were identified on the periphery of machined hole. This may be due to the reaction of anode with NaCl electrolyte. From EDS analysis, the formation of residuals such as sodium (Na), carbon (C), silicon (Si), aluminium (Al), and oxygen (O) were also identified on the machined surface. The ovality in the machined hole was observed that may be due to impede of sodium chloride during electrochemical dissolution. The presence of oxygen was observed in the work piece that may be due to contain of water in the electrolyte.

Figure 4.98 shows EDS of the micro hole surface machined at low level (Figure 4.96). The presence of small particles of sodium and chloride were identified on the periphery of machined hole. This is may be due to the reaction of anode with NaCl electrolyte. From EDX analysis, the formation of residuals such as sodium (Na), carbon (C), silicon (Si), aluminium (Al), and oxygen (O) were also identified on the machined surface. The presence of oxygen also identified in the work piece surface that may be due to presence of water in electrolyte.

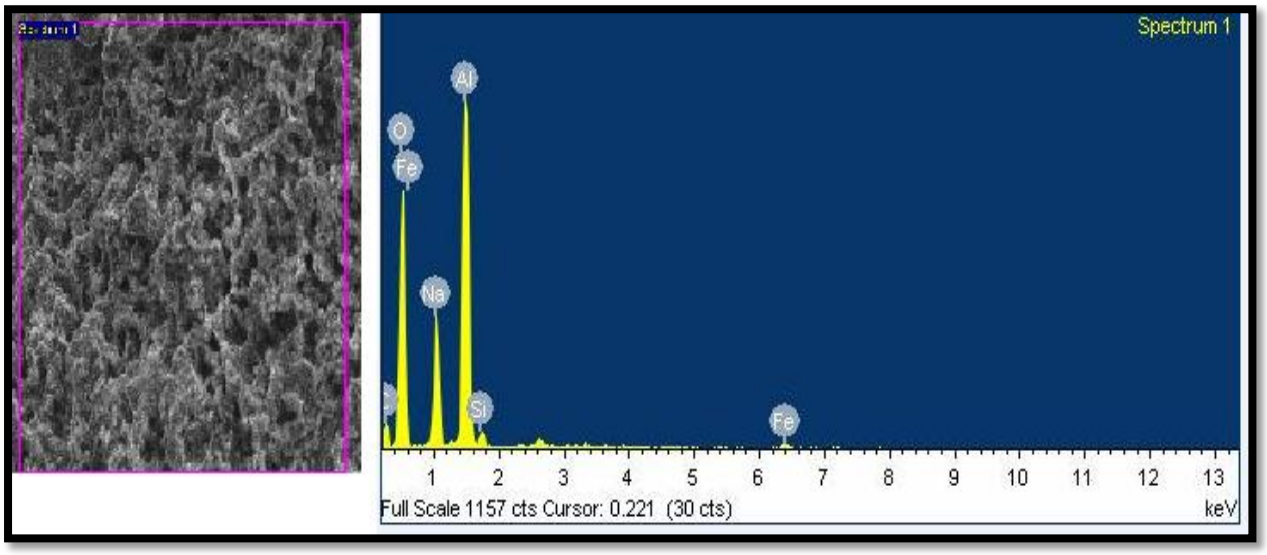

Fig. 4.98 EDS Analysis on Micro Hole Surface Machined at Lower Level of ECMM Machining Parameters

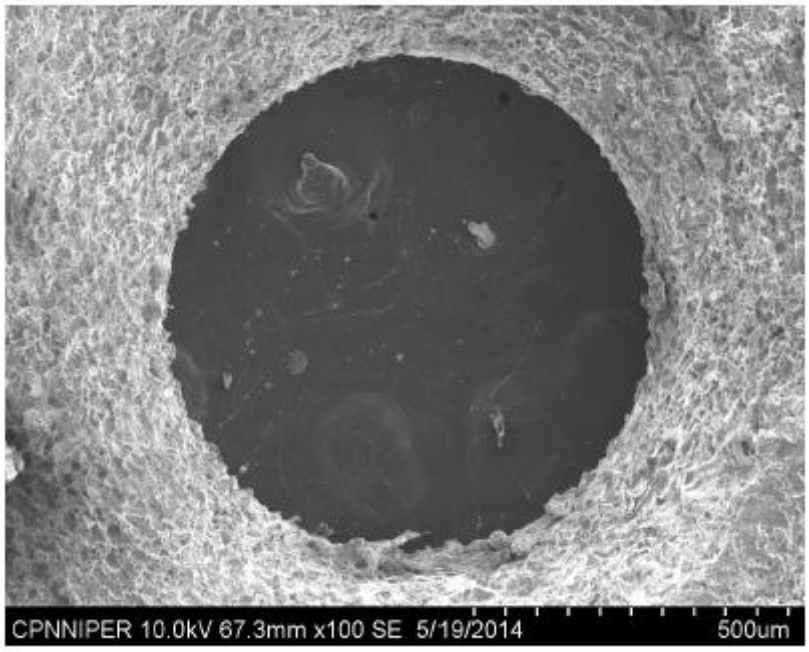

Fig. 4.99 SEM Photograph of Through Micro Holes Machined at 0.5 A Supply Current, 2.00 V Supply Voltage, 3.5 µs Pulse On Time, 6.5 µs Pulse Off Time, 14 g/*l* Electrolyte Concentration and 0.6 *l*/min Electrolyte Flow Rate

Figure 4.99 shows the SEM image of through micro holes generated during micro drilling of hybrid Al/(Al_2O_3p+SiCp+Cp)-MMC on developed ECMM setup. Fig 4.99 shows a micro hole generated with parametric setting at 0.5 A supply current, 2.00 V supply voltage, 3.5 µs pulse on time, 6.5 µs pulse off time, 14 g/*l* electrolyte concentration and 0.6 *l*/min electrolyte flow rate. From SEM Figure 4.99, it is clear that the shape of the generated micro holes is better and circular in shape.

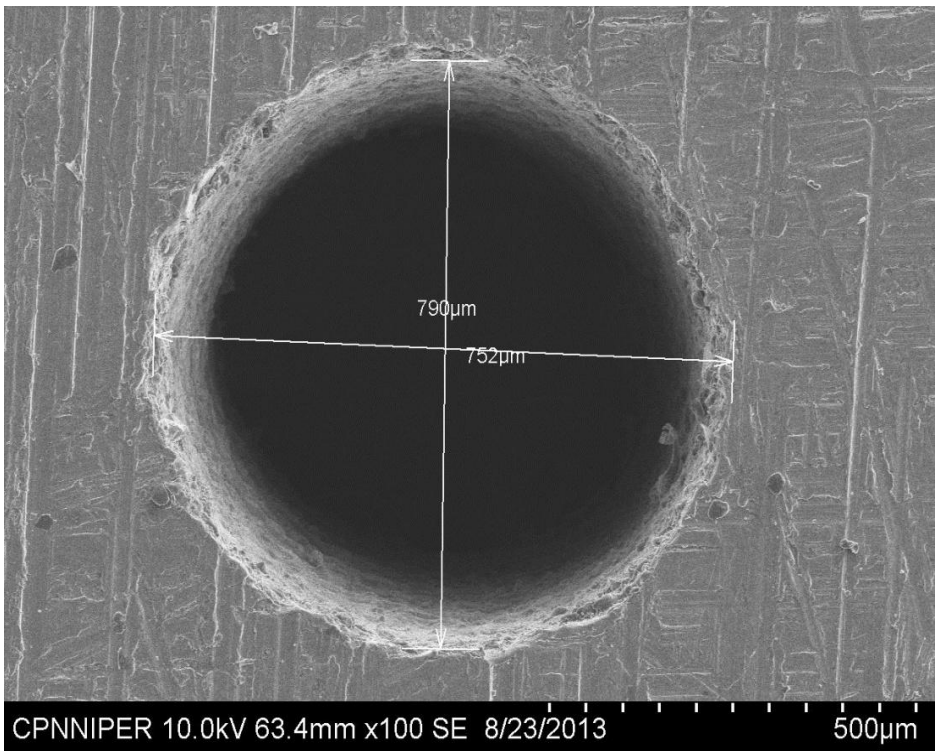

Fig. 4.100 SEM Photograph of Through Micro Holes Machined at 0.5 A Supply Current, 2.0 V Supply Voltage, 3.5 µs Pulse On Time, 5.5 µs Pulse Off Time, 16 g/*l* Electrolyte Concentration and 0.71 *l*/min Electrolyte Flow Rate

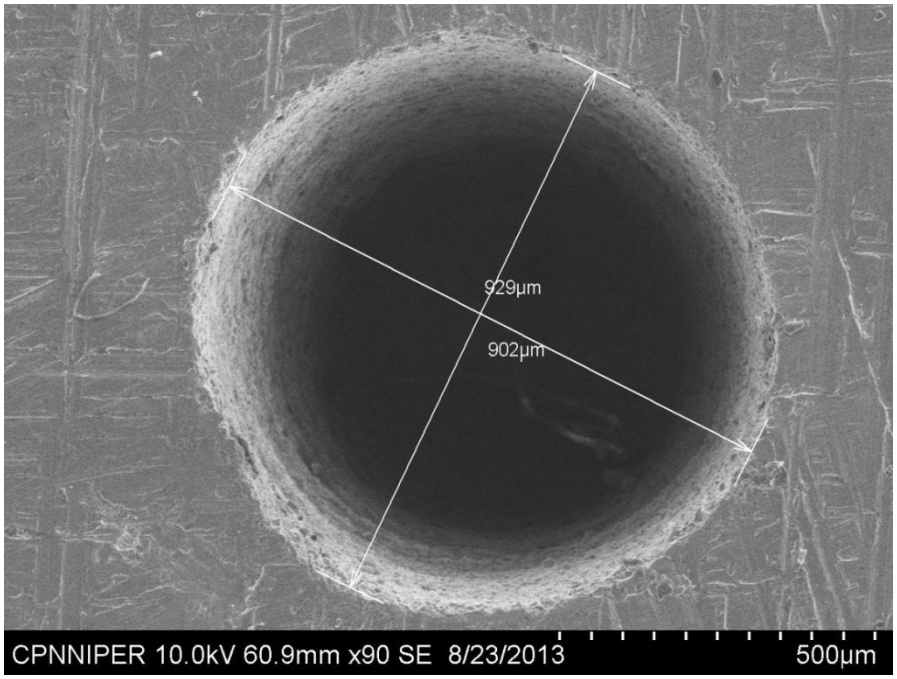

Fig. 4.101 SEM Photograph of Through Micro Holes Machined at 0.5 A Supply Current, 2.5 V Supply Voltage, 3.5 µs Pulse On Time, 6.0 µs Pulse Off Time, 13 g/*l* Electrolyte Concentration and 0.51 *l*/min Electrolyte Flow Rate

Figure 4.100 shows the SEM image of through micro holes generated during micro drilling of hybrid Al/(Al_2O_3p+SiCp+Cp)-MMC on developed ECMM setup. From SEM Figure 4.100, it

is clear that the shape of the generated micro holes is better and circular in shape. It is also clear that the generated micro hole is slightly in taper shape along the depth. It may be due to the taper and wear out of micro tool as well as deformed uncut reinforced particles around the tool during micro drilling but not cleaned out properly by flow of electrolyte at short pulse off time. This may eliminate or reduce by proper coating or masking on the micro tool and work piece exposed area. Figure 4.101 shows the SEM image of through micro holes generated during micro drilling of hybrid Al/(Al_2O_3p+SiCp+Cp)-MMC on developed ECMM setup. It is clear that the shape of the generated micro holes is better and circular in shape.

4.13 SEM, AND EDS ANALYSIS OF MICRO ELECTRODES (TOOLS)

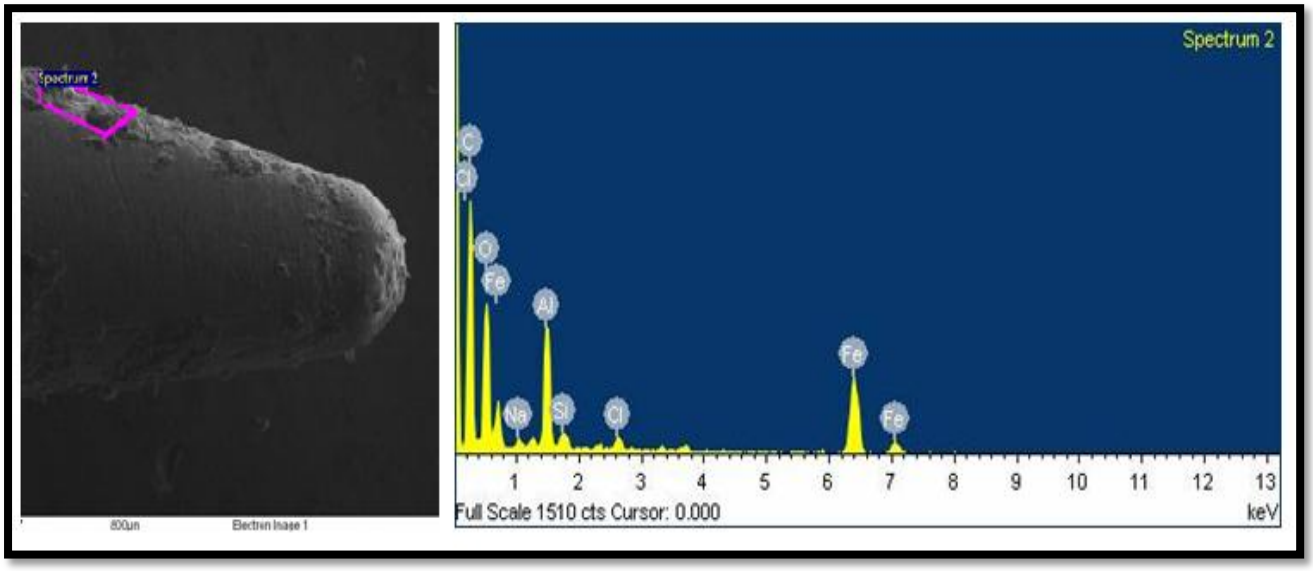

Fig 4.102 SEM Photograph and EDS analysis of Microelectrode

The presence of machined particles in the micro machining inter electrode gap may cause sparking, which may lead to electrode wear. This decreases the machining accuracy due to supply of higher current at higher pulse on time. From the EDS analysis of micro tool shown in Figure 4.102, it is noticed that the reinforced particles present in hybrid Al/MMC also deposited on micro tool. It has been observed that the various residuals such as sodium (Na), carbon (C), silicon (Si), aluminum (Al), sulphur (S), chlorine (Cl), tungsten (W), and oxygen (O) were deposited on the surface of micro-tool. This may be due to the melting, re-solidification and deposition during micromachining of hybrid Al/MMC.

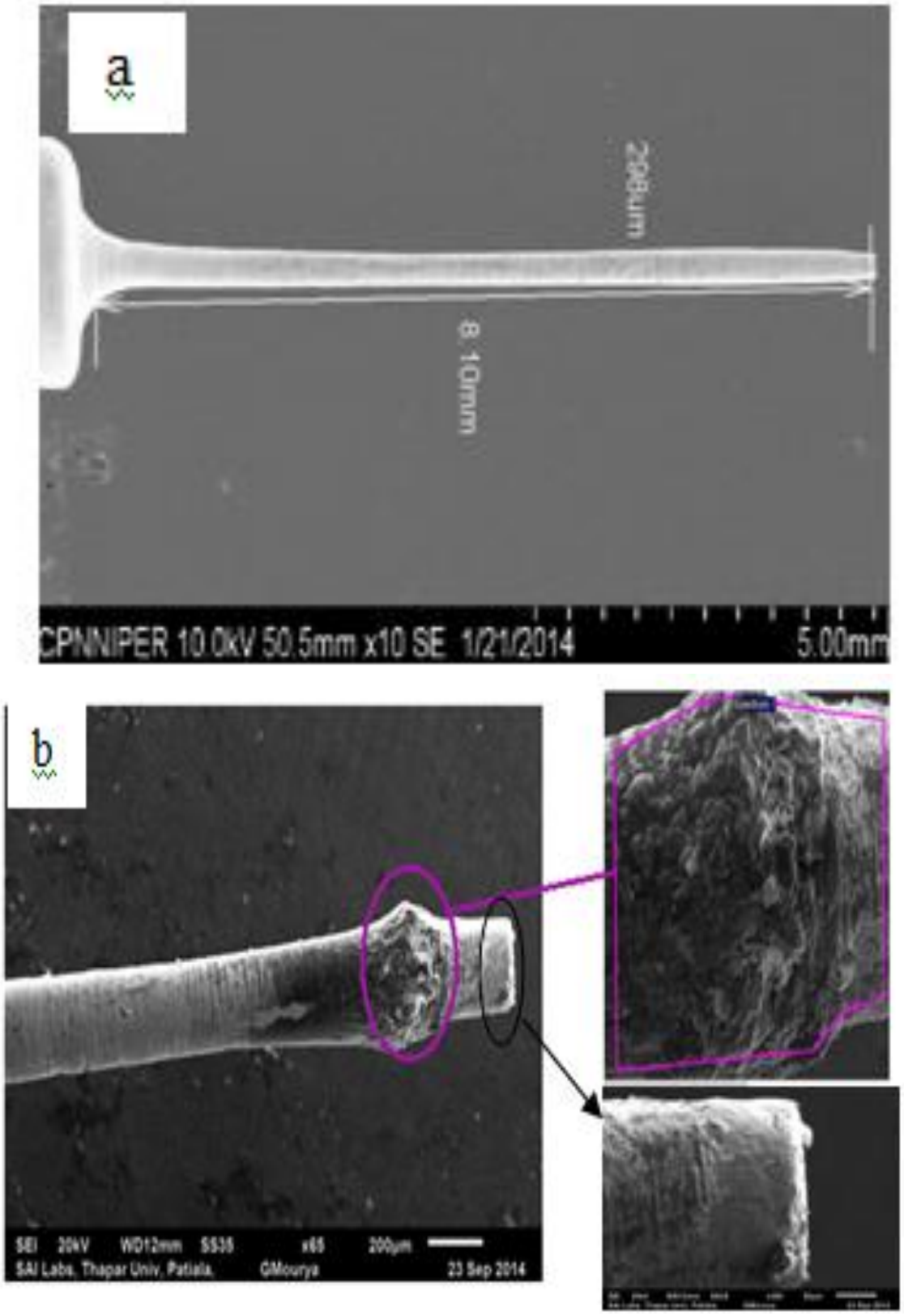

Fig 4.103 (a) SEM Photograph of Fabricated Micro Tool, (b) SEM of Micro Tool After Machining

Fig 4.103 (a) shows the SEM micrograph of micro tool before electrochemical micro machining. Generally, the micro tool is likely to be highly worn out by increasing pulse-on

time from 5.5 to 10 μs with constant setting of 25 V power supply during micro machining is shown in Fig. 4.103 (b). This phenomenon may attribute to the relative increase in electrolyte conductivity and current density when increases pulse-on time; this may be the cause of generating micro sparks, hence increases in tool wear. As the electric field at the site of electrode was stronger, causing the supply current higher than other site, the bottom surface of electrode was corroded and destroyed the surface.

From Figure 4.104, it was clear that the some particles were deposit on tool during micro sparking. It was due to increase of pulse-on time. EDS was conduct to analyze the composition of materials on the electrodes surface. During EDS analysis, the percentage of residuals such as sodium (Na), carbon(C), silicon (Si), aluminium (Al), sulphur(S), chlorine (Cl), tungsten (W), and oxygen (O) were detected as deposited particles on micro tool. This was due to the melting, re-solidification and deposition of the Al/(Al_2O_{3p}+SiC_p+C_p)-MMC during micro machining because of sparking.

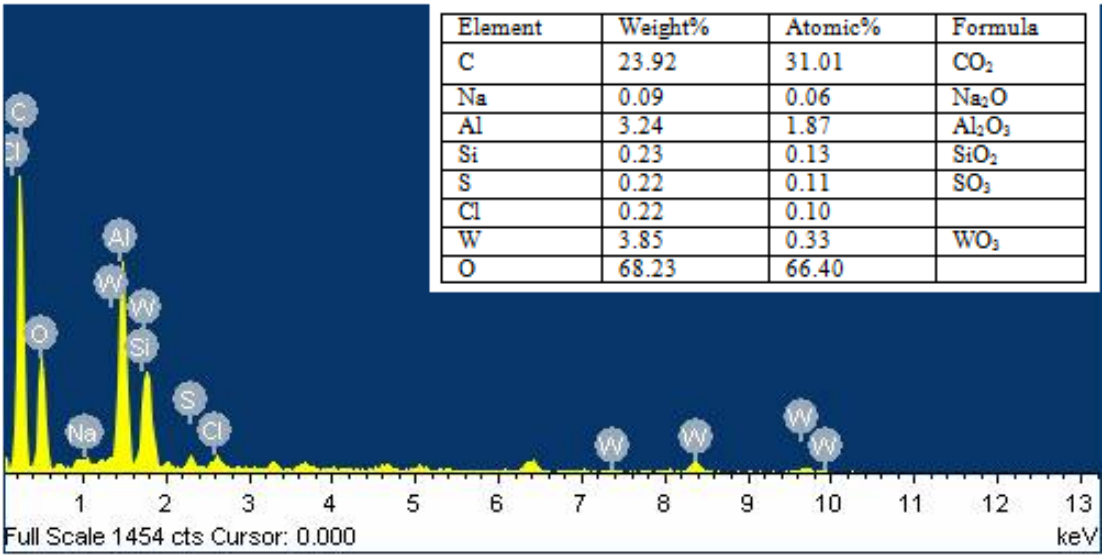

Element	Weight%	Atomic%	Formula
C	23.92	31.01	CO_2
Na	0.09	0.06	Na_2O
Al	3.24	1.87	Al_2O_3
Si	0.23	0.13	SiO_2
S	0.22	0.11	SO_3
Cl	0.22	0.10	
W	3.85	0.33	WO_3
O	68.23	66.40	

Fig 4.104 EDS of Micro Tool After Machining

Summary

The detailed experimental investigations were carried out to identify the important parameters, their ranges and levels, and successfully analyzed the effect of process parameters on machining response characteristics. The detailed experiments were carried out as per planned (explained in chapter 3) based on Taguchi design based L_{27} (3^{13}) orthogonal array. The acquired results were analyzed through ANOVA, and 'F-test' to identify the significant parameters. The S/N ratio graphs were plotted and optimize the parameters for effective micro machining of hybrid Al-MMC on developed ECMM set-up. The acquired results were also utilized to generate the various parameters interaction graphs and identify the effects of the

parameters on response characteristics. The Response Surface Methodology (RSM) based experiments were carried out, analyzed the acquired results on this investigation and optimized the process parameters for multi response characteristics during micro drilling of hybrid Al-MMC. The box-behkan design was used for experiments. Acquired results from RSM based experimentations were utilized to construct the ANOVA and identified the significant process parameters. The acquired results are also utilized to developed mathematical relation between the response and ECMM process parameters. The optimum parameter setting was identified and utilized for validity test. The developed mathematical relation and optimal parameter can be effectively utilized for micro machining of hybrid cast Al-MMC on developed ECMM set-up. The machined surfaces of hybrid Al-MMCs workpiece generated by developed ECMM set-up at different parametric setting were analyzed through various SEM photographs, EDX and XRD micrographs.

Introduction

This section presents the general conclusion drawn based on the outcome of the experimental investigation during micro drilling of hybrid Al/MMCs on developed ECMM set-up. In the research investigation, feasibility and effectiveness of the developed ECMM set-up was established through feasibility test during micro drilling of hybrid Al/MMCs. The liquid stir casting techniques was used to fabricate the hybrid Al/MMCs workpiece samples. The conventional machining i.e. facing, turning, and slicing operations were carried out to prepare the workpiece specimens for mechanical properties analysis, wear testing and micro drilling on ECMM set-up. The effects of machining parameters on response characteristics during micro drilling of Al/MMCs workpiece were analyzed through various graphs and explained in the thesis.

5.1 CONCLUSIONS

In this chapter explained the summary of the research work in the form of conclusions. Based on the results acquired during machining of Al/(SiCp+Al_2O_3p+Cp)-MMC on developed electrochemical micro machining (ECMM) set-up and discussions the following conclusions are drawn:

1. The hybrid Al/MMCs workpiece samples were fabricated utilizing liquid stir cast technique. The fabricated hybrid Al-MMCs samples were used as workpiece specimens. Physical and mechanical properties test were carried out to ascertain the soundness of liquid stir cast Al-MMCs samples. From the test results, it is concluded that the hardness (HRB) of hybrid Al/(10 wt% Al_2O_3p + 10 wt% SiCp + 5 wt% Cp)-MMC increases with increase in weight percentage of hard abrasive reinforcement i.e. SiC, Al_2O_3 and C particulates.
2. The lowest wear rate of hybrid MMC at the composition of Al/(20 wt% SiCp + 7.5 wt% Cp + 10 wt% Al_2O_3p) found to be 0.3 mg/min at applied load of 9.82 N, sliding speed of 300 rpm and track diameter of 60 mm.
3. The highest wear rate (1.5 mg/min) was identified at 14.72N, 300 rpm and 60 mm track diameter when wear tests were carried out on hybrid Al/(20 wt% SiCp + 10 wt% Al_2O_3p + 7.5 wt% Cp) –MMC specimens.
4. Al_2O_3 -10% showed the highest wear resistance under high load and speed at dry sliding condition.

5. From SEM micrograph of wear surface, it was noticed that some hard particles were pulled out, which resulted in formation of grooves. It was also noticed that the surface of composite Al/(10 wt% SiCp + 3 wt% Cp + 5 wt% Al_2O_3p)- MMC and Al/(15 wt% SiCp + 5 wt% Cp + 7.5 wt% Al_2O_3p)- MMC were rough with deep grooves as compared to composite specimen Al/(20 wt% SiCp + 7.5 wt% Cp + 10 wt% Al_2O_3p)- MMC.
6. The composite Al/(20 wt% SiCp + 7.5 wt% Cp + 10 wt% Al_2O_3p)-MMC specimen shows smooth surface, it may be due to the presence of carbon. It smears out during sliding and acts as a layer, protecting the specimen from direct contact with the disc, as a result increase the wear resistance.
7. The impact load was improved by 7.42%, 11.31% and 10.58% for hybrid Al/(10 wt% Al_2O_3p + 10 wt% SiCp + 5 wt% Cp)-MMC over Al/(10 wt% Al_2O_3p + 10 wt% SiCp)-MMC, Al/(10 wt% Al_2O_3p + 5 wt% Cp)-MMC and Al/(10 wt% SiCp + 5 wt% Cp)-MMC respectively.
8. The hardness was improved by 30.39% and 31.41% for Al/(10 wt% Al_2O_3p + 10 wt% SiCp + 5 wt% Cp)-MMC over Al/(10 wt% Al_2O_3p + 5 wt% Cp)-MMC and Al/(10 wt% SiCp + 5 wt% Cp)-MMC respectively.
9. From worn surface analysis by EDS, it is identified that the predominant peaks are aluminium and reinforced particles with carbon, silicon and oxygen. The oxide present in the worn surface act as protective layer. The presence of carbon and silicon carbide are also identified in the hybrid composite thereby enhance wear resistance.
10. The ECMM set-up was indigenously designed and fabricated for experimental investigation. The acquired results from feasibility experiments revealed that the fabricated set-up can be effectively used for drilling of micro holes on hybrid hybrid Al/(Al_2O_{3p}+SiC_p+C_p)-MMC workpiece.
11. Micro machined surface was analyzed through SEM and EDS photographs. The deposition of debris, voids and micro-cracks were identified on some of the machined surfaces. Some deeper and wider micro cracks were also identified on the machined surface and it may be due to supply of high peak current.
12. At high supply voltage, increase the impact of discharge energy in the machining area, this leads to increase the dissolution rate of metal thereby deteriorates the machined surface. The machined surface was poor and it may be due to the presence of small particles of sodium and chloride on the periphery of machined hole.
13. The percentage of contribution of each parameter was evaluated for various output quality characteristics. It was found that the parameters such as supply voltage, pulse on

time and electrolyte concentration are the most significant parameters for response characteristics i.e. MRR, EWR, TC and SR.

14. The surface roughness increases due to increase of electrolyte concentration, supply voltage and pulse on time. It may be due to the non-uniform metallic dissolution of material. The large number of ions associated in the inter electrode gap at high concentration of electrolyte and high supply voltage.
15. The material removal rate and electrode wear rate both increase with increase in supply voltage, electrolyte concentration and pulse-on time. These may be due to increase of current density, which in turn increases the ionization of electrolyte.
16. The flow rate of electrolyte is an important parameter that directly affects the quality of micro-holes. The debris generated during micro electrochemical machining usually does not flush away when machining operation was carried out at low flow rate of electrolyte. This is also one of the significant reasons of more material dissolution along the lateral direction results in increase of overcut.
17. The formation of ferropargasite chlorous compound was identified, it is due to chemical dissolution of ferrous material and reaction with sodium chloride.
18. The micro tool worn out rate increases with increase in pulse-on time. From EDX analysis, it has been observed that the reinforced particles presence in hybrid MMC deposited on micro tool. This is due to the melting and re-solidification of hybrid MMC during machining by means of micro sparking at high supply voltage and pulse on time.
19. The optimal parametric combination for material removal rate is $V_3EC_3Ton_3\ FR_1$ i.e. 25V supply voltage, 25g/*l* Electrolyte concentration, 10µs pulse on time and 0.2 *l*/min flow rate.
20. The optimal parametric combination for minimum electrode wear rate is $V_1\ EC_2\ Ton_1FR_2$ i.e. 2V supply voltage, 10g/*l* Electrolyte concentration, 0.5µs pulse on time and 0.6 *l*/min flow rate.
21. The optimal parametric combination for minimum surface roughness height, Ra(µm) is $V_1\ EC_1Ton_1FR_1$ i.e. 2V supply voltage, 5g/*l* Electrolyte concentration, 0.5µs pulse on time and 0.2 *l*/min flow rate.
22. The parametric combination for minimum taper cut is $V_1EC_1\ Ton_1FR_1$ i.e. 2 V supply voltage, 5g/*l* Electrolyte concentration, 0.5µs pulse on time and 0.2 *l*/min flow rate.
23. Based on the response surface methodology (RSM) detail experiments were carried out and acquired results were used to developed mathematical relation between the ECMM process parameters and response characteristics. Confirmation experiments carried out and compared the results with the calculated values from developed mathematical

relations, and identified that the percentage of error is always less than 8.00%. Therefore, it is clear that the developed mathematical relationships can be effectively utilized for machining of liquid stir cast hybrid Al/(Al_2O_{3p}+SiC_p+C_p)-MMC.

24. The optimal combination for multi response optimization of ECMM parameters is supply current (IP) 0.5 A, supply voltage (V) 2.03 Volts, Pulse on time (Ton) 3.38 μs, Pulse off time (Toff) 6.26 μs, Electrolyte Concentration (EC) 14.38 g/l, and Electrolyte flow rate (Fr) 0.60 l/sec. This optimal parametric combination of ECMM parameters can be effectively used for machining of hybrid Al/(Al_2O_{3p}+SiC_p+C_p)-MMC in micro domain.

5.2 FUTURE SCOPE

1. Study can be performed during electrochemical micro machining of other MMCs and hybrid MMCs and analyze the test results.
2. Micro ECM experiments can be performed with varying the use of electrolyte such as HCL, Distilled water, and mix any additive or acid with NaCl etc. and investigate the results.
3. Study and can develop the machining set-up with assistance of Laser beam, or ultra sonic vibration assisted micro tool or any other advanced technique with ECMM and investigated on the develop set-up during machining of any other advanced conductive materials.
4. Micro channels or any other cavities, dimple array etc may be fabricated by designing the micro tools and investigation may be carried out.
5. Investigation can be done and optimized the ECMM parameters with any other techniques.

REFERENCES

1. Abrate S. and Walton D.A., "Machining of Composite Materials. Part I: Traditional Methods", Journal of Composite Manufacturing, 3, 1992, 75-83.
2. Agarwal S; and Rao PU, "Experimental Investigation of Surface Damage Formation and Material Removal Mechanism in SiC Grinding", International Journal of Machine Tools and Manufacture, 48, 2008, 698-710.
3. Ahlatci Hayrettin, Kocer Tolga, Candan Ercan and Cimenoglu Huseyin, "Wear Behaviour of Al/(Al_2O_{3p} + SiC_p) Hybrid Composites", Tribology International, 39, 2006, 213–220.
4. Ahna Se Hyun, Ryu,Shi Hyoung, Choi Deok Ki and Chu Chong Nam, "Electro-Chemical Micro Drilling Using Ultra Short Pulses", Journal of Precision Engineering, 28, 2004, 129–134.
5. Alidokht S.A., Zadeh A. Abdollah, Soleymani S., and Assadi H., "Microstructure and Tribological Performance of An Aluminium Alloy Based Hybrid Composite Produced by Friction Stir Processing", Materials and Design, 32, 2011, 2727–2733.
6. Andreas Ochsner, Lucas F.M. da Silva, and Holm Altenbach, "Mechanics and Properties of Composites Materials and Structures, Advanced Structured Materials", Springer Publications, 2012, ISSN 1869-8433.
7. Arik Halil, "Effect of Mechanical Alloying Process on Mechanical Properties of α-Si_3n_4 Reinforced Aluminum-Based Composite Materials", Journal of Materials and Design, 29, 2008, 1856–1861.
8. Asad A.B.M.A., Masaki Takeshi, Rahman M., Lim H.S., and Wong Y.S., "Tool-Based Micro-Machining", Journal of Materials Processing Technology, 192-193, 2007, 204–211.
9. Babbage J.M., and Mallick P.K., "Static Axial Crush Performance of Unfilled and Foam-Filled Aluminum–Composite Hybrid Tubes", Journal of Composite Structures, 70, 2005, 177–184.
10. Babu J.S.S., Kang C.G., and Kim H.H., "Dry Sliding Wear Behavior of Aluminum Based Hybrid Composites with Graphite Nanofiber–Alumina Fiber", Materials and Design, 32, 2011, 3920–3925.

11. Babu J.S.S.; and Kang C.G., "Nanoindentation Behaviour of Aluminium Based Hybrid Composites with Graphite Nanofiber/Alumina Short Fiber", Journal of Materials and Design, 31, 2010, 4881–4885.
12. Baradeswaran A., and Perumal A.E., "Influence of B_4C on the Tribological and Mechanical Properties of Al 7075-B_4C Composites", Composite Part B, 54, 2013, 146–152.
13. Baradeswaran A., Vettivel S.C., Elaya Perumal A., Selvakumar N., and Franklin Issac R, "Experimental Investigation on Mechanical Behaviour, Modeling and Optimization of Wear Parameters Of B_4C and Graphite Reinforced Aluminium Hybrid Composites", Materials and Design, 63, 2014, 620–632.
14. Bartolome Jose F., Gutierrez-Gonzalez C.F., and Torrecillas Ramon, "Mechanical Properties of Alumina–Zirconia–Nb Micro–Nano-Hybrid Composites", Journal of Composites Science and Technology, 68, 2008, 1392–1398.
15. Basavarajappa S., Chandramohan G., and Davim J. Paulo, "Application of Taguchi Techniques to Study Dry Sliding Wear Behaviour of Metal Matrix Composites", Journal of Materials and Design, 28, 2007, 1393–1398.
16. Basavarajappa S., Chandramohan G., and Davim J. Paulo, "Some Studies on Drilling of Hybrid Metal Matrix Composites Based on Taguchi Techniques", Journal of Materials Processing Technology, 196, 2008, 332–338.
17. Basavarajappa S., Chandramohan G., Mahadevan Arjun, Thangavelu Mukundan, Subramanian R., and Gopalakrishnan P., "Influence of Sliding Speed on the Dry Sliding Wear Behaviour and the Subsurface Deformation on Hybrid Metal Matrix Composite", Journal of Wear, 262, 2007, 1007–1012.
18. Baughman R H, Zakhidon AA, and Diheer WA, "Carbon Nano Tubes the Route towards Applications", Journal of Science, 2002, 787-792.
19. Belingardi G., Cavatorta M.P. and Frasca C., "Bending Fatigue Behavior of Glass–Carbon/Epoxy Hybrid Composites", Journal of Composites Science and Technology, 66, 2006, 222–232.
20. Benedict G. F., "Nontraditional Manufacturing Processes", Marcel Dekker, New York and Basel, 1987.

21. Bhattacharyya B., “Chapter - Electrochemical Micro Machining”, Introduction to Micromachining, Jain V K, editor, Narosa Publisher, Delhi, 2010, 13.1-13.32, ISBN 10: 8173199159.
22. Bhattacharyya B., and Munda J., “Experimental Investigation into Electrochemical Micro Machining (EMM) Process”, Journal of Materials Processing Technology, 140, 2003, 287–291.
23. Bhattacharyya B., and Munda J., “Experimental Investigation on the Influence of Electrochemical Machining Parameters on Machining Rate and Accuracy in Micromachining Domain”, International Journal of Machine tools & Manufacture, 43, 2003, 1301-1319.
24. Bhattacharyya B., Doloi B., and Sidhar P. S., “Electrochemical Micro-Machining: New Possibilities for Micro-Manufacturing”, Journal of Materials Processing Technology, 113, 2001, 301-305.
25. Bhattacharyya B., Malapati M., and Munda J., “Experimental Study on Electrochemical Micromachining”, Journal of Materials Processing Technology, 169, 2005, 485-492.
26. Bhattacharyya B., Malapati M., Munda J., and Sarkar A., “Influence of Tool Vibration on Machining Performance in Electrochemical Micro Machining of Copper”, International Journal of Machine Tools & Manufacture, 47, 2007, 335–342.
27. Bhattacharyya B., Mitra S., and Boro A.K., “Electrochemical Machining: New Possibilities for Micro Machining”, Robotics and Computer Integrated Manufacturing, 18, 2002, 283-289.
28. Bhattacharyya B., Munda J., and Malapati M., “Advancement in Electrochemical Micro Machining”, International Journal of Machine Tools & Manufacture, 44, 2004, 1577–1589.
29. Botelho E.C., Silva R.A., Pardini L.C., and Rezende M.C., “A Review on the Development and Properties of Continuous Fiber/Epoxy/Aluminum Hybrid Composites for Aircraft Structures”, Journal of Material Resources, 9, 2006, 247–56.
30. Chan Hee Jo, Bo Hyun Kim, and Chong Nam Chu, “Micro Electrochemical Machining for Complex Internal Micro Features”, CIRP Annals - Manufacturing Technology, 58, 2009, 181–184.

31. Chen Xiaolei, Qua Ningsong, Lia Hansong, and Guo Zhongning, “Removal of Islands from Micro Dimple Arrays Prepared by Through Mask Electrochemical Micromachining”, Precision Engineering, 39, 2015, 204–211.
32. Chiou Yuang-Cherng, Lee Rong-Tsong, Chen Tai-Jia, and Chiou Jing-Mei, “Fabrication of High Aspect Ratio Micro-Rod Using A Novel Electrochemical Micro-Machining Method”, Precision Engineering, 36, 2012, 193– 202.
33. Choi S. H., Ryu S. H., Choi D. K. and Chu C. N., “Fabrication of WC Micro-shaft by using Electrochemical Etching”, International Journal of Advanced Manufacturing Technology, 31, 2007, 682-687.
34. Choi Se Hwan, Kim Bo Hyun, Shin Hong Shik, Chung Do Kwan, and Chu Chong Nam, “Analysis of the Electrochemical Behaviors of WC–Co Alloy for Micro ECM”, Journal of Materials Processing Technology, 213, 2013, 621– 630.
35. Da Silva Neto Joao Cirilo, Da Silva Evaldo Malaquias, and Da Silva Marcio Bacci, “Intervening Variables in Electrochemical Machining”, Journal of Materials Processing Technology, 179, 2006, 92-96.
36. Daniel Gay, Suong V. Hoa, and Stephen W. Tsai, “Composite Materials Design and Applications”, Publication by CRC Press LLC, 2003, ISBN 1420031686, 9781420031683.
37. Datta M., “Micro Fabrication of Electrochemical Metal Removal”, IBM Journal of Research and Development, 42, 1998, 655-669.
38. Datta M., Shenoy R. V., and Rominkiw L. T., “Recent Advances in the Study of Electrochemical Micro Machining”, Transactions of ASME, 118, 1996, 29-36.
39. De Silva A. K. M., Altena H. S. J., and McGeough J. A., “Precision ECM by Process Characteristics Modeling”, Annals of CIRP, 49, 2000, 151-156.
40. Deconinck D., Damme S. Van, Albu C., Hotoiu L. and Deconinck J., “Study of The Effects of Heat Removal on the Copying Accuracy of the Electrochemical Machining Process”, Electrochimica Acta, 56, 2011, 5642–5649.
41. Durantea S., Rutellib G. and Rabezzana F., “Aluminum-Based MMC Machining with Diamond-Coated Cutting Tools”, Journal of Surface and Coatings Technology, 94-95, 1997, 632-640.

42. El Hofy Gawad Hassan Abdel, Advanced Machining Processes Nontraditional and Hybrid Machining Processes", McGraw Hill, 2005, ISBN 0-07-145334-2.
43. Fan Zhijian, Wang Tiancheng, and Zhong Ling, "The Mechanism of Improving Machining Accuracy of ECM by Magnetic Field", Journal of Materials Processing Technology, 149, 2004, 409–413.
44. Fan Zhi-Wen, and Hourng Lih-Wu, "Electrochemical Micro-drilling of Deep Holes by Rotational Cathode Tools", International Journal of Advanced Manufacturing Technology, 52, 2011, 555-563.
45. Fan Zhi-Wen, and Hourng Lih-Wu, "The Analysis and Investigation on the Microelectrode Fabrication by Electrochemical Machining", International Journal of Machine Tools & Manufacture, 49, 2009, 659–666.
46. Fang F. Z., Liu K., Kurfess T. R., and Lim G. C., "Tool Based Micro Machining and Applications in MEMS", MEMS/NEMS Handbook Techniques and Applications, 3, Manufacturing Methods, 2006, 63-125.
47. Feng Y.C., Geng L., Li A.B., and Zheng Z.Z., "Fabrication and Characteristics of in Situ Al12W Particles Reinforced Aluminium Matrix Composites by Reaction Sintering", Journal of Materials and Design, 31, 2010, 965–967.
48. Feng Y.C., Geng L., Zheng P.Q., Zheng Z.Z., and Wang G.S., "Fabrication and Characteristic of Al-based Hybrid Composite Reinforced with Tungsten Oxide Particle and Aluminum Borate Whisker by Squeeze Casting", Journal of Materials and Design, 29, 2008, 2023–2026.
49. Fu Hui-Hui, Han Kyung-Seop; and Jung Song, "Wear Properties of Saffil/Al, Saffil/Al_2O_3/Al and Saffil/SiC/Al Hybrid Metal Matrix Composites", Journal of Wear, 256, 2004, 705–713.
50. Grosz Dolata A., Formanek B., Sleziona J., and Wieczorek J., "Al–FeAl–TiAl–Al_2O_3 Composite with Hybrid Reinforcement", Journal of Materials Processing Technology 162–163, 2005, 33–38.
51. Guo Qing Bing, Rong Min Zhi, Jia Guo Liang, Lau Kin Tak, and Zhang Ming Qiu, "Sliding Wear Performance of Nano-SiO_2/Short Carbon Fiber/Epoxy Hybrid Composites", Journal of Wear, 266, 2009, 658–665.

52. Gupta M., Lai M.O., and Lim C.Y.H., "Development of A Novel Hybrid Aluminum-Based Composite with Enhanced Properties", Journal of Materials Processing Technology, 176, 2006, 191–199.
53. Hao Xiuqing, Wang Li, Wang Quandai, Guo Fangliang, Tang Yiping, Ding Yucheng, and Lu Bingheng, "Surface Micro-Texturing of Metallic Cylindrical Surface with Proximity Rolling-Exposure Lithography and Electrochemical Micromachining", Journal of Applied Surface Science, 257 (21), 2011, 8906-8911.
54. Hewidy M.S., Ebeid S.J, El-Taweel T.A. and Youssef A.H., "Modelling the Performance of ECM Assisted by Low Frequency Vibrations", Journal of Materials Processing Technology, 189, 2007, 466–472.
55. Holstein N., Krauss W. and Konys J., "Structuring of Tungsten by Pulsed ECM Processes for He-cooled Divertor Application", Journal of Fusion Engineering and Design, 83, 2008, 1512–1516.
56. Huaiqian Bao, Jiawen Xu and Ying Li, "Aviation-Oriented Micromachining Technology-Micro-ECM in Pure Water", Chinese Journal of Aeronautics, 21, 2008, 455-461.
57. Iacob Gheorghe, Ghica Valeriu Gabriel, Buzatu Mihai, Buzatu Traian, Petrescu Mircea Ionut, "Studies on Wear Rate and Micro-Hardness of the $Al/Al_2O_3/Gr$ Hybrid Composites Produced Via Powder Metallurgy", Composites: Part B, 69, 2015, 603–611.
58. Ibrahim Ciftci, Mehmet Turker, and Ulvi Seker, "CBN Cutting Tool Wear During Machining of Particulate Reinforced MMCs", Journal of Wear, 257, 2004, 1041–1046.
59. Jackson, Mark J., "Micro and Nano Manufacturing", Springer Publications, 2007, ISBN 978-0-387-26132-4
60. Jain V. K., "Advanced Machining Processes", Allied Publishers, Delhi. 2002, ISBN: 9788177642940.
61. Jain V. K., "Introduction to Micromachining", Narosa Publisher, Delhi. 2010, ISBN-10: 1842654853.
62. Jeyasimman D., Narayanasamy R., Ponalagusamy R., Anandakrishnan V., and Kamaraj M., "The Effects of Various Reinforcements on Dry Sliding Wear Behavior of AA 6061 Nanocomposites", Materials and Design, 64, 2014, 783–793.

63. Jo Chan Hee, Kim Bo Hyun, and Chu Chong Nam, "Micro Electrochemical Machining for Complex Internal Micro Features", CIRP Annals - Manufacturing Technology, 58, 2009, 181–184.
64. Khalid Y.A., Mutasher S.A., Sahari B.B., and Hamouda A.M.S., "Bending Fatigue Behavior of Hybrid Aluminum/Composite Drive Shafts", Journal of Materials and Design, 28, 2007, 329–334.
65. Kim B.H., Na C.W., Lee Y.S., Choi D.K., and Chu C.N., "Micro Electrochemical Machining of 3D Micro Structure using Dilute Sulfuric Acid", Annals of CIRP, 54, 2005, 191-194.
66. Kim Hak Sung, Park Sang Wook, Hwang Hui Yun, and Lee Dai Gil, "Effect of the Smart Cure Cycle on the Performance of the Co-Cured Aluminum/Composite Hybrid Shaft", Journal of Composite Structures, 75, 2006, 276–288.
67. Kiran T.S., Kumar M. Prasanna, Basavarajappa S., and Viswanatha B.M., "Dry Sliding Wear Behavior of Heat Treated Hybrid Metal Matrix Composite using Taguchi Techniques", Materials and Design, 63, 2014, 294–304.
68. Kozak Jerzy, Rajurkar Kamlakar P. and Makkar Yogesh, "Selected Problems of Micro-Electrochemical Machining", Journal of Materials Processing Technology, 149, 2004, 426–431.
69. Kozak Jerzy, Rajurkar Kamlakar P., and Wei B., "Modeling and Analysis of Pulse Electrochemical Machining", Transactions of ASME, 116, 1994, 316-323.
70. Kumar K.L. Senthil, Sivasubramanian R., and Kalaiselvan K., "Selection of Optimum Parameters in Non Conventional Machining of Metal Matrix Composite", Journal of Portugaliae Electrochimica Acta, 27, 2009, 477-486.
71. Kunieda M., Mizugai K., Watanabe S., Shibuya N., and Iwamoto N., "Electrochemical Micromachining Using Flat Electrolyte Jet", CIRP Annals - Manufacturing Technology, 60 , 2011, 251–254.
72. Kurita Tsuneo and Hattori Mitsuro, "A study of EDM and ECM/ECM Lapping Complex Machining Technology", International Journal of Machine Tools & Manufacture, 46, 2006, 1804–1810.

73. Kurita Tsuneo, Chikamori Kunio, Kubota Shinichirou, and Hattori Mitsuro, "A Study of Three-dimensional Shape Machining with an ECμM System", International Journal of Machine Tools & Manufacture, 46, 2006, 1311-1318.
74. Kwak J.S., and Kim Y.S., "Mechanical Properties and Grinding Performance on Aluminum-Based Metal Matrix Composites", Journal of Materials Processing Technology, 201, 2008, 596–600.
75. Landolt D., Chauvy P. F., and Zinger O., "Electrochemical Micro Machining, Polishing and Surface Structuring of Metals: Fundamental Aspects and New Developments", Electrochimica Acta, 48, 2003, 3185-3201.
76. Lee E. S., Baek S. Y., and Cho C. R., "A Study of the Characteristics for Electrochemical Micromachining with Ultrashort Voltage Pulses", International Journal of Advanced Manufacturing Technology, 31, 2007, 762-769.
77. Lee Hyunseop, Kasuga Hiroshi, Ohmori Hitoshi, Lee Hojun; and Jeong Haedo, "Application of Electrolytic in-Process Dressing (ELID) Grinding and Chemical Mechanical Polishing (CMP) Process for Emerging Hard–Brittle Materials Used in Light-Emitting Diodes", Journal of Crystal Growth, 326 (1), 2011, 140-146.
78. Lee Shuo-Jen, Lee Chi-Yuan, Yang Kung-Ting, Kuan Feng-Hui, and Lai Ping-Hung, "Simulation and Fabrication of Micro-Scaled Flow Channels for Metallic Bipolar Plates by the Electrochemical Micro-Machining Process", Journal of Power Sources, 185, 2008, 1115–1121.
79. Li Xiaohai, Zhao Lijie, Wang Xinrong, and Wang Zhenlong, "Micro Electrochemical Machining and its Influencing Factors", Proceedings of the 16th International Symposium on Electromachining, 2010, 385-388.
80. Lim Y. M., and Kim S. H., "An Electrochemical Fabrication Method for Extremely Thin Cylindrical Micro Pin", International Journal of Machine Tools & Manufacture, 41, 2001, 2287-2296.
81. Liu Lei, Li Weiwei, Tang Yiping, Shen Bin, and Hu Wenbin, "Friction and Wear Properties of Short Carbon Fiber Reinforced Aluminium Matrix Composites", Journal of Wear, 266, 2009, 733–738.
82. Liu Yixiong, Chen Weiping, Yang Chao, Zhu Dezhi, Li Yuanyuan, "Effects of Metallic Ti Particles on the Aging Behavior and the Influenced Mechanical Properties of Squeeze-

Cast (SiCp+Ti)/7075Al Hybrid Composites", Materials Science & Engineering A, 620, 2015, 190–197.

83. Liu Yong, Zhu Di, Zeng Yongbin and Yu Hongbing, "Development of Microelectrodes for Electrochemical Micromachining. International Journal of Advanced Manufacturing Technology", 55, 2011, 195-203.
84. Liu Yong, Zhu Di, Zeng Yongbin, Huang Shaofu and Hongbing Yu, "Experimental Investigation on Complex Structures Machining by Electrochemical Micromachining Technology", Chinese Journal of Aeronautics, 23, 2010, 578-584.
85. Liu Zhuang, Nouraei Hooman, Spelt Jan K., and Papini Marcello, "Electrochemical Slurry Jet Micro-Machining of Tungsten Carbide with A Sodium Chloride Solution", Precision Engineering, 40, 2015, 189–198.
86. Mahmoud Essam R.I., Takahashi Makoto, Shibayanagi Toshiya and Ikeuchi Kenji, "Wear Characteristics of Surface-Hybrid-Mmcs Layer Fabricated on Aluminum Plate by Friction Stir Processing", Journal of Wear, 268, 2010, 1111–1121.
87. Manna A., and Bhattacharayya B., "A Study on Machinability of Al/SiC-MMC", Journal of Materials Processing Technology 140, 2003, 711-716.
88. Masuzava T., Kua C. L. and Fujino, "A Combined Electrical Machining Process for Micro Nozzle Fabrication", Annals of the CIRP, 43, 1994, 189-192.
89. Mazaheri Y., Karimzadeh F., and Enayati M.H., "A Novel Technique for Development of A356/Al_2O_3 Surface Nanocomposite by Friction Stir Processing", Journal of Materials Processing Technology, 211, 2011, 1614– 1619.
90. Mithu M. A. H., Fantoni G., and Ciampi J., "A Step Towards the In-Process Monitoring for Electrochemical Microdrilling", International Journal of Advanced Manufacturing Technology, 57, 2011, 969-982.
91. Mithu M. A. H., Fantoni G., and Ciampi J., "The Effect of High Frequency and Duty Cycle in Electrochemical Microdrilling", International Journal of Advanced Manufacturing Technology, 55, 2011, 921-933.
92. Mithu M.A.H., Fantoni G., Ciampi J., and Santochi M., "On How Tool Geometry, Applied Frequency and Machining Parameters Influence Electrochemical Microdrilling", CIRP Journal of Manufacturing Science and Technology, 5, 2012, 202–213.

93. Montalba C., Ramam K., Eskin D.G., Ruiz-Navas E.M., and Prat O., “Fabrication of a Novel Hybrid AlMg5/SiC/PLZT Metal Matrix Composite Produced by Hot Extrusion”, Materials and Design, 69, 2015, 213–218.
94. Muller F., and Monaghan J., “Non-Conventional Machining of Particle Reinforced Metal Matrix Composite”, International Journal of Machine Tools and Manufacture, 40, 2000, 1351-1366.
95. Munda J., Malapati M. and Bhattacharyya B., “Control of Micro-Spark and Stray-Current Effect during EMM Process”, Journal of Materials Processing Technology, 194, 2007, 151–158.
96. Mutasher S.A., “Prediction of the Torsional Strength of the Hybrid Aluminum/Composite Drive Shaft”, Journal of Materials and Design, 30, 2009, 215–220
97. Myalski, Wieczorek J., and Grosz A Dolata, “Tribological Properties of Heterophase Composites with an Aluminium Matrix”, Journal of Achivement in Materials and Manufacturing Engineering, 15, 2006, 53-57.
98. Natsu W., Ooshiro S., and Kunieda M., “Research on Generation of Three-Dimensional Surface with Micro-Electrolyte Jet Machining”, CIRP Journal of Manufacturing Science and Technology, 1, 2008, 27–34.
99. Nguyen Minh Dang, Rahman Mustafizur, and Wong Yoke San, “Modeling of Radial Gap Formed by Material Dissolution in Simultaneous Micro-EDM and Micro-ECM Drilling using Deionized Water”, International Journal of Machine Tools & Manufacture, 66, 2013, 95–101.
100. Oh K.H., and Han K.S., “Short-Fiber/Particle Hybrid Reinforcement: Effects on Fracture Toughness and Fatigue Crack Growth of Metal Matrix Composites”, Journal of Composites Science and Technology, 67, 2007, 1719–1726.
101. Ohmori H., Katahira K., Vehara Y., Watanable Y., and W. Liu., “Improvement of Mechanical Strength of Microtools by Controlling Surface Characteristics”,. Annals of the CIRP, 52, 2003, 467-470.
102. Osenbrugger C., Van., and C. De., “Electrochemical Micro Machining”, Philips Tech. Rev., 42, 1985, 22-32.

103. Ozdemir I., Muecklich S., Podlesak H.; and Wielage B., “Thixoforming of AA 2017 Aluminum Alloy Composites”, Journal of Materials Processing Technology 211, 2011, 1260–1267.
104. Pa P.S., “Super Finishing with Ultrasonic and Magnetic Assistance in Electrochemical Micro-Machining”, Electrochimica Acta, 54, 2009, 6022–6027.
105. Park B.J., Kim B.H., and Chu C.N., “The Effects of Tool Electrode Size on Characteristics of Micro Electrochemical Machining”, Annals of the CIRP, 55, 2006, 197-200.
106. Park J.W., Lee E.S., Won C.H., and Moon Y.H., “Development of Electrochemical Micro Machining for Air-lubricated Hydrodynamic Bearings”, Microsystem Technologies, 9, 2002, 61-66.
107. Qian Shuangqing, Zhu Di, Qu Ningsong, Li Hansong and Yan Dongsheng, “Generating Micro-dimples Array on the Hard Chrome-Coated Surface by Modified Through Mask Electrochemical Micromachining”, International Journal of Advanced Manufacturing Technology, 47, 2010, 1121-1127.
108. Qu Ningsong, Chen Xiaolei, Li Hansong, and Zeng Yongbin, “Electrochemical Micromachining of Micro-Dimple Arrays on Cylindrical Inner Surfaces using a Dry-Film Photoresist”, Chinese Journal of Aeronautics, 27(4), 2014, 1030–1036.
109. Rajurkar K. P., Zhu D., McGeough A. J., Kozak J., and De Silva A., “New Developments in Electrochemical Machining”, Annals of the CIRP, 48, 1999, 567–579.
110. Rangelow Ivo W., “Dry Etching Based Silicon Micro Machining for MEMS”, Vacuum, 62, 2001, 279-291.
111. Rao R.N., Das S., Mondal D.P., and Dixit G., “Dry Sliding Wear Behaviour of Cast High Strength Aluminium Alloy (Al–Zn–Mg) and Hard Particle Composites”, Journal of Wear, 267, 2009, 1688–1695.
112. Rathod V., Doloi B., and Bhattacharyya B., “Experimental Investigations into Machining Accuracy and Surface Roughness of Microgrooves Fabricated by Electrochemical Micromachining”, Proc IMechE Part B: J Engineering Manufacture, 229(10), 2015, 1781–1802.

113. Rathod V., Doloi B., and Bhattacharyya B., “Sidewall Insulation of Microtool for Electrochemical Micromachining to Enhance the Machining Accuracy”, Materials and Manufacturing Processes, 29, 2014, 305–313.

114. Reihanian M., Keshavarz F. H., and Paydar M. H., “Fabrication of Al–2 vol% Al_2O_3/SiC Hybrid Composite via Accumulative Roll Bonding (ARB): An Investigation of the Microstructure and Mechanical Properties”, Materials Science & Engineering A, 607, 2014, 188–196.

115. Rosenkranz C., Lohrengel M.M., and Schultze J.W., “The Surface Structure During Pulsed ECM of Iron in $NaNO_3$”, Electrochimica Acta, 50, 2005, 2009–2016.

116. Ryu Shi Hyoung, “Micro Fabrication by Electrochemical Process in Citric Acid Electrolyte”, Journal of Materials Processing Technology 209, 2009, 2831–2837.

117. Sen Mohan and Shan H. S., “A Review of Electrochemical Macro- to Micro-Hole Drilling Processes”, International Journal of Machine Tools & Manufacture, 45, 2005, 137–152.

118. Shahzad Majid, Chaussumier Michel, Chieragatti Rémy, Mabru Catherine, and Farhad Rezai-Aria, “Surface Characterization and Influence of Anodizing Process on Fatigue Life of Al 7050 Alloy”, Materials and Design, 32, 2011, 3328–3335.

119. Shamanian Morteza, Mohammadnezhad Mahyar, Asgari Hamed, and Szpunar Jerzy, “Fabrication and Characterization of Al–Al_2O_3–ZrC Composite Produced by Accumulative Roll Bonding (ARB) Process”, Journal of Alloys and Compounds, 618, 2015, 19–26.

120. Sharifi Mohammad E., and Karimzadeh F., “Wear Behavior of Aluminum Matrix Hybrid Nanocomposites Fabricated by Powder Metallurgy”, Journal of Wear, 271 (7,8), 2011, 1072-1079.

121. Solaiyappan Ayyappan and Karuppan Sivakumar, “Investigation of Electrochemical Machining Characteristics of 20MnCr5 Alloy Steel using Potassium Dichromate Mixed Aqueous NaCl Electrolyte and Optimization of Process Parameters”, Proc IMechE Part B:J Engineering Manufacture, 229(11), 2015, 1984–1996.

122. Spieser Alexandre and Ivanov Atanas, “Design of An Electrochemical Micromachining Machine”, Int J Adv Manuf Technol, 78, 2015, 737–752.

123. Suresh S., Mortensen A., and Needleman A., “Fundamentals of Metal Matrix Composites”, Stoneham Butterworth-Heinemann, 1993, ISBN 0-7506-9321-5.

124. Suresh S., Shenbaga V.M., Vettivel S.C., Selvakumar N., and Jinu G.R., “Effect of Graphite Addition on Mechanical Behavior of Al6061/TiB_2 Hybrid Composite using Acoustic Emission”, Materials Science & Engineering A, 612, 16–27.

125. Suresha S. and Sridhara B.K., “Friction Characteristics of Aluminium Silicon Carbide Graphite Hybrid Composites”, Journal of Materials and Design, 34, 2012, 576-583.

126. Suresha S., and Sridhara B.K., “Effect of Addition of Graphite Particulates on the Wear Behaviour in Aluminium–Silicon Carbide–Graphite Composites”, Journal of Materials and Design, 31, 2010, 1804–1812.

127. Suresha S., and Sridhara B.K., “Effect of Silicon Carbide Particulates on Wear Resistance of Graphitic Aluminium Matrix Composites”, Journal of Materials and Design 31, 2010, 4470–4477.

128. Tahamtan S., Halvaee A., Emamy M., Jiang Z.Y., and Boostani A. Fadavi, “Exploiting Superior Tensile Properties of A Novel Network-Structure AlA 206 Matrix Composite by Hybridizing Micron-Sized Al_3Ti with Al_2O_3 Nano Particulates”, Materials Science & Engineering A, 619, 2014, 190–198.

129. Teng Chih-Chun, Ma Chen-Chi M., Chiou Kuo-Chan; and Lee Tzong-Ming, “Synergetic Effect of Thermal Conductive Properties of Epoxy Composites Containing Functionalized Multi-Walled Carbon Nanotubes and Aluminum Nitride”, Journal of Composites: Part B, 43 (2), 2012, 265-271.

130. Urena A., Rams J., Campo M., and Sanchez M., “Effect of Reinforcement Coatings on the Dry Sliding Wear Behaviour of Aluminium/SiC Particles/Carbon Fibres Hybrid Composites”, Journal of Wear, 266, 2009, 1128–1136.

131. Vogelesang LB., and Vlot A., “Development of Fibre Metal Laminates for Advanced”, Journal of Material Processing Technology, 103, 2000, 1–5.

132. Wang M. H., Zhu D.; and Peng W. (2008), “Experimental Research on Electrochemical Micro-machining”, Conference Proceedings on Advanced Design and Manufacture to Gain Competitive Edge, Springer, 775-784.

133. Wang W., Liu Z.X., Zhang W., Huang Y.H., and Allen D.M., "Abrasive Electrochemical Multi-Wire Slicing of Solar Silicon Ingots into Wafers", CIRP Annals - Manufacturing Technology, 60, 2011, 255–258.

134. Wang Y.Q., Afsar A.M., Jang J.H., Han K.S., and Song J.I., "Room Temperature Dry and Lubricant Wear Behaviors of Al_2O_{3f}/SiCp/Al Hybrid Metal Matrix Composites", Journal of Wear, 268, 2010, 863–870.

135. Wang Y.Q., and Song J.I., "Temperature Effects on the Dry Sliding Wear of Al_2O_{3f}/SiC_p/Al MMCs with Different Fiber Orientations and Hybrid Ratios", Wear, 270, 2011, 499-505.

136. www.metalcasting.com

137. Xiong Lu, and Yang Leng, "Electrochemical Micromachining of Titanium Surfaces for Biomedical Applications", Journal of Materials Processing Technology, 169, 2005, 173–178.

138. Xu Kun, Zeng Yongbin, Li Peng, and Zhu Di, "Study of Surface Roughness in Wire Electrochemical Micro Machining", Journal of Materials Processing Technology, 222, 2015, 103–109.

139. Yang Cheng-Kuang, Wu Kun-Ling, Hung Jung-Chou, Lee Shin-Min, Lin Jui-Che; and Yan Biing-Hwa, "Enhancement of ECDM Efficiency and Accuracy by Spherical Tool Electrode", International Journal of Machine Tools & Manufacture, 51, 2011, 528–535.

140. Yang Ye, Natsub Wataru and Zhao Wansheng, "Realization of Eco-Friendly Electrochemical Micromachining Using Mineral Water as an Electrolyte", Journal of Precision Engineering, 35, 2011, 204–213.

141. Zhang X.N., Geng L., and Wang G.S., "Fabrication of Al-based Hybrid Composites Reinforced with SiC Whiskers and SiC Nanoparticles by Squeeze Casting", Journal of Materials Processing Technology, 176, 2006, 146–151.

142. Zhang Zhaoyang, Wang Yaomin, Chen Fei, and Mao Weiping, "A Micro Machining System Based on Electrochemical Dissolution of Material", Russian Journal of Electrochemistry, 47, 2011, 819-824.

143. Zhao L.Z., Zhao M.J., Cao X.M., Tian C., Hu W.P., and Zhang J.S., "Thermal Expansion of a Novel Hybrid SiC foam–SiC Particles–Al Composites", Journal of Composites Science and Technology, 67, 2007, 3404–3408.

144. Zhu D., Qu N.S., Li H.S., Zeng Y.B., L D.L., and Qian S.Q., "Electrochemical Micromachining of Microstructures of Micro Hole and Dimple Array", CIRP Annals - Manufacturing Technology, 58, 2009, 177–180

145. Zhu D., Wang K., and Qu, N. S. "Micro Wire Electrochemical Cutting by Using in Situ Fabricated Wire Electrode", Annals of the CIRP, 56, 2007, 241-244.

146. Zhu D., Zeng Y.B., Xu Z.Y., and Zhang X.Y., "Precision Machining of Small Holes By The Hybrid Process of Electrochemical Removal and Grinding", CIRP Annals - Manufacturing Technology, 60, 2011, 247–250.

147. Zhu Y., and Kishawy H.A., "Influence of Alumina Particles on the Mechanics of Machining Metal Matrix Composites", International Journal of Machine Tools & Manufacture, 45, 2005, 389–398.

148. ZHU Yongwei, and YUN Naizhangt, "The Basic Study on USM ECM Combined Micro-Machining", International Technology and Innovation Conference, 2006, 581-586.